

Short-stroke, single-phase tubular permanent magnet motors for refrigeration applications

Taib Ibrahim, *BEng., MSc*

A thesis submitted for the degree of Doctor of Philosophy
Department of Electronic and Electrical Engineering
University of Sheffield, Mappin Street
Sheffield S1 3JD
United Kingdom

May 2009



ABSTRACT

The need for reduction of CO₂ emission from refrigerator compressors has motivated the research which is described in this thesis. The main focus is the development of high efficiency linear motors for direct-drive linear compressor systems to be used in domestic refrigerators. Three design variants of tubular moving-magnet linear motors are identified as potential candidates. The analytical methods are established for predicting open-circuit flux density distribution, flux-linkage, back-emf and thrust force for each motor and the results are validated by finite element analysis. The leading design parameters of the motors are optimised analytically for maximum efficiency under the rated operating condition and volumetric constraints, with due account of the effect of compressor loads under the nominal operating condition. The analytically optimised designs are further refined using finite element method, which can accommodate more complex geometries and material non-linearities. Eddy current loss in rare-earth NdFeB permanent magnets and in supporting tube, and iron loss in the stator cores of the moving-magnet motors are also analysed extensively using finite element method. The influence of circumferential segmentation of the permanent magnets and the supporting tube on the eddy current loss is investigated, and the iron loss is evaluated against various armature velocity profiles under both no-load and on-load conditions.

For the purpose of cost reduction, a tubular moving-iron linear motor which employs relatively cheap permanent magnet material, Strontium ferrite, is investigated, and its leading design parameters are optimised using finite element analysis technique.

A representative prototype motor was constructed and its static performance, such as flux linkage, cogging force and thrust force were measured. The measured results are compared with finite element predictions. The measurement of no-load iron loss was also carried out using specially designed test rig and suspension springs to eliminate frictional loss, and the on-load iron loss was obtained by subtracting the copper loss and eddy current loss from the measured input power when the motor was operating at resonant frequencies with variation of strokes. The measured results validate the analytical and finite element predictions. Finally, the motor efficiency has been measured based on separation of mechanical loss and electromagnetic loss.

ACKNOWLEDGEMENTS

First and foremost, I would like to express my sincere gratitude to my supervisors, Dr Jiabin Wang and Emeritus Professor David Howe for their continuous guidance, encouragement and outstanding support that lead to the accomplishment of my four year PhD study at the University of Sheffield. Without their supports, my studies would have been very difficult indeed.

Special thanks go to the top management of Universiti Teknologi PETRONAS in Malaysia for their financial support which has enabled me to pursue my PhD study, and provide the strength motivation to me throughout the research being carried out.

Thanks are also to colleagues of the Electrical Machines and Drives Research Group, past and present, for their technical advice, and for providing a lively and friendly atmosphere.

Finally, I would also like to record my deepest appreciation and thanks to my wife, Asma Binti Shuib and children for their continuous moral support to complete this difficult task.

CONTENTS

Page

ABSTRACT	i
ACKNOWLEDGEMENTS	ii
NOMENCLATURES	vii
List of figures	x
List of tables	xvii
CHAPTER 1: INTRODUCTION AND LITERATURE REVIEW	
1.1 Introduction	1
1.2 Aim of research	6
1.3 Basic operation of linear motors	6
1.4 Literature review on linear machine technologies	8
1.4.1 Linear induction machines	9
1.4.2 Linear synchronous machines	10
1.4.3 Linear switched reluctance machines	10
1.4.4 Linear DC machines	11
1.4.5 Linear permanent magnet machines	11
1.4.5.1 Moving-coil motors	12
1.4.5.2 Moving-iron motors	18
1.4.5.3 Moving-magnet motors	23
1.5 Proposed designs	31
1.6 Conclusions	33
1.7 Scope of research	33
1.7.1 Scope of thesis	34
References	35
CHAPTER 2: ANALYSIS OF OPEN-CIRCUIT MAGNETIC FIELD DISTRIBUTION, FLUX-LINKAGE, BACK-EMF AND THRUST FORCE IN TUBULAR MOVING-MAGNET LINEAR MOTORS	
2.1 Introduction	44
2.2 Open-circuit magnetic field distribution	46
2.3 Flux-linkage, back-emf and thrust force	53
2.4 Magnetisation patterns	55
2.4.1 Quasi-Halbach magnetisation – rectangular magnets	55
2.4.2 Quasi-Halbach magnetisation – trapezoidal magnets	56
2.5 Comparison with results from finite element analyses for open-circuit magnetic field distribution	60
2.5.1 Iron-cored quasi-Halbach magnetised motor with rectangular magnets	61
2.5.2 Air-cored quasi-Halbach magnetised motor with rectangular magnets	62
2.5.3 Iron-cored quasi-Halbach magnetised motor with trapezoidal magnets	64

2.6	Comparison with analytical results for different motors	65
2.6.1	Air-cored and iron-cored quasi-Halbach magnetised motor with rectangular magnets	65
2.6.2	Iron-cored quasi-Halbach magnetised motor with rectangular and trapezoidal magnets	66
2.7	Comparison with finite element predicted back-emf	67
2.7.1	Iron-cored quasi-Halbach magnetised motor with rectangular magnets	67
2.7.2	Air-cored quasi-Halbach magnetised motor with rectangular magnets	68
2.7.3	Iron-cored quasi-Halbach magnetised motor with trapezoidal magnets	69
2.8	Discussions	69
2.9	Conclusions	70
	References	70

CHAPTER 3: DESIGN OPTIMISATION OF SHORT-STROKE, SINGLE-PHASE TUBULAR PERMANENT MAGNET MOTORS

3.1	Introduction	73
3.2	Modelling of direct-drive compressor systems	73
3.2.1	Mechanical model	74
3.2.2	Compressor model	75
3.2.2.1	No pumping operation	76
3.2.2.2	Pumping operation	77
3.2.3	Linear motor model	78
3.2.4	Steady state model	78
3.3	Number of coil turns	81
3.4	Iron loss calculation	83
3.4.1	No-load condition	84
3.4.1.1	Tooth tip region	84
3.4.1.2	Tooth region	86
3.4.1.3	Yoke region	87
3.4.2	On-load condition	87
3.5	Motor design dimensions	90
3.6	Design optimisation	93
3.6.1	Air-cored quasi-Halbach magnetised motor with rectangular magnets	95
3.6.1.1	Influence of T_{mv}/T_p and R_m/R_e	95
3.6.1.2	Influence of tooth pitch width, T_{pw}	98
3.6.1.3	Influence of remanence of permanent magnets, B_{rem}	100
3.6.2	Iron-cored quasi-Halbach magnetised motor with trapezoidal magnets	101
3.6.2.1	Influence of T_{mv}/T_p and R_m/R_e	101
3.7	Design refinement with finite element analysis	105
3.7.1	Air-cored quasi-Halbach magnetised motor with rectangular magnets	106

3.7.2	Iron-cored quasi-Halbach magnetised motor with trapezoidal magnets	107
3.8	Summary of final design dimension	108
3.9	Conclusions	110
	References	110

CHAPTER 4: DESIGN AND OPTIMISATION OF A MOVING-IRON LINEAR MOTOR FOR RECIPROCATING COMPRESSORS USING FINITE ELEMENT ANALYSIS

4.1	Introduction	113
4.2	Performance evaluations	115
4.2.1	Open-circuit flux distribution and back-emf	115
4.2.2	Motor efficiency	117
4.3	Design optimisation	119
4.3.1	Motor design dimensions	119
4.3.2	Influence of width of armature tooth, T_r	123
4.3.3	Influence of height of armature tooth, H_r	125
4.3.4	Influence of R_o/R_e	126
4.3.5	Influence of height of permanent, H_m	127
4.4	Two parameters optimisation	129
4.5	Comparison material cost and performance	130
4.6	Conclusions	134
	References	

CHAPTER 5: ANALYSIS OF EDDY CURRENT LOSS AND IRON LOSS IN TUBULAR PERMANENT MAGNET LINEAR MOTORS USING FINITE ELEMENT METHOD

5.1	Introduction	137
5.2	Eddy current loss	138
5.2.1	Two- and three-dimensional finite elements models	138
5.2.2	Eddy current at no-load condition	141
5.2.2.1	Air-cored quasi-Halbach magnetised motor with rectangular magnets	144
5.2.2.2	Iron-cored quasi-Halbach magnetised motor with trapezoidal magnets	146
5.2.3	Eddy current at on-load condition	149
5.2.3.1	Air-cored quasi-Halbach magnetised motor with rectangular magnets	151
5.2.3.2	Iron-cored quasi-Halbach magnetised motor with trapezoidal magnets	153
5.3	Iron loss calculation	157

5.3.1	No-load condition	160
5.3.2	On-load condition	165
5.4	Conclusions	170
	References	171

CHAPTER 6: EXPERIMENTAL VALIDATION OF SHORT-STROKE, SINGLE-PHASE TUBULAR PERMANENT MAGNET MOTORS

6.1	Introduction	173
6.2	Prototyping of air-cored quasi-Halbach magnetised motor with rectangular magnets	173
6.3	Static test rig	175
6.4	Static test results	176
6.4.1	Flux linkage	176
6.4.2	Cogging force	177
6.4.3	Static thrust force	178
6.5	Iron loss test rig	178
6.6	Iron loss results	181
6.6.1	Measured data	181
6.6.2	Comparison with finite element analysis	184
6.7	Performance test	188
6.8	Conclusions	191
	References	191

CHAPTER 7: CONCLUSIONS AND FUTURE WORKS

7.1	Conclusions	194
7.2	Future works	197

APPENDICES

Appendix A	List of publications	198
Appendix B	Magnetisation formulae of trapezoidal magnets	199
Appendix C	Coefficient of the iron-cored motors	201
Appendix D	Coefficient of the air-cored motor	202
Appendix E	Analysis of eddy current loss in tubular permanent magnet linear motors using finite element method	203
Appendix F	Analytical solutions of iron-cored quasi-Halbach magnetised motor with trapezoidal magnets	211

NOMENCLATURES

Symbol	Description
Ψ_w	Total flux-linkage
θ	Stator tooth tip under cut angle, °
θ_e	Electrical angle, °
α	Coefficient of hysteresis loss component
β	Permanent magnet cut angle, °
ρ	Resistivity of copper at a given temperature, Ωm
μ_0	Permeability of air space, NA^{-2}
μ_r	Relative recoil permeability, NA^{-2}
A_θ	Vector magnetic potential
b_0	Width of slot opening, m
B_r	Flux density in radial direction, T
B_z	Flux density in axial direction, T
B_{rem}	Remanence of permanent magnet, T
e_w	Induced back-emf in a single-phase stator winding, V
f_e	Electromagnetic force of linear motor, N
f_g	Gas force in compressor, N
f_r	Mechanical resonant frequency, Hz
h_{eq}	Hysteretic damping coefficient of gas force
h_m	Radial thickness of magnet, mm
H_{rt}	Thickness of armature tube, mm
H_{st}	Height of stator tooth tip, mm
h_t	Tooth tip height, mm
H_{te}	Height of stator top edge cut, mm
H_{tr}	Height of armature tooth, mm
h_{ym}	Radial thickness of supporting tube, mm
h_{ys}	Thickness of stator yoke, mm

J_{rms}	.	Rms current density, Am^{-2}
K_c	.	Carter coefficient
K_e	.	Back-emf coefficient, Vm/s
k_e	.	Excess loss coefficient
k_{eq}	.	Stiffness coefficient of gas force
k_h	.	Coefficient of hysteresis loss
k_T	.	Total equivalent system spring stiffness, Nm^{-1}
K_T	.	Thrust force coefficient, N/A
L_e	.	Winding inductance of linear motor, H
m	.	Total moving mass, kg
N_c	.	Number of coil turns
P	.	Pressure in compression chamber, N/m^2
P_B	.	Piston back pressure, N/m^2
P_{cu}	.	Copper loss, W
P_D	.	Discharge pressure, N/m^2
P_f	.	Packing factor
P_{fe}	.	Iron loss, W
P_{out}	.	Output power, W
P_s	.	Suction pressure, N/m^2
P_t	.	Total input power, W
R	.	Winding resistance of linear motor, Ω
r	.	Average radius of coil, m
R_a	.	Outer radius of armature, mm
R_e	.	Outer radius of stator core, mm
R_i	.	Inner radius of supporting tube, mm
R_m	.	Outer radius of permanent magnets, mm
S	.	Cross-sectioned area of wire, m^2
S_a	.	Effective slot area, m^2
T_{be}	.	Width of armature tube cut, mm

T_{ex}	.	Stator end disk, mm
T_l	.	Separation distance between the two adjacent armatures, mm
T_m	.	Thickness of permanent magnet, mm
T_{mr}	.	Axial length of radially magnetized magnet at the centre, mm
T_{mr2}	.	Axial length of radially magnetised magnet at two ends, mm
T_{mz}	.	Axial length of axially magnetized magnet, mm
T_p	.	Pole-pitch, mm
T_{pe}	.	Extended tooth tip length, mm
T_{pw}	.	Width of tooth pitch, mm
T_{rt}	.	Width of armature tooth, mm
T_w	.	Width of stator tooth, mm
U	.	Amplitude of piston oscillation, m
V_{rms}	.	Rms supply voltage, V
x	.	Piston position referred to the cylinder head, m
X_o	.	Equilibrium piston position i.e. the centre of reciprocating oscillation, m
X_s	.	Static piston position when there is no displacement in spring, i.e. preset piston position, m

List of figures

- Fig. 1.1 - Schematic of conventional refrigerator compressor
- Fig. 1.2 - Efficiency of induction motor driven compressor
- Fig. 1.3 - Refrigeration cycle
- Fig. 1.5 - Schematic of direct-drive linear compressor
- Fig. 1.6 - Typical variation of mechanical resonant frequency with stoke and evaporator/ambient/compressor temperatures
- Fig. 1.7 - Development of linear induction and permanent magnet motors from rotary
- Fig. 1.8 - Basic concept of linear motion
- Fig. 1.9 - Single phase linear oscillating induction motor
- Fig. 1.10 - Tubular switched reluctance linear machine
- Fig. 1.11 - Tubular permanent magnet linear machine
- Fig. 1.12 - Moving-coil linear motor topologies
- Fig. 1.13 - C-type moving-coil permanent magnet linear motor
- Fig. 1.14 - Moving-coil tubular permanent magnet motor with radially magnetised magnet
- Fig. 1.15 - Moving-coil tubular permanent magnet linear motor with several radially magnetised magnets
- Fig. 1.16 - Moving-coil linear motor with axially magnetised magnets
- Fig. 1.17 - Improved moving-coil linear motor with axially magnetised magnets
- Fig. 1.18 - Moving-coil linear motor with radially magnetised magnet
- Fig. 1.19 - Moving-coil permanent magnet linear motor with trapezoid magnets
- Fig. 1.20 - Moving-iron linear motor for artificial heart
- Fig. 1.21 - Moving-iron of tubular permanent magnet linear motor
- Fig. 1.22 - Moving-iron tubular permanent magnet linear motor
- Fig. 1.23 - Moving-iron tubular permanent magnet linear motor
- Fig. 1.24 - Moving-iron linear generator for low power applications
- Fig. 1.25 - Moving-iron linear generator for wave energy converter
- Fig. 1.26 - Planar configurations of moving-magnet linear motor

- Fig. 1.27 - Tubular configurations of moving-magnet linear motor
- Fig. 1.28 - Trade-off study on moving-magnet linear motors
- Fig. 1.29 - Slotless tubular moving-magnet linear motor for diaphragm compressor
- Fig. 1.30 - Axially tubular permanent magnet linear generator
- Fig. 1.31 - 5-phase tubular moving-magnet linear motor with non ferromagnetic tube
- Fig. 1.32 - Moving-magnet tubular permanent magnet linear machine with 2 air-gaps
- Fig. 1.33 - Moving-magnet tubular permanent magnet machine with Halbach magnetisation
- Fig. 1.34 - Armature for moving-magnet tubular permanent magnet motor with quasi-Halbach magnetisation
- Fig. 1.35 - Iron-cored quasi-Halbach magnetised motor with rectangular magnets
- Fig. 1.36 - Air-cored quasi-Halbach magnetised motor with rectangular magnets
- Fig. 1.37 - Iron-cored quasi-Halbach magnetised motor with trapezoidal magnets
- Fig. 2.1 - Three design variants of tubular linear motors
- Fig. 2.2 - Analytical field models
- Fig. 2.3 - Magnetisation distributions
- Fig. 2.4 - Fourier series representation of M_{rn} and M_{zn} quasi-Halbach magnetisation with rectangular magnets
- Fig. 2.5 - Representation of magnetisation distribution due to central radially magnetised magnet
- Fig. 2.6 - Representation of magnetisation distribution due to end radially magnetised magnets
- Fig. 2.7 - Resultant radial magnetisation distribution
- Fig. 2.8 - Representation of axial magnetisation distribution
- Fig. 2.9 - Open circuit flux distribution
- Fig. 2.10 - B_{lr} for iron-cored quasi-Halbach magnetised motor with rectangular magnets
- Fig. 2.11 - Open-circuit flux distributions
- Fig. 2.12 - B_{lr} for air-cored quasi-Halbach magnetised motor with rectangular magnets
- Fig. 2.13 - Open-circuit magnetic flux distribution

- Fig. 2.14 - B_{fr} for iron-cored quasi-Halbach magnetised motor with trapezoidal magnets
- Fig. 2.15 - B_{fr} for air-cored and iron-cored quasi-Halbach magnetised motor with rectangular magnets
- Fig. 2.16 - B_{fr} for iron-cored quasi-Halbach magnetised motors with rectangular and trapezoidal magnets
- Fig. 2.17 - Comparison of analytical and finite element predicted back- emf for iron-cored quasi-Halbach magnetised motor with rectangular magnets
- Fig. 2.18 - Back-emf of air-cored quasi-Halbach magnetised motor with rectangular magnets
- Fig. 2.19 - Back-emf of iron-cored quasi-Halbach magnetised motor with trapezoidal magnets
- Fig. 3.1 - Schematic of a linear reciprocating compressor system
- Fig. 3.2 - Mass-spring-damper model
- Fig. 3.3 - Pressure-displacement diagram of a compression cycle
- Fig. 3.4 - Electrical equivalent circuit of linear compressor
- Fig. 3.5 - Region of stator core
- Fig. 3.6 - Flux density at tooth tip
- Fig. 3.7 - Geometric parameters of stator core
- Fig. 3.8 - Flux density at tooth
- Fig. 3.9 - Flux density at yoke
- Fig. 3.10 - Equivalent current sheet distribution
- Fig. 3.11 - Armature reaction field model
- Fig. 3.12 - Schematic and design parameters of linear motors
- Fig. 3.13 - Influence of permanent magnet angle, β , on back-emf at velocity 2.1 m/s
- Fig. 3.14 - Variation of output power with T_m/T_p and R_m/R_e
- Fig. 3.15 - Influence of R_m/R_e and T_m/T_p on efficiency
- Fig. 3.16 - Influence of R_m/R_e and T_m/T_p on power loss
- Fig. 3.17 - Influence of T_{pw} on efficiency
- Fig. 3.18 - Influence of T_{pw} on power loss
- Fig. 3.19 - Influence of B_r on efficiency

- Fig. 3.20 - Influence of R_m/R_e and T_m/T_p on efficiency
- Fig. 3.21 - Influence of R_m/R_e and T_m/T_p on power loss
- Fig. 3.22 - Influence of T_{pw} on efficiency
- Fig. 3.23 - Influence of B_r on efficiency
- Fig. 3.24 - Finite element predicted variation of efficiency with T_m/T_p
- Fig. 3.25 - Finite element predicted variation of efficiency with R_m/R_e
- Fig. 3.26 - Finite element predicted variation of efficiency with T_m/T_p
- Fig. 3.27 - Finite element predicted variation of efficiency with R_m/R_e
- Fig. 4.1 - Tubular moving-iron linear motor
- Fig. 4.2 - Open-circuit flux distribution
- Fig. 4.3 - Back-emf and constant speed of moving-iron linear motor
- Fig. 4.4 - Schematic and design parameters of a tubular moving-iron motor
- Fig. 4.5 - B-H curve of Somaloy 700
- Fig. 4.6 - Variation of motor current with height of armature tooth
- Fig. 4.7 - Variation of output power with height of armature tooth
- Fig. 4.8 - Variations of efficiency with height of armature tooth
- Fig. 4.9 - Variation of efficiency with influence of width of armature tooth
- Fig. 4.10 - Variation of iron loss and copper loss with influence of width of armature tooth
- Fig. 4.11 - Variation of efficiency with influence of the height of armature tooth
- Fig. 4.12 - Variation of iron loss and copper loss with influence of height of armature tooth
- Fig. 4.13 - Variation of efficiency with R_o/R_e
- Fig. 4.14 - Variation of iron loss and copper loss with R_o/R_e
- Fig. 4.15 - Variation of efficiency with height of permanent magnet
- Fig. 4.16 - Variation of iron loss and copper loss with height of permanent magnet
- Fig. 4.17 - Influence of T_r and H_r on efficiency
- Fig. 4.18 - Influence of T_r and R_o/R_e on efficiency
- Fig. 5.1 - Magnet and supporting tube configurations
- Fig. 5.2 - 2-D axis-symmetrical cylindrical model linear motors

- Fig. 5.3 - Circuit of 2-D model
- Fig. 5.4 - 3-D meshed model linear motors
- Fig. 5.5 - Variation of flux density in PM1
- Fig. 5.6 - Eddy current loss distribution in ring magnets at no-load
- Fig. 5.7 - Eddy current loss in PM1 for the air-cored quasi-Halbach magnetised motor with rectangular magnets at no-load condition
- Fig. 5.8 - 3-D eddy current distribution in air-cored motor with rectangular magnets
- Fig. 5.9 - Influence of number of segments on average eddy current loss at no-load condition
- Fig. 5.10 - Eddy current loss in PM1 at no-load condition
- Fig. 5.11 - Eddy current loss in the supporting tube at no-load condition
- Fig. 5.12 - 3-D eddy current distribution in iron-cored motor with trapezoidal magnets
- Fig. 5.13 - Influence of number of segments on average of eddy current loss at no-load condition
- Fig. 5.14 - Phasor diagram of motor
- Fig. 5.15 - Current supply and velocity waveforms
- Fig. 5.16 - Magnitude of flux density in PM1 at no-load and on-load condition
- Fig. 5.17 - Comparison of eddy current loss between no-load and on-load conditions
- Fig. 5.18 - Comparison of eddy current loss between no-load and on-load conditions
- Fig. 5.19 - Comparison of average of eddy current loss between no-load and on-load conditions
- Fig. 5.20 - Magnitude of flux density at on-load and no-load conditions
- Fig. 5.21 - Eddy current loss in PM1 at no-load and on-load conditions
- Fig. 5.22 - Eddy current loss in supporting tube at no-load and on-load conditions
- Fig. 5.23 - Comparison of eddy current loss between no-load and on-load conditions
- Fig. 5.24 - Iron-cored quasi-Halbach magnetised motor with rectangular magnets
- Fig. 5.25 - Armature position versus time
- Fig. 5.26 - No-load flux distributions at two armature positions
- Fig. 5.27 - Flux density waveforms over a reciprocating cycle
- Fig. 5.28 - Variation of no-load iron loss with frequency and stroke
- Fig. 5.29 - Variation of velocity for 11.0 mm stroke

- Fig. 5.30 - Variation of no-load iron loss with frequency, assuming three armature velocity profiles and $X_m = 11.0$ mm
- Fig. 5.31 - Eddy current density distribution in SMC stator at 50 Hz with armature position
- Fig. 5.32 - Variation of total no-load eddy current loss in SMC stator with frequency
- Fig. 5.33 - Current and armature position waveforms for on-load iron loss calculation
- Fig. 5.34 - Thrust force and armature velocity waveforms
- Fig. 5.35 - On-load flux density distributions at two armature positions
- Fig. 5.36 - Comparison of no-load and on-load flux density waveforms
- Fig. 5.37 - Variation of no-load and on-load iron losses with frequency at fixed armature amplitude of 11.0 mm
- Fig. 6.1 - Prototype of air-cored quasi-Halbach magnetised motor with rectangular magnets
- Fig. 6.2 - Motor casing
- Fig. 6.3 - Exploded and assembled view of the air-cored motor
- Fig. 6.4 - Static test-rig for single-phase air-cored quasi-Halbach magnetised motor with rectangular magnets
- Fig. 6.5 - Comparison of measured and predicted coil flux-linkage
- Fig. 6.6 - Comparison of measured and predicted cogging force
- Fig. 6.7 - Variation of measured and predicted thrust force with axial position
- Fig. 6.8 - Linear motor components
- Fig. 6.9 - Schematic diagram of the iron loss test rig
- Fig. 6.10 - Measured results as functions of time at 9.0 mm stroke
- Fig. 6.11 - Variations of input current at different stroke with frequency
- Fig. 6.12 - Variations of voltage terminal at different stroke with frequency
- Fig. 6.13 - Variations of total power at different stroke with frequency
- Fig. 6.14 - Comparison of measured and predicted results at 6.0 mm stroke
- Fig. 6.15 - Comparison of measured and predicted iron loss
- Fig. 6.16 - Schematic of load test set-up for prototype motor
- Fig. 6.17 - Measured motor and generator efficiencies as functions of frequency at 10.0 mm stroke

- Fig. E.1 - Eddy current loss in permanent magnets for air-cored motor at no-load condition
- Fig. E.2 - Eddy current loss in permanent magnets for iron-cored motor at no-load condition
- Fig. E.3 - Eddy current loss in permanent magnets for air-cored motor at on-load condition
- Fig. E.4 - Eddy current loss in permanent magnets for iron-cored motor at on-load condition

List of tables

- Table 2.1 - Design parameters and specification of linear motors**
- Table 3.1 - Fixed design parameters and operational conditions**
- Table 3.2 - Optimal design parameters of air-cored quasi-Halbach magnetised motor with rectangular magnets**
- Table 3.3 - Optimal design parameters for iron-cored quasi-Halbach magnetised motor with trapezoidal magnets**
- Table 4.1 - Initial dimension parameters and operational conditions**
- Table 4.2 - Price and density of materials**
- Table 4.3 - Volume of motors**
- Table 4.4 - Material costs**
- Table 4.5 - Efficiency, output power, losses, and moving mass**
- Table 5.1 - Average of eddy current loss in the supporting tube**
- Table 5.2 - Design parameters of the iron-cored quasi-Halbach magnetised motor with rectangular magnets**
- Table 6.1 - Total power, copper loss and eddy current loss at different stroke**

CHAPTER 1

INTRODUCTION AND LITERATURE REVIEW

1.1 Introduction

Worldwide energy consumption has risen by around 30 % in the last 25 years [1] and the rate of increase appears to be accelerating. Currently, industrialised countries consume about four times as much energy as developing countries. However, economic growth which is being encouraged in countries such as China, India and Brazil is expected to increase significantly for the foreseeable future, and this will put further pressure on energy supplies and necessitate energy conservation measures.

Of the various household appliances, refrigeration represents a significant and growing electrical load, accounting for approximately 14 % of the total UK electrical power consumption [2] [3]. Thus, the refrigeration load has a very significant impact on the UK's emissions of carbon and CO₂. The electrical power consumption of refrigerators is obviously related to the efficiency of their compressor systems. Hence, cost-effective measures for improving efficiency are highly desirable, and are in demand on a global scale.

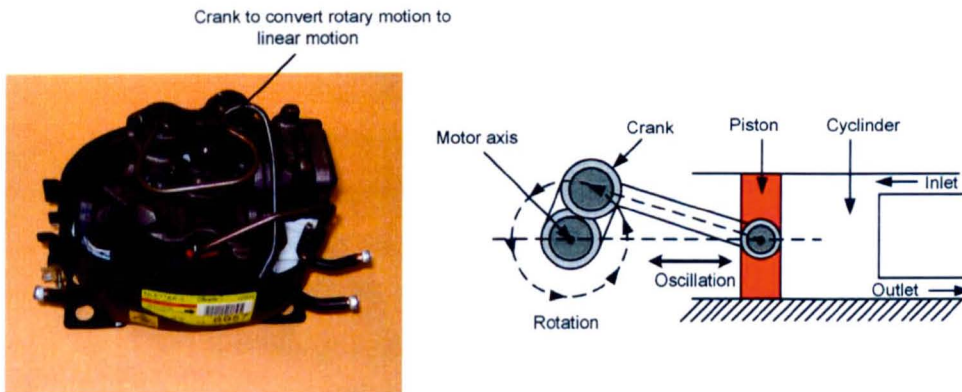


Fig. 1.1 Schematic of conventional refrigerator compressor

The conventional refrigerator compressor comprises a rotary electric motor, usually a single-phase induction motor, which drives a reciprocating pump through a crank, as shown in Fig. 1.1. The overall efficiency is relatively low, due to the inherently low efficiency of induction motors and the mechanical friction of the crank-driven piston movement. This will be evident from Fig. 1.2, from which it will be seen that the

overall efficiency of the such a compressor is around 60 %, although incremental improvements in efficiency continue to be made, by reducing both the induction motor losses and the side force between the piston and cylinder.

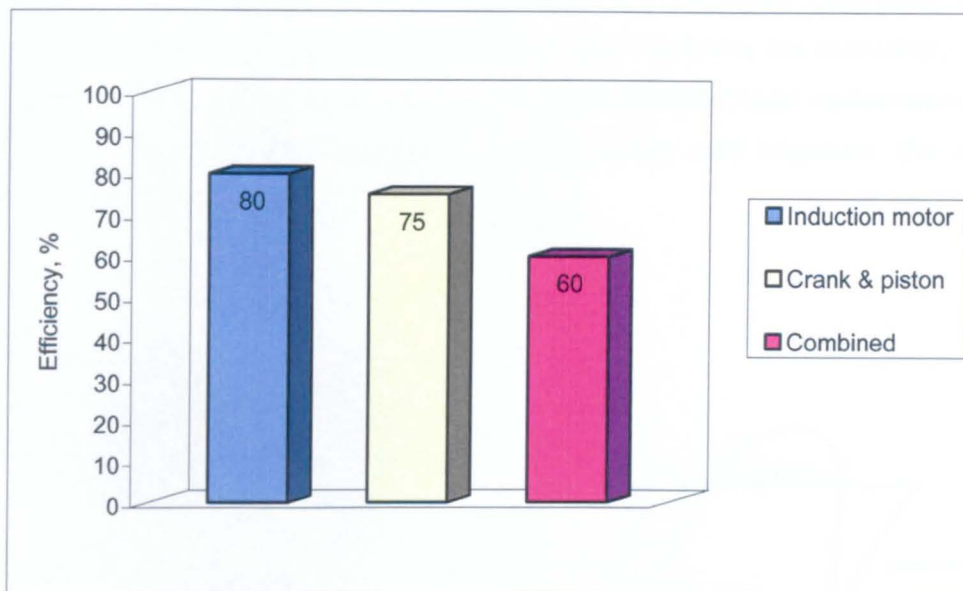


Fig. 1.2 Efficiency of induction motor driven compressor [4]

Fig. 1.3 highlights the role of the compressor in the refrigeration cycle. As well as compressing the refrigerant gas, the compressor raises its temperature. The condenser dissipates the heat and the gas condenses before flowing through an expansion valve. This reduces the pressure and the refrigerant expands and evaporates. Finally, the evaporating refrigerant absorbs heat from inside the refrigerator. Standard conditions for measuring the refrigerator efficiency are: an evaporator temperature of $-25\text{ }^{\circ}\text{C}$, an ambient temperature of $32\text{ }^{\circ}\text{C}$ and a condenser temperature of $55\text{ }^{\circ}\text{C}$. Clearly, in practice the actual temperatures will vary over quite a wide range, and typically might be $-10\text{ }^{\circ}\text{C}/32\text{ }^{\circ}\text{C}/55\text{ }^{\circ}\text{C}$.

Currently, most refrigerators employ simple on-off refrigeration systems, the on/off duty cycle of a fixed-speed compressor being determined by the refrigerator temperature setting and the load. Although variable-speed compressors are available to enable the refrigerant gas flow rate to be continuously varied to meet the required cooling capacity, and, thereby, improve the compressor efficiency to $\sim 85\%$, low speed operation is not possible because of piston lubrication problems. Further, variable-speed operation increases manufacturing cost, and since the consumer

product sector is very cost-sensitive, the commercial take-up of variable cooling capacity refrigerators has been poor.

Nevertheless, refrigerators have recently been introduced which employ a direct-drive linear motor driven compressor [5] [6]. Such a compressor eliminates the need for a rotary-to-linear motion conversion cranks which reduces the complexity, volume and power loss due to mechanical friction. A direct-drive linear compressor is also more robust, quieter, more reliable and less costly, and improves the dynamic performance [7].

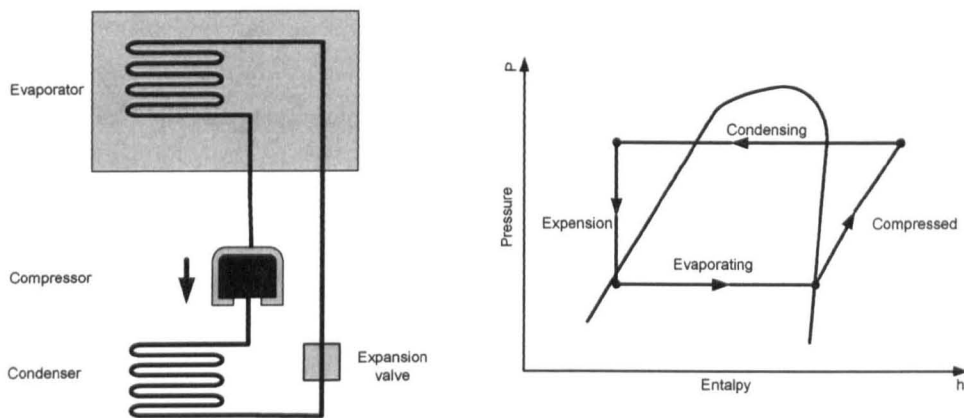


Fig. 1.3 Refrigeration cycle

A further feature of direct-drive linear compressors is the fact that both the frequency and the amplitude of the piston stroke can be easily varied [8], whilst a conventional compressor with a rotary motor and a crank has a fixed stroke. Thus, it readily facilitates variable cooling capacity, whilst eliminating the side force on the cylinder wall caused by the crank. This not only significantly reduces the frictional loss, but also makes it possible to operate without a lubricant, i.e. oil-free operation, since the clearance of a few micrometers between the cylinder and the piston is filled with gas, which acts as both lubricant and seal. Fig. 1.4 illustrates the scale of the reduction in energy consumption which should be achievable by employing a direct-drive linear compressor rather than a rotary/crank driven compressor, and by implementing variable cooling capacity operation.

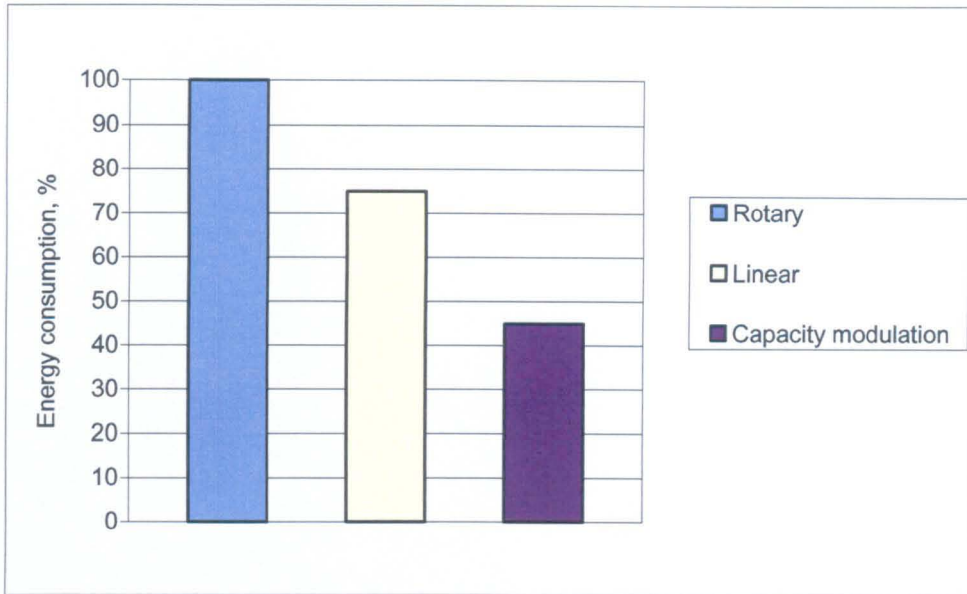


Fig. 1.4 Energy consumption of different compressor technologies [4]

Fig. 1.5 shows a schematic of a direct-drive linear compressor, although in practice the linear motor and compressor would be much more highly integrated.

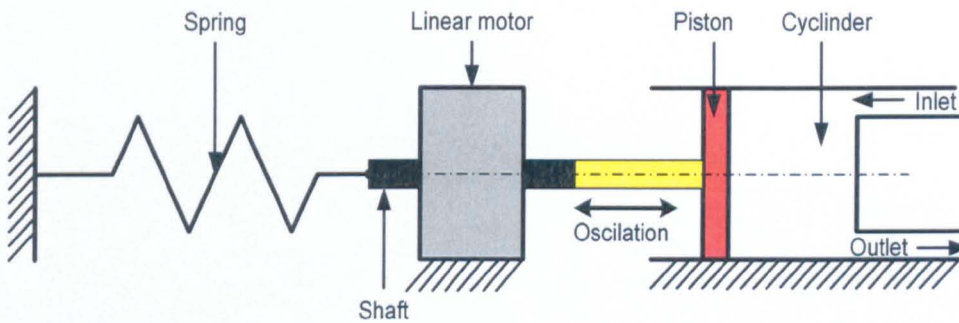


Fig. 1.5 Schematic of direct-drive linear compressor [4]

For maximum efficiency and piston stroke for a given supply current, and therefore, maximum refrigerant gas flow, the electrical supply frequency to the linear motor should coincide with the mechanical resonant frequency of the moving mass (i.e. mover of linear motor plus piston). The mechanical resonant frequency, f_r is given by:

$$f_r = \frac{1}{2\pi} \sqrt{\frac{k_T}{m}}$$

1.1

where k_T and m are the total equivalent system spring stiffness and the total moving mass, respectively.

In addition to eliminating the friction loss associated with the crank and facilitating continuous by variable cooling capacity, by varying the supply current and the frequency (over a relatively narrow range), although a small amplitude stroke will compromise the volumetric efficiency; a direct-drive linear compressor enables soft start/stop operation, which is conducive to low noise.

The total equivalent spring stiffness results from the stiffness, k , of the suspension springs on which the mover and piston are supported, the stiffness, k_g , of the refrigerant gas as it is compressed and the stiffness, k_c , due to the cogging force of the linear motor. Both k_g and k_c are highly non-linear functions of the piston stroke, whilst k_g also depends on the evaporator/ambient/compressor operating temperatures. Thus, as will be evident from equation 1.1, the mechanical resonant frequency may vary significantly, typically as shown in Fig. 1.6, and the electrical supply frequency needs to track this at all times in order to maintain maximum operational efficiency under all operating conditions.

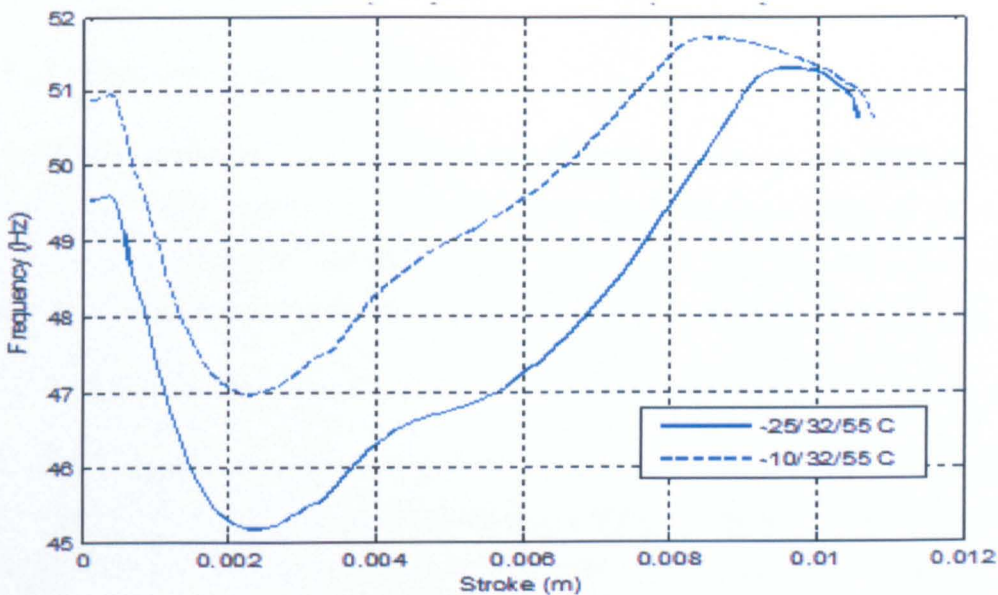


Fig. 1.6 Typical variation of mechanical resonant frequency with stroke and evaporator/ambient/compressor temperatures [4]

Clearly, the design of the linear motor will have an important influence on the operation of a direct-drive reciprocating compressor. The research which is reported in this thesis assesses the merits of favoured motor topologies, and presents comprehensive analyses and performance predictions, validated by experimental measurements.

1.2 Aim of research

The aim of the research was to develop a reciprocating linear motor for use in domestic refrigeration compressor systems. The specific objectives were:

- i. To identify the most promising candidate topologies of linear reciprocating motor in terms of their stroke, mass, efficiency and cost.
- ii. To establish an analytical framework for the analysis and design optimisation of the most appropriate linear reciprocating motors and to validate the results by finite element analysis.
- iii. To undertake design optimisation, using finite element analysis and the findings from the analytical study.
- iv. To prototype the most efficient of the linear motors and perform comprehensive static and dynamic testing and validate the performance predictions.

1.3 Basic operation of linear motors

In principle, for every rotary electrical machine configuration a linear counter part may be realised. The process of slicing and unrolling a rotary induction motor to obtain a linear motor, either planar or tubular, is illustrated in Fig. 1.7 (a) [9], whilst the same process for realising flat and tubular linear permanent magnet motors is illustrated in Fig. 1.7 (b).

A linear machine produces a thrust force directly to a load. As with all doubly-excited electromagnetic machines, the thrust force is developed when a straight current-carrying conductor is placed in a magnetic field, as shown in Fig. 1.8, the direction of the force being determined by Fleming's left-hand rule.

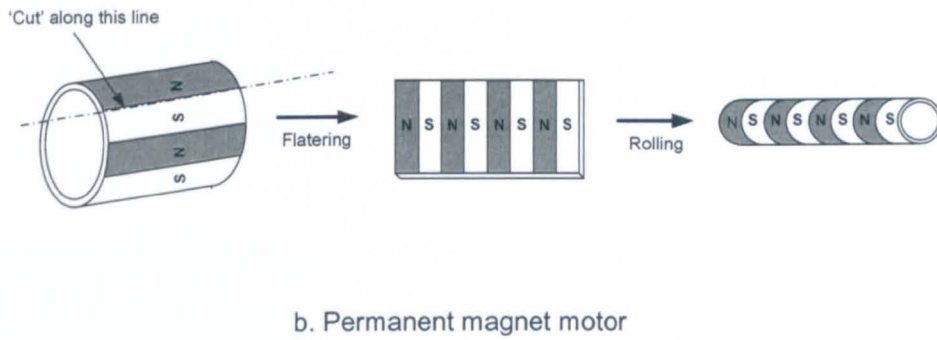
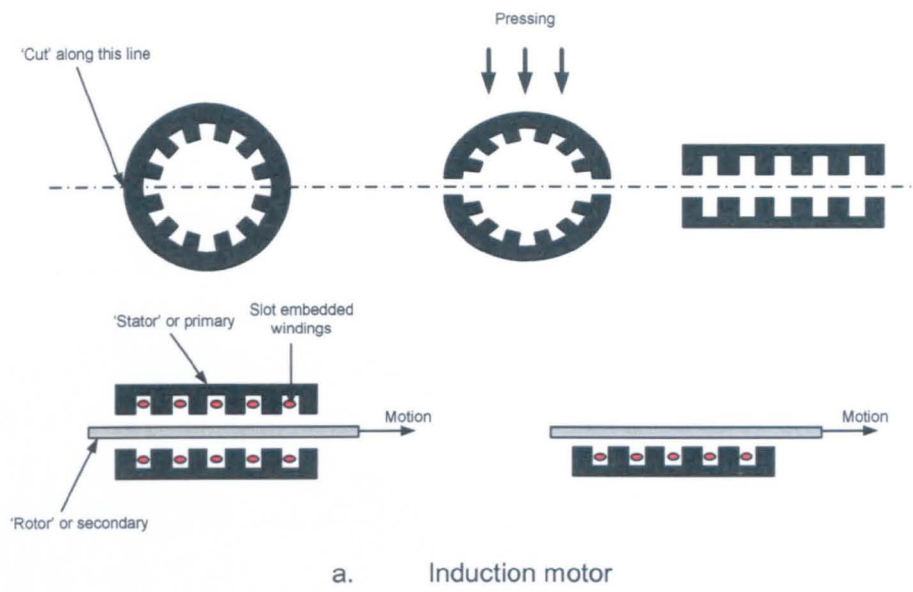


Fig. 1.7 Development of linear induction and permanent magnet motors from rotary motors [9]

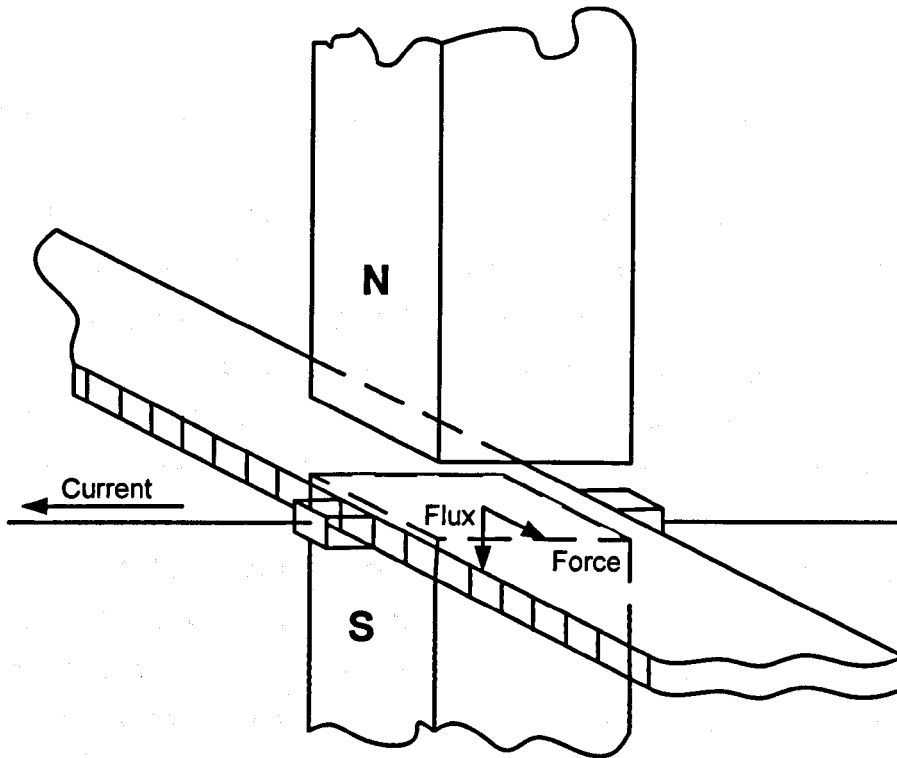


Fig. 1.8 Basic concept of linear motion [10]

1.4 Literature review on linear machine technologies

The first linear electric motor was patented in the USA more than a century ago [9]. Over the years, thousands of international papers and monographs have dealt with the topic of linear motors in a variety of applications, such as artificial heart devices [11], cryogenic coolers [12], compressors [8] and automotive actuators [13].

Essentially, there are five linear machine technologies which can be considered [14] as candidates for linear compressor refrigerator systems, viz:

- i. linear induction machines
- ii. linear synchronous machines
- iii. linear switched reluctance machines
- iv. linear DC machines
- v. linear permanent magnet brushless machines

1.4.1 Linear induction machines

Linear induction machines have been developed predominantly for producing continuous linear motion, especially for heavy duty applications such as transportation, conveyor systems and, more recently, lifts [15]. They generally require a poly-phase power supply and a multi-phase primary winding in order to produce a travelling magnetic field and induce current in the secondary. Various topologies are feasible, such as short secondary/long primary, long secondary/short primary, moving secondary or moving primary, single or double-sided. For oscillatory operation, a controllable inverter drive is used to reverse the direction of the travelling magnetic field. The direction of movement may also be reversed by interchanging two phases of the 3-phase power supply. However, a single-phase power supply can still also drive a linear induction machine, as reported by West and Jayawant [16]. They designed an oscillatory induction motor for shuttle propulsion. The motor consisted of two ring coils placed symmetrically at the two ends, as shown in Fig. 1.9. The conducting ring acts as the secondary and was placed around the lamination stack located between the two coils. The motor produced a stroke of 25.0 mm at 12 Hz at an input of 100VA.

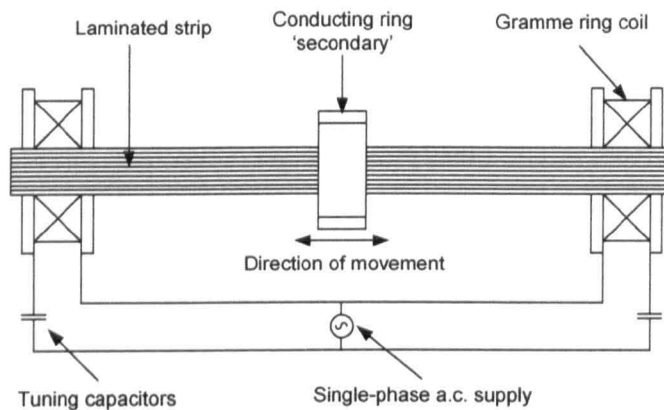


Fig. 1.9 Single phase linear oscillating induction motor [15] [16]

However, the motor had poor performance especially at low speed, and due to the relative complexity of the physical assembly of the stator, the need for a multi-phase winding and a poly-phase supply, the use of linear induction machine in low power reciprocating applications is limited.

1.4.2 Linear synchronous machines

Linear synchronous machines with permanent magnet excitation have been employed widely in high performance systems, especially for long stroke applications [17]. However, such machines have also been applied in reciprocating motion applications such as cryogenic refrigerators, vibrators [18] and artificial hearts [19]. Again, however, their application is limited due to the relative complexity of the stator winding and the power supply requirement. The production of reciprocating motion also requires a reversal of the multi-phase voltage sequence or a power electronic inverter to facilitate speed reversal, whilst position feedback is required to sense the end of the travel. However, complexity of the stator winding configuration and the need for a multi-phase power supply makes the conventional topology of linear synchronous machine un-suitable for low power reciprocating applications.

1.4.3 Linear switched reluctance machines

Linear switched reluctance machines, of the form illustrated in Fig. 1.10, are available in various commercial sectors and their design, optimisation and control remain the subject of ongoing research [20] [21]. In general, the machine requires position feedback to synchronise the commutation of the phase currents with the relative position between the stator and mover teeth. Mechanically switched reluctance machines are very robust and relatively simple, and may be cheaper than other technologies. However, their relatively poor operating characteristics, in term of their thrust force capability and efficiency, means that such machines are generally inappropriate for low power, high efficiency reciprocating applications.

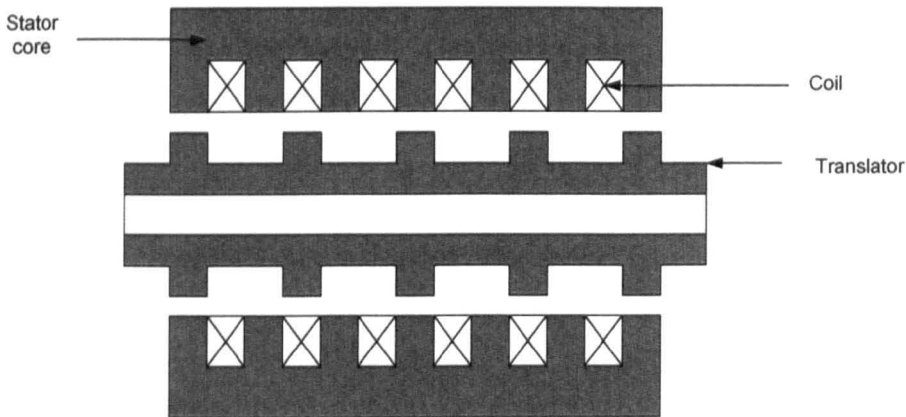


Fig. 1.10 Tubular switched reluctance linear machine [20]

1.4.4 Linear DC machines

Linear DC (commutator) machines are usually used for long stroke applications, with position feedback, in applications such as robotics and positioning tables, and they offer advantages due to their smooth, easy and accurate control of force and position [22]. Basak [23] described variants to brushed DC linear motors, in which the armature consists of a helical winding on a cylindrical armature which is energised via brushes. However, such motors are relatively expensive to manufacture, suffer from brush wear, and, hence, are high maintenance, and there are relatively noisy during operation.

1.4.5 Linear permanent magnet machines

In general, the use of direct-drive linear motors in the reciprocating motion applications under consideration is prohibitive due to their complexity, cost and power supply requirements. The problems with reversing the phase sequence for bi-directional operation from a poly-phase power supply [16] and position feedback to facilitate synchronisation of the excitation current [17] with the mover position is likely to exclude the use of linear induction machines, linear synchronous machines, linear switched reluctance machines and linear DC machines for low power reciprocating applications, especially in linear vapour compressor systems.

Linear permanent magnet machines offer certain advantages for reciprocating compressor applications for which the machines are required to produce a high force capability and have a high efficiency, whilst requiring a low power supply and being easy to control [24]. The permanent magnet linear machine shown in Fig. 1.11 is arguably the simplest configuration. No field winding is required since the permanent magnet produces the excitation flux for the motor [15]. The moving armature has a short active length whilst the length of the permanent magnet array corresponds to the desired stroke in order to produce optimum thrust force.

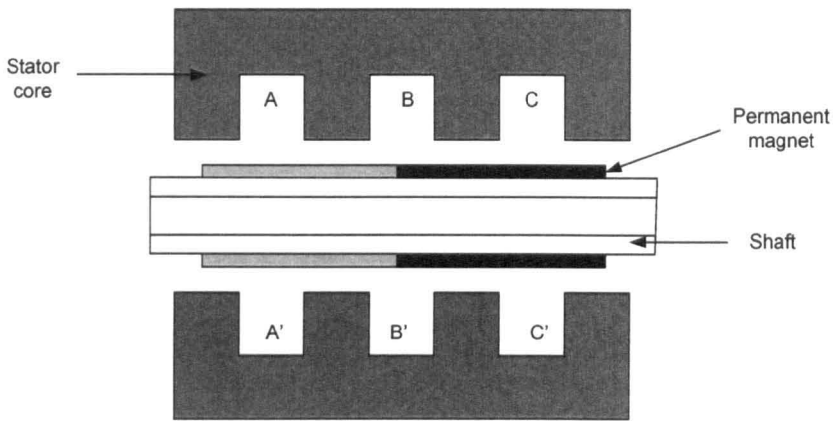


Fig. 1.11 Tubular permanent magnet linear machine

Both planar and tubular topologies can be realised a tubular topology being preferred for a higher thrust force capability. In addition, both slotted and slotless topologies should be considered [25] for improving the thrust force and for reducing the cogging force, respectively. Other topologies which should be considered are iron-cored and air-cored armature configurations, in order to enhance the dynamic capability of a linear motor. As intimated at earlier, a lightweight armature is generally preferred for a vapour linear compressor [26]. In general, however, the permanent magnet linear motors can be classified into three categories, viz.;

- i. moving-coil
- ii. moving-iron
- iii. moving-magnet

1.4.5.1 Moving-coil motors

Normally, a moving-coil linear motor comprises a stationary permanent magnet, either radially or axially magnetised in the stator and a moving-coil armature. The various generic forms of moving-coil linear motors have been compiled by Clark [15], as illustrated in Fig. 1.12. The motors in Fig. 1.12 (a) and (b) are used extensively in loud-speaker applications, which often use low cost sintered ferrite for the permanent magnet and mild steel for the magnetic circuit. However, a low air-gap flux density is produced due to the low remanence of the permanent magnet material.

However, rare-earth permanent magnet materials, such as Samarium Cobalt, SmCo or Neodymium Iron Boron, NdFeB are generally used in the topologies shown in Fig. 1.12 (c) –(g) in order to produce more thrust force for specific applications such as

computer disk drives [26] [27], robotics and aerospace actuators [28] [29]. The use of high energy, high coercivity rare-earth magnets is conducive to a high magnetic loading, which reduces the electrical loading, while at the same time reducing the volume of copper, which may reduce the moving mass. The magnetic loading is the peak radial flux density in air-gap of the machine, meanwhile, the electrical loading is the total rms current per unit length of periphery of the machine. Other advantages of moving-coil linear motors include a small hysteresis loss, a light-weight armature, and high-speed operation under closed-loop servo-control.

The slotless C-type moving-coil permanent magnet linear motor shown in Fig. 1.13 is a well-known topology which is often used to improve the accuracy of the speed and position control [30] [31] [32] [33]. Such motors also provide the significant advantage of minimising or even eliminating the cogging force and also enhancing the dynamic capability due to the light-weight nature of the moving-coil armature [33].

Bruno [8] introduced the tubular moving-coil linear motor comprising either a single or several radially magnetised permanent magnets, as shown in Fig. 1.14 and Fig. 1.15, respectively. The linear motors were designed for 5.0 mm to 20.0 mm strokes. The use of rare-earth NdFeB permanent magnets reduced the inertia and improved the performance of the linear motors. However, the linear motors required a special arrangement to supply the current to the moving coil in order to avoid flying leads, whilst a position sensor was required in order to achieve bi-directional motions, which increases the manufacturing cost.

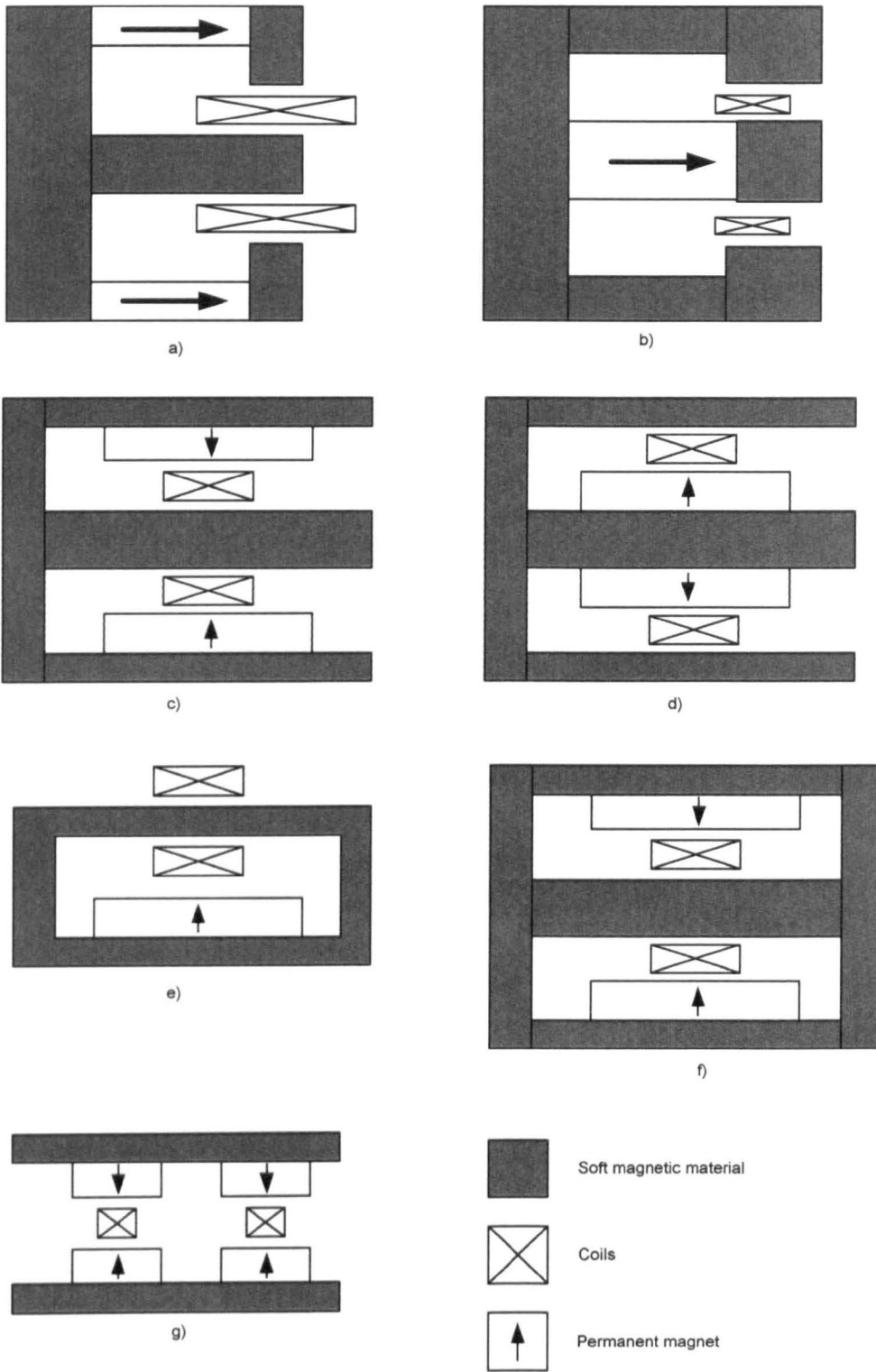


Fig. 1.12 Moving-coil linear motor topologies [15]

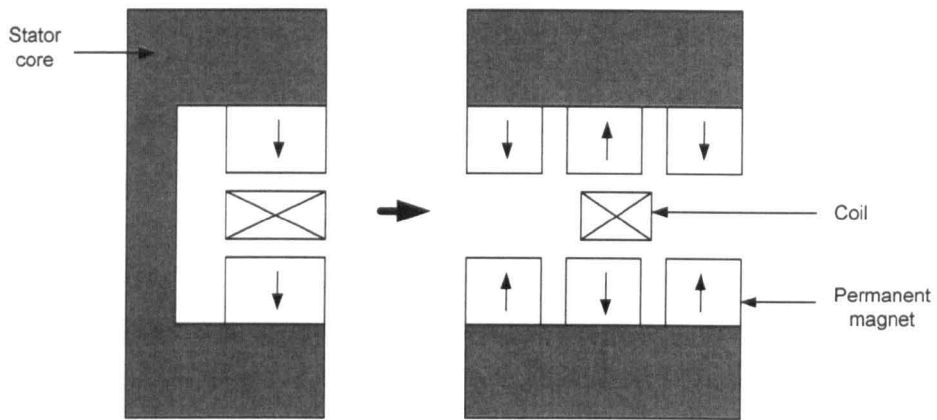


Fig. 1.13 C-type moving-coil permanent magnet linear motor [30] [31] [32] [33]

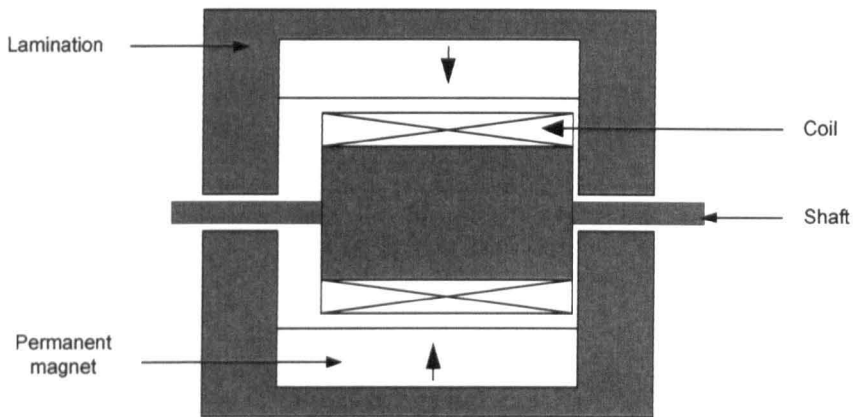


Fig. 1.14 Moving-coil tubular permanent magnet motor with radially magnetised magnet [8]

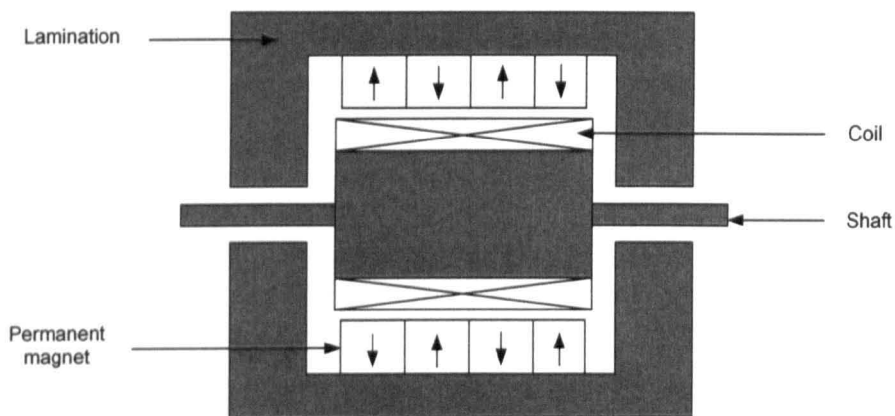


Fig. 1.15 Moving-coil tubular permanent magnet linear motor with several radially magnetised magnets [8] [34] [35]

In addition, the axially magnetised tubular permanent magnet linear motor illustrated in Fig. 1.16 has been developed [36] [37]. It is claimed to have a higher specific thrust force capability than other topologies, but requires more permanent magnet material. To improve the design, the modified topology [38] shown in Fig. 1.17 has been proposed. Both the magnets and the associated pole-pieces are annular shaped and supported on a non-ferromagnetic rod. It offers several advantageous, such as eliminating the need for a non-magnetic tube to contain the magnets and pole-pieces, and reducing the volume of permanent magnet material.

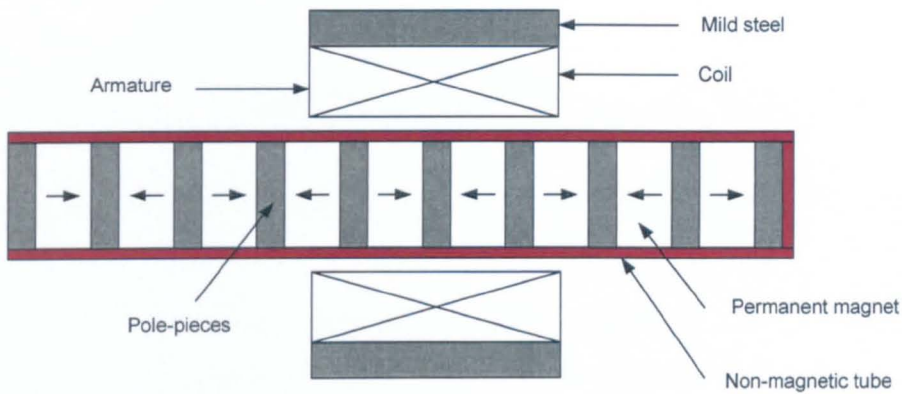


Fig. 1.16 Moving-coil linear motor with axially magnetised magnets [36] [37]

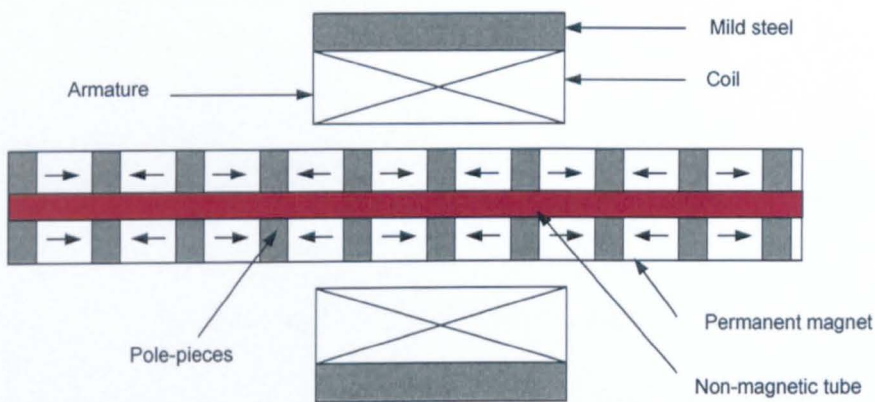


Fig. 1.17 Improved moving-coil linear motor with axially magnetised magnets [38]

Wang et al [39] introduced the radially magnetised tubular permanent magnet linear motor shown in Fig. 1.18. The radial magnetised magnets have significant advantage in providing radial fluxes directly to moving-coil armature in order to produce better performance of the motor. The up-side down radially magnetised magnets provide

faster returning fluxes and significant in reducing the thickness of back iron. Therefore, the cost of material can be reduced.

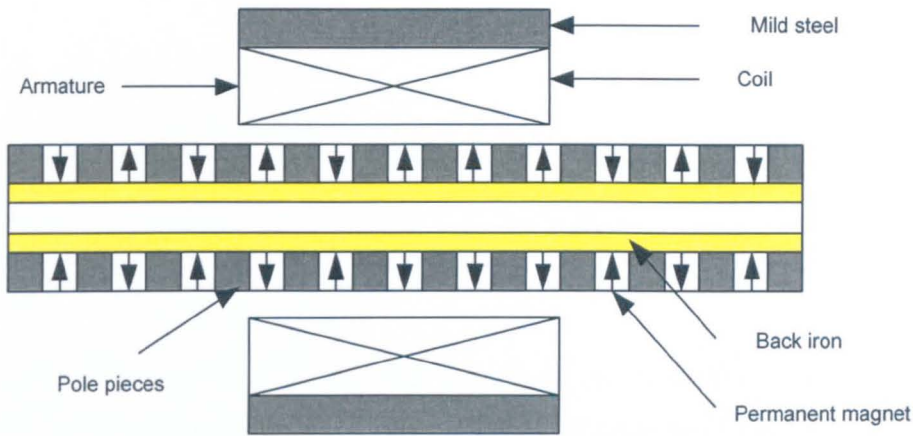


Fig. 1.18 Moving-coil linear motor with radially magnetised magnet [39]

A further improvement was proposed by M.G. Lee et al [40] who introduced the planar moving-coil linear motor with trapezoidal magnet arrays shown in Fig. 1.19 for use in a high precision positioning system. After optimisation, the motor was shown to produce a higher thrust force per volume than an equivalent motor equipped with conventional quasi-Halbach magnetised magnet arrays. However, the design can be improved by employing a tubular topology to enhance the force capability, as will be discussed in Chapter 2.

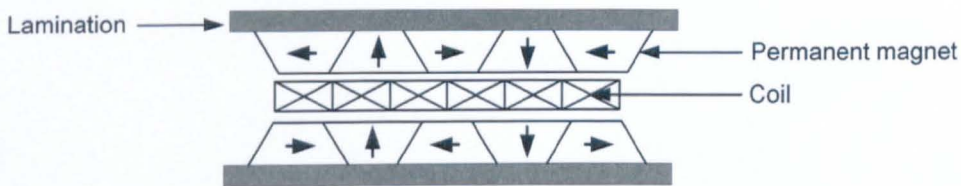


Fig. 1.19 Moving-coil permanent magnet linear motor with trapezoid magnets [40]

However, moving-coil linear motors do suffer from a number of disadvantages [3] [15], viz.:

- i. Difficulty in dissipating heat from the coils
- ii. Fragility of the connections and flying leads
- iii. Limited access to moving-coil.

- iv. Limited stroke and thrust force capability

Based on the foregoing, a moving-coil topology was not considered suitable for a low power reciprocating linear motor for a refrigerator compressor system.

1.4.5.2 Moving-iron motors

Moving-iron permanent linear motors lead to be simpler designs since they are often only required to have a uni-directional force capability and use a mechanical spring to reverse the motion of the plunger when the motor is de-energised [9].

Linear moving-iron motors have been developed for implanting in the human body [11]. For example, the motor shown in Fig. 1.20 was designed by Yamaguchi et al [41] for use in an artificial heart. It had a diameter of 70.0 mm, an axial length of 40.0 mm and used a radially magnetised NdFeB ring magnet, and had a stroke of up to 14.0 mm and a maximum force capability of 20 N, the plunger moving mass being 40 g. In order to produce the maximum thrust force, the minimum air-gap clearance between the armature and magnet was relatively small, 0.35 mm. This small clearance necessitated careful assembly, which, in turn, lead to a relatively high manufacturing cost.

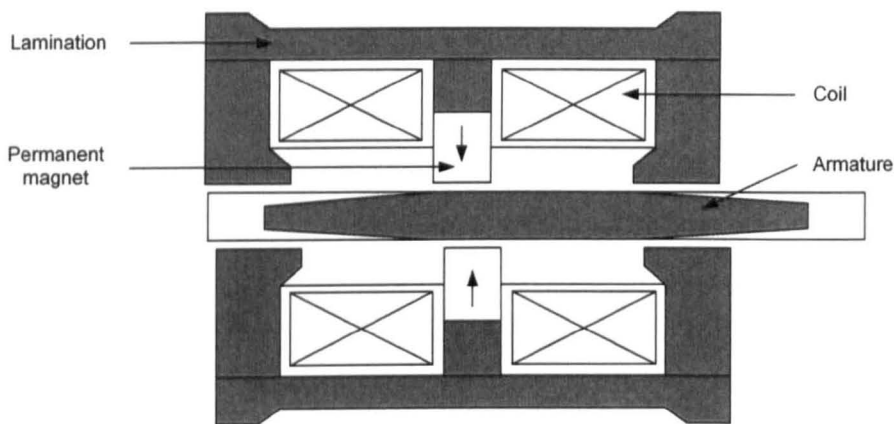


Fig. 1.20 Moving-iron linear motor for artificial heart [11]

The tubular moving-iron linear motor shown in Fig. 1.21 was introduced by Evan [7] for multi-purpose applications. The machine has a diameter of 46.0 mm, an axial length of 57.0 mm and employs axially magnetised NdFeB magnets with a

remanence of 1.125 T. The thrust force was 40 N. The linear armature motion was varied by current control in open-loop, without the need for a position sensor. However, whilst various design parameters were optimised, certain design features need to be further optimised, especially for the armature. The depth and width of the central section of the armature are very significant parameters in order to achieve optimum performance. If the width of the armature teeth is too narrow, a high flux density results in the armature teeth which causes a high iron loss, whilst if the tooth height is too small, the change of flux with axial displacement of the armature may be reduced, which results in poor performance. The dimensions of the permanent magnets also need to be optimised in order to enhance the performance. Details of the optimisation and modification of this linear motor are discussed in Chapter 4.

Boldea [9] introduced the moving-iron linear motor topology shown in Fig. 1.22, in which a rare-earth NdFeB permanent magnet and two coils are mounted on the stator. The merit of this topology is that the permanent magnet flux interacts directly with current-carrying coils in order to produce optimum thrust force. However, the armature mass is relatively heavy, so the frequency of oscillations is limited to a few Hertz [11], although the mass of the armature may be reduced by employing a ferromagnetic tube instead of a solid armature.

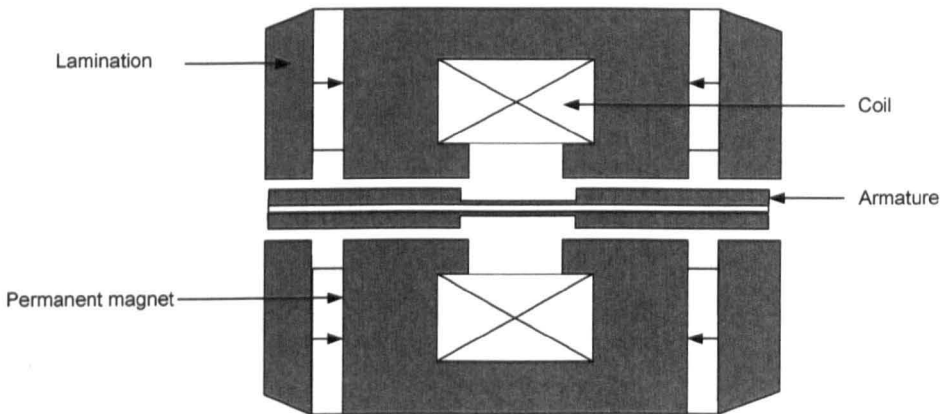


Fig. 1.21 Moving-iron of tubular permanent magnet linear motor [2]

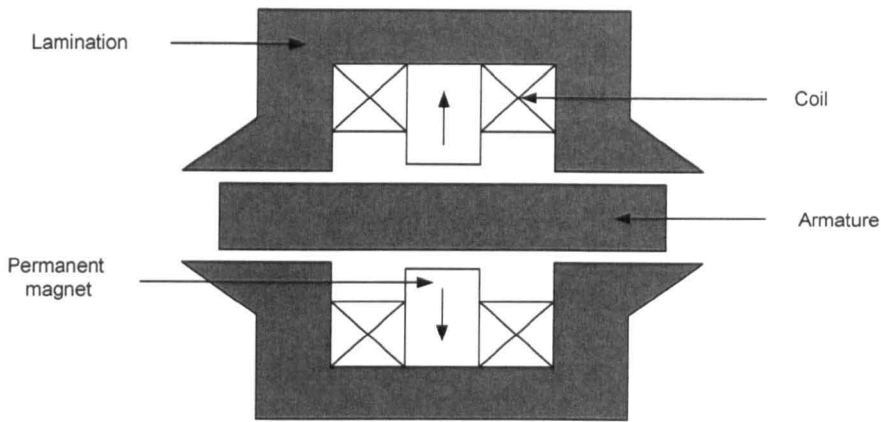


Fig. 1.22 Moving-iron tubular permanent magnet linear motor [9]

Lequesne [8] introduced the modified armature shown in Fig. 1.23 in order to reduce the moving mass and improve the force/volume capability. 2-springs are used to support the armature in order to produce bi-directional force. When the armature is at one end of its stroke, one of the spring is compressed whilst the other spring is released. The compressed spring is held in that state by the permanent magnet. When linear motion is desired, the coils are excited in such a way as to reduce the level of the magnetic force below that of the spring force, and the spring then drives the plunger to the other end of the stroke. The performance of the linear motor was compared to that of a moving-coil linear motor, on the basis of devices designed for the same stroke, i.e. 10.0 mm and the same volume. It was concluded that the moving-iron linear motor is relatively poor in terms of energy conversion from electrical to mechanical compared to the moving-coil linear motor and limited in the frequency of operation. The relative complexity of the moving-iron linear motor also required high precision manufacture and assembly, especially for the armature in order to avoid damage during the reciprocating operation, which increases manufacturing cost.

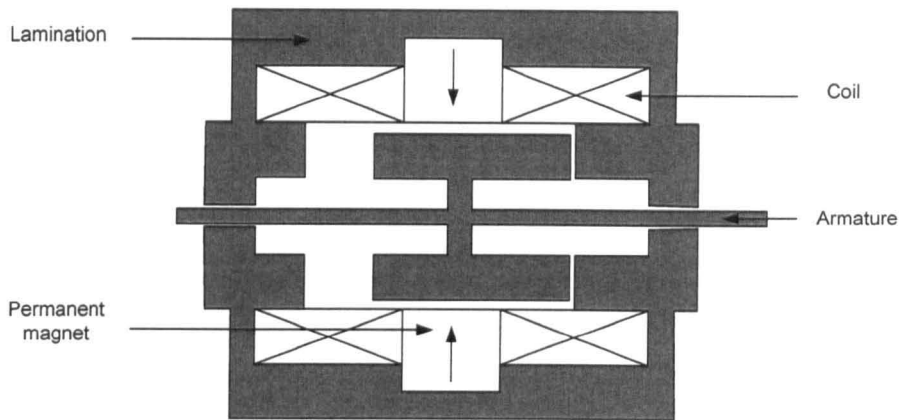


Fig. 1.23 Moving-iron tubular permanent magnet linear motor [8] [42]

Sidell and Jewell [43] designed the moving-iron linear motor for high temperature applications, up to 800 °C. The bi-directional motor has a diameter of 130.0 mm, an axial length of 128.0 mm and an air-gap length of 1.0 mm. The thrust force at 800 °C with 40 A excitation was 260 N. The design study illustrated the fact that there are no fundamental limitations to the operation of electromagnetic devices in ambient temperature of up to 800 °C, although there is inevitably a marked reduction in performance compared to devices operating near room temperature. This is due to the large increase in the resistance of the windings which, in turn, limits the current density that can be employed, and the reduced flux carrying capability of the cobalt-iron material from which the ferromagnetic cores were machined.

Wang et al [44] developed a small linear permanent magnet machine for generating electrical power as illustrated in Fig. 1.24. It is a two-phase tubular device, the stator having both permanent magnets and coils, while the moving-armature is a simple salient iron core. With an axial stroke of 48.0 mm at a velocity of 0.3 m/s , the generator could generate 3 mJ of a energy. Despite the small amount of energy which is produced, the generator is suitable for applications that require relatively low levels of electrical power, such as remote electronic locks.

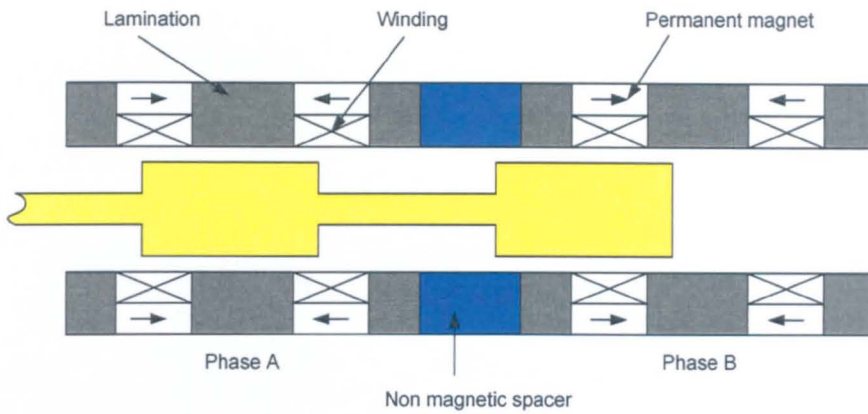


Fig. 1.24 Moving-iron linear generator for low power applications [44]

However, a higher energy moving-iron linear permanent magnet generator has been developed by Mueller et al [45] for renewable energy applications. It is a low speed, 3-phase linear electrical generator for a wave energy converter. Fig. 1.25 shows only a single-phase to ease understanding of the system. The toothed armature constructed from iron laminations, moves between two C cores, which have a coil wound around each pole and magnets mounted on the pole-faces. The rotor tooth and slot width are similar in dimension to the magnet pitch. When the armature teeth are fully aligned with the magnets, flux flows as shown by the dotted line. As the armature moves this flux decays to zero at the unaligned position and then reverses polarity. In this way, the coils experience a change in flux-linkage over a small displacement of the armature. The machine generated 2.8 kW at an rms current of 28 A. The toothed armature is an attractive concept for a tubular linear reciprocating motor with light-weight armatures.

However, even though many applications have been considered for moving-iron linear motor topologies, they tend to suffer from a number of disadvantages, viz. :

- i. Heavy moving mass, which can reduce the dynamic capability of the motor.
- ii. A relatively low thrust force capability due to low air-gap flux density.

Based on the foregoing, moving-iron topologies were not considered to be suitable candidates for use in low power linear reciprocating for vapour compressor systems

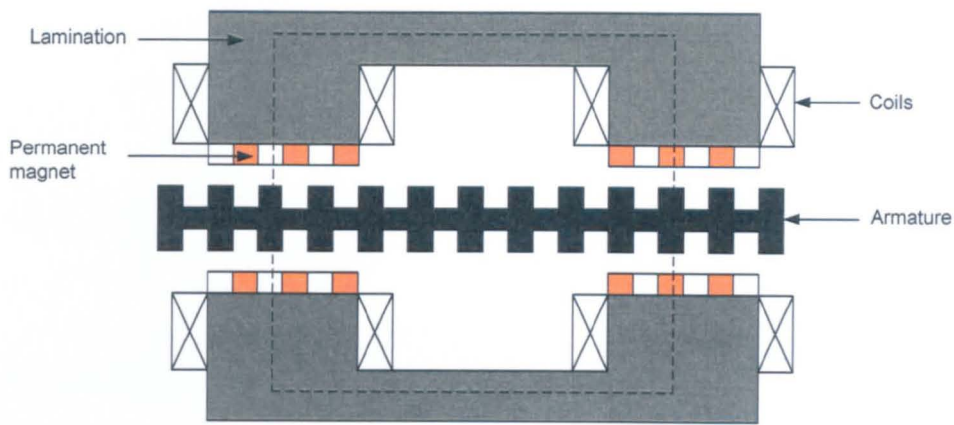


Fig. 1.25 Moving-iron linear generator for wave energy converter [45]

1.4.5.3 Moving-magnet motors

Moving-magnet linear motors have been designed for widely varying applications, such as air-compressors [12], artificial hearts [46], automotive systems [13], and robotics [47] [48].

Various possible design variants for both planar and tubular linear motors have been compiled by Clark [15], the linear motors shown in Fig. 1.26 and Fig. 1.27 encompassing slotted and slotless stators, permanent magnet and permanent magnets/ferromagnetic armatures, and variable and constant air-gap designs.

Jack et al [49] conducted a trade-off study on the moving-magnet linear motors illustrated in Fig. 1.28. The single-phase short-stroke tubular motors were designed for use in refrigerator compressor systems, and used soft magnetic composites and rare-earth NdFeB permanent magnets. All the designs were optimised and had same thrust force, 113 N, and copper loss, 1.75 W. In order to full-fill the requirements, the slot area, the outer diameter and the number of turns needed to be adjusted. The two designs in Figs. 1.28 (a) and (b) were proposed in order to achieve a light moving armature. However the motors inherently had very weak performance capabilities, and required more slot area to obtain the desired thrust force. A special support for the permanent magnets especially for the motor in Fig. 1.28 (b), is required and not easy to fabricate, which increases the manufacturing cost. The design shown in Fig. 1.28 (c) had three magnets attached to the armature, and exhibited significantly improved performance, whilst the outer diameter of motor was reduced. Due to the cost of NdFeB, only a single magnet is used in the motor shown in Fig. 1.28 (d),

whilst the orientation of the permanent magnet was changed from radial to axial in the motor illustrated in Fig. 1.28 (e).

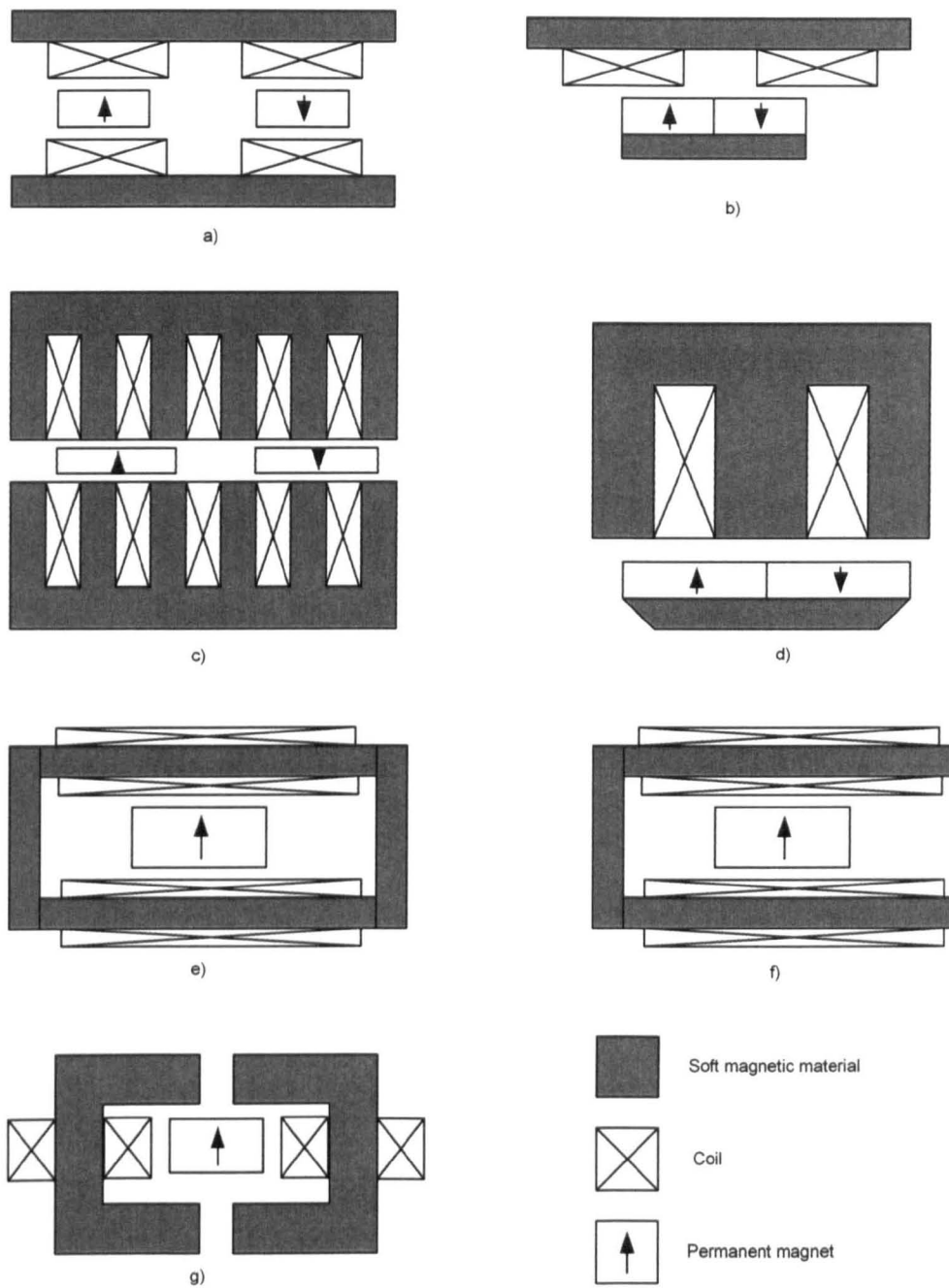


Fig. 1.26 Planar configurations of moving-magnet linear motor [15]

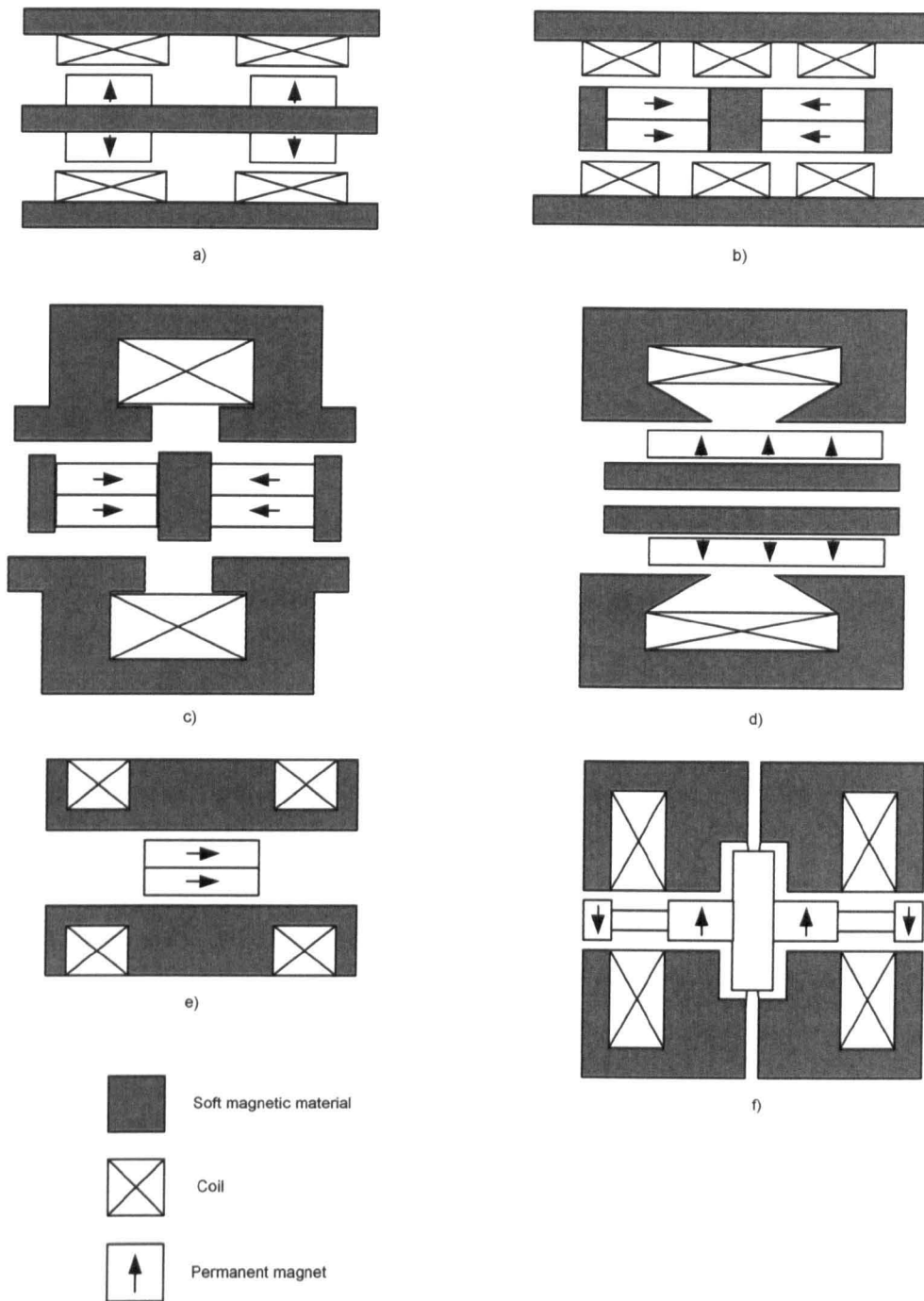


Fig. 1.27 Tubular configurations of moving-magnet linear motor [15]

The slotless moving-magnet tubular motor illustrated in Fig. 1.29 was employed in a diaphragm compressor for a medical bed by Mitchell et al [50]. The outer diameter and axial length of the motor were 40.0 mm and 34.0 mm, respectively, whilst the radially magnetised bonded NdFeB permanent magnets had a remanence of 0.57 T. The maximum thrust force produced was 2.5 N with a supply current of 1 A. However, by employing a slotted stator configuration and higher remanence NdFeB

magnets the force capability can be increased significantly. Other applications for the moving-magnet linear motors in the healthcare sector especially include implantable artificial hearts [11] [46] [51], and implantable hearing aids [15] [52] [53].

The axially tubular permanent magnet linear generator shown in Fig. 1.30 has been developed [24] for on-board generation of electrical power for telemetry vibration monitoring systems. It is a single-phase device, which is capable of generating 20 mW at 5 V, with a nominal resonant frequency of 50 Hz and a stroke of 0.8 mm. The two axially magnetised sintered NdFeB magnets and the mild steel pole-pieces give rise to an essentially radial magnetic field in the region occupied by the stator winding. However, the generator has a relatively heavy armature although this can be reduced by using the technique illustrated in Fig. 1.17 [38], which also reduces the volume of permanent magnet material. The technique has been applied to the slotted, five-phase, tubular permanent magnet linear motor [54] shown in Fig. 1.31. In this case, the non-ferromagnetic tube is employed and it is more lighter than the solid non-magnetic rod, which illustrated in Fig. 1.17. The axially tubular permanent magnet linear generator has also been developed by [55] for the direct drive marine energy conversion application. The generator can produce the rated power of 3 kW at 0.5 m/s. Another application of the axially tubular permanent magnet linear generator was used in automotive applications [56] [57] [58] [59]. For example, Zheng et al [58] developed a free piston energy converter in a series hybrid electric vehicle. The free piston energy converter converts chemical energy directly to electrical energy, and is a potential energy efficiency power source for use in a hybrid vehicle [57]. The design is compact structure and reliable [60].

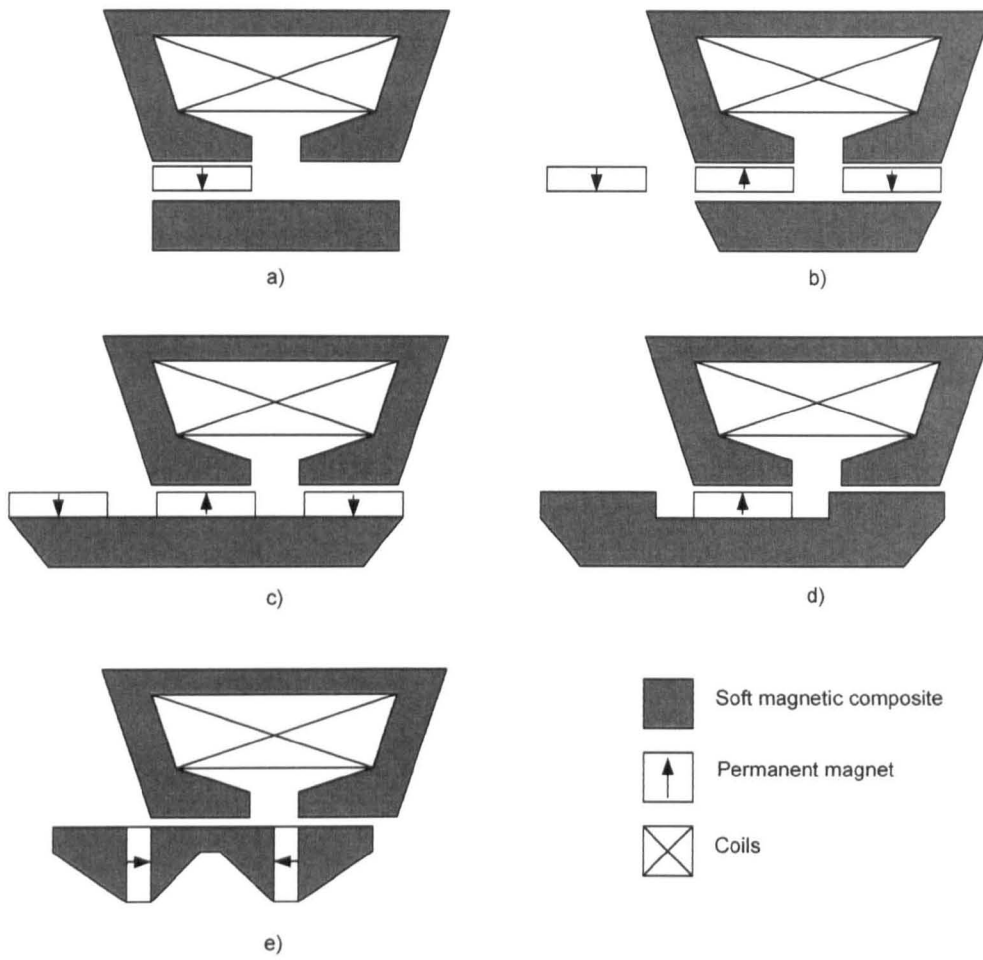


Fig. 1.28 Trade-off study on moving-magnet linear motors [49]

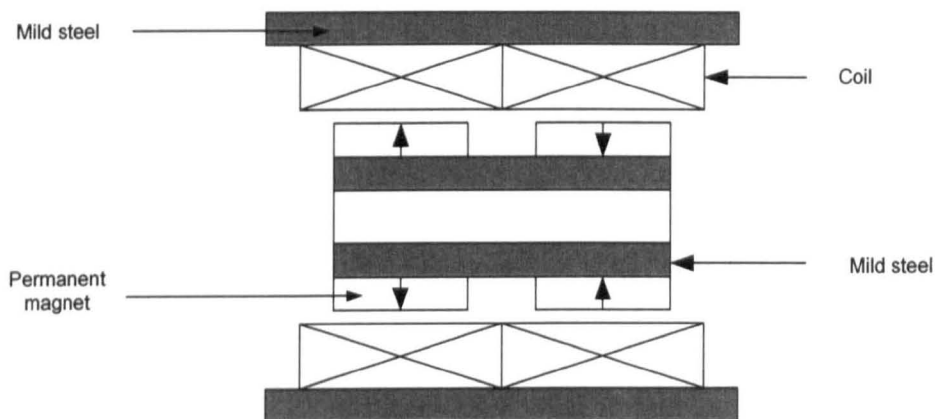


Fig. 1.29 Slotless tubular moving-magnet linear motor for diaphragm compressor [50] [61]

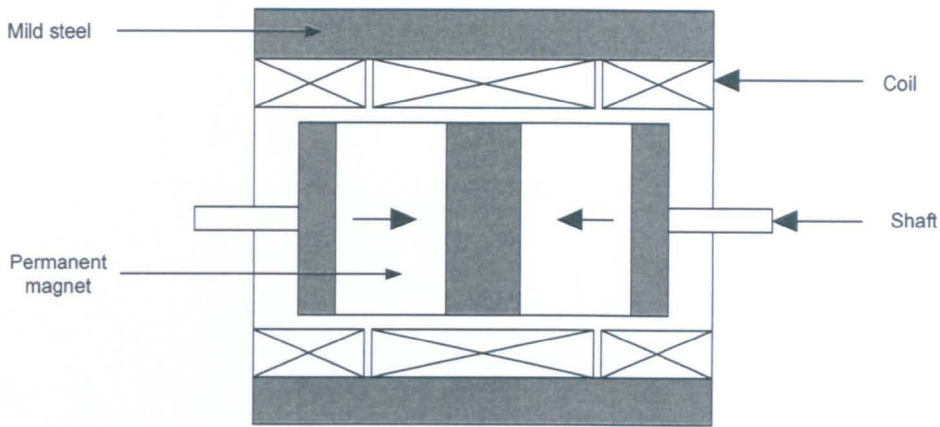


Fig. 1.30 Axially tubular permanent magnet linear generator [24]

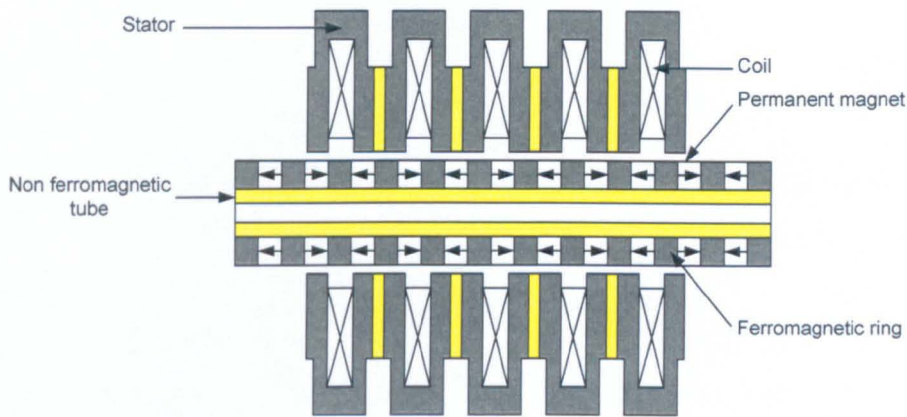


Fig. 1.31 5-phase tubular moving-magnet linear motor with non ferromagnetic tube [54]

Sunpower Inc [62] patented and manufactured a low moving mass design of moving-magnet tubular motor which had stationary armature back iron and a homopolar radially magnetised magnet, as shown in Fig. 1.32, in which only the permanent magnet reciprocates. The motor has been employed commercially in applications, such as linear alternators, and refrigerator and gas compressors. Almost the same topology has been considered in [63] and applied to a household linear refrigerator compressor system. Physically, the topology results in an additional air-gap, which compromises the force capability as well as a high leakage (external) field. Even though the design results in a light-weight armature for improving the dynamic capability, the motor has a relatively high manufacturing cost especially because of the need to provide a special support for the permanent magnet armature in order to facilitate robust reciprocating operation. Further, for same thrust force capability, the

number of turns needs to be increased, which results in a higher copper loss and reduced efficiency.

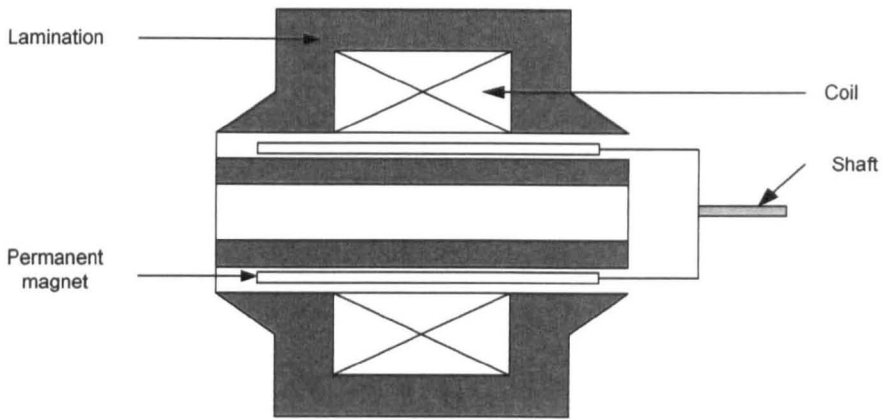


Fig. 1.32 Moving-magnet tubular permanent magnet linear machine with 2 air-gaps [62]

By employing a Halbach magnetised armature [34], based on bonded NdFeB magnet material in a slotted tubular motor as shown in Fig. 1.33, an essentially sinusoidal back-emf and virtually zero cogging force can be achieved. Compared with a conventional moving-magnet linear machine, the Halbach magnetised armature does not require back-iron and can have significantly reduced armature mass, which improves the dynamic capability, whilst the permanent magnet material is more effectively utilised, which results in a higher air-gap flux density for a given grade and size of magnet.

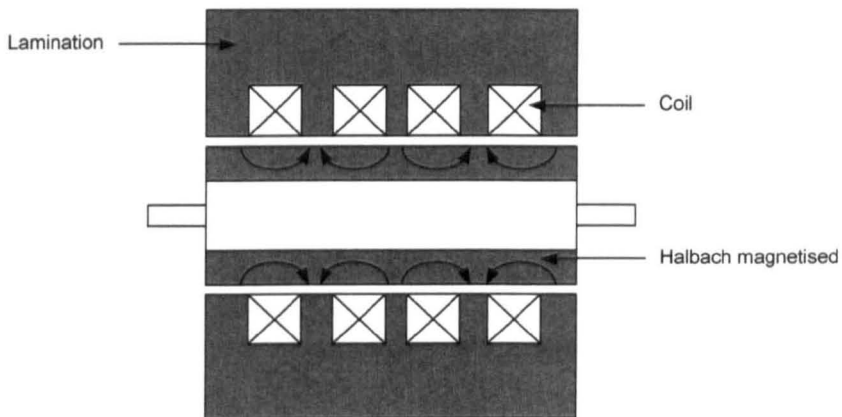


Fig. 1.33 Moving-magnet tubular permanent magnet machine with Halbach magnetisation

[34]

Improvement have been reported for such motors [34] [57] [64] [65] [66] since the manufacture of an ideal Halbach magnetised cylinder is relatively difficult, in particular using quasi-Halbach magnetised magnet. The unique feature of such a magnetisation is that axially and radially magnetised magnets are combined as shown in Fig. 1.34. The axially magnetised magnets effectively provide a return path for the radial air-gap flux easily, so that the flux in the armature back-iron is relatively small. Hence, a very thin ferromagnetic tube or even a non-magnetic tube can be used to support the magnets. Thus, the structure is simplified and the manufacturing cost will also be reduced. Moreover, the fundamental field of Halbach array is stronger, by a factor of 1.4 for an ideal Halbach magnetisation distribution, compared with that of a conventional radially magnetised magnet array, and, thus, the efficiency is increased [65].

A number of studies have demonstrated that moving-magnet linear motors can offer higher efficiencies than moving-coil linear motors [67] [68]. Further, a comparison between moving-coil and moving-magnet linear motors has indicated that the volume of magnet required for a moving-coil is greater than for a moving-magnet linear motors of the same power [15] [62]. In addition, the absence of flying leads to the armature makes moving-magnet linear motors more reliable and rugged, making them more suitable for higher duty operation [69].

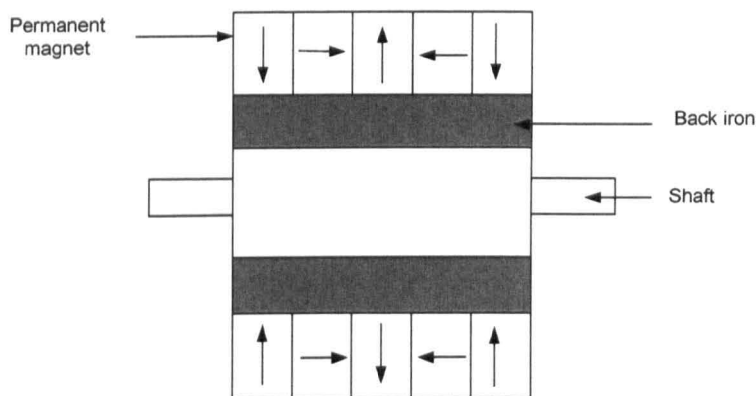


Fig. 1.34 Armature for moving-magnet tubular permanent magnet motor with quasi-Halbach magnetisation [64] [66]

1.5 Proposed designs

Of the competing machine topologies and technologies which have been reviewed, the 'best' design is quite hard to establish and certainly needs a comprehensive evaluation [49] due to the requirements of the applications. However, the most important criteria for the evaluation of linear motors for air-vapour compressor applications are based on their force capability, simplicity and cost-effectiveness. From that basis, a single-phase, moving-magnet tubular linear motor with a slotted stator manufactured from a soft magnetic composite is considered to be most suitable for the compressor application [70] [71].

Thus, three design variants have been selected for further analyses viz. a single-slot tubular moving-magnet magnet linear motor, with different magnet configurations – viz. iron-cored and air-cored quasi-Halbach magnetised magnets having a rectangular or trapezoidal cross-sections as illustrated in Fig. 1.35 and Fig. 1.36 and Fig. 1.37. In all cases, the quasi-Halbach magnetised armature generates a magnetic field which links with the single-phase stator coil, and a reciprocating thrust force is produced as the result of the interaction between the permanent magnetic field and the stator current when it is synchronised with the armature motion [72].

A ferromagnetic support tube will be used in the iron-cored quasi-Halbach magnetised motors with rectangular and trapezoidal magnets since this results in a stronger air-gap field, and, therefore, a better force capability. However, since a lightweight armature is frequently desirable, for comparison purposes, a non-ferromagnetic support tube will also be considered for the air-cored quasi-Halbach magnetised motor with rectangular magnets, since may have merit in terms of a higher dynamic capability [71].

Actually, the iron-cored quasi-Halbach magnetised motor with trapezoidal section magnets shown in Fig. 1.37 derives from Fig. 1.19, which is transformed from a planar moving-coil motor into a tubular moving-magnet motor. Due to the volumetric effect, the tubular motor topology may provide an enhanced thrust force density.

In terms of the stator configuration, there are difficulties in constructing a tubular core from laminations formed in the radial or axial planes since the magnetic field is basically in a radial/circumferential plane to produce axial force and the stator coils carries alternating current [49]. Thus, the most appropriate materials for tubular cores

are soft magnetic composites, SMC, which are made of compression compacted insulated iron powder. SMC has isotropic magnetic properties and this not only easily accommodates time-varying magnetic fields in all directions but allows a large number of design variants to be realised.

All the design variants will go through the complete design process in order to establish the most suitable candidate tubular motor for the linear air compressor system under consideration. The design process involves evaluating analytically the open-circuit flux distribution, the back-emf and the thrust force for each of the armature magnetisation patterns, the analytical solutions being validated by finite element calculations.

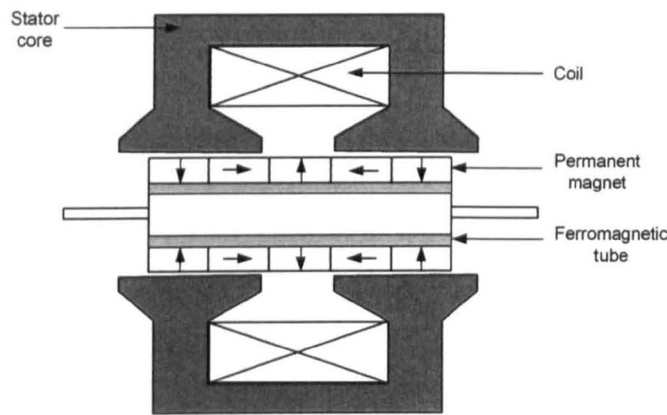


Fig. 1.35 Iron-cored quasi-halbach magnetised motor with rectangular magnets

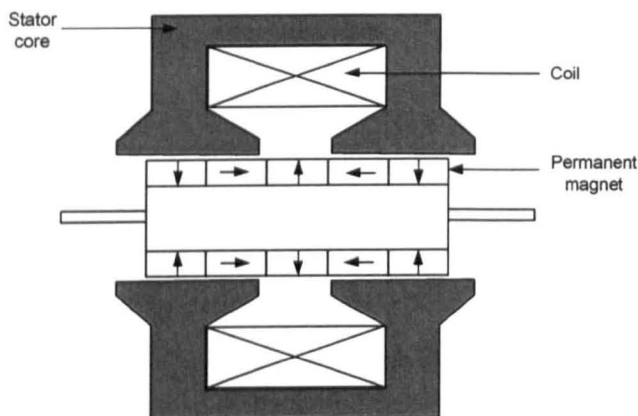


Fig. 1.36 Air-cored quasi-Halbach magnetised motor with rectangular magnets

1.7.1 Scope of thesis

The thesis is structured into 7 chapters:

Chapter 1: Introduction and literature review

This chapter presents the fundamentals of refrigerator compressor systems, the aim of the research and an extensive literature review of various linear machine technologies and topologies. Based on their force densities, reliability, simplicity of construction and electrical supply requirements, three promising candidates of tubular moving-magnet linear motor have been selected for further analysis.

Chapter 2: Analysis of open-circuit magnetic field distribution, flux-linkage, back-emf and thrust force of tubular moving-permanent magnet linear motors

In order to minimise the time for design optimisation, analytical solutions have been developed for the three tubular motor design variants, to predict the open-circuit magnetic field distribution, the coil flux-linkage, the back-emf and the thrust force. The analytical results are validated using finite element analysis. A comparison the open-circuit air-gap magnetic field distribution in the three design variants has also been carried-out.

Chapter 3: Design and optimisation of moving-magnet linear motors

The design optimisation of the moving-magnet linear motors is discussed in this chapter. The developed analytical method is employed to optimise the leading design parameters, whilst due to the limitation of analytical techniques in term of accounting for the influence of saturation, for example, and the relative complexity of the designs, finite element analysis is undertaken to refine the parameters.

Chapter 4: Design and optimisation of moving-iron linear motor for reciprocating compressors using finite element analysis

In order to investigate a potentially low cost motor topology, a moving-iron linear motor has been introduced and optimised using finite element analysis. The motor employs a low cost magnet material, Strontium ferrite and produces the same rated output power. Further, this chapter compares four design variants based on material cost and performance in order to obtain the most cost-effective solution.

Chapter 5 : Analysis of eddy current loss and iron loss in moving-magnet linear motors using finite element analysis

This chapter addresses the analysis of the eddy current loss in the tubular permanent magnet linear motors using the finite element technique. The influence of the eddy current loss in the permanent magnets of various segmentations i.e. solid magnet ring , single slit, 8 segments and 12 segment magnets. The iron loss which results in the stator core is also analysed using axi-symmetric step finite element analysis, for various velocity profile, viz, sinusoidal, rms constant and average constant velocities. This variation of iron loss with the stroke and on no-load and on-load conditions is also considered.

Chapter 6 : Prototyping and measurements

This chapter describes the prototyping of the moving-magnet linear motors, and the static test-rig which was established to measure the flux linkage, the cogging force and the thrust force. The measured results are used to validate finite element predictions. This chapter also describes the measurement of the iron loss when the linear motor is operated at resonant frequency with different strokes, the results again being used to validate the finite element predictions.

Chapter 7: Conclusions

The main findings of the research are summarised, and the areas which are worthy of further investigation are identified.

References

- [1] L. Lopes, S. Hokoi, H. Miura, and K. Shuhei, "Energy efficiency and energy saving in Japanese residential " *Science Direct: Energy and Building*, vol. 37, no. 7, pp. 698-706, July 2005.
- [2] J. Wang and D. Howe, "Summary of literature review of linear compressor patents for refrigeration applications," *University of Sheffield, Carbon Trust Project Number 2003-3-51-1-1*, April 2004.
- [3] J. Wang, D. Howe, and Z. Lin, "Comparative studies on linear motor topologies for reciprocating vapour compressors," *IEEE International Electric*

Machine and Drives Conference, IEMDC'07, Turkey, vol. 1, pp. 364-369, May 2007.

- [4] Z. Lin, J. Wang, and D. Howe, "A resonant frequency tracking technique for linear vapour compressors," *IEEE International Electric Machine and Drives Conference, IEMDC'07, Turkey*, vol. 1, pp. 370-375, May 2007.
- [5] K. Kim, D. Kim, Y. Song, and K. Kim, "Linear compressor," *US patent. no. 20040247457A1*, 2004.
- [6] Z. S. Al-Otaibi and A. G. Jack, "Utilising SMC in single-phase permanent magnet linear motors for compressor applications," *14th IET International Conference on Power Electronics, Machines and Drives, PEMD, York, UK*, vol. 1, pp. 752-753, 2-4 April 2008.
- [7] S. A. Evans, I. R. Smith, and J. G. Kettleborough, "Permanent magnet linear actuator for static and reciprocating short stroke electromechanical systems," *IEEE/ASME Transactions on Mechatronics*, vol. 6 , no. 1, pp. 36-42, March 2001.
- [8] B. Lequesne, "Permanent magnet linear motors for short strokes," *IEEE Transactions on Industry Applications*, vol. 32, no. 1, pp. 161-168, February 1996.
- [9] Boldea and S. A. Nasar, "Linear electric actuators and generators," *IEEE Transactions on Energy Conversion*, vol. 14, no. 3, pp. 712-717, September 1999.
- [10] I. Boldea and S. A. Nasar, "Linear motion electromagnetic systems," *New York ; Chichester : Wiley, ISBN 0471874515*, 1985.
- [11] M. Watada, K. Yanashima, Y. Oishi, D. Ebihara, and H. Dohneki, "Improvement on characteristics of linear oscillatory actuator for artificial hearts," *IEEE Transactions on Magnetics*, vol. 29, no. 6, pp. 3361-3363, November 1993.

- [12] R. E. Clark, D. S. Smith, P. H. Mellor, and D. Howe, "Design and optimisation of moving-magnet actuators for reciprocating electro-mechanical systems," *IEEE Transactions on Magnetics*, vol. 31, no. 6, pp. 3746-3748, November 1995.
- [13] I. Martins, J. Esteves, G. D. Marques, and F. P. D. Silva, "Permanent magnet linear actuators applicability in automotive active suspensions," *IEEE Transactions on Vehicular Technology*, vol. 55, no. 1, pp. 86-94, January 2006.
- [14] D. Howe, Z. Q. Zhu, and R. E. Clark, "Status of linear drives in Europe," *Invited Paper at Linear Drives for Industry Applications, LDIA 2001, Nagano, Japan*, October 2001.
- [15] R. E. Clark, "Resonant linear permanent magnet actuator for compressor," PhD Thesis, University of Sheffield, 2000.
- [16] J. C. West and B. R. Jayawant, "A new oscillatory motor," *Proceedings of IEE 109A*, pp. 292-300, August 1962.
- [17] G. W. M. Lean, "Review of recent progress in linear motors," *IEEE Transactions on Magnetics*, vol. 135, no. 6, pp. 115-128, November 1998.
- [18] O. Roubicek and Z. Pejsek, "Oscillatory synchronous linear motor with permanent magnet excitation," *IEEE Proceeding.*, vol. 127, no. 1, January 1980.
- [19] H. Yamada, M. Nirei, H. Ota, K. Kawakatsu, and T. Nakajima, "Development of linear electromagnetic actuator for implantable artificial hearts," *IEEE Transactions on Magnetics* vol. 4, no. 9, 1989.
- [20] J. Corda and E. Skopljak, "Linear switched reluctance actuator," *Sixth International Conference on Electrical Machines and Drives, ICEMS1993*, vol. 376, pp. 535-539, September 1993.
- [21] P. J. Hor, "Direct linear electrical drive system for high speed packaging applications," PhD Thesis, University of Sheffield,, 1998.

- [22] G. W. McLean, "Review of recent progress in linear motors," *IEE Proceedings of Electric Power Applications*, vol. 135, no. 6, pp. 380-416, November 1998.
- [23] A. Basak, *Permanent magnet linear motor*. Clarendon Press, Oxford Science Publications, 1996.
- [24] J. Wang, W. Wang, G. W. Jewell, and D. Howe, "Design and experimental characterisation of a linear reciprocating generator," *IEE Proceeding in Electrical Power Applications*, vol. 145, no. 6, pp. 509-518, November 1998.
- [25] P. J. Hor, Z. Q. Zhu, D. Howe, and J. Rees-Jones, "Minimisation of cogging force in a linear permanent magnet motor," *IEEE Transactions on Magnetics*, vol. 34, no. 5, pp. 3544-3547, September 1998.
- [26] I. Boldea and S. A. Nasar, "Linear electric actuators and generators," *IEEE International Electric Machine and Drives Conference Record, USA*, 1997.
- [27] I. Boldea and S. A. Nasar, *Linear electric actuators and generators*. Cambridge, UK: Cambridge University Press, 1997.
- [28] G. P. Widdowson, "Design optimisation of permanent magnet actuators," PhD Thesis, University of Sheffield, 1992.
- [29] D. S. Smith, "High performance actuators for automotive and aerospace applications," PhD Thesis, University of Sheffield, 1994.
- [30] G. H. Kang, J. P. Hong, and G. T. Kim, "A novel design of an air-cored type permanent magnet linear brushless motor by space harmonics field analysis," *IEEE Transactions on Magnetics*, vol. 37, no. 5, pp. 3732-3736, September 2001.
- [31] J. K. Kim, S. W. Joo, S. C. Hahn, J. P. Hong, D. H. Kang, and D. H. Koo, "Static characteristic of linear BLDC motor using equivalent magnetic circuit and finite element method," *IEEE Transactions on Magnetics*, vol. 40, no. 2, pp. 742-745, March 2004.

- [32] Y. B. Tang, Y. G. Chen, B. H. Teng, H. Fu, H. X. Li, and M. J. Tu, "Design of a permanent magnetic circuit with air-gap in a magnetic refrigerator," *IEEE Transactions on Magnetics*, vol. 40, no. 3, pp. 1597-1600, May 2004.
- [33] M. Andriollo, G. Baccini, G. Martinelli, A. Morini, and A. Tortela, "Design optimisation of slotless linear PM motors," *Proceedings of 4th International Symposium on Linear Drives for Industry Applications, LDIA2003, Birmingham, United Kingdom*, pp. 203-206, September 2003.
- [34] J. Wang, G. W. Jewell, and D. Howe, "A general framework for the analysis and design of tubular linear permanent magnet machines," *IEEE Transactions on Magnetics*, vol. 35, no. 3, pp. 1986-2000, May 1999.
- [35] Y. He, Z. Q. Zhu, and D. Howe, "A PWM controlled linear servo motor system for friction welding," *Proceedings of 2nd International Conference on Electrical Machines, CICEM '95, Hangzhou, China*, vol. 2.3, pp. 51-55, August/September 1995.
- [36] J. Wang, D. Howe, and G. W. Jewell, "Design optimisation and comparison of tubular permanent magnet machines," *Proceedings of Industrial Electrical and Engineering, Electrical Power Applications*, vol. 148, no. 5, pp. 456-464, September 2001.
- [37] Z. P. Xia, Z. Q. Zhu, and D. Howe, "Magnetic field distribution in tubular PM motors with axially magnetised magnets," *Proceedings of 4th International Symposium on Linear Drives for Industry Applications, LDIA 2003, Birmingham, United Kingdom*, pp. 442-445, September 2003.
- [38] J. Wang, D. Howe, and G. W. Jewell, "Analysis and design optimisation of an improved axially magnetised tubular permanent magnet machine," *IEEE Transactions on Energy Conversions*, vol. 19, no. 2, pp. 289-295, June 2004.
- [39] J. Wang and D. Howe, "Design optimisation of radially magnetised iron cored, tubular permanent magnet machines and drive systems," *IEEE Transactions on Magnetics*, vol. 40, no. 5, pp. 3262-3277, September 2004.

- [40] M. G. Lee and D. G. Gweon, "Optimal design of a double-sided linear motor with a multi-segmented trapezoid magnet arrays for a high precision positioning system," *Journal of Magnetism and Magnetic Materials*, vol. 281, no. 2-3, pp. 226-346, October 2004.
- [41] M. Yamaguchi, M. Nagumo, M. IIO, and H. Yamada, "Static thrust analysis of a cylindrical moving core linear oscillatory actuator," *Electrical Engineering in Japan*, vol. 133, no. 6, 1993.
- [42] S. Guerin, E. Sedda, C. Fageon, J. P. Yonnet, and C. Chillet, "An original configuration of linear motor with parallel polarisation," *Proceedings of 4th International Symposium on Linear Drives for Industry Applications, LDIA2003, Birmingham, United Kingdom*, pp. 557-559, September 2003.
- [43] N. Sidell and G. W. Jewell, "Short stroke, bidirectional linear actuator for high temperature applications," *IEE Proceedings of Electric Power Applications*, vol. 147, no. 3, pp. 175-180, May 2000.
- [44] J. Wang, W. Wang, G. W. Jewell, and D. Howe, "A low power, linear, permanent generator/energy storage system," *IEEE Transactions on Industrial Electronics*, vol. 49, no. 3, pp. 640-648, June 2002.
- [45] M. A. Mueller, N. J. Baker, P. R. M. Brooking, and J. Xiang, "Low speed linear electrical generators for renewable energy applications," *Proceedings of 4th International Symposium on Linear Drives for Industry Applications, LDIA2003, Birmingham, United Kingdom*, pp. 29-32, September 2003.
- [46] C. H. Yang and S. A. Nasar, "A permanent magnet linear oscillatory motor for the total artificial heart," *Electrical Machines and Power System*, vol. 15, pp. 381-395, 1988.
- [47] H. Lu, J. Zhu, and Y. Guo, "Development of a slotless tubular linear interior permanent magnet micrometer for robotic applications," *IEEE Transactions on Magnetics*, vol. 41, no. 10, pp. 3988-3990, October 2005.
- [48] H. Lu, J. Zhu, Y. Guo, and Z. Lin, "A miniature short stroke tubular linear actuator and its control," *Proceedings of International Conference on*

Electrical Machines and Systems, ICEMS2007, Seoul, Korea, pp. 1680-1685, October 2007.

- [49] A. G. Jack, Z. S. Al-Otaibi, and M. Persson, "Alternative designs for oscillating linear single-phase permanent magnet motors using soft magnetic composites," *International Conference on Electrical Machines and Drives, ICEMS 2006, Nagasaki, Japan, November 2006.*
- [50] J. K. Mitchell, J. Wang, R. E. Clark, and D. Howe, "Analytical modelling of the air-gap field in reciprocating moving magnet actuators," *Journal of Magnetism and Magnetic Materials*, vol. 272-276, no. 1, pp. E1783-1785, May 2004.
- [51] D. Ebihara and M. Watada, "Development of a single winding linear oscillatory actuator," *IEEE Transactions of Magnetics*, vol. 28, no. 5, pp. 3030-3032, September 1992.
- [52] W. Affane and T. S. Birch, "A micro-miniature electromagnetic middle-ear implant hearing device," *Proceedings of 8th Euro-sensors Conference, Toulouse, France, September 1994.*
- [53] H. Bernhard, C. Stieger, and Y. Perriard, "Micro-actuator for new implantable hearing device," *41th IEEE Industry Applications Conference Annual Meeting, IAS2006, Florida, USA, October 2006.*
- [54] B. Tomczuk, G. Schroder, and A. Waindok, "Finite element analysis of the magnetic field and electromechanical parameter calculation for a slotted permanent magnet tubular linear motor," *IEEE Transactions on Magnetics*, vol. 43, no. 7, pp. 3229-3236, July 2007.
- [55] N. J. Baker, M. A. Mueller, and E. Spooner, "Permanent magnet air-cored tubular linear generator for marine energy converters," *2nd International Conference on Power Electronics, Machines and Drives, PEMD 2004, Edinburgh, United Kingdom, March/April 2004.*
- [56] A. Canova, G. Grusso, M. Otella, M. Repetto, and N. Schofield, "Soft magnetic composites for tubular linear actuators," *International Conference on Electrical Machines and Drives, ICEM2002, Brugge, Belgium, 2002.*

- [57] J. Wang and D. Howe, "A linear permanent magnet generator for a free-piston energy converter," *IEEE International Electric Machines and Drives Conference, IEMDC2005, Texas, USA*, pp. 1521-1528, May 2005.
- [58] P. Zheng, A. Chen, P. Thelin, W. M. Arshad, and C. Sadarangani, "Research on a tubular longitudinal flux PM linear generator used for free-piston energy converter," *13th International Symposium on Electromagnetics, Bradenburg, Germany*, May 2006.
- [59] N. Schofield, A. Canova, and M. Ottella, "A tubular linear actuator for steer-by-wire applications," *Proceedings of 4th International Symposium on Linear Drives for Industry Applications, LDIA2003, Birmingham, United Kingdom*, pp. 560-563, September 2003.
- [60] T. A. Johansen, O. Egeland, E. A. Johannessen, and R. Kvamsdal, "Free piston diesel engine timing and control - toward electronic cam and crankshaft," *IEEE Transactions on Control System Technology*, vol. 10, no. 2, pp. 177-190, March 2002.
- [61] R. E. Clark, D. Howe, and G. W. Jewell, "The influence of magnetisation pattern on the performance of a cylindrical moving-magnet linear actuator," *IEEE Transactions on Magnetics*, vol. 36, no. 5, pp. 3571-3574, September 2000.
- [62] R. Redlich, "A summary of twenty years experience with linear motors and alternators," *Sunpower Inc., Athens, Ohio, U.S.A.*, 1996.
- [63] B. C. Woo, D. H. Kang, and D. K. Hong, "A simulation of the transient state in linear actuator for household electric appliances," *7th International Conference on Electrical Machines and Systems, ICEMS2004, Seoul, Korea*, 2004.
- [64] M. G. Lee, S. Q. Lee, and D. G. Gweon, "Analysis of Halbach array and its applications to linear motor," *Pergamon, Mechatronics*, vol. 14, no. 1, pp. 115-128, February 2004.

- [65] S. M. Jang, J. Y. Choi, H. W. Cho, and S. H. Lee, "Thrust analysis and measurement of tubular linear actuator with cylindrical Halbach array," *IEEE Transactions on Magnetics*, vol. 41, no. 5, pp. 2028-2031, May 2005.
- [66] S. M. Jang, J. Y. Choi, S. H. Lee, H. W. Cho, and W. B. Jang, "Analysis and experimental verification of moving magnet linear actuator with cylindrical Halbach array," *IEEE Transactions on Magnetics*, vol. 40, no. 4, pp. 2068-2070, July 2004.
- [67] T. Yamada, S. Koganezawa, K. Aruga, and Y. Mizoshita, "A high performance and low profile moving magnet actuator for disk drives," *IEEE Transactions on Magnetics*, vol. 30, no. 6, pp. 4227-4229, November 1994.
- [68] E. Byckling and E. Perkio, "Dynamic properties of moving magnet transducers," *IEEE Transactions on Magnetics*, vol. 16, no. 2, pp. 68-73, March 1990.
- [69] B. Lequesne, "Permanent magnet linear motors for short strokes," *IEEE Industry Applications Symposium Annual Meeting, IAS 1992*, vol. 1, pp. 162-170, 1992.
- [70] J. F. Eastham, "Novel synchronous machines: Linear and disc," *Proceedings of Instrumentation Electrical Engineering*, vol. B-137, pp. 49-58, 1990.
- [71] J. Wang and D. Howe, "Tubular modular permanent magnet machines equipped with quasi-Halbach magnetised magnet - Part 1: Magnetic field distribution, EMF and thrust force," *IEEE Transactions on Magnetics*, vol. 41, no. 9, pp. 2470-2478, September 2005.
- [72] J. Wang, Z. Lin, and D. Howe, "Analysis of a short stroke, single phase quasi-Halbach magnetised tubular permanent magnet motor for linear compressor applications," *IET Electric Power Application*, vol. 2, no. 3, pp. 193-200, January 2008.

CHAPTER 2

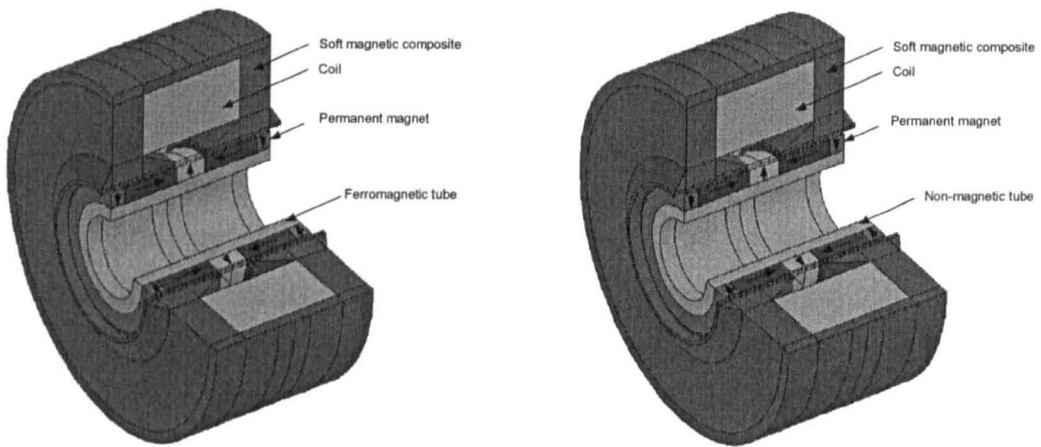
ANALYSIS OF OPEN-CIRCUIT MAGNETIC FIELD DISTRIBUTION, FLUX-LINKAGE, BACK-EMF AND THRUST FORCE IN TUBULAR MOVING-MAGNET LINEAR MOTORS

2.1 Introduction

A comprehensive literature review on linear motors was conducted in Chapter 1, and it was concluded that a single-phase, a single-slot tubular moving permanent magnet linear motor, which could have various magnet configurations - such as iron-cored or air-cored quasi-Halbach magnetised magnets having rectangular or trapezoidal cross-sections, is the most appropriate topology for a direct-drive linear refrigerator compressor system. All the motors have been employed a soft magnetic composite (SMC) material, Somaloy 700, for stator core, and carries a single coil as shown in Fig. 2.1. The use of an SMC material facilitates near net-shape, low cost manufacture, as well as good utilization of the available space to achieve a compact design. In addition, a coil is easy to manufacture and results in a very high packing factor, which is conducive to high efficiency [1]. The maximum armature stroke is approximately 10.5 mm and Table 2.1 summaries the key design parameters and specification of the tubular linear motors.

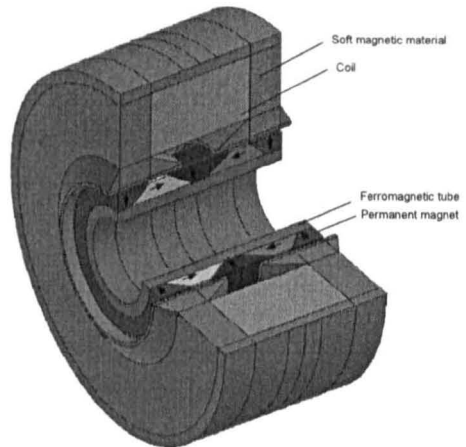
This chapter describes the analytical predictions of the open-circuit magnetic field distribution, the flux-linkage, the back-emf and the thrust force for the three design variants, the results being validated by extensively finite element analysis. Analytical models are a particularly useful tool to aid the design of permanent magnet linear motors. Although unable to account directly for material non-linearities and the complex leakage flux paths which exist in many devices, the ability to generate algebraic equations relating operational performance to leading design parameters enables a direct insight into the influence of the various parameters to be obtained. In turn, this allows initial dimensioning of a motor to be performed. In addition, such equations are well suited to being incorporated into computer aided design algorithms, and numerical design optimisation schemes, which facilitates easier and faster solutions compared to the finite element method [2]. However, the determination of a suitable valued for a leading design parameter from an analytical solution generally needs to be checked and possibly refined using the finite element method, since this can accommodate more complex geometries of magnetic circuit,

material non-linearities, distributed field sources, time-transient excitation, and relative motion effects [3].



i. Iron-cored quasi-Halbach magnetised motor with rectangular magnet

ii. Air-cored quasi-Halbach magnetised motor with rectangular magnet



iii. Iron-cored quasi-Halbach magnetised motor with trapezoidal magnet

Fig. 2.1 Three design variants of tubular linear motors

Table 2.1 Design parameters and specification of linear motors

Item	Value	Units
Rated Voltage (rms)	230	V
Rated Current (rms)	0.5	A
Outer diameter of stator	100	mm
Axial length	50	mm
Pole-pitch	25	mm
Air-gap length	0.8	mm
Radial thickness of magnets	5	mm
Permanent magnet material	Sintered NdFeB	-
Remanence	1.14	T
Soft magnetic material	Somaloy 700	-

2.2 Open-circuit magnetic field distribution

The determination of the open-circuit magnetic flux distribution is fundamental to an analytical method and a key element of the design process. Additionally, it enables the air-gap average flux density, coil flux-linkage and thrust force to be determined. These are the most significant considerations in predicting the geometry and performance of a linear motor. A variety of techniques have been employed to predict open-circuit magnetic field distributions, arguably the most common approach being to use a lumped parameter magnetic equivalent circuit [4] [5]. However, this technique suffers from problems associated with model inaccuracy, particularly when the flux leakage is significant and the flux paths are complex. Hence, general frameworks and comprehensive analytical solutions have been established and reported, for various moving-magnet linear motors such as axially [6] [7], radially [8] [9] and Halbach magnetised designs [2] [10]. These analytical tools provide significant information, especially in regard to the open-circuit flux distribution which results with each magnetisation distribution.

In order to establish an analytical solution for the open-circuit flux distribution in all three linear motor design variants under consideration, the following assumptions have been made:

- i. The stator core is slotless and the permeability of the ferromagnetic core is infinite. However, a Carter coefficient will be introduced if the influence of stator slotting effect is to be taken into account [2] [10] [11].
- ii. The axial lengths of the machines are infinite and the analytical model comprise an infinitely long sleeve and a series of permanent magnet armatures extending to infinity along the machine axis. If the separation distance, T_i , between the two adjacent armatures is sufficiently large, the magnetic field distributions of the motor can be represented by one of the repeated elements [11] [12].

The three magnetisation distribution variants to be considered are:

- i. Iron-cored quasi-Halbach, rectangular section magnets
- ii. Air-cored quasi-Halbach, rectangular section magnets
- iii. Iron-cored quasi-Halbach, trapezoidal section magnets

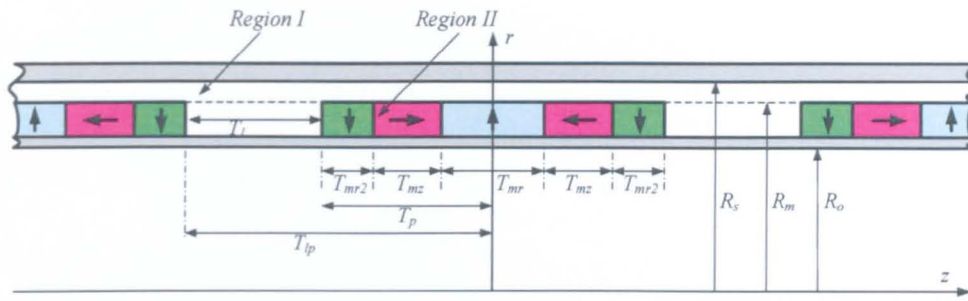
The iron-cored and air-cored quasi-Halbach magnetized motors are shown in Figs. 2.2 (i) and (ii), and each moving-magnet armature comprises three radially

magnetized magnets and two axially magnetized magnets, each of which has a rectangular cross-section radially magnetized magnet at the centre of the armature is twice that of the radially magnetised magnets in the ends. In order to produce a higher air-gap field, a ferromagnetic support tube is used in the iron-cored quasi-Halbach magnetised linear motor. However, a non-magnetic support tube has an advantage in term of reducing the mass, and eddy current loss in the moving armature, as will be described in Chapter 5.

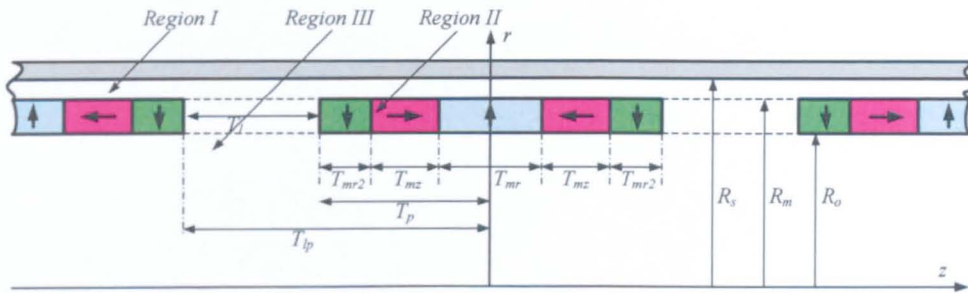
The quasi-Halbach magnetised motor in Fig. 2.2 (iii) comprises three trapezoidal cross section radially magnetized magnets and two trapezoidal cross section axially magnetized magnets, the shape of the trapezoids being governed by the angle, β . It may produce a better air-gap field distribution than the motors shown in Figs. 2.2(i) and (ii), which may result in a higher force capability [13]. A ferromagnetic support tube is used to further enhance the force capability of the motor.

For, both iron-cored quasi-Halbach magnetised motors, the open-circuit magnetic field analysis is confined to two regions: region *I* is an airspace region where the permeability is μ_0 , and region *II* is the permanent magnet region where the permeability is $\mu_0\mu_r$, μ_r being the relative recoil permeability which for rare-earth permanent magnets is close to unity. However, in the air-cored quasi-Halbach magnetised motor, the magnetic field analysis has to encompass three regions, viz., airspace regions *I* and *III*, and the permanent magnet region *II*.

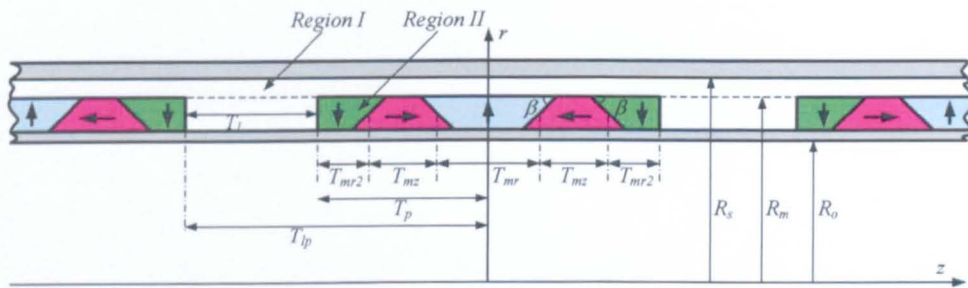
T_{mr} and T_{mz} are the axial length of the central radially and axially magnetized magnets respectively. The pole-pitch is defined as $T_p = T_{mr} + T_{mz}$, and the fundamental period of the magnetization is given by T_{ip} . The separation distance T_s between two adjacent armatures must be much greater than the pole-pitch, T_p . The magnetization distribution for each analytical model are represented in Fig. 2.3, the iron-cored and air-cored quasi-Halbach magnetised motor with rectangular section magnets having the same magnetisation distribution as in Fig. 2.3 (i), since they have identical configuration of permanent magnets.



i. Iron-cored quasi-Halbach magnetisation, rectangular section magnets [1]

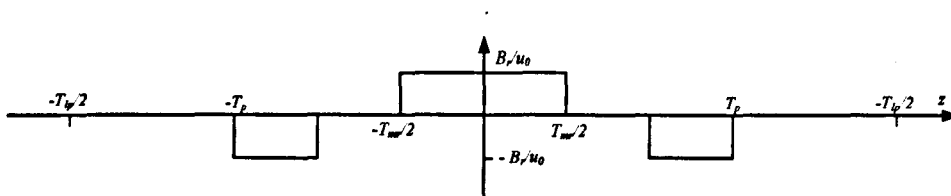


ii. Air-cored quasi-Halbach magnetisation, rectangular section magnets [11]

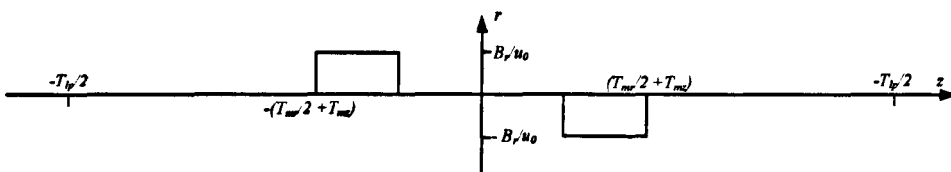


iii. Iron-cored quasi-Halbach magnetisation, trapezoidal section magnets [14]

Fig. 2.2 Analytical field models

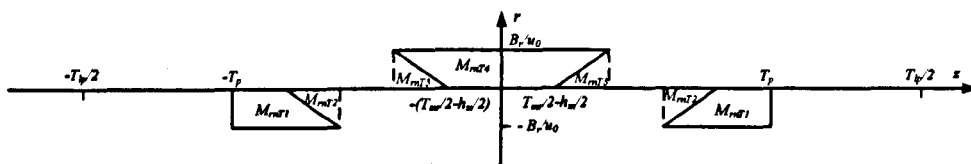


a. Radial component

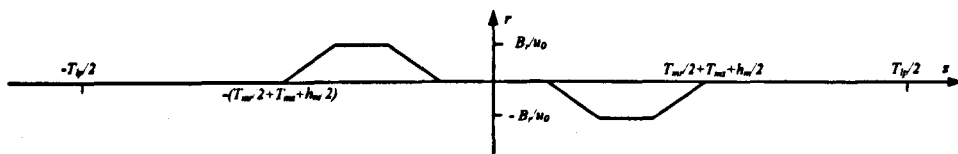


b. Axial component

i. Iron and air-cored quasi-Halbach magnetised, with rectangular magnets



a. Radial component



b. Axial component

ii. Iron-cored quasi-Halbach magnetised, with trapezoidal magnets

Fig. 2.3 Magnetisation distributions

Generally, the field equations in term of the vector magnetic potential A_θ for the tubular (axi-symmetric) motors are:

$$\frac{\partial}{\partial z} \left(\frac{1}{r} \frac{\partial}{\partial z} (rA_{I\theta}) \right) + \frac{\partial}{\partial r} \left(\frac{1}{r} \frac{\partial}{\partial r} (rA_{I\theta}) \right) = 0 \quad 2.1$$

$$\frac{\partial}{\partial z} \left(\frac{1}{r} \frac{\partial}{\partial z} (rA_{II\theta}) \right) + \frac{\partial}{\partial r} \left(\frac{1}{r} \frac{\partial}{\partial r} (rA_{II\theta}) \right) = -\mu_0 \nabla_x M$$

Whilst for the tubular axi-symmetric air-cored motor, the field equations are:

$$\frac{\partial}{\partial z} \left(\frac{1}{r} \frac{\partial}{\partial z} (rA_{I,III\theta}) \right) + \frac{\partial}{\partial r} \left(\frac{1}{r} \frac{\partial}{\partial r} (rA_{I,III\theta}) \right) = 0 \quad 2.2$$

$$\frac{\partial}{\partial z} \left(\frac{1}{r} \frac{\partial}{\partial z} (rA_{II\theta}) \right) + \frac{\partial}{\partial r} \left(\frac{1}{r} \frac{\partial}{\partial r} (rA_{II\theta}) \right) = -\mu_0 \nabla_x M$$

The magnetization, M in the cylindrical coordinate system is given by:

$$M = M_r e_r + M_z e_z \quad 2.3$$

where M_r and M_z denote the components of M in the radial and axial directions, respectively. The magnetization distributions shown in Fig. 2.3, may be expanded into Fourier series, with M_r and M_z expressed as functions of z as:

$$M_r = \sum_{n=1,2,3,\dots} \tilde{M}_{rn} \cos m_n z; \quad 2.4$$

$$M_z = \sum_{n=1,2,3,\dots} \tilde{M}_{zn} \sin m_n z$$

where $m_n = 2\pi n / T_{lp}$ and $T_{lp} = T_p + T_l$.

For the motors equipped with rectangular section quasi-Halbach magnetised magnets:

$$M_{rn} = -\frac{2B_{rem}}{\mu_0 \pi l} \left[\sin \frac{m_n T_{mr}}{2} - \sin m_n T_p + \sin m_n \left(T_{mz} + \frac{T_{mr}}{2} \right) \right]$$

$$M_{zn} = -\frac{4B_{rem}}{\mu_0 \pi l} \sin \frac{m_n T_{mz}}{2} \sin \frac{m_n T_p}{2} \quad 2.5$$

For the motor with trapezoidal section magnets:

$$\begin{aligned}
M_{rn} &= (M_{rnT1} - M_{rnT2}) + (M_{rnT4} - M_{rnT3}) \\
M_{zn} &= (M_{znT1} + M_{znT2} + M_{znT3})
\end{aligned}
\tag{2.6}$$

where M_{rnT1} , M_{rnT2} , M_{rnT3} , M_{rnT4} , M_{znT1} , M_{znT2} , and M_{znT3} are described in Appendix B.

Thus, equation 2.1 and 2.2 may be further written as equation 2.7 and 2.8 respectively:

$$\begin{aligned}
\frac{\partial}{\partial z} \left(\frac{1}{r} \frac{\partial}{\partial z} (rA_{I\theta}) \right) + \frac{\partial}{\partial r} \left(\frac{1}{r} \frac{\partial}{\partial r} (rA_{I\theta}) \right) &= 0 \\
\frac{\partial}{\partial z} \left(\frac{1}{r} \frac{\partial}{\partial z} (rA_{II\theta}) \right) + \frac{\partial}{\partial r} \left(\frac{1}{r} \frac{\partial}{\partial r} (rA_{II\theta}) \right) &= \sum_{n=1,2,3,\dots} P_n \sin m_n z
\end{aligned}
\tag{2.7}$$

$$\begin{aligned}
\frac{\partial}{\partial z} \left(\frac{1}{r} \frac{\partial}{\partial z} (rA_{I,III\theta}) \right) + \frac{\partial}{\partial r} \left(\frac{1}{r} \frac{\partial}{\partial r} (rA_{I,III\theta}) \right) &= 0 \\
\frac{\partial}{\partial z} \left(\frac{1}{r} \frac{\partial}{\partial z} (rA_{II\theta}) \right) + \frac{\partial}{\partial r} \left(\frac{1}{r} \frac{\partial}{\partial r} (rA_{II\theta}) \right) &= \sum_{n=1,2,3,\dots} P_n \sin m_n z
\end{aligned}
\tag{2.8}$$

where for the motors having rectangular sections magnets:

$$P_n = \frac{4B_{rem}}{T_p} \left[\sin m_n \frac{T_{mr}}{2} - \sin m_n T_p + \sin m_n \left(T_{mz} + \frac{T_{mr}}{2} \right) \right]
\tag{2.9}$$

whilst for the motor having trapezoidal section magnets:

$$P_n = \mu_0 m_n M_{rn}
\tag{2.10}$$

For the iron-cored motors, the boundary conditions that need to be satisfied are:

$$\begin{aligned}
B_{zI} \Big|_{r=R_s} &= 0; & B_{rI} \Big|_{r=R_m} &= B_{rII} \Big|_{r=R_m}; \\
H_{zI} \Big|_{r=R_m} &= H_{zII} \Big|_{r=R_m}; & H_{zII} \Big|_{r=R_s} &= 0;
\end{aligned}
\tag{2.11}$$

Solving equation 2.7 subject to the boundary conditions 2.11 results in the following expressions for the flux density components:

$$B_{rI}(r, z) = - \sum_{n=1,2,\dots}^{\infty} [a'_{In} BI_1(m_n r) + b'_{In} BK_1(m_n r)] \cos(m_n z) \quad 2.12$$

$$B_{zI}(r, z) = \sum_{n=1,2,\dots}^{\infty} [a'_{In} BI_0(m_n r) + b'_{In} BK_0(m_n r)] \sin(m_n z)$$

$$B_{rII}(r, z) = - \sum_{n=1,2,\dots}^{\infty} \{ [F_{AN}(m_n r) + a'_{IIIn}] BI_1(m_n r) + [-F_{BN}(m_n r) + b'_{IIIn}] BK_1(m_n r) \} \cos(m_n z) \quad 2.13$$

$$B_{zII}(r, z) = - \sum_{n=1,2,\dots}^{\infty} \{ [F_{AN}(m_n r) + a'_{IIIn}] BI_0(m_n r) - [-F_{BN}(m_n r) + b'_{IIIn}] BK_0(m_n r) \} \sin(m_n z)$$

where $BI_0(\bullet)$, $BI_1(\bullet)$ are modified Bessel functions of the first-kind and $BK_0(\bullet)$, $BK_1(\bullet)$ are modified Bessel function of the second-kind of order 0 and 1, respectively, and $F_{AN}(\bullet)$, $F_{BN}(\bullet)$, a'_{In} , b'_{In} , a'_{IIIn} , and b'_{IIIn} are defined in Appendix C.

For the air-cored motor, the boundary conditions that need to be satisfied are:

$$\begin{aligned} B_{zI} \Big|_{r=R_s} &= 0; & A_{zII} \Big|_{r=0} &= 0; \\ B_{rI} \Big|_{r=R_m} &= B_{rII} \Big|_{r=R_m}; & H_{zI} \Big|_{r=R_m} &= H_{zII} \Big|_{r=R_m}; \\ B_{rII} \Big|_{r=R_0} &= B_{rIII} \Big|_{r=R_0}; & H_{zII} \Big|_{r=R_0} &= H_{zIII} \Big|_{r=R_0}; \end{aligned} \quad 2.14$$

Solving equation 2.8 subject to the boundary conditions 2.14 results in the following expressions for the flux density components:

$$B_{rI}(r, z) = - \sum_{n=1,2,\dots}^{\infty} [a'_{In} BI_1(m_n r) + b'_{In} BK_1(m_n r)] \cos(m_n z) \quad 2.15$$

$$B_{zI}(r, z) = \sum_{n=1,2,\dots}^{\infty} [a'_{In} BI_0(m_n r) + b'_{In} BK_0(m_n r)] \sin(m_n z)$$

$$B_{rII}(r, z) = - \sum_{n=1,2,\dots}^{\infty} \{ [F_{AN}(m_n r) + a'_{IIIn}] BI_1(m_n r) + [-F_{BN}(m_n r) + b'_{IIIn}] BK_1(m_n r) \} \cos(m_n z) \quad 2.16$$

$$B_{zII}(r, z) = - \sum_{n=1,2,\dots}^{\infty} \{ [F_{AN}(m_n r) + a'_{IIIn}] BI_0(m_n r) - [-F_{BN}(m_n r) + b'_{IIIn}] BK_0(m_n r) \} \sin(m_n z)$$

$$B_{rIII}(r, z) = \sum_{n=1,2,\dots}^{\infty} [a'_{III} BI_1(m_n r)] \cos(m_n z) \quad 2.17$$

$$B_{zIII}(r, z) = \sum_{n=1,2,\dots}^{\infty} [a'_{III} BI_o(m_n r)] \sin(m_n z)$$

where a'_{In} , b'_{In} , a'_{III} , b'_{III} and a'_{III} are defined in Appendix D.

2.3 Flux -linkage, back-emf and thrust force

For all three design variants, when a slotted stator is employed, the slotting effect may be accounted [2] by introducing a carter coefficient, K_c , given by

$$K_c = \frac{\tau_{sp}}{\tau_{sp} - \gamma g'} \quad 2.18$$

where $g' = g + h_m / \mu_r$, τ_{sp} is the stator slot-pitch, g is the air-gap length, h_m is the radial thickness of the magnets, and γ is a slotting factor [2] [11] given by

$$\gamma = \frac{4}{\pi} \left(\frac{b_o}{2g'} \tan^{-1} \left(\frac{b_o}{2g'} \right) - \ln \sqrt{1 + \left(\frac{b_o}{2g'} \right)^2} \right) \quad 2.19$$

where b_o is the width of slot opening. The effective air-gap length, g_e and the equivalent stator bore radius R_{se} are given, respectively :

$$g_e = g + (K_c - 1)g'$$

$$R_{se} = R_m + g_e \quad 2.20$$

where R_m is the outer radius of the magnets. A general framework established in [2] has shown that the flux-linkage which results with a stator coil can be obtained by integrating the radial flux density component at $r = R_{se}$. Therefore, the total flux-linkage, ψ_w is given by

$$\psi_w = \sum_{n=1}^{\infty} \phi_{wn} \sin m_n z_d \quad 2.21$$

where

$$\phi_{wm} = 2\pi N_{wp} K_m K_{dpm} / m_n \quad 2.22$$

N_{wp} = number of series turns per phase

K_{dpm} = winding factor

$$= K_{dn} K_{pn}$$

$$K_{dn} = \frac{\sin m_n b_o / 2}{m_n b_o / 2}$$

$$K_{pn} = -1$$

and

$K_m = R_{se} [a_{in} B I_1(m_n R_{se}) + b_{in} B K_1(m_n R_{se})]$ for the iron-cored motors.

$K_m = R_{se} [a'_{11n} B I_1(m_n R_{se}) + b'_{in} B K_1(m_n R_{se})]$ for the air-cored motor.

The induced back-emf, e_w , in a single-phase stator winding is obtained as:

$$e_w = -\frac{d\psi_w}{dt} = -\left(\sum_{n=1}^{\infty} K_{En} \cos m_n z_d \right) \frac{dz_d}{dt} = K_E(z_d) v \quad 2.23$$

where $K_{En} = 2\pi N_{wp} K_m K_{dpm}$, $K_E(z_d)$ is the back-emf coefficient and v is the velocity of the armature.

By passing the current i into the stator coil, the instantaneous thrust force, F_T can be obtained from:

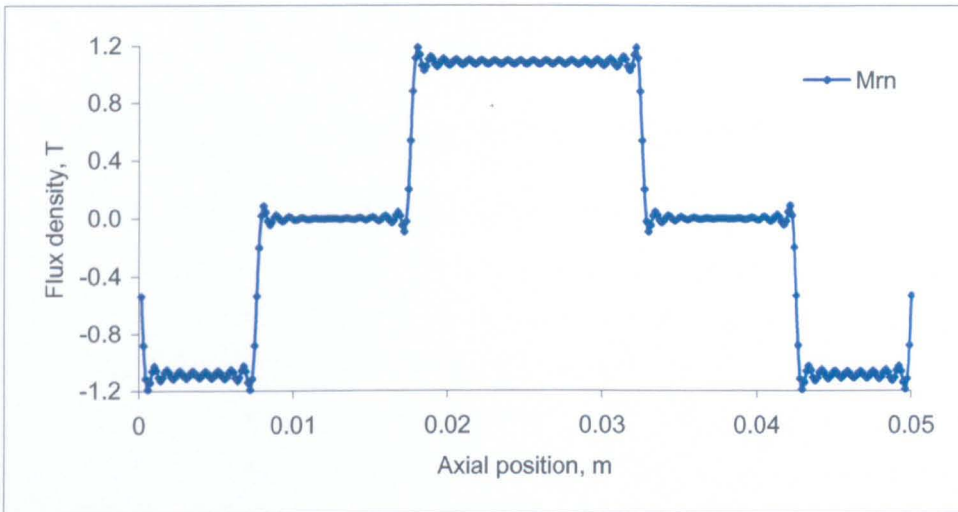
$$F_T = e_w i / v = K_T(z_d) i \quad 2.24$$

where $K_T(z_d)$, is defined as the thrust force coefficient of the motor, is identical to $K_E(z_d)$ and is also dependent on the displacement of the permanent magnet armature.

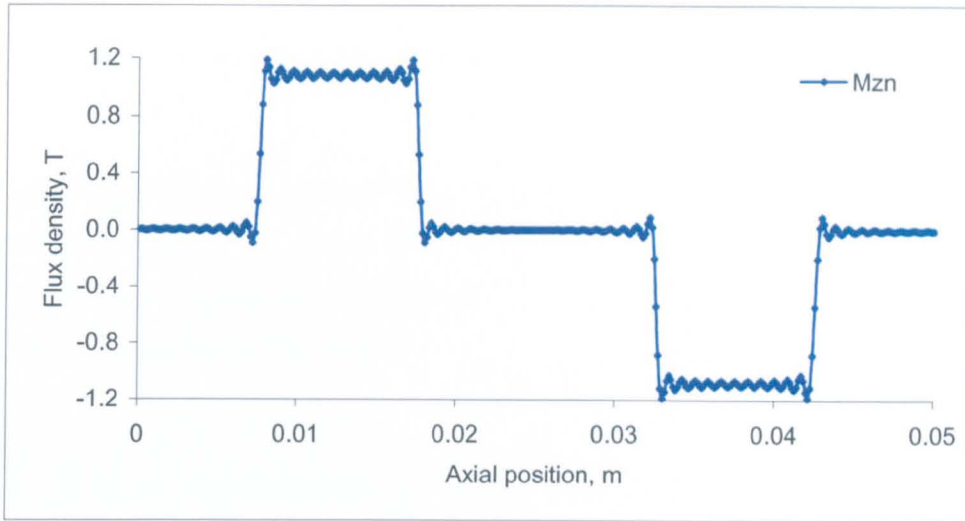
2.4 Magnetisation patterns

2.4.1 Quasi-Halbach magnetisation – rectangular magnets

Confirmation of each magnetization distribution i.e radial and axial component of magnetization, is clearly essential in order to determine accurate results from the derived analytical expressions and to predict the performance of the motors. Fig. 2.4 shows that the Fourier series approach used to model quasi-Halbach magnetizations provides a sufficient accurate representation when the number of harmonics is equal to 80 for both the radial and axial magnetisation components. However, the magnetisation waveforms will be smoothed by increasing number of harmonic. Therefore, the number of harmonics is doubled for iron-cored quasi-Halbach magnetisation for trapezoid magnets.



a. Axial component



b. Radial component

Fig. 2.4 Fourier series representation of M_{rn} and M_{zn} quasi-Halbach magnetisation with rectangular magnets

2.4.2 Quasi-Halbach magnetisation – trapezoidal magnets

Normally, for a quasi-Halbach magnetisation distribution, the M_r and M_z components of magnetisation are determined only as function of z . However, when magnets having a trapezoidal cross-section magnets are employed, the field components vary in a much more complex manner with respect to both r and z , as shown in Fig. 2.3 (ii). Both M_r and M_z of Trapezoidal magnetisation need to be expressed as functions of r and z in order to obtain accurate predictions of the resulting air-gap field, and this can be quite time-consuming to establish.

However, a relative simple approach has been developed whereby the distribution of the M_r and M_z are synthesised by subtracting and/or adding much simpler magnetisation distributions. These are expressed as function z alone, and each of these simple magnetisation distributions is expanded into a Fourier series. For example, in order to obtain the radial magnetisation distribution, M_{rnT4} at the middle of the central radially magnetised magnet is subtracted from M_{rnT3} as illustrated in Fig. 2.5. The same process is employed to obtain the magnetisation distribution due to the two ends radially magnetised magnets, M_{rnT1} being subtracted from M_{rnT2} as shown in Fig. 2.6. By adding the two magnetisation distribution, the resultant radial magnetisation distribution can be synthesised as shown in Fig. 2.7 i.e.

$$M_r = \left(\sum_{n=1,2,3,\dots}^{\infty} (M_{rnT4} - M_{rnT3}) + (M_{rnT1} - M_{rnT2}) \right) (\cos m_n z) \quad 2.26$$

The axial magnetisation distribution, M_z , is similarly synthesised from three simplified distributions i.e. M_{znT1} , M_{znT2} and M_{znT3} of which represented by Fourier series. By adding all three magnetisation distributions, the resultant axially magnetisation is obtained as illustrated in Fig. 2.8, i.e.

$$M_z = \left(\sum_{n=1,2,3,\dots}^{\infty} (M_{znT1} + M_{znT2} + M_{znT3}) \right) (\sin m_n z) \quad 2.27$$

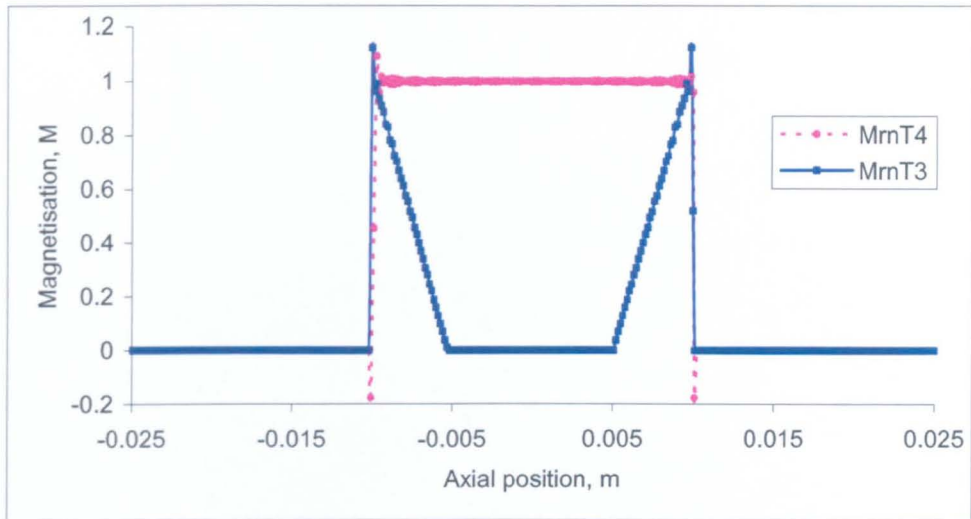


Fig. 2.5 Representation of magnetisation distribution due to central radially magnetised magnet

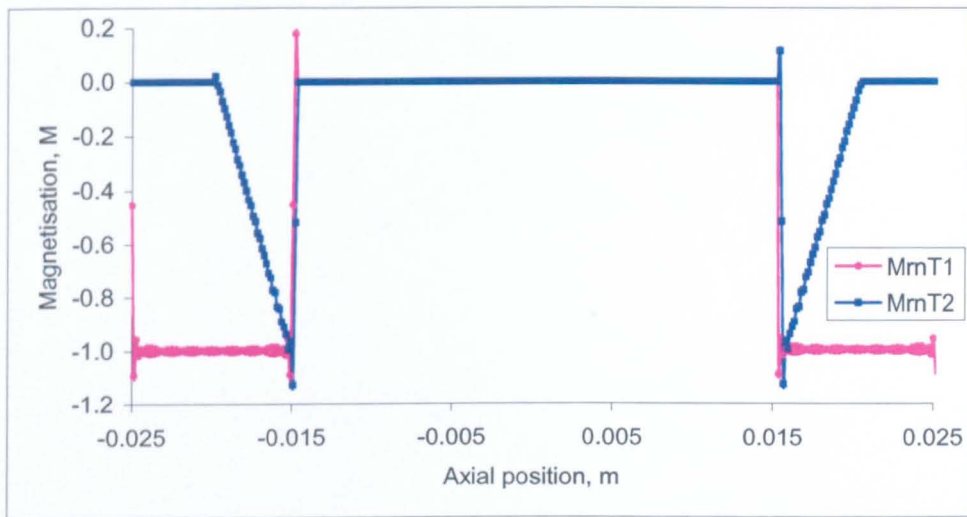


Fig. 2.6 Representation of magnetisation distribution due to end radially magnetised magnets

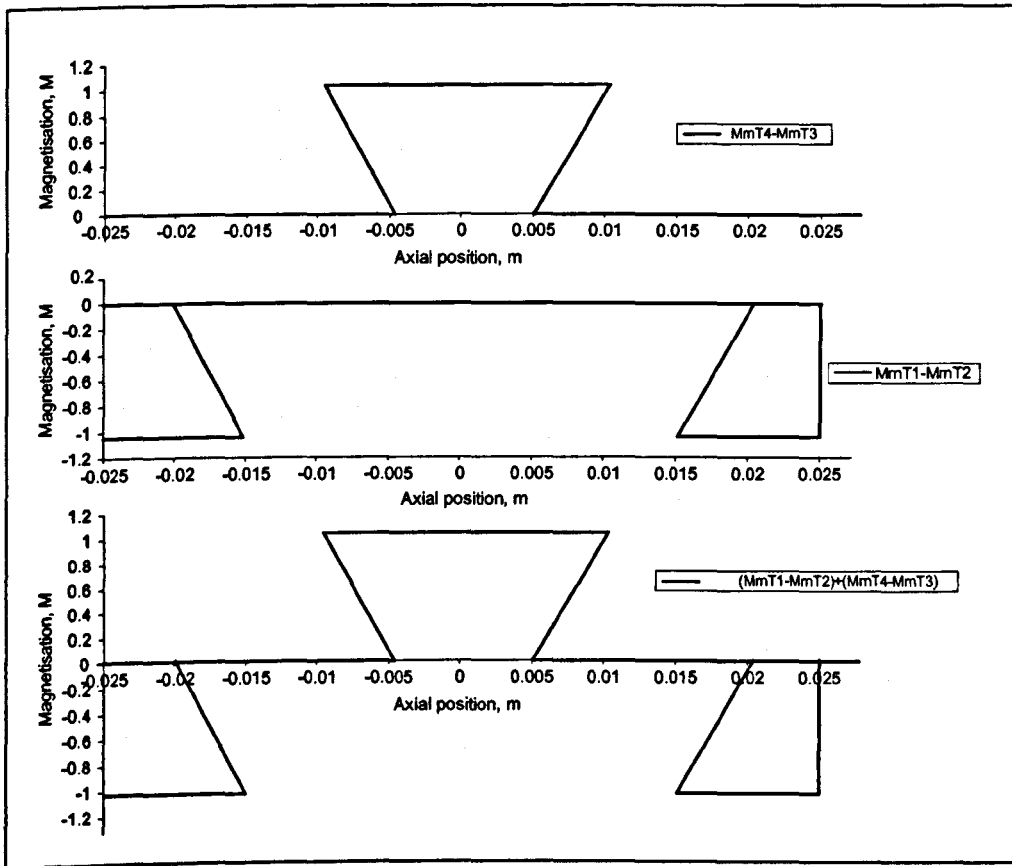


Fig. 2.7 Resultant radial magnetisation distribution

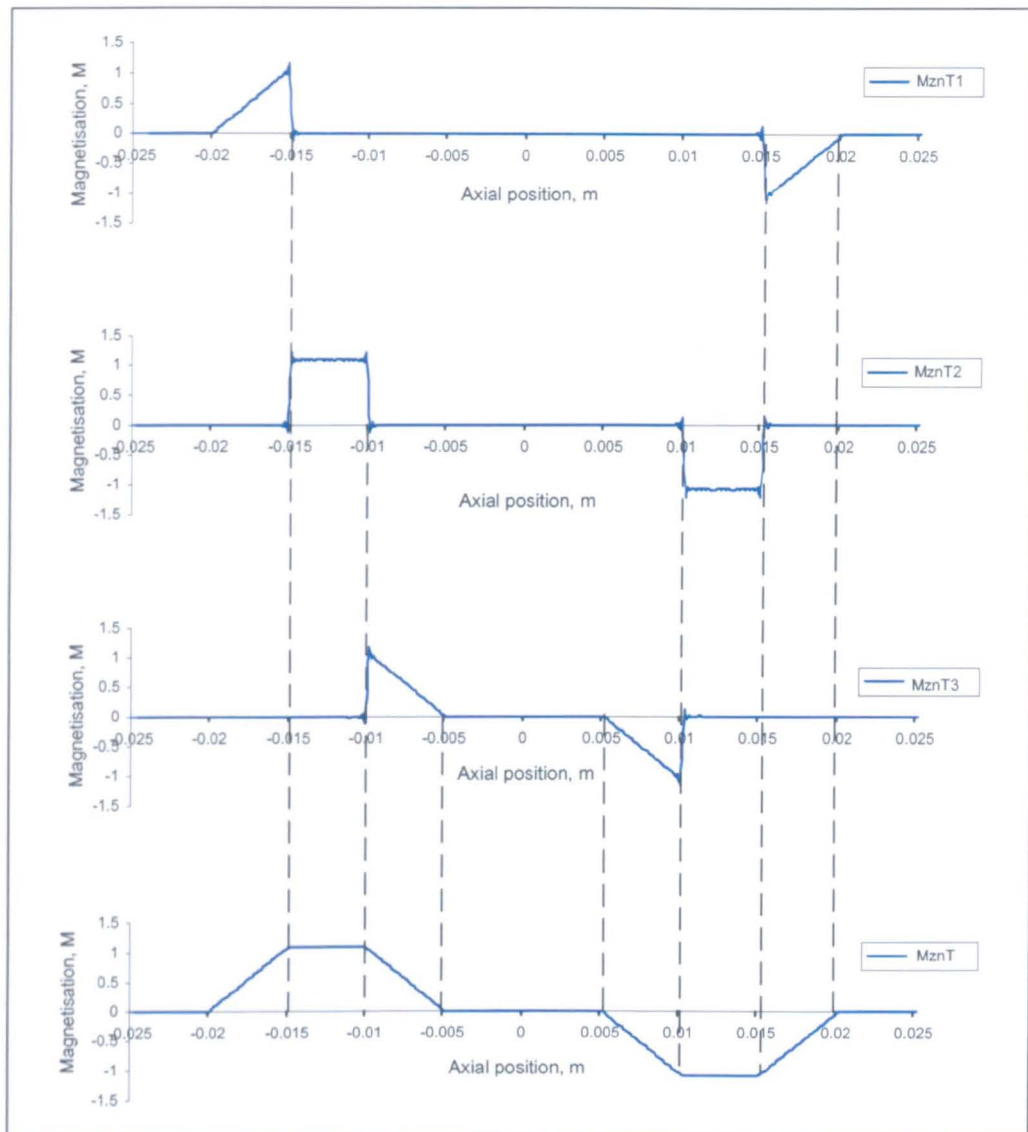


Fig. 2.8 Representation of axial magnetisation distribution

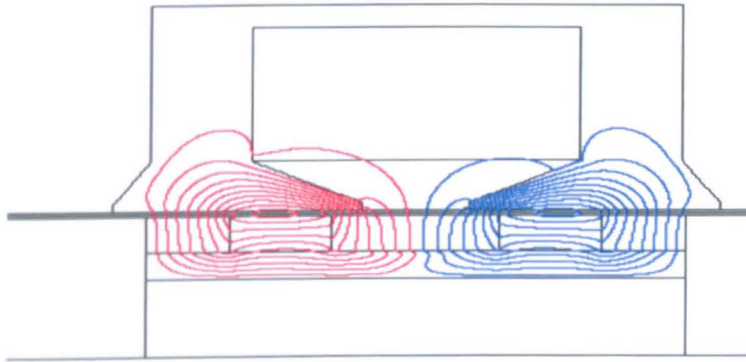
2.5 Comparison with results from finite element analyses for open-circuit magnetic field distribution

Once sufficiently accurate Fourier series representation of the radial and axial components of magnetisation have been established, the analytical model for the open-circuit magnetic field distribution for each of these tubular motors can be investigated. Initially, the main design parameters for three motors were assumed to be identical. The dimension of the outer radius of magnets, R_m , the axial length of radially magnetised magnet, T_{mr} and the axial length of axially magnetised magnets, T_{mz} are 20.0 mm, 7.5 mm and 5.0 respectively. The magnets are sintered NdFeB, for which the remanence, B_{rem} is 1.14 T and recoil permeability, $\mu_r = 1.05$. For each

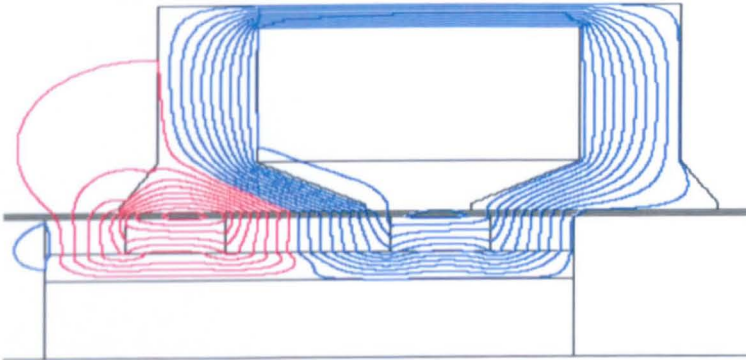
motor, the analytically predicted and finite element calculated distribution the radial flux density component, B_{lr} in the air-gap as a function of the axial position, z , at a constant radius = 0.024 m and zero displacement of the moving-magnet armature, were compared.

2.5.1 Iron-cored quasi-Halbach magnetised motor with rectangular magnets

Figs. 2.9 (a) and (b) show the no-load flux distribution at the initial position and maximum stroke position respectively. For the initial position, the flux distribution is symmetrical with respect to the axial centre of the motor, and hence, the coil flux-linkage will be zero. At maximum position the coil flux linkage is essentially produced by one magnet pole.



a. $z = 0.0$ mm



b. $z = 10.5$ mm

Fig. 2.9 Open circuit flux distribution

Fig. 2.10 compares the analytically predicted and finite element calculated distributions of radial flux density, B_{lr} for the iron-cored quasi-Halbach magnetised motor with rectangular magnets. As will be seen, the analytical and finite element prediction are quite similar. The average value of B_{lr} over one pole-pitch from the analytical and finite element analyses are 0.64 T and 0.67 T, respectively, the percentage difference being relatively small, viz. 4.30 %.

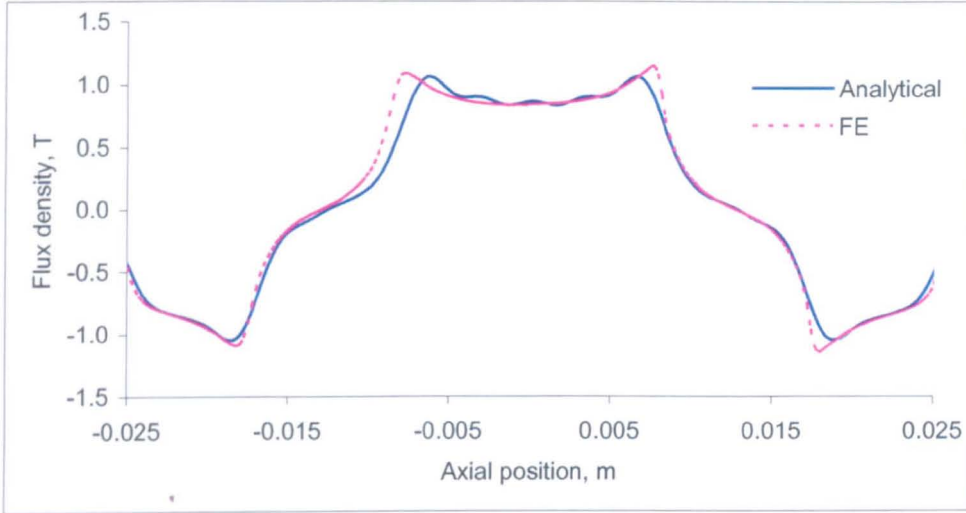
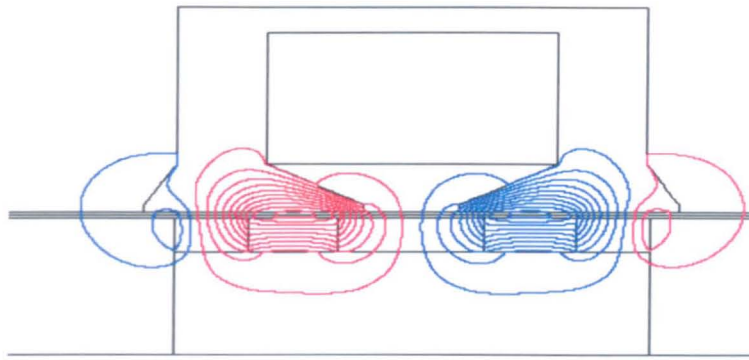


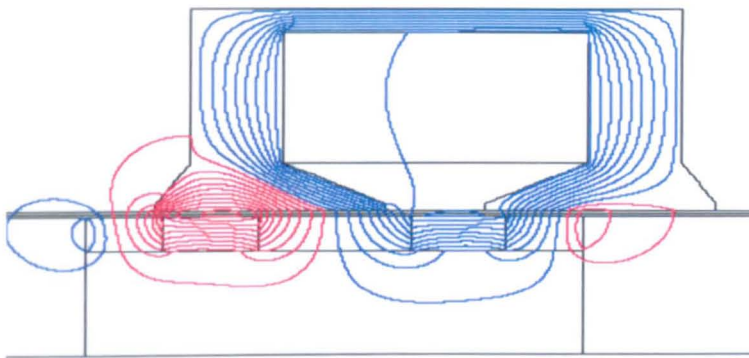
Fig. 2.10 B_{lr} for iron-cored quasi-Halbach magnetised motor with rectangular magnets

2.5.2 Air-cored quasi-Halbach magnetised motor with rectangular magnets

Fig. 2.11 shows open-circuit flux distributions corresponding to two armature positions, viz. zero displacement and the maximum stroke position. As will be seen, leakage flux in the inner bore of the air-cored quasi-Halbach magnetised armature with rectangular magnets is relatively small, which justifies the use of a non-magnetic support tube [14].



a. $z = 0.0$ mm



b. $z = 10.5$ mm

Fig. 2.11 Open-circuit flux distributions

Fig. 2.12 compares the analytical and finite element predicted distributions of B_{lr} for the air-cored quasi-Halbach magnetised motor with rectangular magnets. Again the analytical solution agrees extremely well with the finite elements prediction. The average values of B_{lr} from the analytical and finite elements analyses are 0.46 T and 0.48 T, respectively, the percentage difference being only 5.10 % .

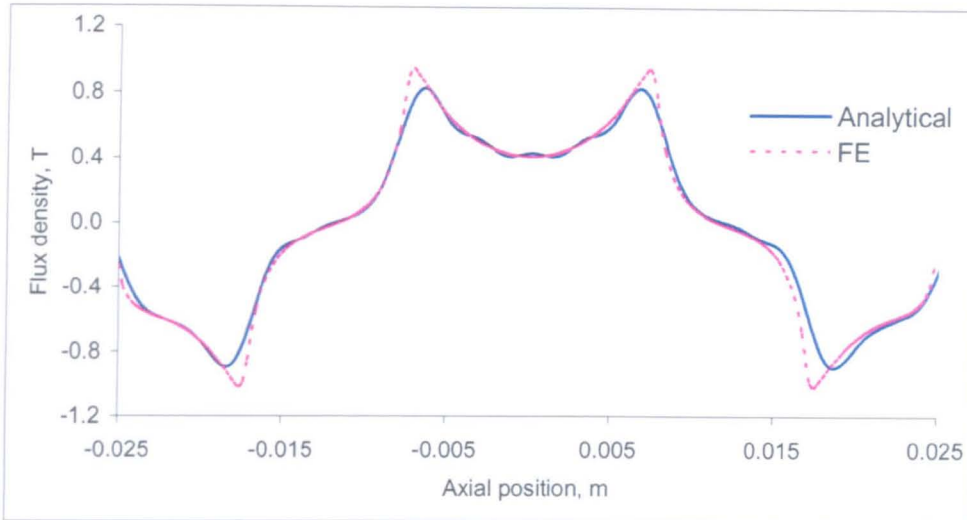
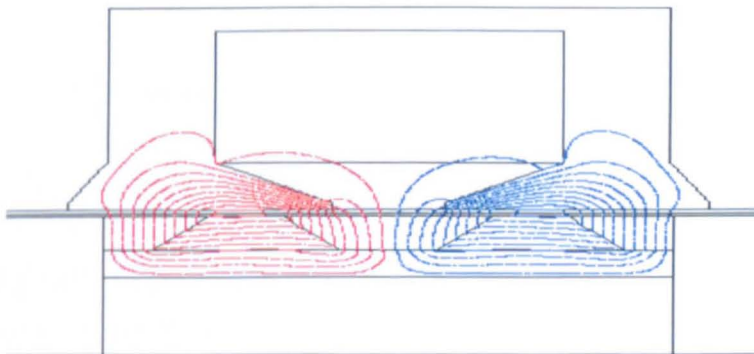


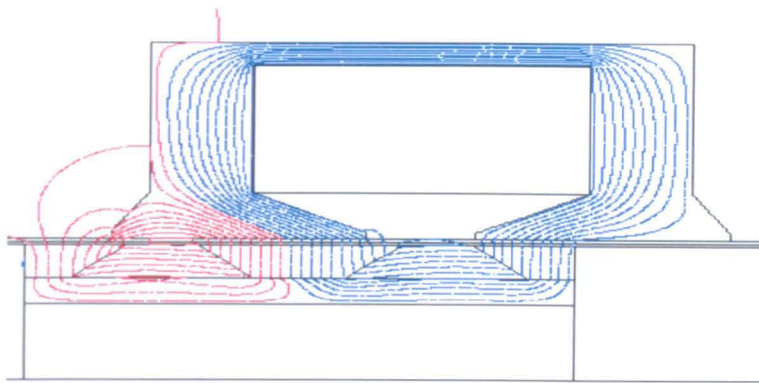
Fig. 2.12 B_{lr} for air-cored quasi-Halbach magnetised motor with rectangular magnets

2.5.3 Iron-cored quasi-Halbach magnetised motor with trapezoidal magnets

Figs. 2.13 (a) and (b) shows the no-load flux distribution of initial position and maximum position respectively. For the initial position, the flux distribution is symmetrical with respect to the axial centre. Hence, the coil flux-linkage is zero. As the armature move to the left, the flux-linkage increases and reaches nearly a maximum value at the maximum stroke position. Fig. 2.14 compares analytical and finite element prediction distribution of B_{lr} for the iron-cored quasi-Halbach magnetised motor with trapezoidal magnets. As will be observed, the analytical and finite element solution are almost similar, the average value of B_{lr} from the analytical and finite element analyses being 0.66 T and 0.67 T, respectively, the percentage difference being 2.54 %.



a. $z = 0.0 \text{ mm}$



b. $z = 10.5 \text{ mm}$

Fig. 2.13 Open-circuit magnetic flux distribution

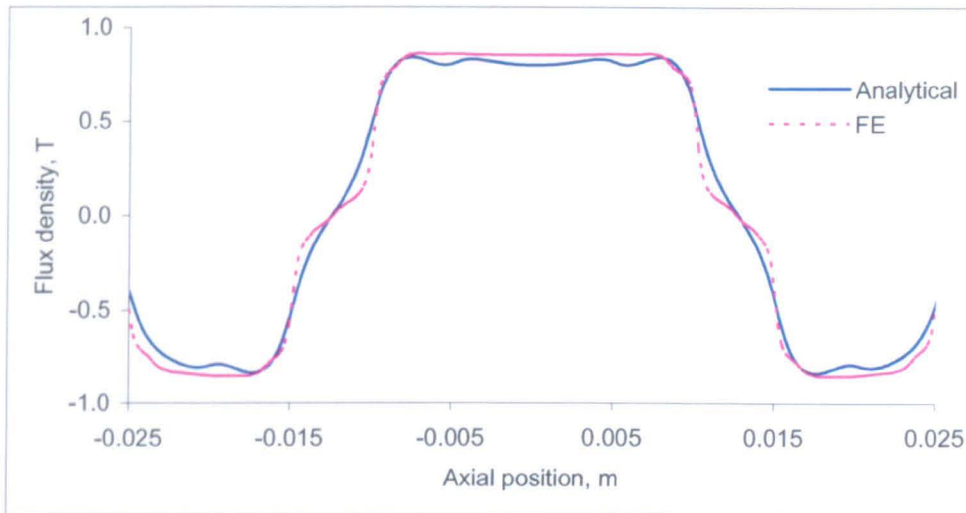


Fig. 2.14 B_r for iron-cored quasi-Halbach magnetised motor with trapezoidal magnets

2.6 Comparison with analytical results for different motors

2.6.1 Air-cored and iron-cored quasi-Halbach magnetised motor with rectangular magnets

Fig. 2.15 compares the radial flux density component which results in the iron-cored (ferromagnetic support tube) and the air-cored (non-magnetic support tube) quasi-Halbach magnetised motors with rectangular magnets. It shows that the iron-cored motor produced a higher air-gap flux density than the air-cored motor, the average values for the iron-cored and air-cored motors being 0.64 T and 0.46 T respectively, i.e. the iron-cored motor has an air-gap flux density which is 29 % higher, and,

hence, has a higher thrust force capability. However, the mass of the armature also needs to be considered when evaluating the performance as will be discussed later.

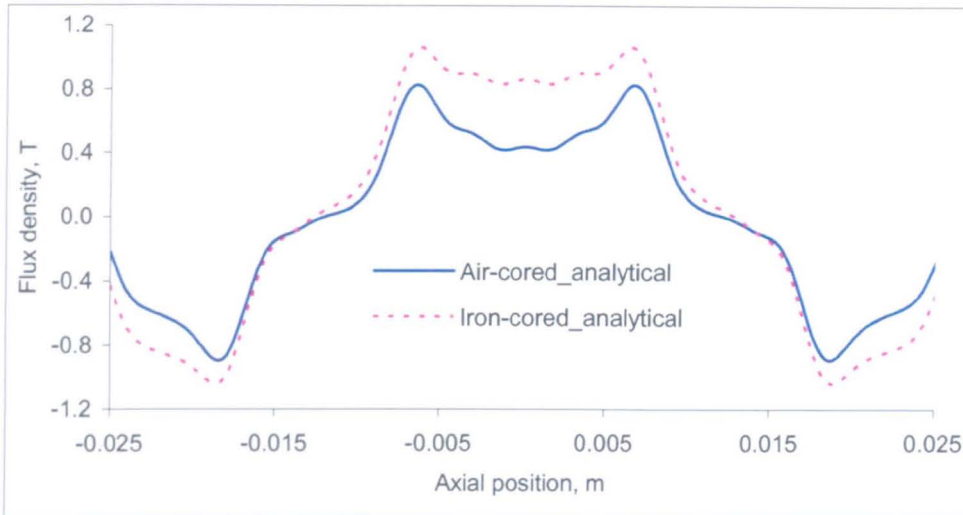


Fig. 2.15 B_r for air-cored and iron-cored quasi-Halbach magnetised motor with rectangular magnets

2.6.2 Iron-cored quasi-Halbach magnetised motors with rectangular and trapezoidal magnets.

Fig. 2.16 compares the air-gap flux density distribution of the iron-cored quasi-Halbach magnetised motors equipped with rectangular and trapezoidal magnets. As will be seen, a slightly different distributions result due to the different magnet configurations. However, the average values of B_r for the motors with rectangular and trapezoidal magnets are 0.64 T and 0.66 T, respectively, i.e. the use of trapezoidal magnets increased the air-gap flux density by 2.49 %, and hence, result in a higher thrust force capability.

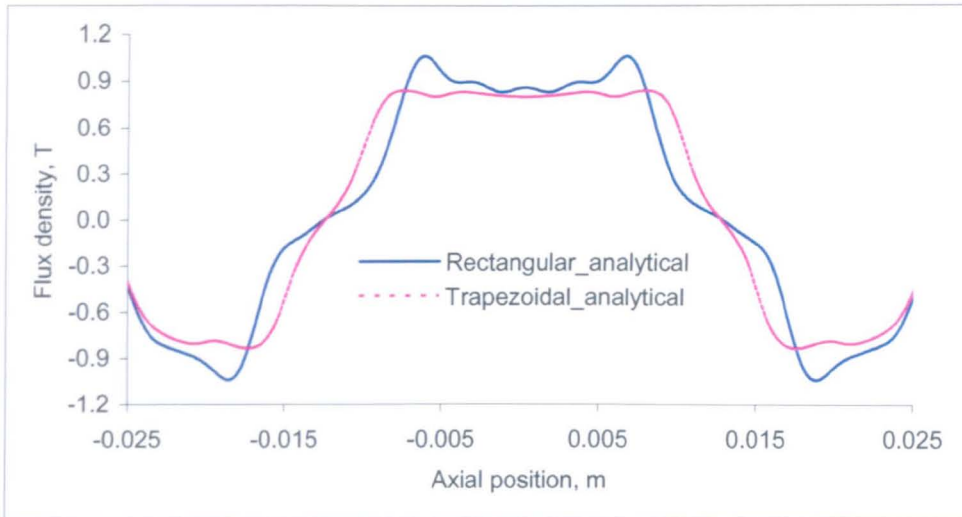


Fig. 2.16 B_r for iron-cored quasi-Halbach magnetised motors with rectangular and trapezoidal magnets

2.7 Comparison with finite element predicted back-emf

2.7.1 Iron-cored quasi-Halbach magnetised motor with rectangular magnets

Fig. 2.17 compares the analytical and finite element predicted back-emf for the iron-cored quasi-Halbach magnetised motor with rectangular magnets at a constant armature velocity of 1.0 m/s. The number of coil turns is 1024. As will be seen, the agreement is fairly good, the average values of the back-emf calculated by the analytical expression and from finite element analyses being 95.14 V and 100.88 V respectively, the percentage difference is 6.04 %.

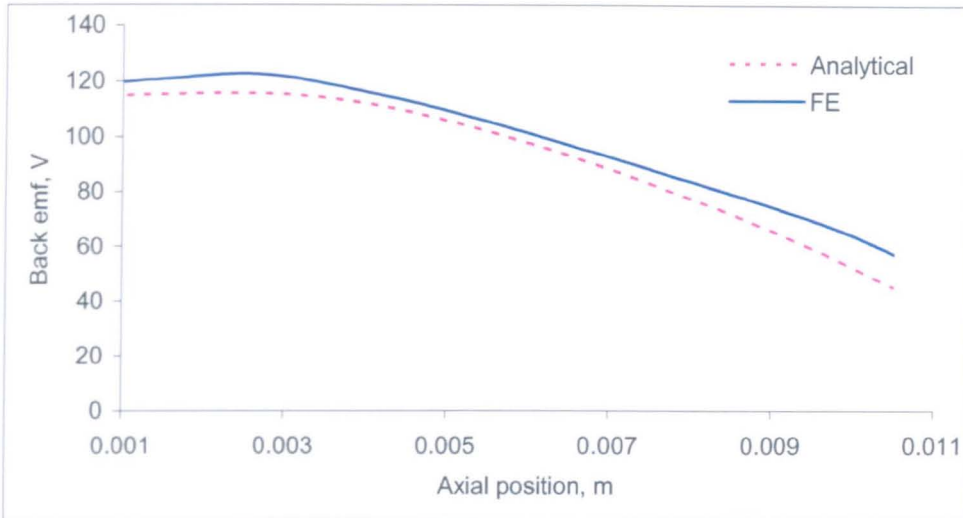


Fig. 2.17 Comparison of analytical and finite element predicted back- emf for iron-cored quasi-Halbach magnetised motor with rectangular magnets

2.7.2 Air-cored quasi-Halbach magnetised motor with rectangular magnets

Fig. 2.18 compares the back-emf for the air-cored quasi-Halbach magnetised motor with rectangular magnets. The armature velocity and the number of coil turns are same as previously stated. The analytical prediction agrees reasonably well with the finite element prediction, the average value of back-emf derived from the analytical expression and finite element analyses being 82.74 V and 79.19 V, respectively, the percentage difference being 4.29 %.

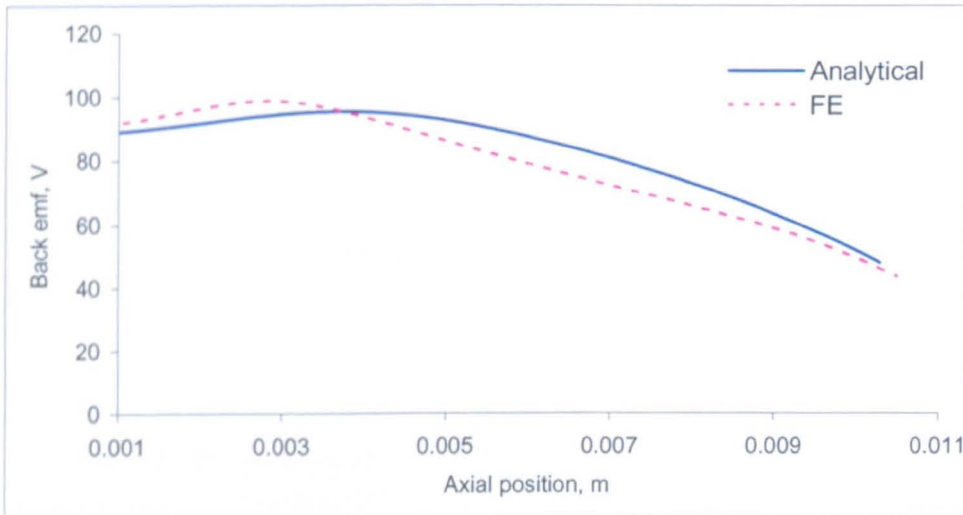


Fig. 2.18 Back-emf of air-cored quasi-Halbach magnetised motor with rectangular magnets

2.7.3 Iron-cored quasi-Halbach magnetised motor with trapezoidal magnets

Fig. 2.19 compares the back-emf for the iron-cored quasi-Halbach magnetised motor with trapezoidal magnets. As can be observed, the analytically derived waveform still agrees reasonably well with that derived from finite element analyses, the average values being 96.08 V and 102.38 V, respectively, for the analytical and finite element predicted values, the percentage difference being slightly higher at 6.55 %. The effect on copper loss may be different.

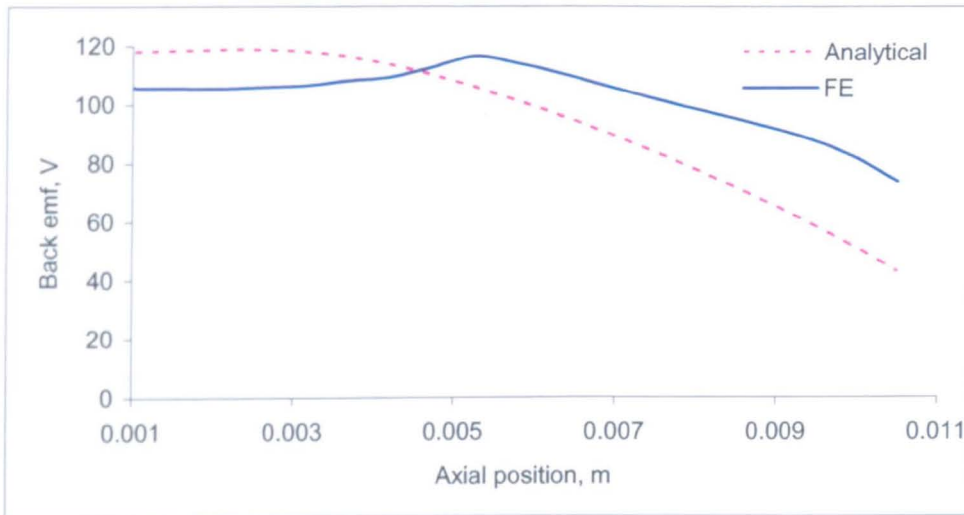


Fig. 2.19 Back-emf of iron-cored quasi-Halbach magnetised motor with trapezoidal magnets

2.8 Discussions

As regard the open-circuit flux distributions for the three variants of the quasi-Halbach magnetised motors, the analytical solutions agree well with finite element predictions. The percentage difference between the analytical solutions and the finite element predictions for the air-cored and iron-cored motors with rectangular magnets and the iron-cored motor with trapezoidal magnets being 5.1 %, 4.3 % and 2.54 %, respectively.

The comparison of the open-circuit field distribution for the air-cored and iron-cored quasi-Halbach magnetised motor with rectangular magnets showed that the iron-cored increased the magnitude of the air-gap flux density by 29 %. Thus, the quasi-Halbach magnetised magnets on a ferromagnetic tube, yields a higher force capability. However, the air-cored motor also offers significant advantageous in term

of a lower mass armature which may actually increase the force/mass capability. Also, due to the lower flux density in the air-cored motor, the iron loss and the eddy current loss in the magnets are likely to be decreased. Hence, the efficiency of the motor may be increased. These issues will be considered later.

The comparison of the open-circuit field distributions for the iron-cored quasi-Halbach magnetised motor with rectangular and trapezoidal magnets showed that the trapezoidal magnets result in a slightly higher air-gap flux density i.e. 2.49 %, and, hence, yields a marginally higher force capability.

The good agreement between the analytical and finite element predicted air-gap flux density distributions and back-emf waveforms provided assurance that the analytical method should be used for further analyses, since it is less time-consuming and a more effective way of optimising the motor design.

2.9 Conclusions

In summary, analytical formulae for predicting the open-circuit magnetic field distribution, the flux linkage, and the back-emf and thrust force of single-phase, single slot, tubular moving permanent magnet motors have been established. The accuracy of the analytically derived formulae has been validated by comparing with results deduced from finite element analyses. Analytical solutions and finite element predictions of the open-circuit magnetic field distribution and back-emf agree reasonably well for all these motors under consideration. The developed analytical tool should provide a useful means of aiding for the design optimisation of the proposed motors [15].

References

- [1] J. Wang, Z. Lin, and D. Howe, "Analysis of a short stroke, single phase quasi-Halbach magnetised tubular permanent magnet motor for linear compressor applications," *IET Electric Power Application*, vol. 2, no. 3, pp. 193-200, 2008.
- [2] J. Wang, G. W. Jewell, and D. Howe, "A general framework for the analysis and design of tubular linear permanent magnet machines," *IEEE Transactions on Magnetics*, vol. 35, no. 3, pp. 1986-2000, May 1999.

- [3] J. Wang, D. Howe, and M. Inoue, "Magnetic field distribution of quasi-Halbach magnetised cylinder for tubular permanent magnet machines," *Proceedings of 4th International Symposium on Linear Drives and Industry Applications, LDIA 2003, Birmingham, United Kingdom*, pp. 481-484, September 2003.
- [4] T. Mizuno and H. Yamada, "Magnetic circuit analysis of a linear synchronous motor with permanent magnets," *IEEE Transactions on Magnetics*, vol. 28, no. 5, pp. 3027-3029, September 1992.
- [5] I. Boldea and S. A. Nasar, *Linear electric actuators and generators*. Cambridge, UK: Cambridge University Press, 1997.
- [6] J. Wang, D. Howe, and G. W. Jewell, "Analysis and design optimisation of an improved axially magnetised tubular permanent magnet machine," *IEEE Transactions on Energy Conversions*, vol. 19, no. 2, pp. 289-295, June 2004.
- [7] Z. P. Xia, Z. Q. Zhu, and D. Howe, "Magnetic field distribution in tubular PM motors with axially magnetised magnets," *Proceedings of 4th International Symposium on Linear Drives for Industry Applications, LDIA 2003, Birmingham, United Kingdom*, pp. 442-445, September 2003.
- [8] J. Wang and D. Howe, "Design optimisation of radially magnetised iron cored, tubular permanent magnet machines and drive systems," *IEEE Transactions on Magnetics*, vol. 40, no. 5, pp. 3262-3277, September 2004.
- [9] N. Bianchi, "Analytical field computation of a tubular permanent magnet linear motor," *IEEE Transactions on Magnetics*, vol. 36, no. 5, pp. 3798-3801, September 2000.
- [10] J. Wang and D. Howe, "Tubular modular permanent magnet machines equipped with quasi-Halbach magnetised magnet - Part II: Armature reaction and design optimisation," *IEEE Transactions on Magnetics*, vol. 41, no. 9, pp. 2479-2489, September 2005.
- [11] T. Ibrahim, J. Wang, and D. Howe, "Analysis of a single-phase, quasi-Halbach magnetised tubular permanent magnet motor with non-ferromagnetic

support tube," *14th IET International Conference on Power Electronics, Machines and Drives, PEMD, York, United Kingdom*, vol. 1, pp. 762-766, April 2008.

- [12] J. Wang, D. Howe, and G. W. Jewell, "Fringing in tubular permanent magnet machines: Part 1. Magnetic field distribution, flux-linkage and thrust force," *IEEE Transactions on Magnetics*, vol. 39, no. 6, pp. 3507-3516, November 2003.
- [13] M. G. Lee and D. G. Gweon, "Optimal design of a double-sided linear motor with a multi-segmented trapezoid magnet arrays for a high precision positioning system," *Journal of Magnetism and Magnetic Materials*, vol. 281, no. 2-3, pp. 226-346, October 2004.
- [14] T. Ibrahim, J. Wang, and D. Howe, "Analysis and experimental verification of a single-phase, quasi-Halbach magnetised tubular permanent magnet motor " *IEEE International Magnetic Conference, INTERMAG2008, Madrid, Spain*, 4-8 May 2008.
- [15] Y. Amara, J. Wang, and D. Howe, "Analytical prediction of eddy current loss in modular tubular permanent magnet machines," *IEEE Transactions on Energy Conversion*, pp. 761-760, December 2004.

CHAPTER 3

DESIGN OPTIMISATION OF SHORT-STROKE, SINGLE-PHASE TUBULAR PERMANENT MAGNET MOTORS

3.1 Introduction

An extensively analysis of open-circuit magnetic field distribution, flux-linkage, back-emf and thrust force in the air-cored and iron-cored quasi-Halbach magnetised motors having rectangular and trapezoidal magnets have been established in Chapter 2. The good agreement between the analytical and finite element predictions provided assurance that the analytical method can be used for further analyses, and computationally efficient design optimisation.

This chapter describes a design methodology to achieve optimal performance for the linear motors which drive a reciprocating vapour compressor using analytical method. The direct-drive linear compressor has been modelled and it was integrated with the linear motors in order to produce a complete system model. The optimisation procedures of the motors will take into account of the effect of compressor loads under the nominal operating condition [1] [2].

The leading design parameters of the motors have been optimised for maximum efficiency under the rated operating condition and volumetric constraints. The optimisation of leading design parameters using analytical model may have limited accuracy and, therefore the parameters will be refined using the finite element method, which can accommodate more complex geometries of magnetic circuit, material non-linearities, distributed field sources, time-transient excitation, and relative motion effects [3].

3.2 Modelling of direct-drive compressor systems

Fig. 3.1 shows a schematic of a direct-drive compressor system which consists of a linear motor and compressor system, and both are integrated using a direct-drive shaft. The direct-drive compressor system model consists of mechanical model, compressor model and electrical model, which are derived and combined to form a complete system model.

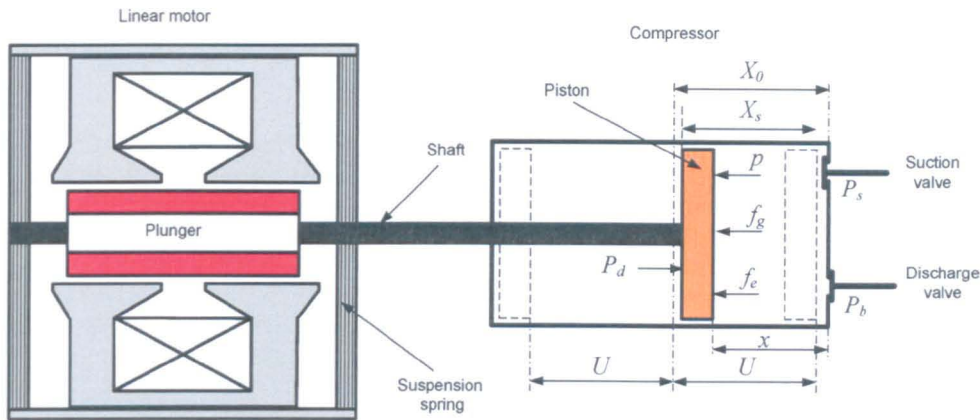


Fig. 3.1 Schematic of a linear reciprocating compressor system [4]

The relevant symbols and variables are defined as follows:

Symbol	Description
X_o	Equilibrium piston position i.e. the centre of reciprocating oscillation, m
X_s	Static piston position when there is no displacement in spring, i.e. preset piston position, m
x	Piston position referred to the cylinder head, m
U	Amplitude of piston oscillation, m
p	Pressure in compression chamber, N/m^2
P_s	Suction pressure, N/m^2
P_b	Piston back pressure, N/m^2
P_d	Discharge pressure, N/m^2
f_g	Gas force in compressor, N
f_e	Electromagnetic force of linear motor, N

3.2.1 Mechanical model

With reference to Fig. 3.1, the mechanical behaviour can be modelled as mass-spring-damper system as shown in Fig. 3.2. The governing equation of motion is

$$m \frac{dx^2}{dt^2} + B \frac{dx}{dt} + K(x(t) - X_s) = f_e(t) + f_c(x(t)) + f_g(t) \quad 3.1$$

where the gas force, f_g , and the electromagnetic force, f_e , and the cogging force, f_c , of the linear motor act on the combined mass of the piston, the linear motor plunger and the connecting parts. K is the total stiffness of springs and B is the viscous damping coefficient that represents the frictional effect between cylinder and the piston.

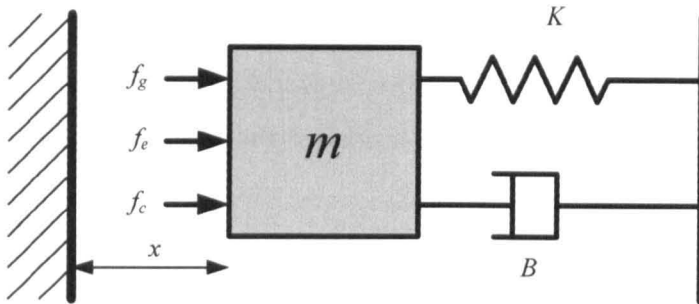


Fig. 3.2 Mass-spring-damper model

3.2.2 Compressor model

Referring to Fig. 3.1, when the pressure in the compression chamber is greater than the discharge pressure, P_d , the discharge valve opens, and as a result, the pressure will stay at the discharge pressure until it start to fall. If the pressure is less than the suction pressure, P_s , the suction valve opens, and consequently the pressure remains at the suction pressure until it start to increase. The gas force, f_g , acting on the piston results from the pressure difference between the front and the back surface of the piston. The force is given by

$$f_g(t) = A_p(p(t) - P_b) \quad 3.2$$

where A_p , $p(t)$ and P_b are the piston pressure, the pressure in compression chamber and the piston back pressure, respectively.

The piston back pressure, P_b , can be assumed to be equal to the suction pressure, P_s , in an ideal gas compression cycle. In addition, it can be assumed that the refrigerant gas in the compression chamber satisfies, the ideal gas law:

$$pV_g^n = \text{constant}$$

3.3

where the pressure will be dependent on the compression chamber volume, V_g or piston displacement.

3.2.2.1 No pumping operation

No pumping operation occurs when the gas pressure in the cylinder neither exceeds the discharge pressure, P_d , nor falls below the suction pressure P_s . Referring to Fig. 3.3, if the piston moves to the rightmost, $x = X_0 + U_{mn}$, and leftmost position, $x = X_0 - U_{mn}$, the pressure in cylinder is equal to P_s and P_d respectively. This will be described as

$$P_s(X_0 + U_{mn})^n = \text{constant} \quad 3.4$$

$$P_d(X_0 - U_{mn})^n = \text{constant} \quad 3.5$$

where U_{mn} is the displacement of the piston from the central position, X_0 .

Combining equations 3.4 and 3.5 yields

$$P_s(X_0 + U_{mn})^n = P_d(X_0 - U_{mn})^n \quad 3.6$$

and solving for U_{mn} gives

$$U_{mn} = \frac{P_d^{1/n} - P_s^{1/n}}{P_d^{1/n} + P_s^{1/n}} X_0 \quad 3.7$$

It can be concluded that no pumping take place when $U < U_{mn}$.

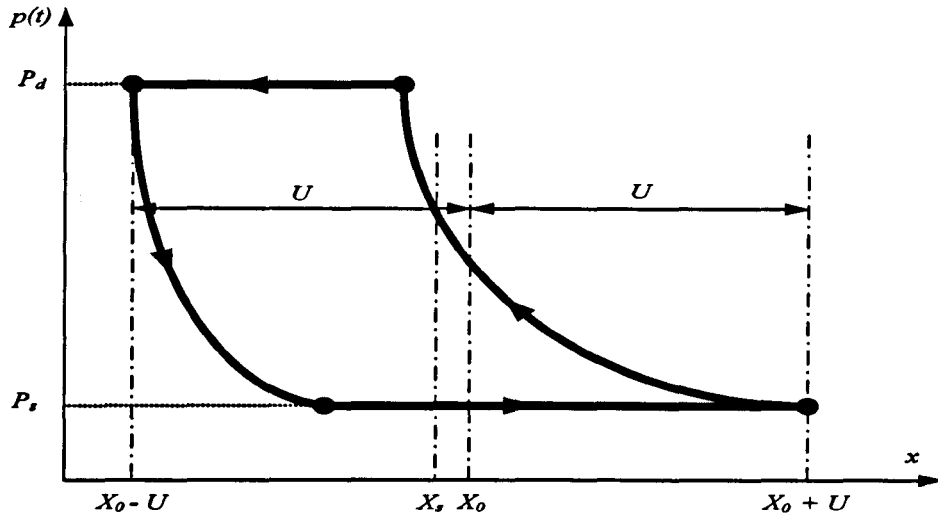


Fig. 3.3 Pressure-displacement diagram of a compression cycle

3.2.2.2 Pumping operation

The pumping operation occurs when the piston amplitude is greater than U_{mn} . Referring to Fig. 3.3, the operation take place when compression chamber pressure $p(t)$ is higher than P_s and equal or less to P_d . This will be illustrated as

$$p(t) = P_s \left(\frac{U + X_0}{x(t)} \right)^n \quad P_s < p(t) \leq P_d \quad 3.8$$

$$p(t) = P_d \left(\frac{U - X_0}{x(t)} \right)^n \quad P_s < p(t) \leq P_d \quad 3.9$$

Once the piston amplitude U is determined, the clearance volumetric efficiency, η_{vc} ,

and the mass flow rated, \dot{m} , can be calculated by:

$$\eta_{vc} = 1 - \frac{(X_0 - U)}{2U} \left[\left(\frac{P_d}{P_s} \right)^{1/n} - 1 \right] \quad 3.10$$

$$\dot{m} = \frac{2UfA_p}{v_{\alpha}} \left(1 - \frac{X_0 - U}{2U} \left[\left(\frac{P_d}{P_s} \right)^{1/n} - 1 \right] \right) \quad 3.11$$

where v_{α} is the specific volume of the gas at the suction temperature and pressure, and is determined from the thermodynamic properties of the refrigerant [5].

3.2.3 Linear motor model

The electromagnetic force, $f_e(t)$, of the linear permanent magnet motor is produced by the interaction between the stator current, i_a , and the permanent magnet field. The force can be evaluated by:

$$f_e(t) = K_T(x(t))i_a \quad 3.12$$

where the force coefficient, K_T , is slightly position dependent due to the finite armature length, as described in Chapter 2.

The voltage equation of the motor is governed by

$$v(t) = L_e \frac{di_a}{dt} + R_e i_a + K_e(x(t)) \frac{dx}{dt} \quad 3.13$$

where the back-emf coefficient, K_e , is equal to the force coefficient K_T [6]. The cogging force, $f_c(x(t))$, may exist especially for a slotted motor due to the interaction between the permanent magnet and the stator tooth. L_e and R_e are the winding inductance and resistance of the linear motor, respectively.

3.2.4 Steady state model

The gas force, $f_g(t)$ in the steady-state is assumed periodic with a fundamental frequency equal to the supply frequency, f . The force may be expanded into a Fourier series of the following form:

$$f_g(t) = F_s + \sum_{j=1}^{\infty} a_j \cos(j\omega t) + b_j \sin(j\omega t) \quad 3.14$$

where F_s , a_j and b_j are the static gas force and j^{th} harmonic force components respectively.

If high order harmonic force component are filtered out, equation 3.14 may be simplified to:

$$f_g(t) = F_s + a_1 \cos(j\omega t) + b_1 \sin(j\omega t) \quad 3.15$$

and the resulting piston motion in the steady-state will be sinusoidal. Thus, the piston displacement may be assumed to be:

$$x(t) = X_0 + u(t) \quad 3.16$$

where $u(t) = U \cos(\omega t)$. Substituting equations 3.14 - 3.16 into equation 3.1, and decoupling the static and dynamic component results in two separate equations:

$$K(X_0 - X_s) - F_s = 0 \quad 3.17$$

$$m \frac{d^2 u(t)}{dt^2} + \left(B + \frac{h_{eq}}{\omega} \right) \frac{du}{dt} + (K + k_{eq}) u(t) = K_T i_a \quad 3.18$$

where k_{eq} and h_{eq} are the equivalent stiffness and hysteretic damping coefficient of the gas force, respectively and are given by

$$k_{eq} = -\frac{a_1(U, X_0)}{U}$$

$$h_{eq} = -\frac{b_1(U, X_0)}{U} \quad 3.19$$

It follows that the mechanical and electrical dynamics equations 3.13 and 3.18 in the steady state may be represented by the frequency domain equations:

$$\left[(K + k_{eq} - \omega^2 m) + j(\omega B + h_{eq}) \right] \dot{U} = K_T \dot{I} \quad 3.20$$

$$jK_T \omega \dot{U} + (j\omega L_e + R_e) \dot{I} = \dot{V}$$

where ω is the angular frequency of the supply, \dot{U} , \dot{I} and \dot{V} represent the piston amplitude phasor, and the motor current and voltage phasors, respectively [7].

Using the analogy between mechanical and electrical quantities, equations 3.20 can be represented by the electrical equivalent circuit shown in Fig. 3.4, in which the

displacement phasor, \dot{U} , is analogous to the electric charge phasor, and $j\omega\dot{U}$ is the equivalent current phasor. Thus the mass is equivalent to an inductor whilst the spring is analogous to a capacitor. The power dissipated in the equivalent resistance h_{eq}/ω represents the effective work which is done on the gas compression. The interaction between the electrical and mechanical systems is represented by the two current controlled voltage sources.

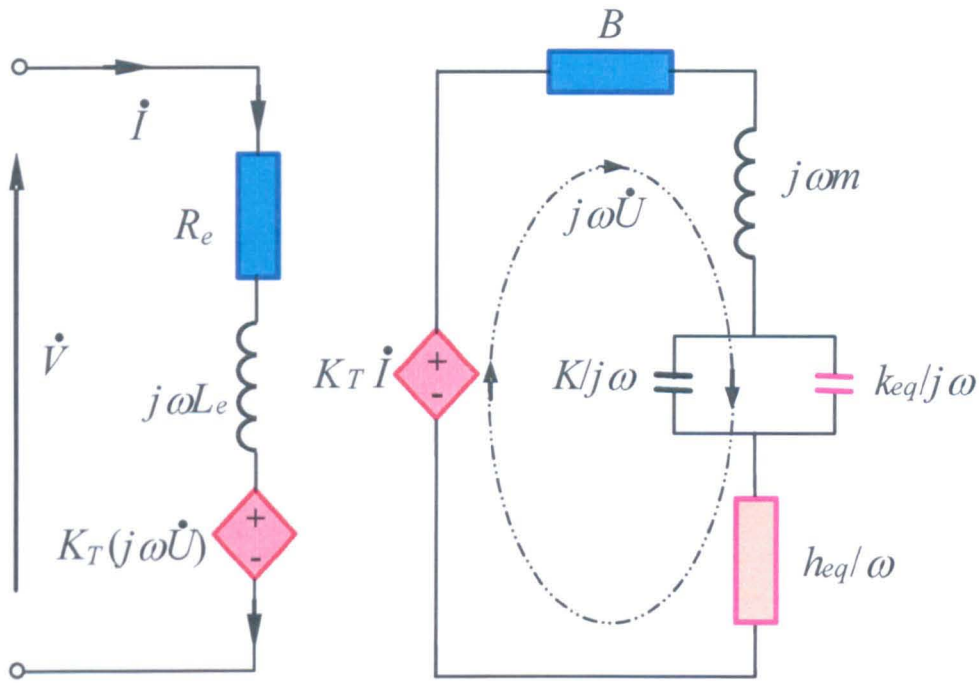


Fig. 3.4 Electrical equivalent circuit of linear compressor

Solving for \dot{I} yields:

$$\dot{I} = \frac{\dot{V}}{Z_{es}} = \frac{\dot{V}}{R_{es} + j\omega L_{es}} = \frac{V}{|Z_{es}|} \angle \varphi \quad 3.21$$

where Z_{es} , R_{es} and L_{es} are the equivalent impedance, resistance and inductance of the linear compressor system, and are given by:

$$\begin{aligned} R_{es} &= R_e + R_{ec} \\ L_{es} &= L_e + L_{ec} \\ R_{ec} &= \omega K_T^2 (\omega B + h_{eq}) / \Delta \end{aligned} \quad 3.22$$

$$L_{ec} = K_T^2 (K + k_{eq} - \omega^2 m) / \Delta$$

$$\Delta = (K + k_{eq} - \omega^2 m)^2 + (\omega B + h_{eq})^2$$

The equivalent resistance, R_{ec} , representing the mechanical system and gas compression cycle can be separated into the viscous damping component, R_{ev} , and compressor work component, R_{ep} , i.e.,

$$R_{ec} = R_{ev} + R_{ep}$$

$$R_{ev} = \omega^2 K_T^2 B / \Delta \quad 3.23$$

$$R_{ep} = \omega K_T^2 h_{eq} / \Delta$$

The input and output powers, P_{in} , and P_{out} , the efficiency, η , and the power factor, $\cos \varphi$, of the system, therefore, can be calculated from:

$$\cos \varphi = \frac{R_{es}}{\sqrt{R_{es}^2 + (\omega L_{es})^2}}$$

$$P_{in} = VI \cos \varphi = R_{ep} I^2 + P_{fe} \quad 3.24$$

$$P_{out} = R_{ep} I^2$$

$$\eta = \frac{P_{out}}{P_{in}} = \frac{R_{ep} I^2}{R_{ep} I^2 + P_{fe}}$$

where P_{fe} is the iron loss of the motor and can be predicted analytically or by finite element analysis. It can be shown [8] that the system operates most efficiently at the resonant frequency, $f_o = \sqrt{(k_{eq} + K) / m} / 2\pi$. It is evident that operating conditions of the compressor will affect the input impedance of the electrical system.

3.3 Number of coil turns

Equation 3.21 can be used to determine the number of coil turns for a given rms supply voltage, V_{rms} under nominal operating conditions. The rms value of the motor current, I , can be expressed in terms of the rms current density, J_{rms} , the packing factor, P_f , the number of coil turns, N_c , and the effective coil area, A_e :

$$I = J_{rms} A_e P_f / N_c \quad 3.25$$

The resistance of the coil is given by:

$$R = (2\pi l_e \rho / P_f A_e) / N_c^2 \quad 3.26$$

where l_e is the average length of the coil per turn, and ρ is the resistivity of the copper wire. Thus the voltage across the equivalent resistance can be expressed as:

$$I(R + R_{ec}) = (KR_e + KR_{ec})N_c$$

$$KR_e = 2\pi l_e \rho J_{rms} \quad 3.27$$

$$KR_{ec} = \omega J_{rms} A_e P_f K_{FPT}^2 (\omega B + h_{eq}) / \Delta$$

where $K_{FPT} = K_T / N_c$ is the average motor force coefficient over the piston stroke per turn. Similarly, the inductance of the motor is proportional to the square of coil turn N_c :

$$L = L_{s0} N_c^2 \quad 3.28$$

where L_{s0} is the average inductance over the piston stroke per turn. The voltage across the equivalent inductance is written as:

$$I\omega(L + L_{ec}) = (KL_e + KL_{ec})N_c$$

$$KL_e = \omega L_{s0} J_{rms} A_e P_f \quad 3.29$$

$$KL_{ec} = \omega J_{rms} A_e P_f K_{FPT}^2 (K + K_{eq} - m\omega^2) / \Delta$$

For a given value of permissible rms current density, J_{rms} , which is dependent on the thermal constraints of the motor, the number of coil turns can be obtained from equation 3.21 and is given by:

$$N_c \leq V_{rms} / \sqrt{(KR_e + KR_{ec})^2 + (KL_e + KL_{ec})^2} \quad 3.30$$

As is evident, the number of coil turns, N_c , is strongly influenced by the compressor operating conditions as well as the motor design parameters. Thus it is essential that

the steady state operational behavior of the compressor is taken into account in the motor design optimization.

3.4 Iron loss calculation

An analytical model of iron loss calculation for tubular permanent magnet machine has been reported in [9]. The paper described a simple analytical method to predict flux density waveforms in discrete regions of the laminated stator of a tubular permanent magnet machine, and employs an established iron loss model to determine the iron loss components.

In this study, the same technique has been employed to establish an analytical method for predicting iron loss, P_{fe} , in short-stroke single-phase tubular permanent magnet motors. The stator core is divided into three regions viz. the tooth, tooth tip and yoke as shown in Fig. 3.5.

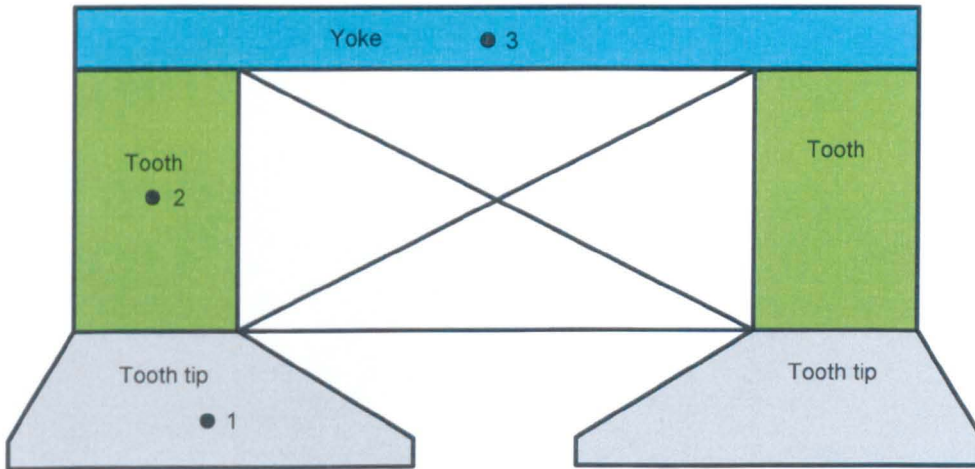


Fig. 3.5 Region of stator core

The prediction is based on the flux density waveforms for each region being analytically determined. The total iron loss is given by:

$$P_{fe} = \sum_{i=m} (P_{hi} + P_{ci} + P_{ei}) \quad 3.31$$

P_{hi} , P_{ci} and P_{ei} are the hysteresis loss, the classical eddy current loss and excess eddy current loss in i^{th} region, respectively. For SMC materials, the classical eddy current loss component, P_c , is negligible due to the conductivity of the material is virtually zero. However, the excess eddy current loss component which is associated with domain wall effects may still exist [10].

3.4.1 No load condition

3.4.1.1 Tooth tip region

Fig. 3.6 shows the finite element predicted flux density waveforms in the tooth tip region of the iron-cored quasi-Halbach magnetised motor with rectangular magnets. As can be seen, the waveforms both radial and axial flux density components can be approximated as trapezoidal.

On open-circuit, the peak flux entering in the tooth tip can be evaluated analytically from:

$$\psi_n = \frac{1}{2} \left(\int_0^{\tau_p/2} 2\pi R_s B_r dz \right) \quad 3.32$$

where B_r is determined using the expression given in equation 2.12.

The resulting peak flux density in the tooth tip region can be obtained from:

$$B_{n \max} = \frac{\psi_n}{\pi((R_s + h_t + t_{hh})^2 - R_s^2)} \quad 3.33$$

where R_s is the inner radius of stator core and the other geometric parameters being given in Fig. 3.7.

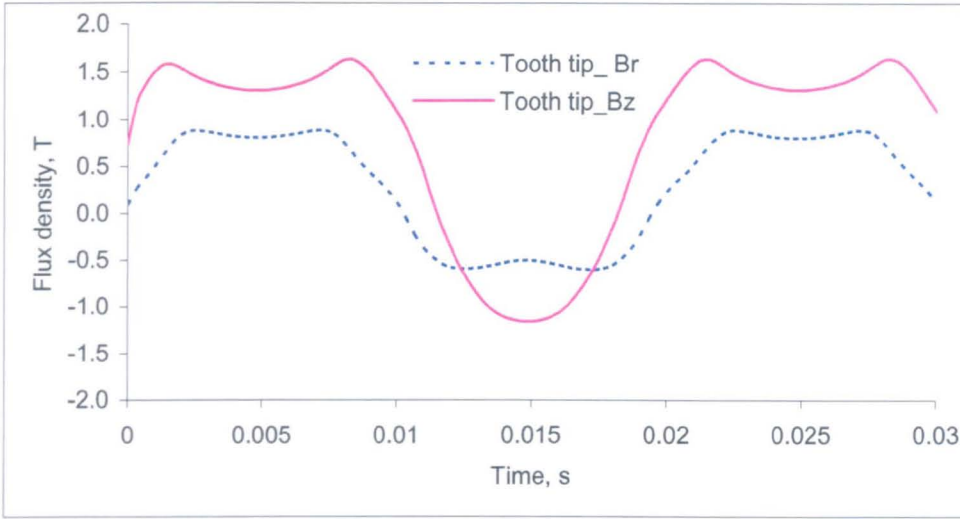


Fig. 3.6 Flux density at tooth tip

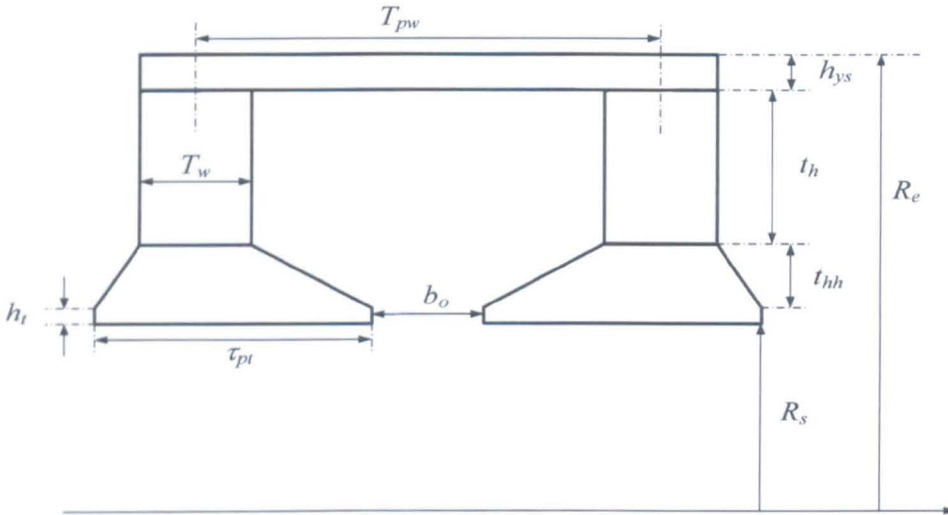


Fig. 3.7 Geometric parameters of stator core

The transition time, t_a , of the trapezoidal flux density waveform is given by the following empirical equation:

$$t_a = \frac{T_{mz}}{v} \cdot \frac{T_p}{(T_{mr} + 2g / \mu_r)} \quad 3.34$$

where g is the air-gap length, μ_r is the relative recoil permeability of the magnets, v is the linear speed of the armature, T_{mr} and T_{mz} are, respectively, the axial lengths of the radially and axially magnetised magnets and T_p is the pole pitch. Equation 3.34 is

based on the fact that the transition time, t_d , is approximately proportional $\frac{T_{mz}}{v}$ with

$$\frac{T_p}{(T_{mr} + 2g / \mu_r)} \text{ as scaling factor}$$

3.4.1.2 Tooth region

The flux passing through the tooth can be obtained from the following integration:

$$\psi_t(t) = \left(\int_{b_0/2-z_d}^{b_0/2+\tau_{pt}-z_d} 2\pi R_s B_r dz \right) \quad 3.35$$

where $z_d = vt$ is the axial displacement of the moving armature. The flux is dominantly in radial direction. The resulting flux in the tooth region varies with time as the armature reciprocates. The average flux density in the tooth can be estimated by:

$$B_{tr}(t) = \frac{\psi_t}{2\pi((R_s + h_t + t_{hh} + \frac{t_h}{2})T_w)} \quad 3.36$$

Fig. 3.8 shows the finite element predicted flux density components at the centre of the tooth region. It is evident that the radial flux density component is dominant. Hence, equation 3.36 can be used to predict iron loss in the tooth region.

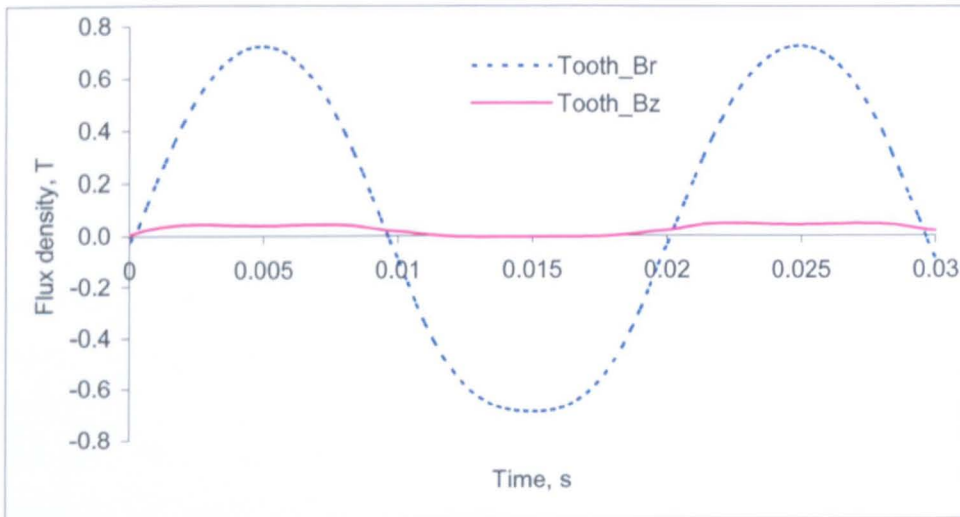


Fig. 3.8 Flux density at tooth

3.4.1.3 Yoke region

The flux passing through the yoke is the same as in the tooth given in equation 3.35. However, the resulting flux density component in the yoke region is essentially in the axial direction as illustrated by finite element predicted flux density waveforms shown in Fig. 3.9. Therefore, the flux density in the yoke region can be evaluated analytically by

$$B_{yz} = \frac{\psi_y}{\pi((R_e^2 - (R_e - h_{ys})^2))} \quad 3.37$$

where R_e and h_{ys} are the outer radius of the stator and the yoke thickness, respectively

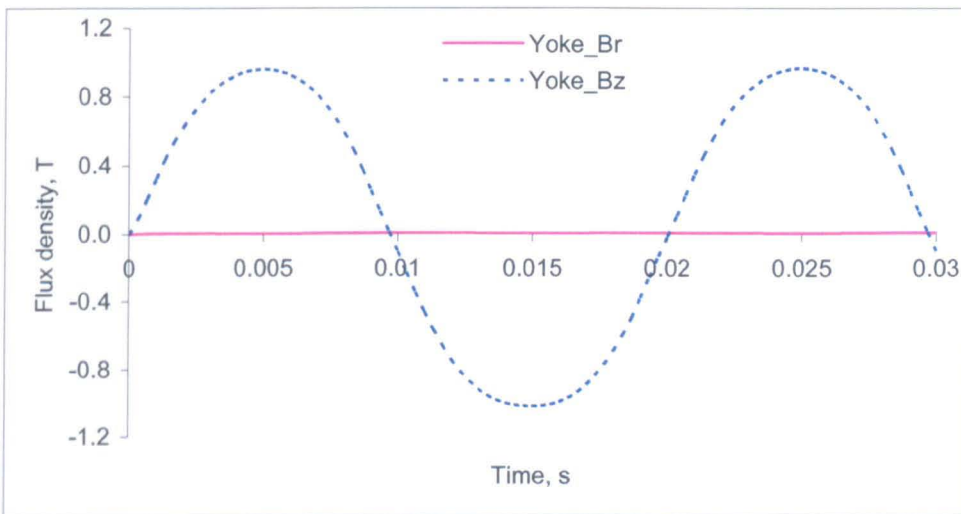


Fig. 3.9 Flux density at yoke

3.4.2 On-load condition

The armature reaction field can also be derived using the analytical model described in Chapter 2. The resultant field in the air-gap is obtained by superposition of the open-circuit and the armature reaction fields. The flux density waveforms in the different regions and the on-load iron loss are then evaluated in the same way as under the no-load operation.

With reference to the assumption made in section 2.2, the current distribution may be represented using a current sheet model, as shown in Fig. 3.10 and can be expanded into Fourier series of the following form:

$$J_s(z) = \sum_{n=1,2,\dots}^{\infty} J_n \cos m_n z \tag{3.38}$$

where

$$J_n = \frac{2N_c I}{T_{lp}} K_{dn} K_{pn} \tag{3.39}$$

$$m_n = \frac{2\pi n}{T_{lp}} \tag{3.40}$$

$$K_{dn} = \frac{\sin(m_n b_0 / 2)}{m_n b_0 / 2} \tag{3.41}$$

$$K_{pn} = -1 \tag{3.42}$$

If the separation distance between two adjacent coils, T_{lp} , is sufficiently large, the armature reaction field can essentially be represented the one in the middle.

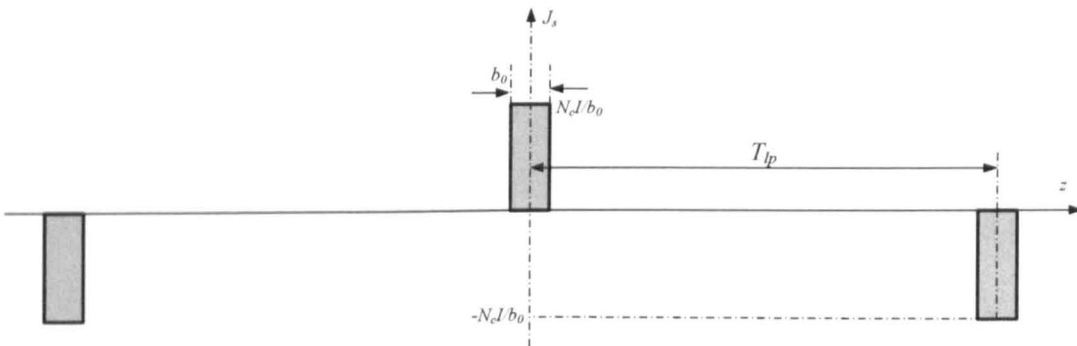


Fig. 3.10 Equivalent current sheet distribution

By assuming the recoil permeability of the magnets is equal to that of free space, the magnetic field is confined in the air-region as shown in Fig. 3.11.

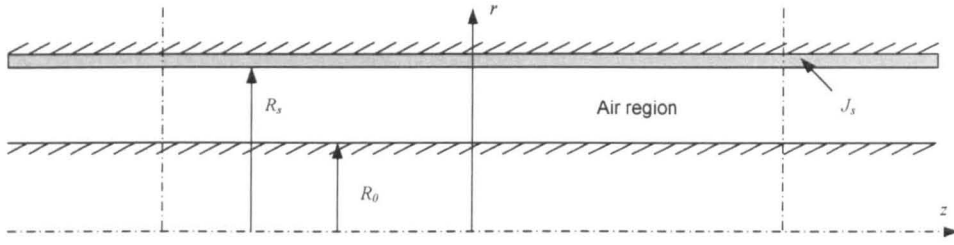


Fig. 3.11 Armature reaction field model

The magnetic vector potential A_θ is governed by:

$$\frac{\partial}{\partial z} \left(\frac{1}{r} \frac{\partial}{\partial z} (r A_\theta) \right) + \frac{\partial}{\partial r} \left(\frac{1}{r} \frac{\partial}{\partial r} (r A_\theta) \right) = 0 \quad 3.43$$

The boundary conditions to be satisfied by equation 3.43 are given by:

$$\begin{aligned} B_z \Big|_{r=R_0} &= 0; \text{ for ferro-magnetic supporting tube} \\ B_r \Big|_{r=0} &= 0; \text{ for non-magnetic supporting tube} \\ H_z \Big|_{r=R_s} &= J_s \end{aligned} \quad 3.44$$

where R_0 is the outer radius of the mild-steel supporting tube of the motor. Solving equation 3.43 and subject to boundary conditions of 3.44 yields the expressions for flux density components:

$$B_r = - \sum_{n=1}^{\infty} [A_n B I_0(m_n r) m_n \cos(m_n z)] \quad 3.45$$

$$B_z = \sum_{n=1}^{\infty} [A_n B I_0(m_n r) m_n \sin(m_n z)] \quad 3.46$$

For the motor with non-magnetic supporting tube, where

$$A_n = \frac{J_n \mu_0}{B I_0(m_n R_s) m_n} \quad 3.47$$

The flux density components for the motor with magnetic support tube can be similarly derived. Using analytically predicted flux density waveforms, the hysteresis and excess loss densities in each region can be evaluated by:

$$P_h = k_h f B_m^\alpha \quad 3.48$$

$$P_e = \sqrt{2\pi} k_e f^{\frac{3}{2}} \int_{2\pi} \left| \frac{dB}{d\theta_e} \right|^{\frac{3}{2}} d\theta_e \quad 3.49$$

where f , B_m and θ_e are the frequency, amplitude of the fundamental flux density, and electrical degree, respectively. The coefficients α , k_h and k_e associated with the hysteresis and excess loss components and determined from manufactured data sheet.

3.5 Motor design dimensions

Since design optimisation of the iron-cored quasi-Halbach magnetised motor with rectangular magnets has been reported [1], only two motors i.e. air-cored quasi-Halbach magnetised motor with rectangular magnets and iron-cored quasi-Halbach magnetised motor with trapezoidal magnets, will be optimised for the direct-drive linear compressor system.

Fig. 3.12 (a) and (b) show the schematic and design parameters of air-cored motor with rectangular and iron-cored motor with trapezoid magnets, respectively. The relevant variables and symbols are defined as follows

Symbol	Description
θ	Stator under cut angle
b_0	Width of slot opening
B_{rem}	Remanence of permanent magnet
h_t	Tooth tip height
h_m	Radial thickness of magnets
h_{ym}	Radial thickness of supporting tube
h_{ys}	Yoke thickness of stator core
R_e	Outer radius of stator core

R_i	Inner radius of supporting tube
R_m	Outer radius of magnets
T_{mr}	Axial length of radially magnetised magnet at the centre
T_{mr2}	Axial length of radially magnetised magnet at two ends
T_{mz}	Axial length of axially magnetised magnets
T_p	Pole pitch
T_{pe}	Extended tooth tip length
T_{pw}	Tooth pitch width
T_w	Tooth width

As will be observed, the design parameters such as stator slot opening, b_o , and height of tooth tip, h_t , have less significant influence on the performance of motors and their values are fixed to 10.0 mm and 1.0 mm, respectively. In general, the performance improves as h_m is increased. However, an increase in the volume of rare-earth magnet material will increase the cost and result in a heavier armature, which is usually adverse for a reciprocating moving-magnet motor [11]. Therefore, the radial thickness of magnet is fixed at 5.0 mm to produce an acceptable air-gap flux density and thrust force capability. The air-gap length, G , is fixed to 0.8 mm due to minimum assembly tolerances. The motor efficiency improves as the outer stator radius, R_o , increases. However, an initial design scan shows [1] [12] that for the given design specification the efficiency improvement diminishes when R_o is greater than 50.0 mm. Hence, this value is chosen for the outer stator radius, R_o .

For the iron-cored quasi-Halbach magnetised motor with trapezoidal magnets, the permanent magnet angle, β , has been optimised using finite element technique. Fig. 3.13 shows finite element predicted back-emf waveforms with different values of β when the armature velocity is 2.1 m/s. As will be observed, the angle of 45 degrees is selected where it produced the highest average of back emf.

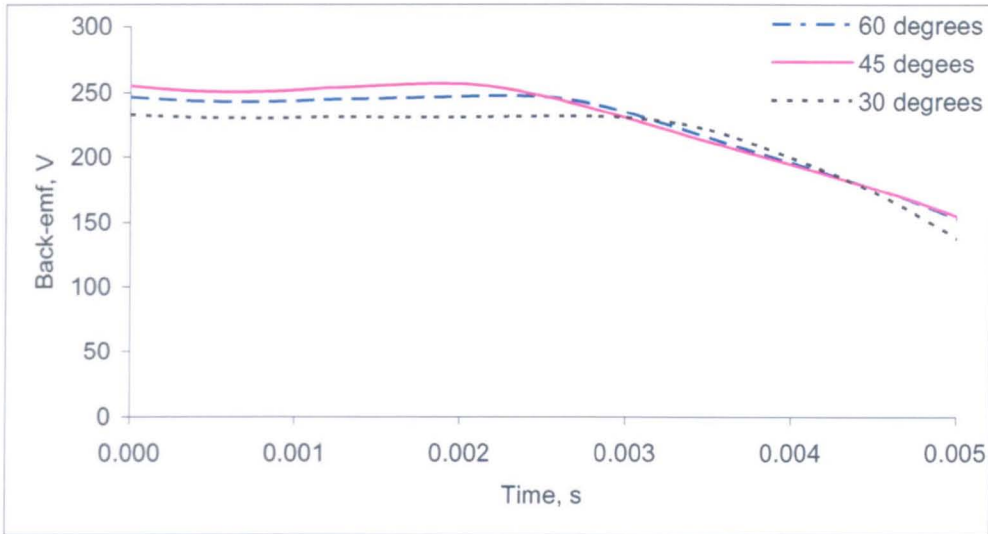


Fig. 3.13 Influence of permanent magnet angle, β , on back-emf at velocity 2.1 m/s

The leading design parameters, which have significant influences on the motors performance and require to be optimised are the dimension ratios, R_m/R_e and T_{mr}/T_p . In addition, the influence of the pole-pitch width, T_{pw} , and the remanence of permanent magnet, B_{rem} , on the motor/system efficiency is also investigated.

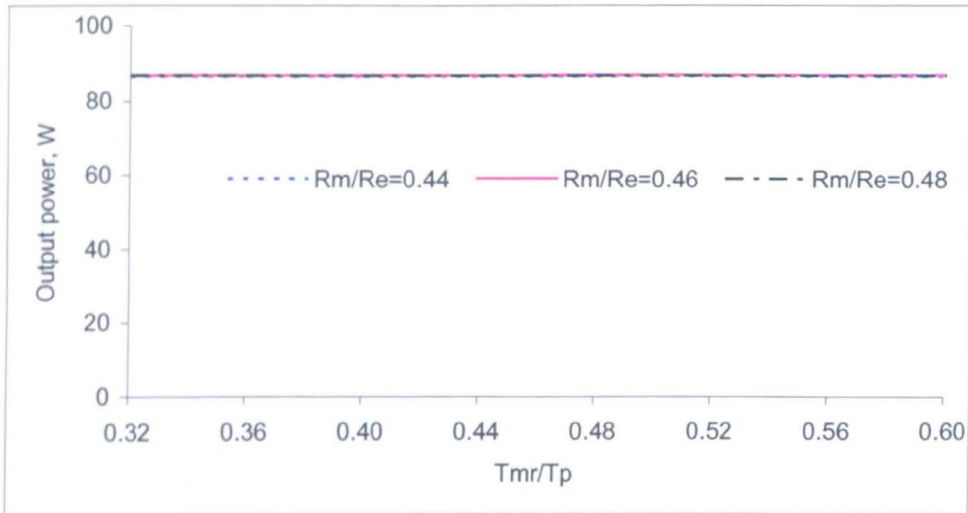
The tooth width T_w , the stator yoke thickness, h_{ys} , and the radial thickness of the mover back-iron, h_{ym} , are dependent on given flux density levels in these regions, and their values are determined during the optimisation process. In addition, the area of the tooth width is approximately similar with the area of the stator yoke in order to avoid the saturation of flux density.

3.6 Design optimisation

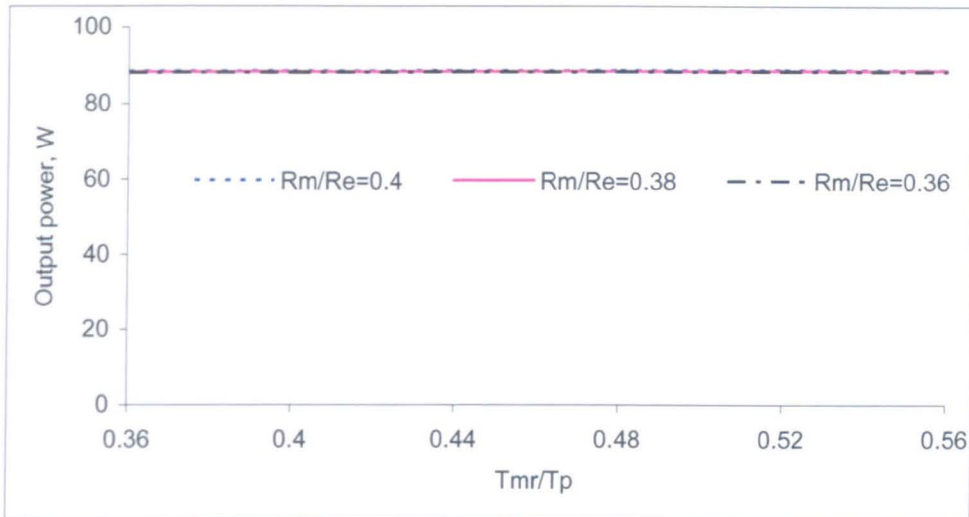
The optimisation is aimed to achieve maximum motor or system efficiency under specified operating conditions and volumetric constraints as tabulated in Table 3.1. The motor output power is kept to its rated value of 88.5 W by adjusting the magnitude of current when the leading design parameters change. By example, Figs. 3.14 (a) and (b) show that the output power is kept to 88.5 W as the two leading dimensional ratios, R_m/R_e and T_{mr}/T_p are varied for both air-cored and iron-cored motors. This ensures motor efficiency is calculated against the same output power during the optimisation process.

Table 3.1 Fixed design parameters and operational conditions

Description	Value	Units
θ	30	°
b_o	10	mm
G	0.8	mm
h_t	1	mm
R_e	50	mm
T_p	25	mm
T_{pe}	3.5	mm
Output power, P_{out}	88.5	W
Rated armature stroke, X_m	10.5	mm
Rms voltage supply, V_{rms}	230	V
Frequency, f	50	Hz
Stator core material	Somaloy 700	-
Permanent magnet material	NdFeB	-



a. Air-cored quasi-Halbach magnetised motor with rectangular magnets



b. Iron-cored quasi Halbach magnetised motor with trapezoidal magnets

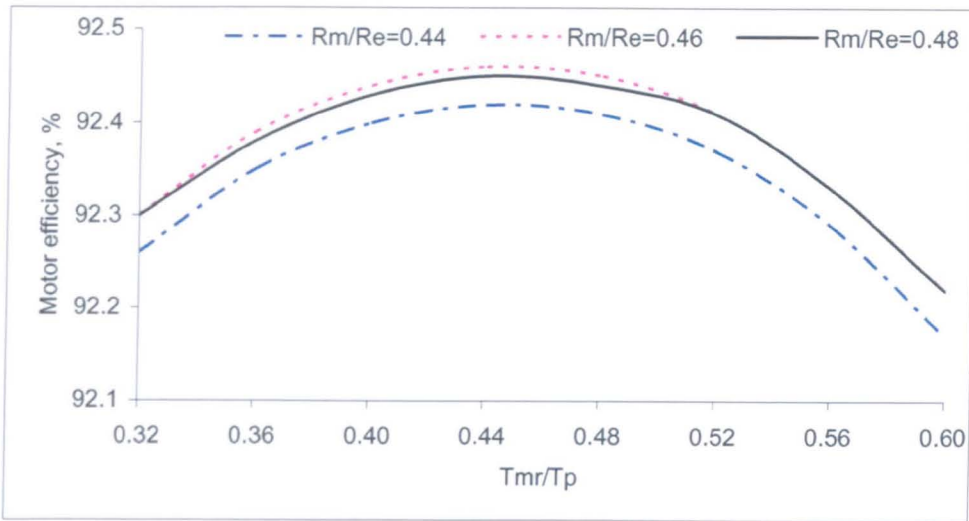
Fig. 3.14 Variations of T_{mr}/T_p and R_m/R_e with constant output power

3.6.1 Air-cored quasi-Halbach magnetised motor with rectangular magnets

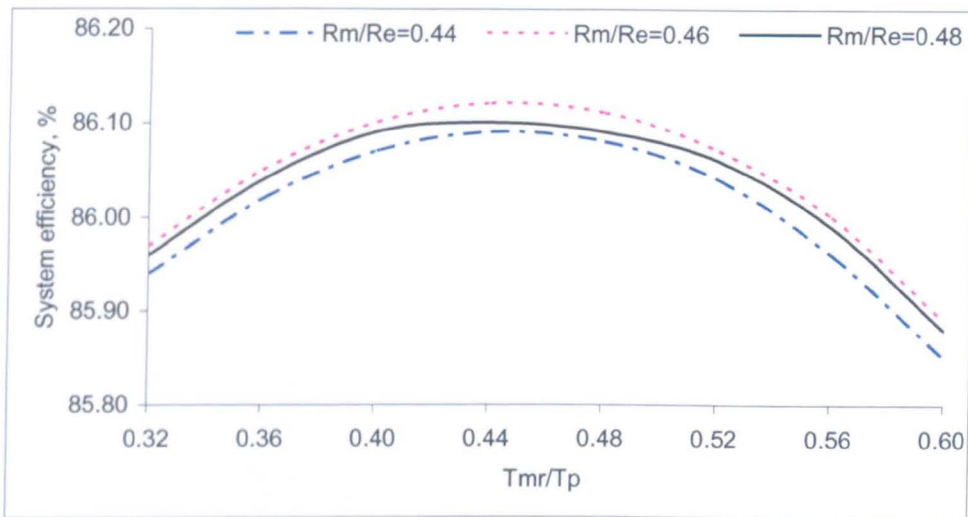
3.6.1.1 Influence of T_{mr}/T_p and R_m/R_e

The ratio of T_{mr}/T_p represents the combined effect of radially and axially magnetised magnets in order to produce a maximum fundamental radial flux density in the air gap [13]. Meanwhile, the ratio of R_m/R_e represents the optimal balance between electrical loading and magnetic loading [11] in order to achieve maximum motor efficiency. In this study, the motor efficiency is optimised with respect to both dimensional ratios.

Fig. 3.15 shows the variations of the motor efficiency and compressor system efficiency with the two dimensional ratios when air-cored motor drives a typical compressor for household refrigerators. As will be seen, there are optimal ratios of $T_{mr}/T_p = 0.44$, $R_m/R_e = 0.46$ which yields the maximum motor efficiency and compressor system efficiency of 92.46 % and 86.12 %, respectively. It is evident that the optimal ratios of T_{mr}/T_p and R_m/R_e for the maximum system efficiency essentially coincide with the values for the maximum motor efficiency.



a. Motor efficiency

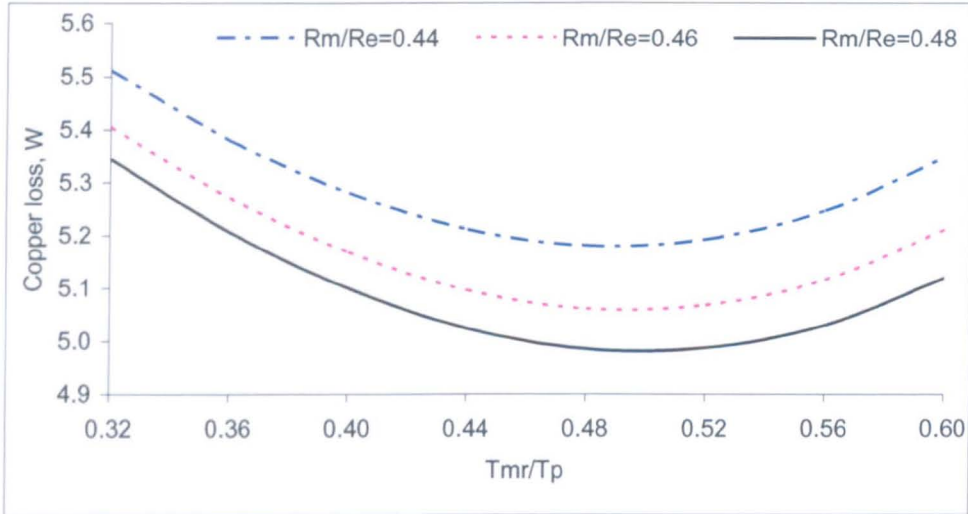


b. System efficiency

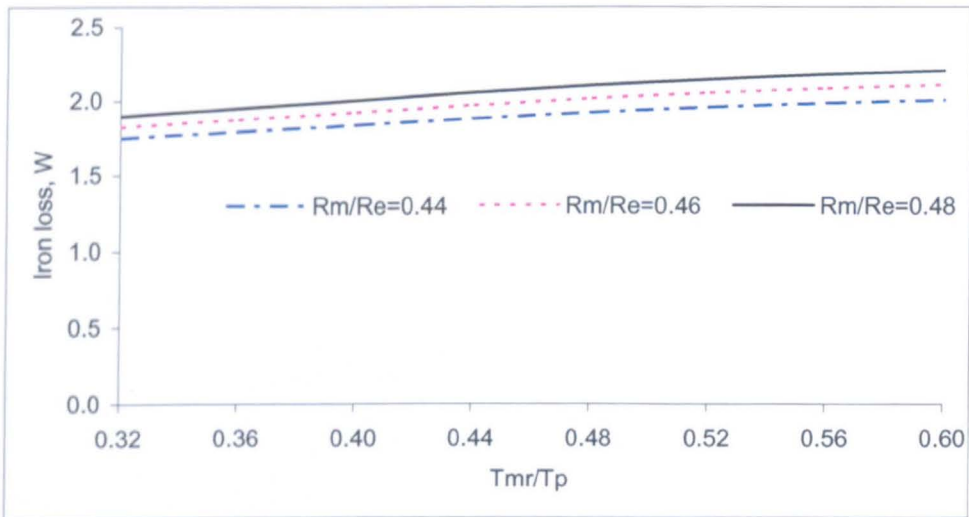
Fig. 3.15 Influence of R_m/R_e and T_{mr}/T_p on efficiency

Fig. 3.16 shows the variations of copper loss and iron loss with T_{mr}/T_p and R_m/R_e . As will be observed in Fig. 3.16 (a), copper loss decreased when the ratio of R_m/R_e is increased from 0.44 to 0.48. This is because the slot area decreases as R_m/R_e increases, which tends to increase resistance of the coil. However, the coil flux per turn increases and the motor current for the same output power decreases, resulting in the decrease of copper loss. It is also evident that for a given R_m/R_e there is a specific T_{mr}/T_p ratio which yields minimum copper loss. At this ratio, the coil flux per turn reaches the maximum, and hence the minimum current and copper loss.

Meanwhile, the iron loss increases with the increases of R_m/R_e of as shown in Fig. 3.16 (b). This is due to the increase in flux density in the stator core which yields the increase of iron loss. Further, the iron loss tends to increase when T_{mr}/T_p is varied from 0.32 to 0.60. As T_{mr}/T_p increases, the radial flux density component becomes more significant in the tooth tip region. Consequently, the iron loss increases.



a. Copper loss



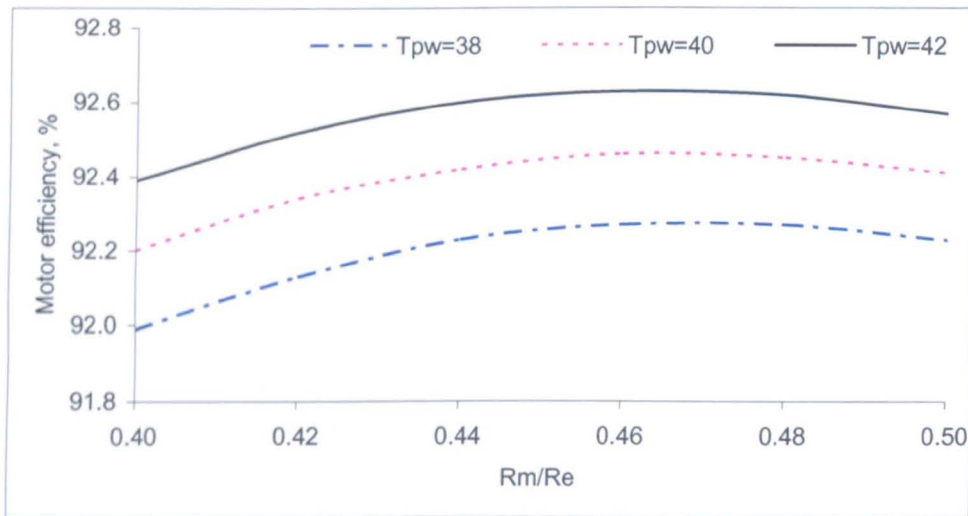
b. Iron loss

Fig. 3.16 Influence of R_m/R_e and T_{mr}/T_p on power loss

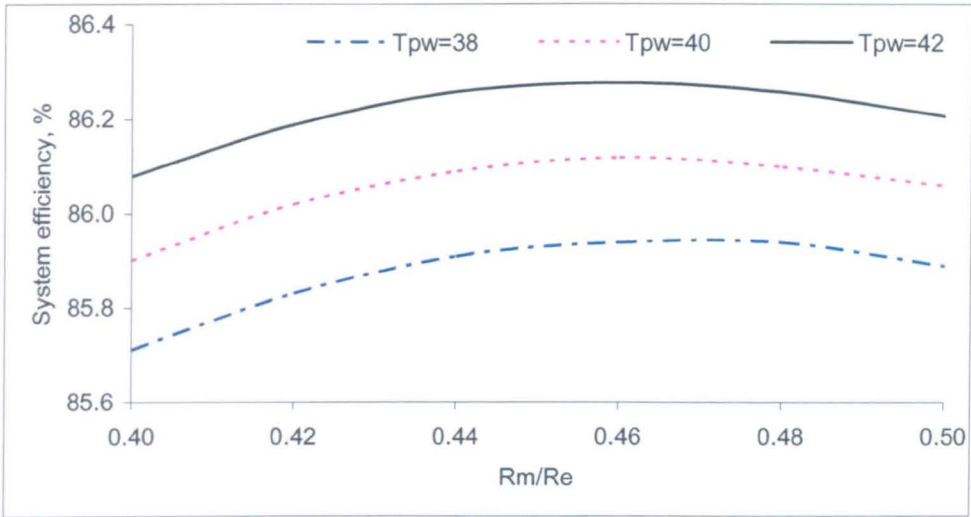
3.6.1.2 Influence of tooth pitch width, T_{pw}

Fig. 3.17 shows the variation of motor efficiency and compressor system efficiency with tooth pitch width, T_{pw} and the ratio of R_m/R_e , at the optimal ratio of $T_{mr}/T_p = 0.44$ and other parameter being the same as stated in Table 3.1. As will be seen, motor efficiency and compressor system efficiency increased when T_{pw} was increased. However, the increase in T_{pw} gives rise to a large motor size, and hence great cost. Considering the overall system dimensions and cost, a tooth pitch width $T_{pw} = 40.0$ mm is selected. It is also evident that the optimal ratio R_m/R_e for the maximum motor and system efficiency with different values of T_{pw} are virtually the same, which implies that this optimal ratio is independent of the tooth pitch width.

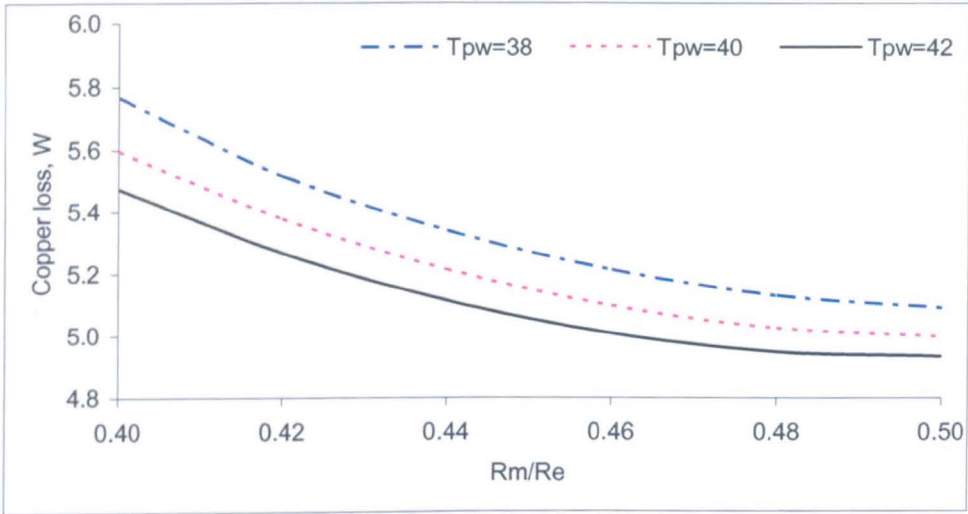
Fig. 3.18 shows the variation of copper loss and iron loss with T_{pw} and the ratio of R_m/R_e . As will be seen, the copper loss decreases when the T_{pw} is increased. This is due to the slot area increase which allows more space for the coil and hence, a reduction of the coil resistance. The iron loss, on the other hand, decreases when T_{pw} is increased. This is due to flux density being decreased in stator core.



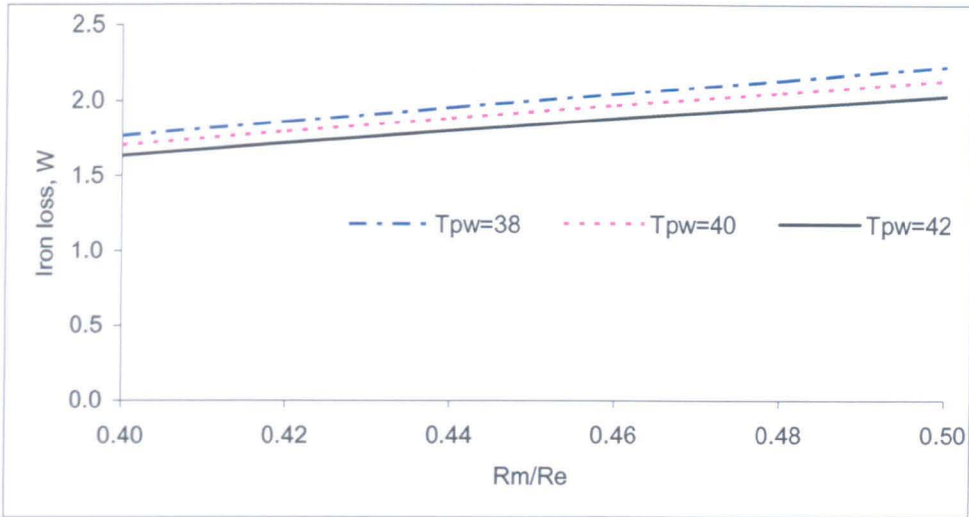
a. Motor efficiency



b. System efficiency
 Fig. 3.17 Influence of T_{pw} on efficiency



a. Copper loss

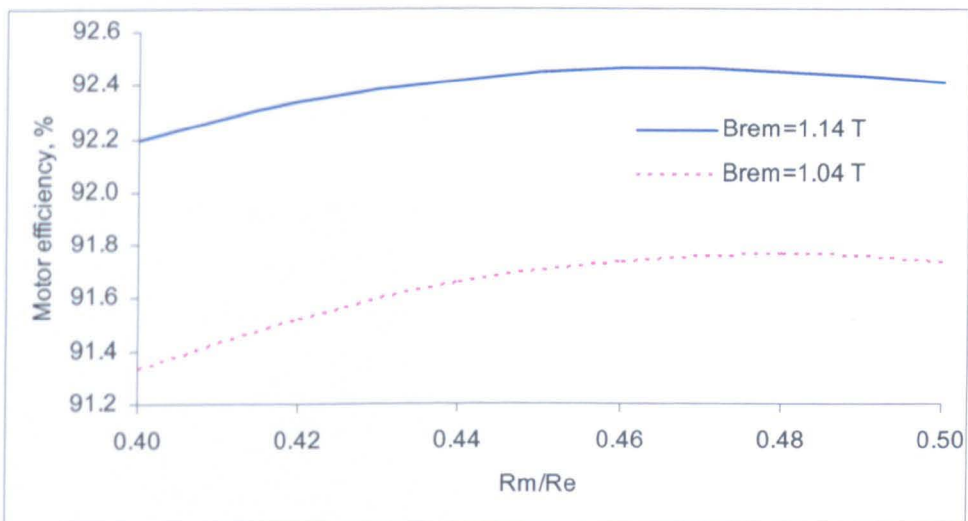


b. Iron loss

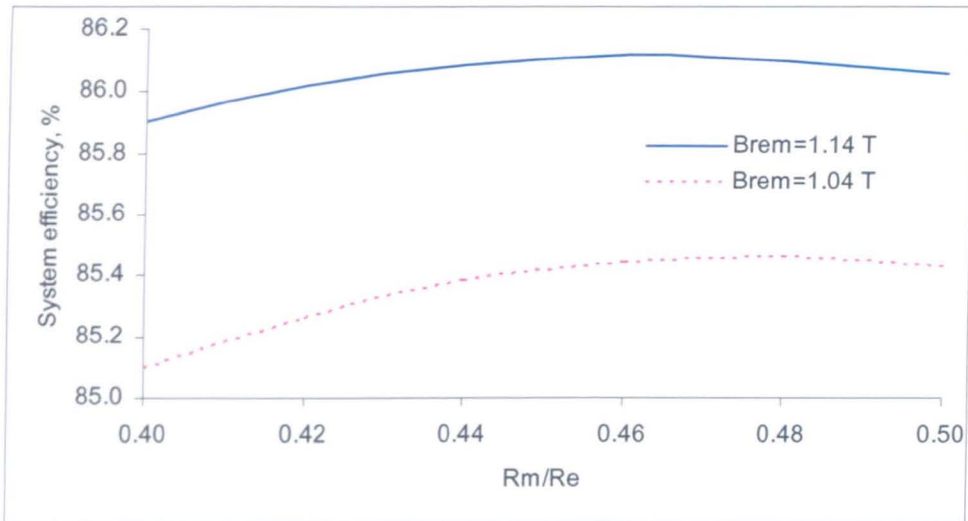
Fig. 3.18 Influence of T_{pw} on power loss

3.6.1.3 Influence of remanence of permanent magnets, B_{rem}

Fig. 3.19 shows the variation of motor efficiency, compressor system efficiency with the ratio of R_m/R_c for two values of B_{rem} at $T_{pw} = 40.0$ mm. As will be seen, the performance of motor and system efficiency increased with a higher value of remanence, B_{rem} . This is due to the fact that a larger B_{rem} , produces stronger magnetic field, which results in a higher coil flux per turn and a better performance. It should be noted that the optimal ratio of R_m/R_c for maximum motor or system efficiency decreases slightly with an increase in B_{rem} .



a. Motor efficiency



b. System efficiency

Fig. 3.19 Influence of B_{rem} on efficiency

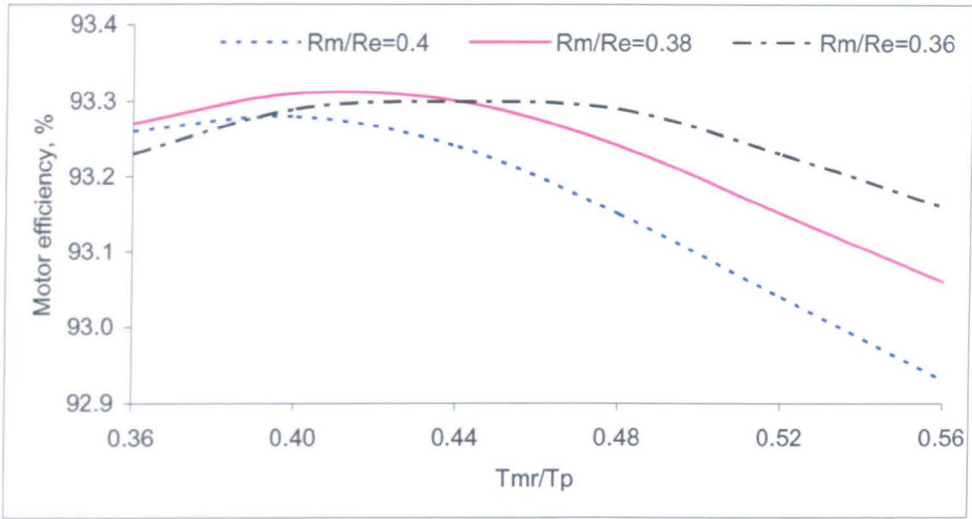
3.6.2 Iron-cored quasi-Halbach magnetised motor with trapezoidal magnets

3.6.2.1 Influence of T_{mr}/T_p and R_m/R_e

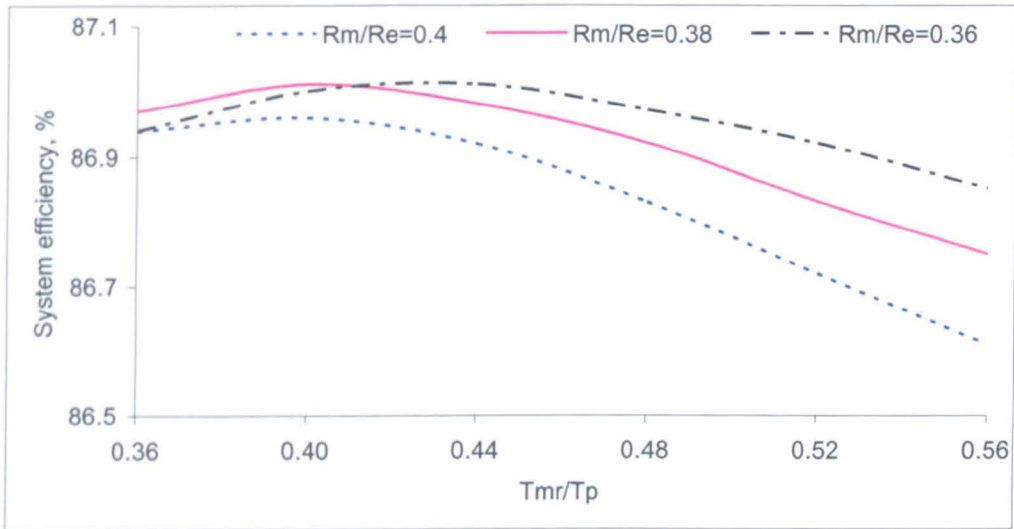
Fig. 3.20 shows the variation of the motor efficiency and compressor system efficiency with T_{mr}/T_p and R_m/R_e ratios. As will be seen, there are optimal ratios of $T_{mr}/T_p = 0.4$, $R_m/R_e = 0.38$ which yields the maximum motor efficiency of 93.31 %. Again the optimal dimensional ratios for the maximum motor efficiency appears to coincide with those for the maximum system efficiency.

Fig. 3.21 shows the variation of copper loss and iron loss when the ratios of T_{mr}/T_p and R_m/R_e are varied. As will be seen, copper loss decreases when the ratio of R_m/R_e is increased. This trend is similar to that observed for the air-cored quasi-halbach magnetised motor with rectangular magnets.

However, the copper loss continues to decrease as T_{mr}/T_p increases. The opposite trend is observed for the iron loss which increases with T_{mr}/T_p . The optimal T_{mr}/T_p occurs when the total loss is at minimum.

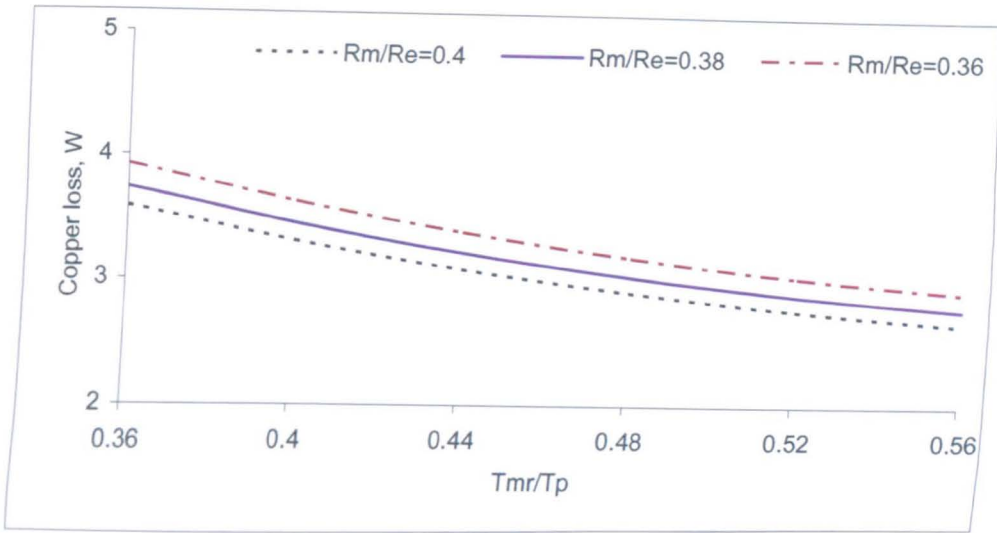


a. Motor efficiency

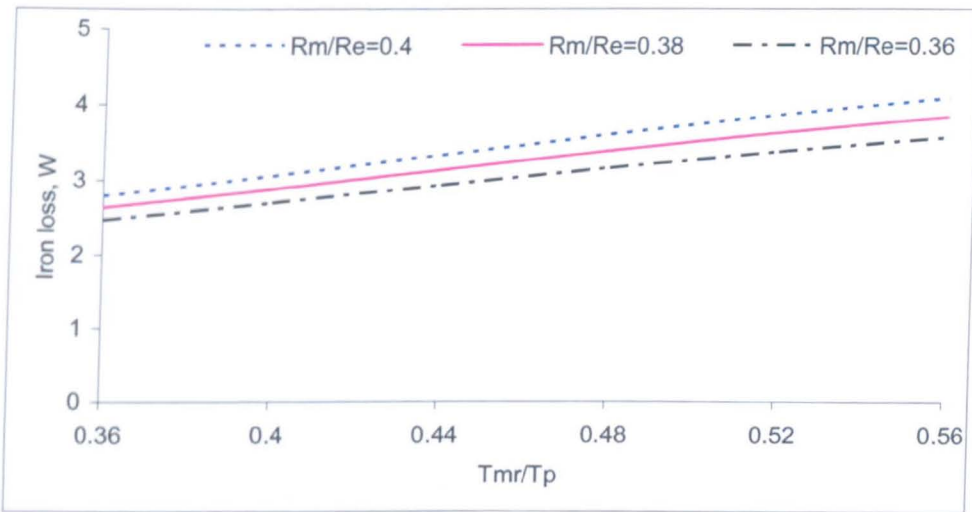


b. System efficiency

Fig. 3.20 Influence of R_m/R_e and T_{mr}/T_p on efficiency



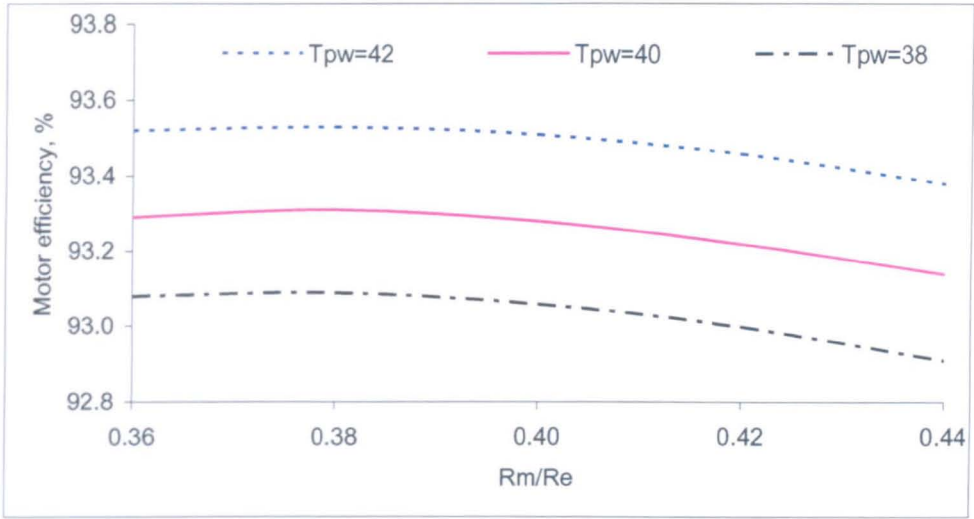
a. Copper loss



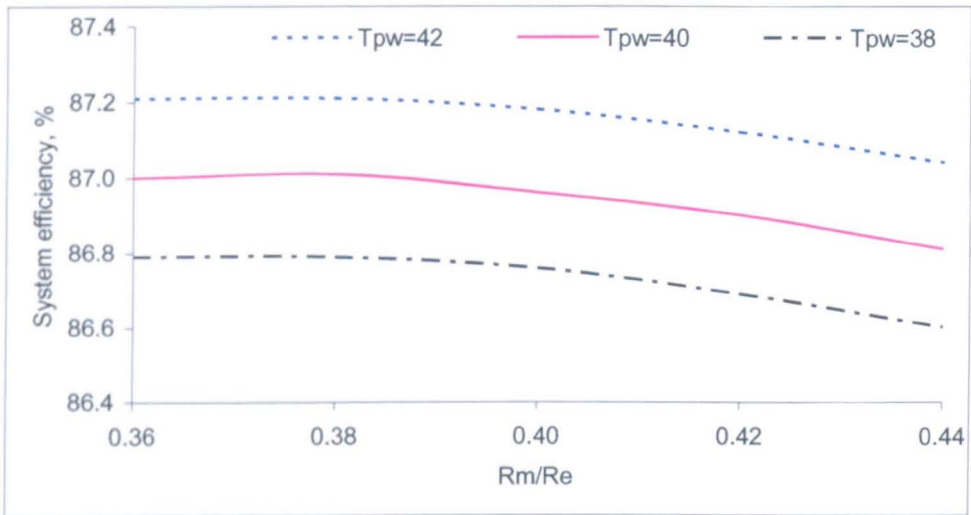
b. Iron loss

Fig. 3.21 Influence of R_m/R_e and T_{mr}/T_p on power loss

The influence of tooth pitch width, T_{pw} , and the remanence of magnets, B_{rem} , on motor or system efficiency is similar to those observed in sections 3.6.1.2 and 3.6.1.3. The results are shown in Figs. 3.22 and 3.23 for completeness.

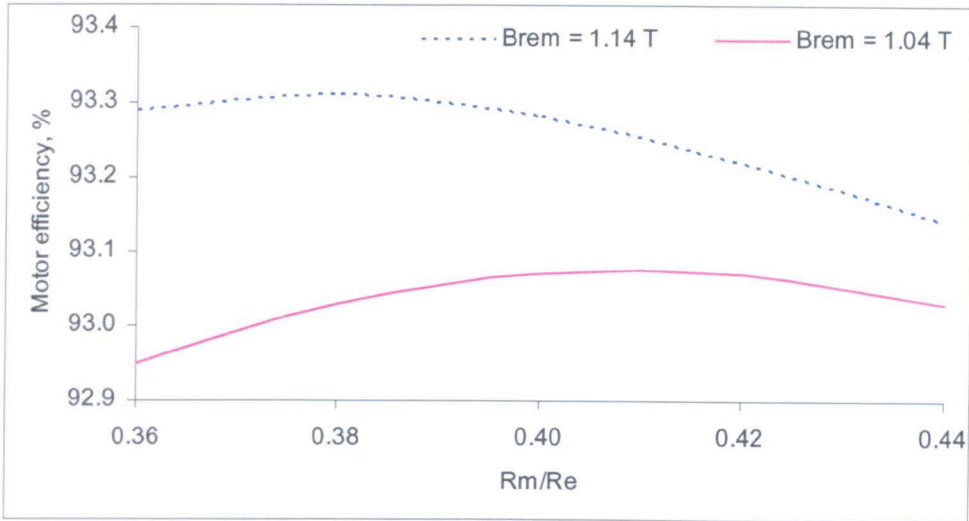


a. Motor efficiency

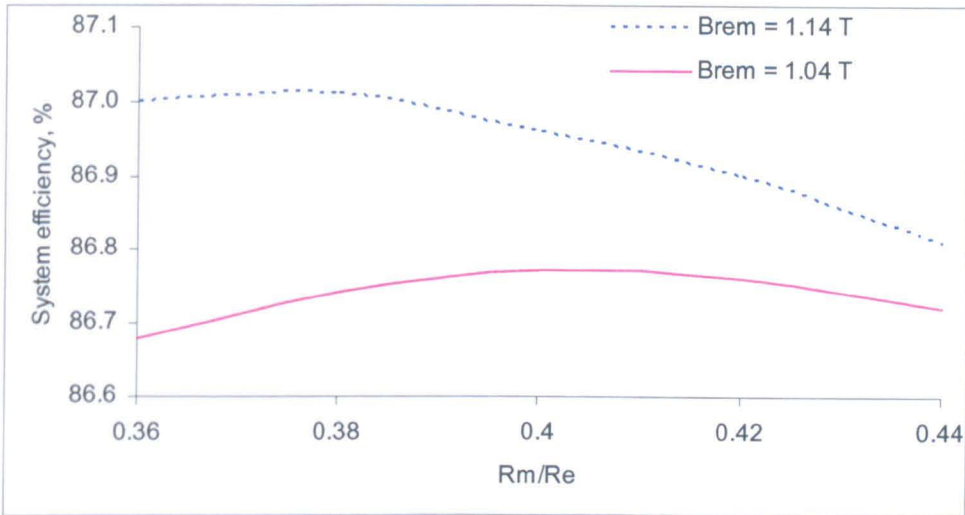


b. System efficiency

Fig. 3.22 Influence of T_{pw} on efficiency



a. Motor efficiency



b. System efficiency

Fig. 3.23 Influence of B_{rem} on efficiency

3.7 Design refinement with finite element analysis

The analytical model is a useful tool to aid the initial design optimisation. However, it cannot accommodate complex geometries and material non-linearities [14]. These limitations can be overcome by employing finite element technique in order to obtain more accurate results. Therefore, the leading parameters such as the ratios of T_m/T_p and R_m/R_e , need to be refined. All operational parameters and motor dimensions obtained from the design optimisation described in section 3.6 was used to build an initial two-dimensional axi-symmetrical finite element model.

By neglecting the friction loss and eddy current loss, the efficiency of the motors, η , is evaluated by:

$$\eta = \frac{P_{out}}{P_{out} + P_{fe} + P_{cu}} * 100\% \quad 3.50$$

where P_{out} , P_{fe} and P_{cu} are output power, iron loss and copper loss, respectively. The iron loss was calculated using finite element predicted flux density distribution in stator core, and the iron loss model given by equations 3.48 and 3.49, details of which will be described in Chapter 5.

3.7.1 Air-cored quasi-Halbach magnetised motor with rectangular magnets

Fig. 3.24 shows the finite element predicted variation of efficiency of the air-cored motor with T_m/T_p ratio at $R_m/R_e = 0.4$ when operating at the rated conditions. The maximum efficiency, 93.47 %, was achieved at $T_m/T_p = 0.4$. It is evident that the optimal T_m/T_p ratio is slightly lower than that obtained from the analytical model, $T_m/T_p = 0.44$. In addition, the efficiency is slightly increased from 92.4 % (analytical) to 93.47 % (finite element). This is due to the fact that the radial air-gap flux density predicted by finite element is slightly greater than that of analytical prediction. Thus, for the same output power, the motor current will be lower, resulting in an increase in efficiency.

The ratio of R_m/R_e has also been refined in order to achieve more accurate optimal design. Fig. 3.25 shows the efficiency of the air-cored motor as a function of the R_m/R_e ratio at $T_m/T_p = 0.4$. As will be observed, the maximum efficiency, 93.50 % is achieved at $R_m/R_e = 0.42$. The optimal ratio of R_m/R_e is also slightly lower compared to that of the analytical design, $R_m/R_e = 0.46$. This has a benefit that higher efficiency is achieved with less magnet material/volume.

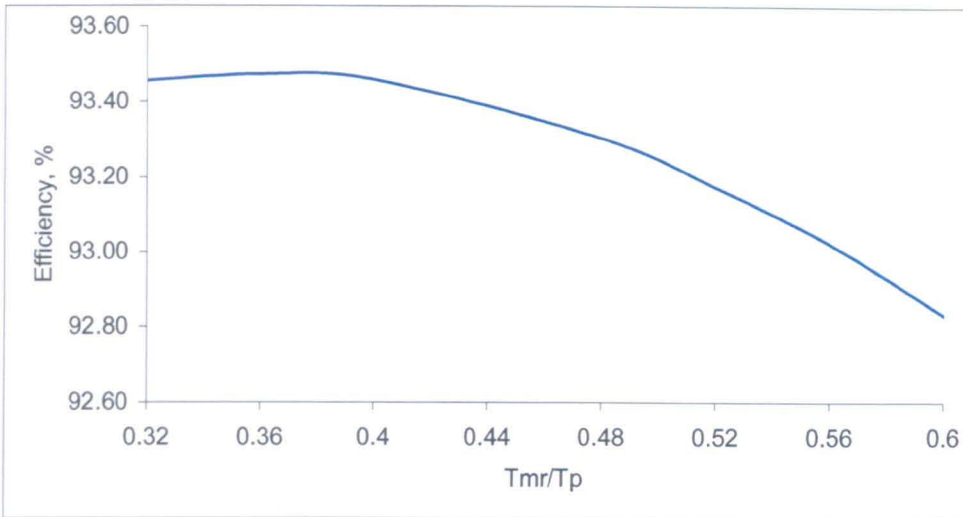


Fig. 3.24 Finite element predicted variation of efficiency with T_{mr}/T_p

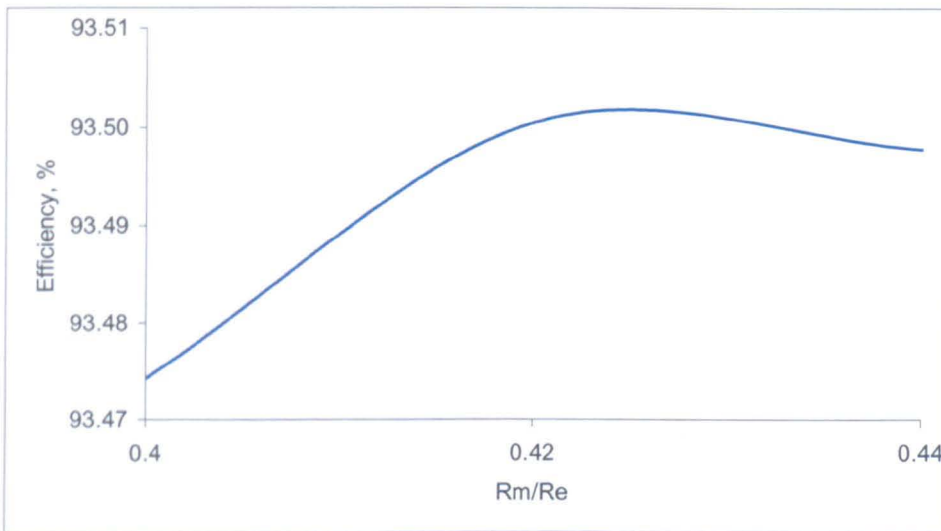


Fig. 3.25 Finite element predicted variation of efficiency with R_m/R_e

3.7.2 Iron-cored quasi-Halbach magnetised motor with trapezoidal magnets

Fig. 3.26 shows the finite element predicted variation of efficiency of the iron-cored motor with T_{mr}/T_p ratio at $R_m/R_e = 0.4$. The maximum efficiency, 94.12 % is achieved at $T_{mr}/T_p = 0.4$. In this case, the optimal T_{mr}/T_p ratio is the same as that of the analytical design but the efficiency is higher than the analytical prediction due to the same reason as explained in Chapter 3.7.1.

Fig. 3.27 shows the variation of efficiency with R_m/R_e ratio at $T_{mr}/T_p = 0.4$. As will be observed, the maximum efficiency, 94.24 % is occurs at $R_m/R_e = 0.36$, i.e $R_m = 18.0$ mm, which is 1.0 mm less than that obtained from the optimisation based on the analytical model.

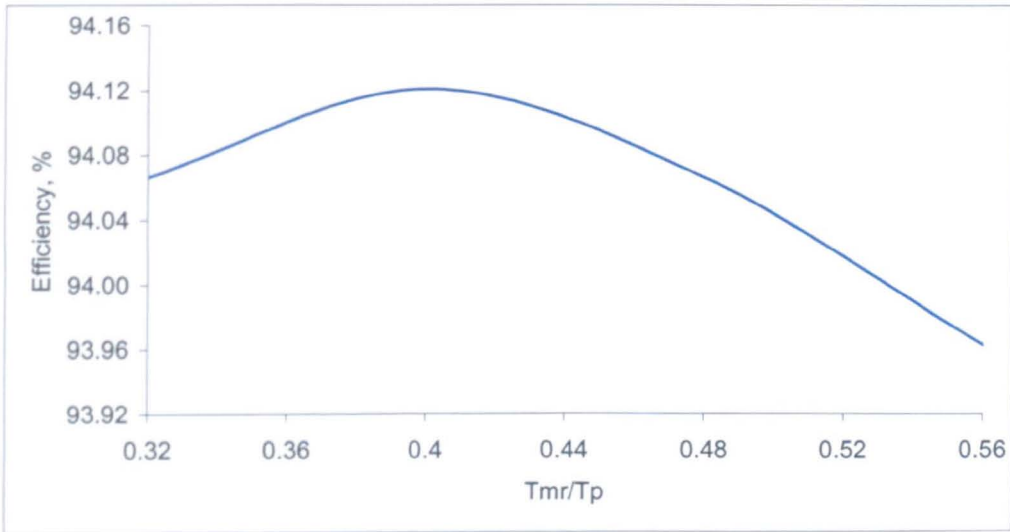


Fig. 3.26 Finite element predicted variation of efficiency with T_{mr}/T_p

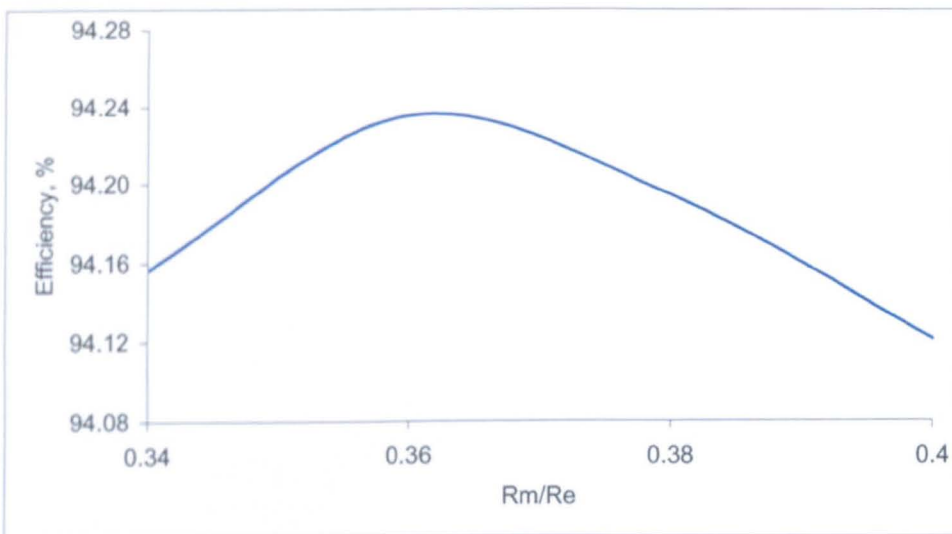


Fig. 3.27 Finite element predicted variation of efficiency with R_m/R_e

3.8 Summary of final design dimension

Table 3.2 and Table 3.3 shows the design parameters obtained from the design optimisation for air-cored quasi-Halbach magnetised motor with rectangular magnets

and iron-cored quasi-Halbach magnetised motor with trapezoidal magnets, respectively.

Table 3.2 Optimal design parameters of air-cored quasi-Halbach magnetised motor with rectangular magnets

Description	Dimension	Units
Outer radius of stator core, R_e	50.0	mm
Yoke thickness, h_{ys}	3.3	mm
Airgap length, G	0.8	mm
Outer radius of magnet, R_m	21.0	mm
Magnet height, h_m	5.0	mm
Pole pitch, T_p	25.0	mm
Tooth width, T_w	9.4	mm
Tooth pitch width, T_{pw}	40.0	mm
Axial length of radially magnetised magnet, T_{mr}	10.0	mm
Axial length of radially magnetised at ends, T_{mr2}	5.0	mm
Axial length of axially magnetised magnets, T_{mz}	15.0	mm
Slot opening width, b_o	10.0	mm
Tooth tip height, h_t	1.0	mm
Stator under cut angle, θ	30.0	°

Table 3.3 Optimal design parameters for iron-cored quasi-Halbach magnetised motor with trapezoidal magnets

Description	Dimension	Units
Outer radius of stator core, R_e	50.0	mm
Yoke thickness, h_{ys}	3.3	mm
Air-gap length, G	0.8	mm
Outer radius of magnet, R_m	18.0	mm
Magnet height, h_m	5.0	mm
Supporting tube height, h_{ym}	3.5	mm
Pole pitch, T_p	25.0	mm
Tooth width, T_w	9.4	mm
Tooth pitch width, T_{pw}	40.0	mm
Axial length of radially magnetised magnet, T_{mr}	10.0	mm
Axial length of radially magnetised at ends, T_{mr2}	5.0	mm
Axial length of axially magnetised magnets, T_{mz}	15.0	mm

Slot opening width, b_o	10.0	mm
Tooth tip height, h_t	1.0	mm
Permanent magnet angle, β	45.0	°
Stator under cut angle, θ	30.0	°

3.9 Conclusions

A design methodology to achieve optimal performance of the direct-drive linear compressor system employing two-types of linear permanent magnet motors have been described, and the influence of the leading design parameters on the system efficiency have been studied analytically. According to Fig. 3.4 and equation 3.21, the compressed gas has a significant effect on input impedance of linear motor, and it is essential that the gas load effect is taken into account in the design optimization.

Due to the limitation of analytical solution which cannot accommodate complex geometries and material non-linearities, the leading design parameters have been refined with finite element analysis, which results in slightly different values and improved efficiency.

The efficiency of the iron-cored quasi-Halbach magnetized motor with trapezoidal magnets is higher than that of the air-cored quasi-Halbach magnetized motor with rectangular magnets. However, the air-cored motor has a lower moving-mass, and requires a less stiffer spring for reciprocating compressor operation, which is conducive to improving dynamic capability [15].

References

- [1] J. Wang, T. Ibrahim, and D. Howe, "Design optimisation of short-stroke, single phase tubular permanent magnet motor for refrigeration applications," *Proceedings of the 2008 International Conference on Electrical Machines, ICEM2008, Portugal, Paper ID 1402, September 2008.*
- [2] M. Utsuno, M. Takai, T. Yaegashi, T. Mizuno, H. Yamamoto, K. Shibuya, and H. Hamada, "Efficiency characteristic of a linear oscillatory actuator under simulated compressor load," *Proceedings of Linear Drives and Industry Applications, LDIA2001, Nagano, Japan, pp. 264-267, October 2001.*

- [3] J. Wang, D. Howe, and M. Inoue, "Magnetic field distribution of quasi-Halbach magnetised cylinder for tubular permanent magnet machines," *Proceedings of 4th International Symposium on Linear Drives and Industry Applications, LDIA 2003, Birmingham, United Kingdom*, pp. 481-484, September 2003.
- [4] Z. Lin, J. Wang, and D. Howe, "A resonant frequency tracking technique for linear vapour compressors," *IEEE International Electric Machine and Drives Conference, IEMDC'07, Turkey*, vol. 1, pp. 370-375, May 2007.
- [5] J. Wang and D. Howe, "Modelling of linear reciprocating compressor system," *Carbon Thrust Project Number 2003-3-51-1-1, University of Sheffield*, June 2004.
- [6] G. S. Choe and K. J. Kim, "Analysis of non-linear dynamics in linear compressor," *JSME International Journal, Series C*, vol. 43, no. 3, pp. 545-552, 2000.
- [7] J. Wang, D. Howe, and Z. Lin, "Comparative studies on linear motor topologies for reciprocating vapour compressors," *IEEE International Electric Machine and Drives Conference, IEMDC'07, Turkey*, vol. 1, pp. 364-369, May 2007.
- [8] J. Wang, Z. Lin, and D. Howe, "Characteristics of linear compressors under current source excitation," *Proceeding of IMechE, Part A, Journal of Power and Energy*, vol. 221, no. 7, pp. 1057-1064, 2007.
- [9] Y. Amara, J. Wang, and D. Howe, "Stator iron loss of tubular permanent magnet machines," *IEEE Transactions on Industry Applications*, vol. 41, no. 4, pp. 989-995, July/August 2005.
- [10] T. Ibrahim, J. Wang, and D. Howe, "Iron loss calculation in a reciprocating tubular permanent magnet motor with soft magnetic composite," *Proceeding of XVII International Conference on Electrical Machines, ICEM2006, Chania, Greece*, September, 2006.

- [11] J. Wang and D. Howe, "Design optimisation of radially magnetised iron cored, tubular permanent magnet machines and drive systems," *IEEE Transactions on Magnetics*, vol. 40, no. 5, pp. 3262-3277, September 2004.

- [12] J. Wang and D. Howe, "Design and optimisation of linear motors for reciprocating compressor," *Carbon Thrust Project Number 2003-3-51-1-1*, 2004.

- [13] J. Wang and D. Howe, "Tubular modular permanent magnet machines equipped with quasi-Halbach magnetised magnet - Part 1: Magnetic field distribution, EMF and thrust force," *IEEE Transactions on Magnetics*, vol. 41, no. 9, pp. 2470-2478, September 2005.

- [14] R. E. Clark, "Resonant linear permanent magnet actuator for compressor," PhD Thesis, University of Sheffield, 2000.

- [15] T. Ibrahim, J. Wang, and D. Howe, "Analysis of a single-phase, quasi-Halbach magnetised tubular permanent magnet motor with non-ferromagnetic support tube," *14th IET International Conference on Power Electronics, Machines and Drives, PEMD, York, United Kingdom*, vol. 1, pp. 762-766, April 2008.

CHAPTER 4

DESIGN AND OPTIMISATION OF A MOVING-IRON LINEAR MOTOR FOR RECIPROCATING COMPRESSORS USING FINITE ELEMENT ANALYSIS

4.1 Introduction

A comprehensive design optimisation for the leading design parameters of the moving-magnet linear motors have been described in Chapter 3. However, the moving-magnet linear motors employ NdFeB permanent magnet which may increase the material cost. The permanent magnets have to be circumferentially segmented as will be described in Chapter 5 in order to reduce the eddy current loss [1] where this process may increase manufacturing cost. This chapter introduces an alternative design, moving-iron linear motor as shown in Fig. 4.1 for refrigerator compressor system. The motor is evolved from the original design of Evan [2] and employ relatively cheap permanent magnet material, viz., Strontium ferrite. The ring magnets mounted on the stator are easy to manufacture [2] [3] and their resistivity is a few order of magnitude higher than that of NdFeB. Hence, eddy current loss in the magnets is negligible. Further, the moving-iron armature has a robust structure and may be optimised to have a lower mass which is conducive to improve dynamic capability of the compressor system [4].

The thrust force of linear motor, F , may be estimated by the following equation:

$$F = \frac{\pi}{2} D^2 L B Q \quad 4.1$$

where D , L , B and Q are the outer diameter, the axial length, the magnetic loading and the electric loading of the motor, respectively. As will be seen, the thrust force can be enhanced by increasing the motor size, its magnetic loading and electrical loading. Due to the use of Strontium ferrite, which has a low remanence, the magnetic loading of the motor will be reduced. To achieve the same thrust force with satisfactory efficiency, the motor size i.e. the axial length and the outer radius have to be increased. Since the ring magnet are mounted on the stator, the required volume will be much greater than that of the moving-magnet designs. However, the cost of magnet material will be much cheaper [5] [6]. The increase in electrical load can

increase thrust force capability at the expense of reduction in motor efficiency when the available slot area is fixed.

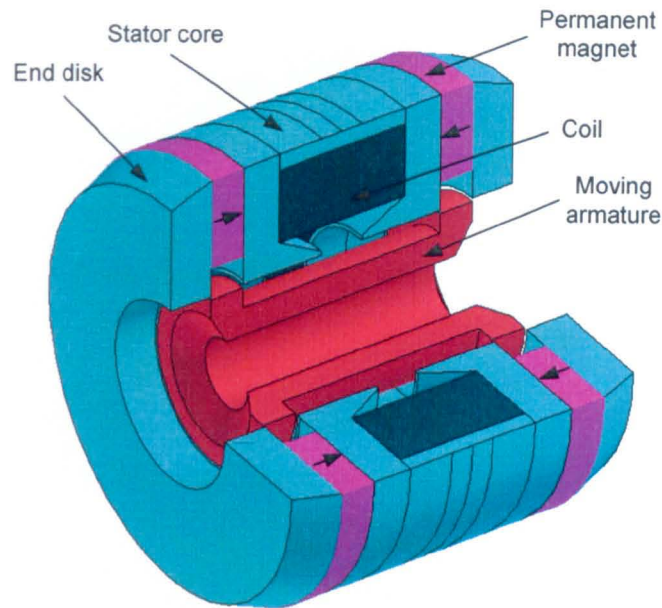


Fig. 4.1 Tubular moving-iron linear motor

Similar to the moving-magnet motor designs, the tubular stator core is made of soft magnetic composite (SMC) material, Somaloy 700, and carries a single coil. The use of an SMC material facilitates near net-shape, low cost manufacture, as well as good utilization of the available space to achieve a compact design. Also, the eddy current component of iron loss at the mains operating frequency of 50 Hz is negligible [7] [8] due to very low conductivity.

Finite element technique is employed to optimise all leading design parameters of moving-iron linear motor. Although the technique is more time consuming compared to the analytical method [9] [10], it is more accurate and can accommodate relatively complex geometries of the motor topology [11]. The design optimisation is aimed to achieve maximum efficiency at the rated output power of 88.5 W subject to volumetric constraints.

The principle of operation of the motor is similar to that of single-phase flux switching motor. A constant polarising magnetomotive force, mmf, is produced by two-ring-shaped permanent magnets, and the variable mmf that is produced by current in the coil acts in different directions relative to the polarising mmf at the two ends of the

motor. This increases the air-gap flux density at one end of the toothed moving-armature and reduces it at the other, causing the armature to move [2] back and forth as the polarity of the current changes. Since the moving armature is exposed in alternating magnetic field, SMC material should be used to minimising eddy current loss.

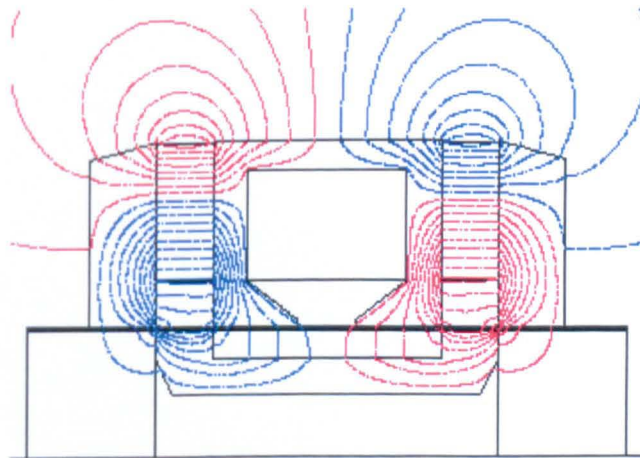
This chapter also compares the performance and the cost of material for a number of design variants, including: iron-cored quasi-Halbach magnetised motors with rectangular magnets and trapezoidal magnets, and air-cored quasi-Halbach magnetised motor with rectangular magnets.

4.2 Performance evaluations

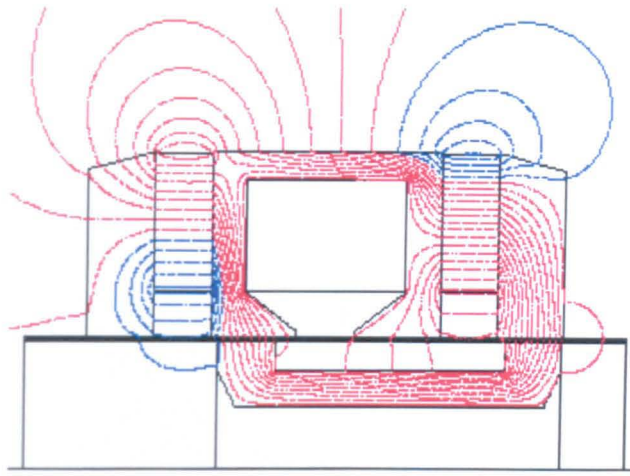
4.2.1 Open-circuit flux distribution and back-emf

Figs. 4.2 (a) and (b) show the open-circuit flux distribution of an initial design at the initial position and maximum position respectively. At the initial position, the flux distribution is symmetrical with respect to the axial centre. Hence, the coil flux-linkage is zero. As the mover moves to the right, the flux-linkage increases. However the rate of increase in the flux-linkage decreases as the mover displacement increases.

The mover moves from initial position at the constant speed and reaches the rate of stroke of 10.5 mm at $t = 0.005$ s. After this, the direction of movement is reversed, the mover return to the initial position at $t = 0.01$ s.



a. $z = 0.0$ mm



b. $z = 10.5$ mm

Fig. 4.2 Open-circuit flux distribution

Fig. 4.3 shows the back-emf waveform for the moving-iron linear motor with a constant speed in both directions. The constant speed was chosen for illustration purpose. However, the sinusoidal speed will be used for the optimisation process in order to represent the actual operating condition. As will be seen from the back-emf waveform, the induced voltage decreases rapidly when the mover displacement is greater than 5.0 mm. This indicates that 10.5 mm stroke is not appropriate for this design, or in order to improve performance for the required stroke, the motor design needs to be optimised.

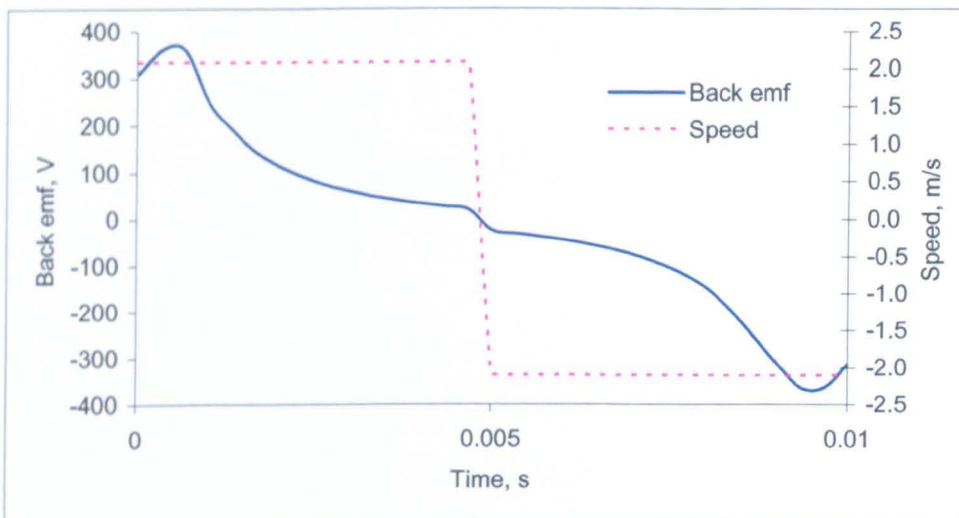


Fig. 4.3 Back-emf and constant speed of moving-iron linear motor

4.2.2 Motor efficiency

The optimisation is based on achieving maximum efficiency produced by the motor. By neglecting the eddy current and friction losses, the efficiency of the motor is calculated by the following equation:

$$\eta = \frac{P_{out}}{P_{out} + P_{fe} + P_{cu}} 100\% \quad 4.2$$

where P_{out} , P_{fe} and P_{cu} are output power, iron loss and copper loss, respectively.

The average output power, P_{out} , over an electrical period of T , is determined by:

$$P_{out} = \frac{1}{T} \int_0^T E_T(t) i_s(t) dt \quad 4.3$$

where $E_T(t)$ and $i_s(t)$ are the instantaneous of terminal voltage and motor current, respectively, obtained from finite element analysis.

If the coil resistance is not included in the finite element model, the induced voltage across the coil from finite element analysis includes inductance effect, $L \frac{di}{dt}$, and back-emf, e_w , and from equation 4.3, the output power is given by

$$P_{out} = \frac{1}{T} \int_0^T \left(L \frac{di}{dt} + e_w \right) i_s dt = \frac{1}{T} \int_0^T e_w i_s dt + \frac{1}{T} \int_{i_1}^{i_2} L i_s di \quad 4.4$$

The second terms in equation 4.4 is zero since $i_1 = i_2$ for a periodically current waveform.

The basic equation to quantify the copper loss is determined by

$$P_{cu} = i_{rms}^2 R \quad 4.5$$

where i_{rms} and R are the rms current and resistance of the winding respectively. The winding resistance, R , can be determined by

$$R = \frac{\rho l}{S} \quad 4.6$$

where ρ , l and S are the resistivity of copper at a given temperature, the length of wire and the cross-sectioned area of wire, respectively. In this study, the resistivity at nominal operating temperature of 80 °C, 0.0068e-8 Ω/m , is used.

The length of wire and the cross-sectioned area of wire are determined as follows

$$l = 2\pi r N_c \quad 4.7$$

$$S = \frac{S_a P_f}{N_c} \quad 4.8$$

where r , N_c , S_a and P_f are the average radius of the coil, the number of turns, the effective slot area and the packing factor, respectively.

From the above equations, the winding resistance is given by

$$R = 2\pi\rho \frac{r}{P_f S_a} N_c^2 \quad 4.9$$

As will be seen from equation 4.9, the resistance, R , is a function of the effective slot area, S_a , and the number of turns, N_c . They may vary with design parameters.

In the Flux-2D post processor, iron loss can be calculated based on Bertotti model [12] using transient magnetic field solution over a specified electrical period. In order to quantify the iron loss, P_{fe} , hysteresis losses coefficient, k_h , and excess loss coefficient, k_e , need to be identified. For the SMC material, Somaloy 700, conductivity, σ , is set to zero and the coefficients of k_h and k_e are determined from the manufacturer data sheet using curve fitting.

4.3 Design optimisation

4.3.1 Motor design dimensions

Fig. 4.4 shows the schematic and design parameters for the moving-iron linear motor. The relevant variables and symbol are defined as follows:

Symbol	Description
θ	Stator tooth tip under cut angle
b_0	Slot opening
G	Air-gap
H_r	Thickness of armature tube
H_{tr}	Height of armature tooth
H_m	Height of permanent magnet
H_{st}	Height of stator tooth tip
R_a	Outer radius of armature
R_e	Outer radius of stator
T_r	Width of armature tooth
T_w	Width of stator tooth
T_{ex}	Stator end disk
T_{be}	Width of armature tube cut
H_{te}	Height of stator top edge cut
T_m	Thickness of permanent magnet
T_{pw}	Tooth pitch width

In the above 16 design parameters, H_{st} , T_{be} , H_{te} and θ have insignificant influence on the motor performance and therefore, their values are fixed to 1.0 mm, 2.0 mm, 2.0 mm and 30 °, respectively. Although the force capability of the motor increases as the air-gap length decreases, its minimum value is limited by manufacture and assemblies tolerances. In this design study, the air-gap length, G , is fixed to 0.8 mm which is the same as the air-gap of the moving-magnet motors described in Chapter 3.

In order to achieve satisfactory performance, the outer radius of the stator, R_e , and the thickness of permanent magnet, T_m are increased to 55.0 mm and 10.0 mm, respectively. With the axial length of the stator core T_{pw} being the same as the moving-magnet designs, the total axial length of the stator, including the two SMC disks at both ends, has been increased to a 90.0 mm. The resulting motor size represents the maximum available volume for a typical refrigerator compressor.

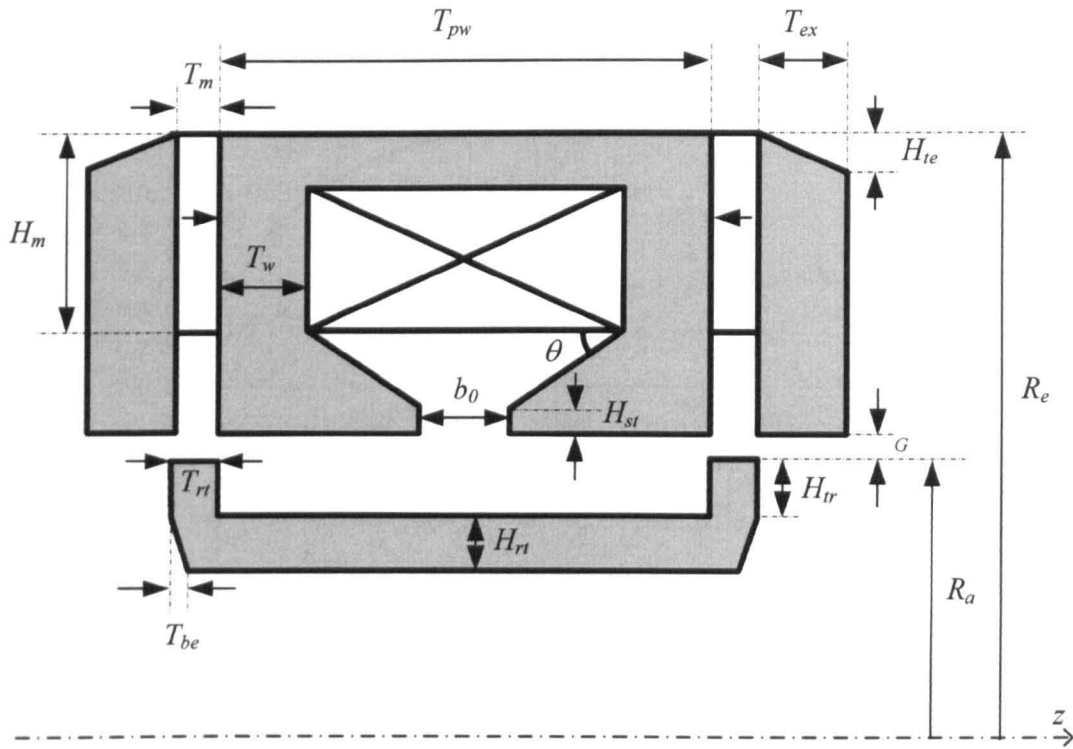


Fig. 4.4 Schematic and design parameters of a tubular moving-iron motor

The thickness of armature tube, H_{rt} , the width of stator tooth, T_w , and the thickness of the stator back-iron are determined by the maximum permissible flux density in order to avoid high level of saturation in SMC material. The maximum permissible of flux density is set to 1.15 T which is close to the knee point of the Somaloy 700 B-H curve as shown in Fig. 4.5.

The thickness of stator end disk, T_{ex} , also need to be determined in order to provide sufficiently permeable path for the coil flux when the armature is at the maximum stroke as shown in Fig. 4.2 (b). The thickness should be closed to the width of the armature tooth, T_{rt} . This is to avoid the flux travels to a large air-gap which may reduce the motor performance. In this design study, T_{ex} is initially set to 11.5 mm.

Thus, the leading design parameters which have significant influences on the motor are:

- i. Width of armature tooth, T_{rt}
- ii. Height of armature tooth, H_{tr}
- iii. Ratio of R_a/R_e
- iv. Height of permanent magnet, H_m

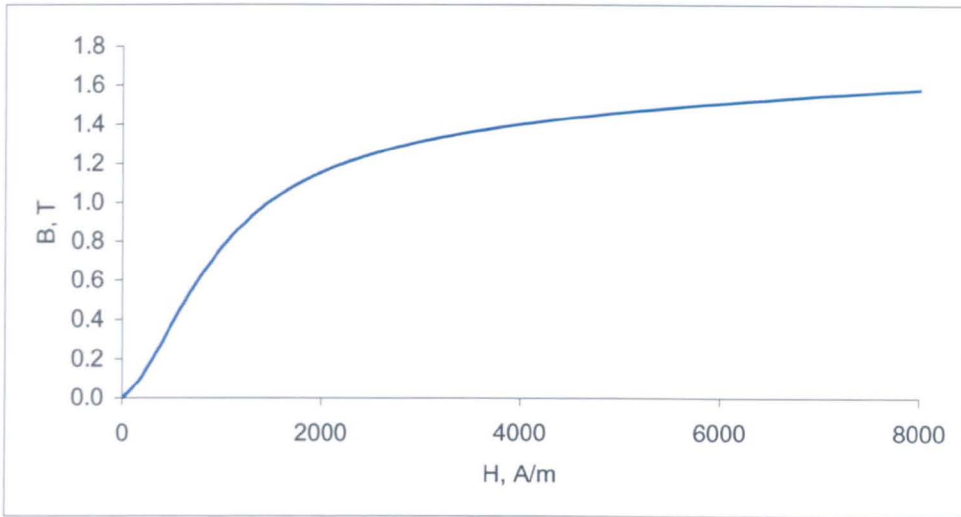


Fig. 4.5 B-H curve of Somaloy 700

The initial design dimensions and the specified operating conditions are illustrated in Table 4.1. The design optimisation of the linear motor is aimed to achieve the maximum efficiency at the rated output power, i.e., $P_{spec} = 88.5$ W under the volumetric constraint. The optimisation is initially undertaken with a fixed peak value of motor current, I_1 , and assuming sinusoidal armature velocity at 50 Hz and the rated stroke, and the resulting output power will vary as design parameters change. In order to obtain the same output power, P_{spec} , for a given set of design parameters, and by assuming the output power is proportional to the motor current, the motor current, I_{new} which yields P_{spec} , is adjusted using the following formula:

$$I_{new} = \frac{P_{spec}}{P_1} I_1 \tag{4.10}$$

Table 4.1 Initial dimension parameters and operational conditions

Description of parameter	Value	Units
Air-gap, G	0.8	mm
Height of armature tooth, H_{tr}	5.0	mm
Height of stator tooth tip, H_{st}	1.0	mm
Outer radius of armature, R_a	20.0	mm
Outer radius of stator, R_e	55.0	mm
Stator tooth tip under cut angle, θ	30	°
Thickness of armature tube, H_{rt}	6.0	mm

Thickness of permanent magnet, T_m	10.0	mm
Tooth pitch width, T_{pw}	40.0	mm
Width of armature tooth, T_{rt}	10.0	mm
Width of stator tooth, T_w	6.0	mm
Output power, P_{out}	88.5	W
Rated armature stroke, X_m	10.5	mm
Rms voltage supply, V_{rms}	230.0	V
Frequency, f	50.0	Hz
Stator core material	Somaloy 700	-
Remanence of Strontium ferrite, B_{rem}	0.396	T

With the new current, I_{new} , the motor performance is calculated again. Fig. 4.6 shows the variation of initial and adjusted motor current with height of the armature tooth. The resulting output powers are shown in Fig. 4.7. As will be seen, with the fixed peak current of 0.5 A, the output power varies slightly with the design parameter and is below the rated value of 88.5 W. Thus the motor current has to be increased proportionally. With the adjusted current values, the efficiency of the motor is evaluated by finite element simulations, and results are shown in Fig. 4.8. As will be seen, the level of current adjustment is relatively small, and hence, the assumption that the output power is proportional to the current is justified. The same procedure is used to determine efficiency variations with other design parameters.

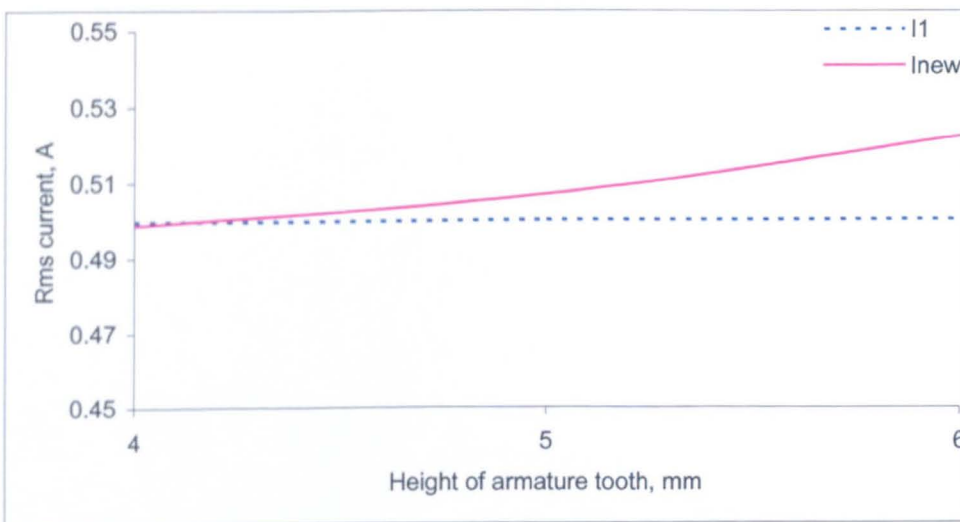


Fig. 4.6 Variation of motor current with height of armature tooth

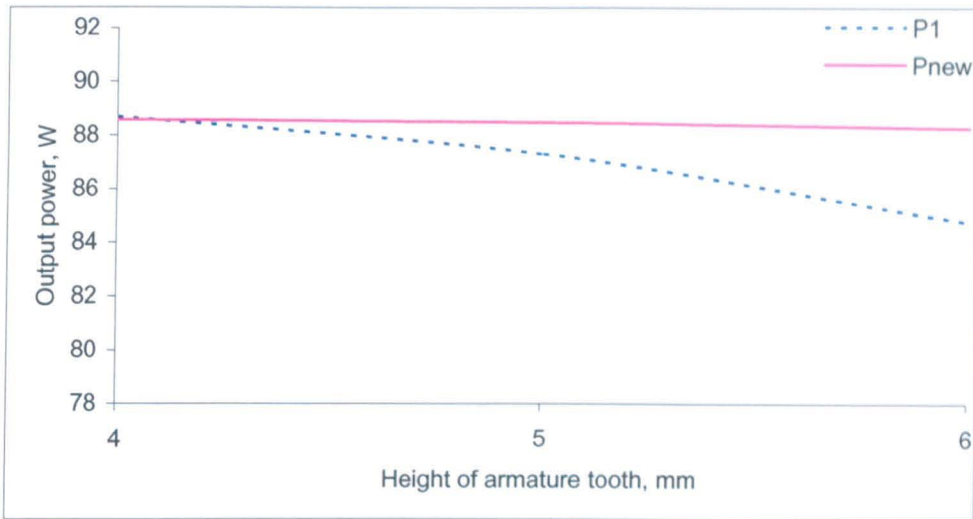


Fig. 4.7 Variation of output power with height of armature tooth

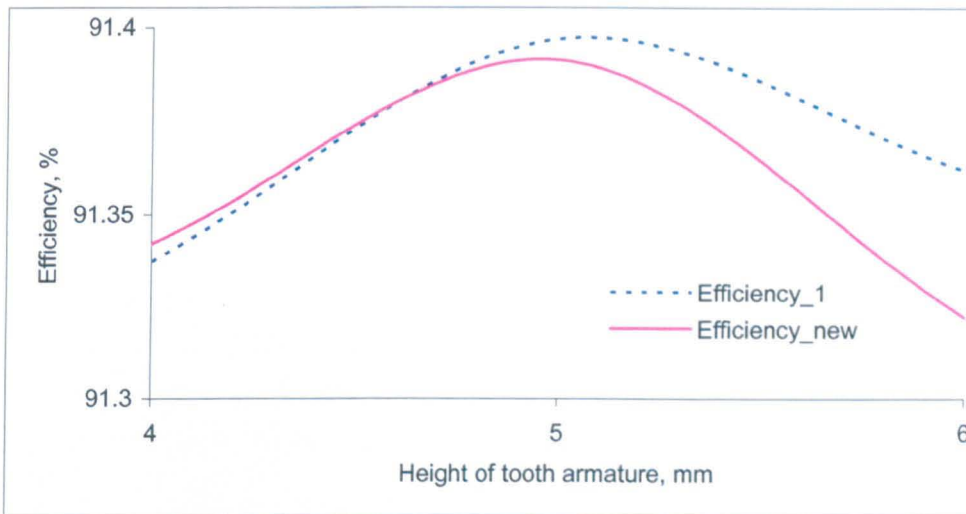


Fig. 4.8 Variations of efficiency with height of armature tooth

4.3.2 Influence of width of armature tooth, T_{rt}

The width of armature tooth, T_{rt} provides the main path for magnetic flux to flow from the stator to the armature. If the tooth is too narrow, the flux cannot path through easily to the armature, which reduces flux-linkage and motor efficiency. However, if the tooth is too wide, the saliency effect is reduced which affect the rate of change of flux, and results in a poor performance of the motor.

With other leading parameters fixed to their initial values, the armature tooth width is varied from 9.0 mm to 11.0 mm and the resulting variation of motor efficiency is shown in Fig. 4.9. As will be seen, at $T_{rt} = 10.0$ mm, the motor produces the maximum efficiency, 90.56 %. It should be noted that the optimal T_{rt} coincides with the thickness of the permanent magnet disk, T_m .

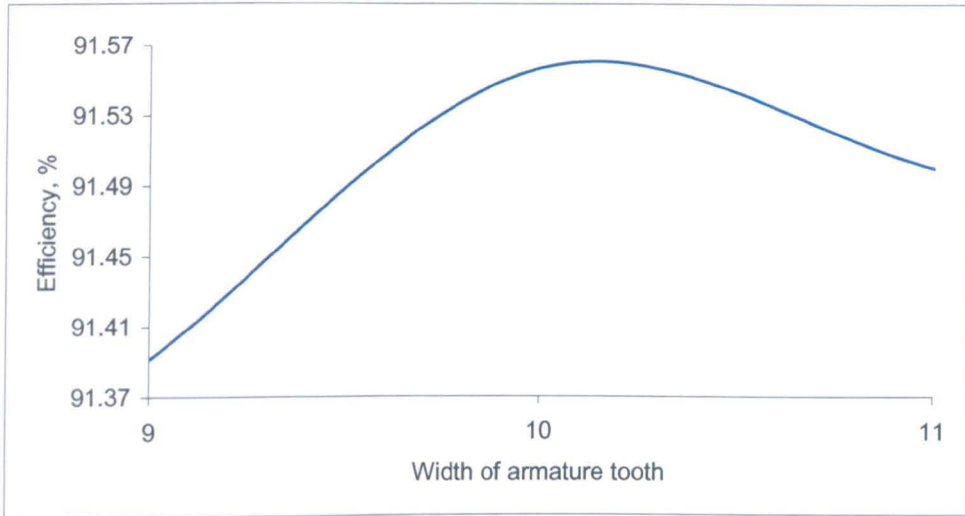


Fig. 4.9 Variation of efficiency with influence of width of armature tooth

Fig. 4.10 shows the variation of copper loss and iron loss with T_{rt} . The iron loss includes the losses in the stator core, in the two end disks, and in the moving armature. As can be seen, the iron loss increases slightly with T_{rt} , while the copper loss decreases with T_{rt} . At $T_{rt} = 10.0$ mm, the sum of the two losses is at minimum.

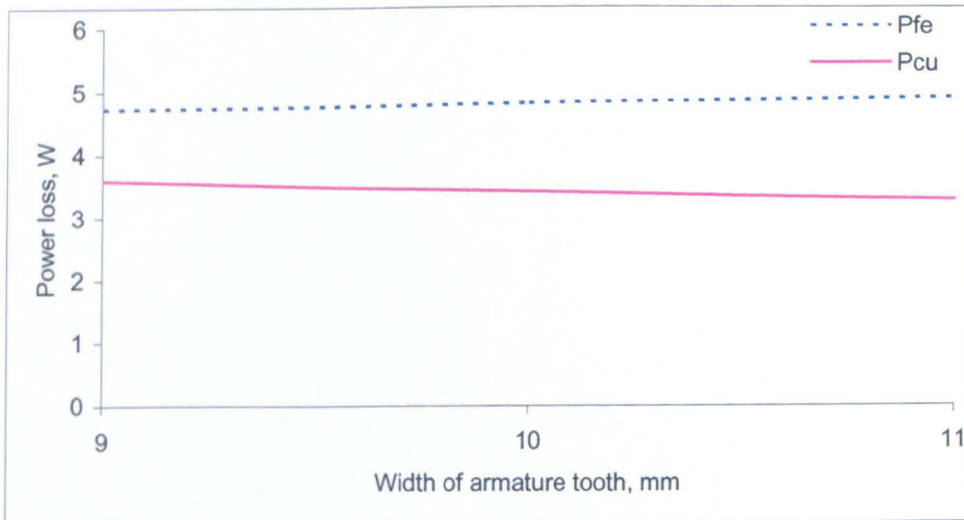


Fig. 4.10 Variation of iron loss and copper loss with influence of width of armature tooth

4.3.3 Influence of height of armature tooth, H_{tr}

The armature tooth height has a significant impact on the performance of the motor. For example, if the armature tooth height is too small again the saliency effect is not significant which reduces the rate of change of flux and results in poor performance. If the armature tooth is too high, reluctance is increased which also leads to a low performance.

Fig. 4.11 shows the variation of motor efficiency with H_{tr} , when T_{rt} is set to its optimal value of 10.0 mm, the other parameters unchanged. The maximum motor efficiency, 91.56 %, occurs at $H_{tr} = 5.0$ mm.

The iron loss decreases when the height of armature tooth increases as shown in Fig. 4.12. This is due to the decrease in flux density in the stator and armature, as the reluctance increases. Meanwhile, the copper loss increases when the height of armature tooth is increased. This is because the motor current has to increase in order to provide the same output power.

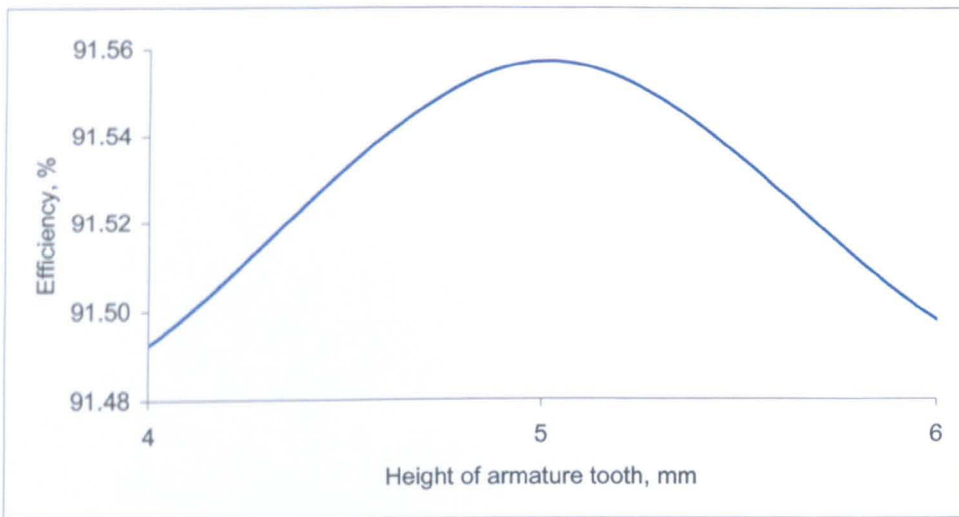


Fig. 4.11 Variation of efficiency with influence of the height of armature tooth

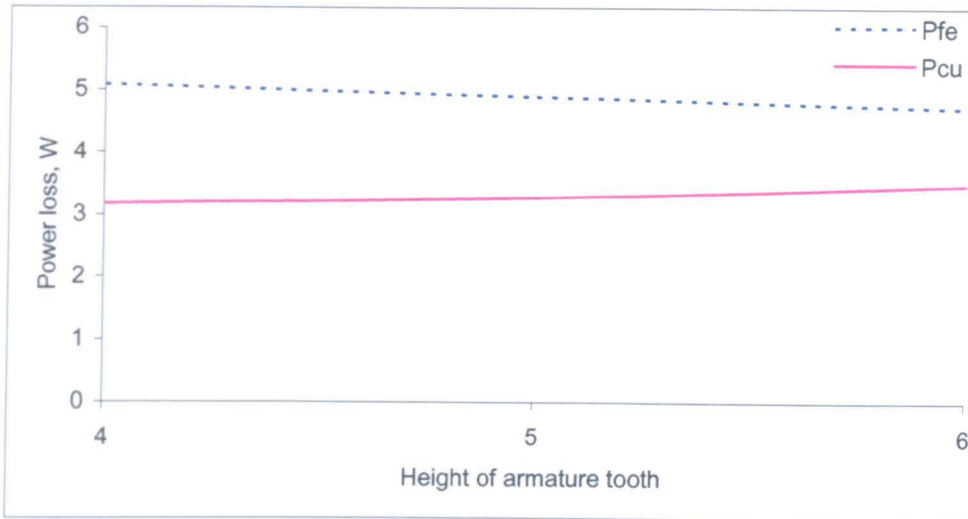


Fig. 4.12 Variation of iron loss and copper loss with influence of height of armature tooth

4.3.4 Influence of R_a/R_e

The ratio of R_a/R_e determines the balance between electrical and magnetic loadings of the motor. This balance is important in order to achieve maximum performance. Increase in the outer radius of the armature, results in a great change of flux-linkage but reduces electrical loading since the slot area becomes less. In addition, the magnetic flux due to permanent magnets also reduces due to the reduction of the magnet volume.

Initially, the height of the magnet, H_m , varies with changes of the inner radius of the coil as shown in Fig. 4.4. The R_a/R_e ratio is varied from 0.364 to 0.418 when H_{tr} and T_{rt} are set to their optimal values. As will be seen from Fig. 4.13, the maximum efficiency, ~ 91.60 % is obtained at $R_a/R_e = 0.4$.

The copper loss reduces slightly when the ratio of R_a/R_e is increased as shown in Fig. 4.14. As R_a/R_e increases although the slot area decreases which tends to increase the motor resistance, the coil flux-linkage and back-emf per turn increase. The motor current required to achieve the rated output power decreases. Thus, the combined effect results in very slight decrease in copper loss. The iron loss increases slightly when the ratio of R_a/R_e is increased. This is mainly due to the volume of the armature in which flux density varies rapidly as the armature moves is increased, resulting in a higher iron loss.

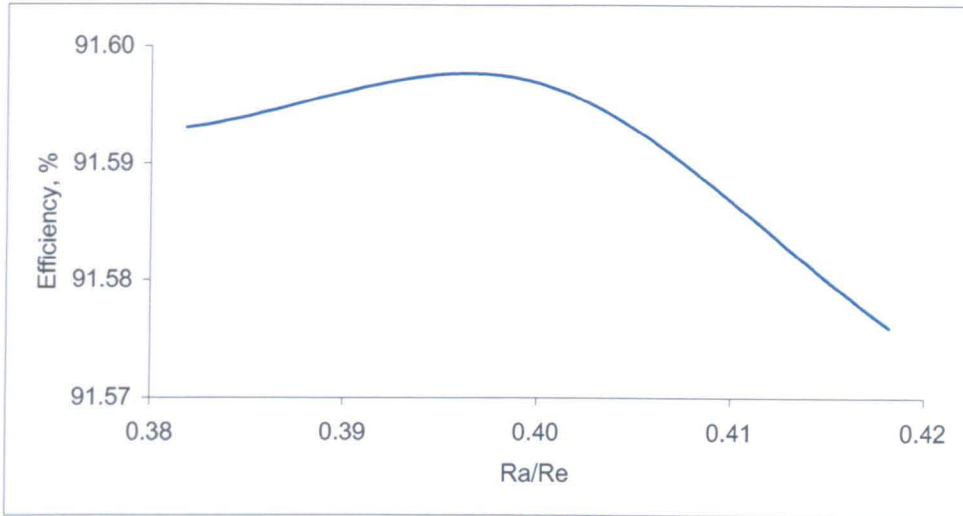


Fig. 4.13 Variation of efficiency with R_a/R_e

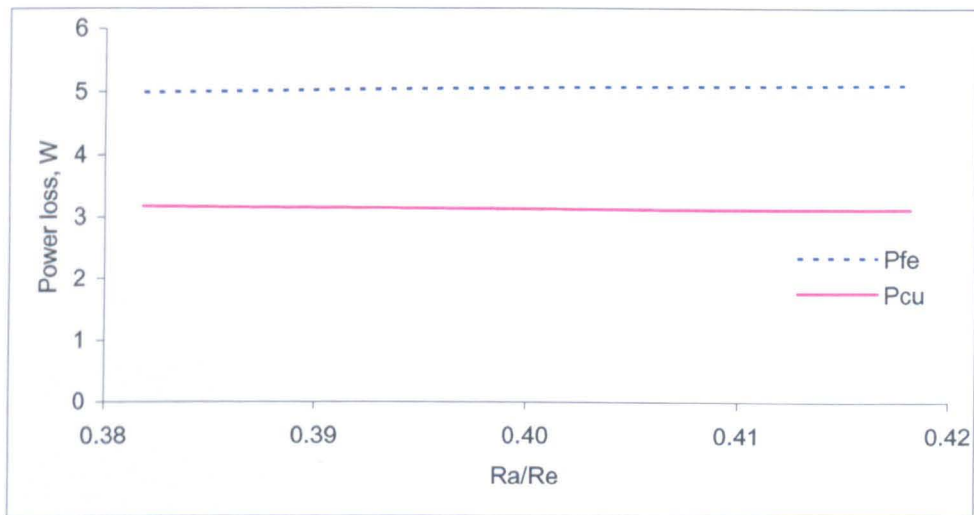


Fig. 4.14 Variation of iron loss and copper loss with R_a/R_e

4.3.5 Influence of height of permanent magnet, H_m

Theoretically, increases the height of permanent magnet, H_m , will produce more output power and, hence better motor efficiency. The disadvantage of this is that the cost of permanent magnet material will also increase. However Strontium ferrite is relatively cheap and the increase in magnet material cost is not significant.

Fig. 4.15 shows the variation of motor efficiency with the height of magnet, H_m , when H_w , T_{rt} and R_a/R_e are at their optimal values. As will be seen, the motor efficiency

continues to increase as H_m increase. However, the maximum H_m value of 32.0 mm is limited by R_d/R_e ratio, and the motor produces the maximum efficiency, 92.10 %.

Fig. 4.16 shows the variation of the copper loss and iron loss with the magnet height, H_m . The copper loss reduces when the height of magnet increases. This is due to the reduction of motor current for the same output power. The iron loss increases slightly when the magnet height is increased due to increase in flux density in the stator and moving armature.

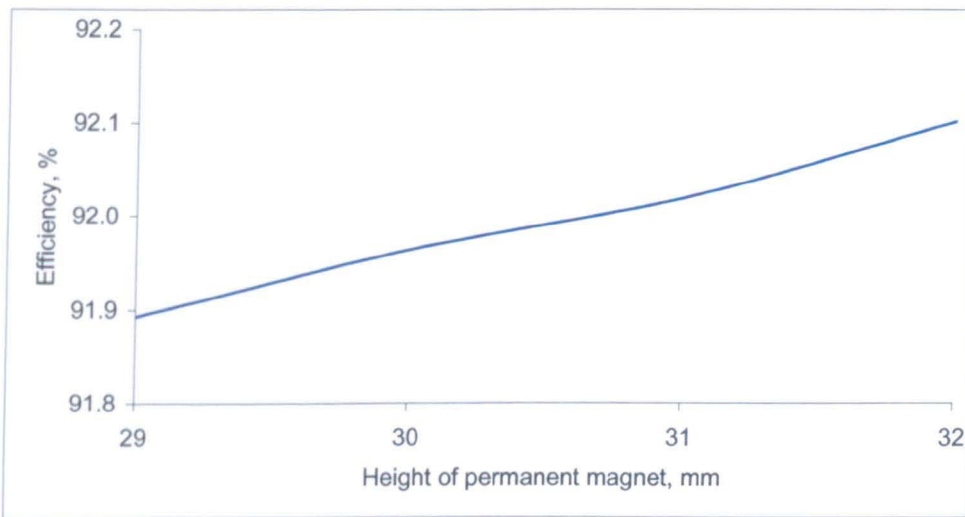


Fig. 4.15 Variation of efficiency with height of permanent magnet

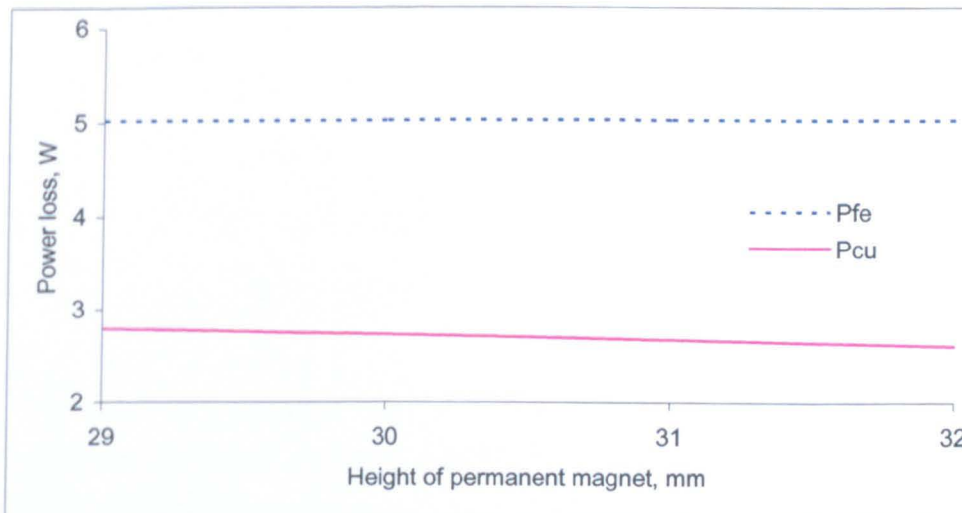


Fig. 4.16 Variation of iron loss and copper loss with height of permanent magnet

4.4 Two parameters optimisation

The four leading design parameters discussed in sections 4.3.2 to 4.3.5 are optimised individually using finite element analysis. However, one parameter may influence other parameters in term of optimal performance of the motor. In order to check if the above design process reaches an optimal design, two leading parameters varied simultaneously. As has previously stated, only three leading design parameters are considered for optimisation, i.e. width of armature tooth T_{rt} , height of armature tooth H_{rt} and the ratio of R_d/R_e , and the height of magnet, H_m varies with the inner radius of the coil.

Fig. 4.17 shows the variation of motor efficiency with T_{rt} and H_{rt} and other parameters being the same as stated in Table 4.1. As will be observed, the motor produces the maximum efficiency, 91.56 % at $T_{rt} = 10.0$ mm and $H_{rt} = 5.0$ mm. This result T_{rt} coincides with those obtained previously, which implies the influence of one parameter on the optimal design on the other is insignificant.

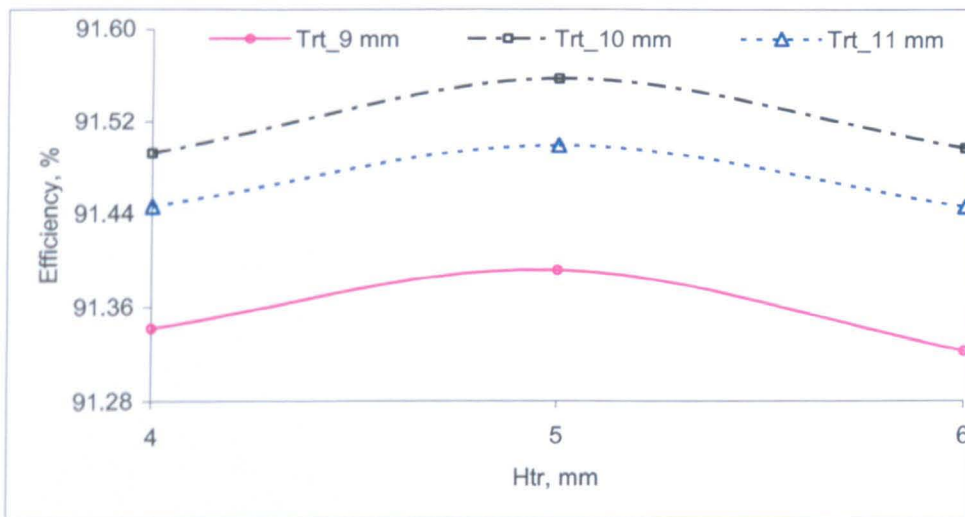


Fig. 4.17 Influence of T_{rt} and H_{rt} on efficiency

Fig. 4.17 shows the variation of motor efficiency with T_{rt} and R_d/R_e at the optimal value of $H_{rt} = 5.0$ mm and other parameters being the same as stated in Table 4.1. As will be seen, the optimal dimensions for T_{rt} and R_d/R_e are 10.0 mm and 0.4, respectively, which yields the maximum motor efficiency of 91.6 %.

Based on the results shown in Figs. 4.19 and 4.20, the optimal dimensions of T_{rt} , H_{tr} , and R_a/R_e are essentially the same as those obtained in sections 4.3.2, 4.3.3 and 4.3.4.

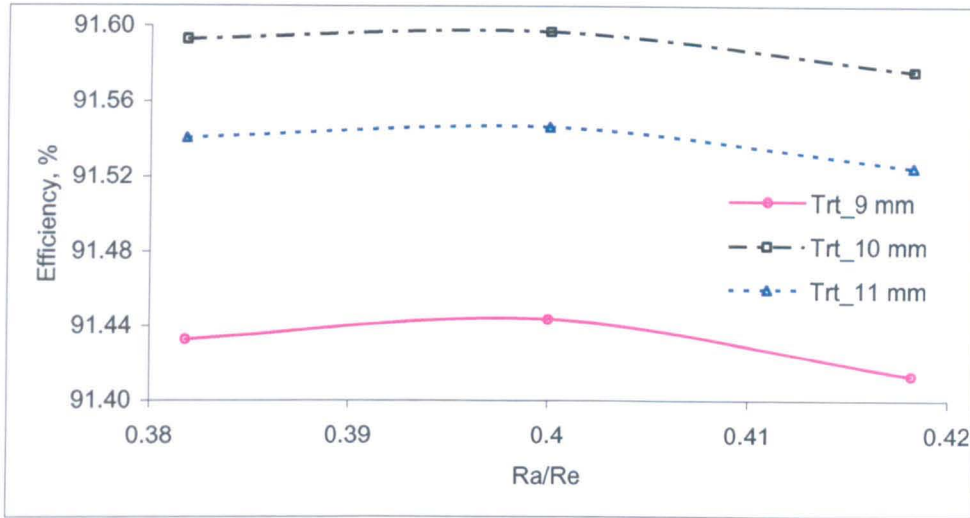


Fig. 4.18 Influence of T_{rt} and R_a/R_e on efficiency

4.5 Comparison material cost and performance

To evaluate the relative merits of the moving-iron motor design, material costs and performance of four design variants, viz.; iron-cored quasi-Halbach magnetised motor with rectangular magnets; iron-cored quasi-Halbach magnetised motor with trapezoidal magnets, air-cored quasi-Halbach magnetised motor with rectangular magnets and moving-iron linear permanent magnet motor are compared.

All the linear motors were optimised and employs soft magnetic composite material, Somaloy 700 for the stator core. The stator carries a single coil supplied from 240 Vrms at 50 Hz. Rare-earth NdFeb permanent magnet is employed in all motors except for the moving-iron linear motor which uses low cost permanent magnet material Strontium ferrite.

The price and the density of materials used for comparison are tabulated in Table 4.2. The price for each material is in US dollars per kilogram. As will be seen, the price of NdFeB permanent magnet is 15 times higher than that of Strontium ferrite and the most expensive material.

The volumes of each material used in four designs are given in Table 4.3. The moving-iron linear motor requires the largest volume of Strontium ferrite permanent magnet. This is due to the fact that the thickness of the magnets and the size of the stator has to be increased in order to achieve reasonably high efficiency. In addition, the magnets are placed on the stator, and hence has a large volume. For moving-magnet motors, air-cored quasi-Halbach magnetised motor with rectangular magnets uses more rare-earth NdFeB material than the other two. This is because the optimal R_m/R_e ratio of the air-cored motor ($R_m/R_e = 0.42$) is higher than that of the iron-cored designs ($R_m/R_e = 0.36$). The magnet volume of iron-cored quasi-Halbach magnetised motor with rectangular magnets and iron-cored quasi-Halbach magnetised motor with trapezoidal magnets are very close because both motors have the same axial length and virtually identical optimal R_m/R_e ratios.

Table 4.2 Price and density of materials

Material	Price (2007) USD/kg	Density kg/m ³
Somaloy 700	3.69	7320
NdFeB	45.00	7500
Strontium ferrite	3.00	4800
Copper	8.00	8230
Mild steel	1.00	7800

Somaloy 700 material is employed for the stator core of all four motors and the plunger of moving-iron motor. It is evident that the moving-iron motor needs more Somaloy material, due to the motor size being increased and the additional material for the plunger. For all moving-magnet linear motors, the volume of Somaloy material decreases as the optimal R_m/R_e ratio increases. The same trend is observed for the volume of copper being used.

Mild steel is used to support permanent magnets in iron-cored quasi-Halbach magnetised motors with rectangular or trapezoidal magnets. As will be observed from Table 4.3, the iron-cored quasi-Halbach magnetised motor with rectangular magnets uses slightly more mild steel compared to the iron-cored quasi-Halbach magnetised motor with trapezoidal magnets, since it requires a thicker tube for a given peak flux density.

Table 4.3 Volume of motors

Linear motor	Magnet m ³	Somaloy 700 m ³	Mild steel m ³	Copper m ³	Total m ³
Iron-cored quasi-Halbach magnetised motor with rectangular magnets	2.43E-05	1.71E-04	1.35E-05	1.46E-04	3.55E-4
Iron-cored quasi-Halbach magnetised motor with trapezoidal magnets	2.43E-05	1.71E-04	1.24E-05	1.46E-04	3.54E-4
Air-cored quasi-Halbach magnetised motor with rectangular magnets	2.91E-05	1.65E-04	-	1.30E-04	3.24E-4
Moving-iron permanent magnet motor	1.26E-04	3.98E-04	-	1.37E-04	6.60E-4

Table 4.4 shows the material costs for each linear motor using the data in Table 4.2 and Table 4.3. As will be observed, the total material cost for each motor is virtually the same. For moving-magnet linear motors, the material cost is dominated by rare-earth NdFeB permanent magnet and copper.

However, for moving-iron linear motor, the cost is mainly contributed from Somaloy 700 and copper. This is due to a large stator volume. In contrast, the cost of Strontium ferrite is less significant.

Table 4.4 Material costs

Linear motor	Magnet USD	Somaloy 700 USD	Mild steel USD	Copper USD	Total price USD
Iron-cored quasi-Halbach magnetised motor with rectangular magnets	8.22	4.62	0.106	9.61	22.55
Iron-cored quasi-Halbach magnetised motor with trapezoidal magnets	8.22	4.62	0.096	9.61	22.54
Air-cored quasi-Halbach magnetised motor with rectangular magnets	9.81	4.47	-	8.57	22.85

Moving-iron permanent magnet motor	1.81	10.74	-	9.01	21.56
------------------------------------	------	-------	---	------	-------

All the linear motors have been optimised against the same rated output power, 88.5 W. The efficiency, η , iron loss, P_{fe} , and copper loss, P_{cu} as well as moving mass, m , of all the linear motors have been shown in Table 4.5.

Table 4.5 Efficiency, output power, losses, and moving mass

Linear motor	η %	P_{out} W	P_{fe} W	P_{cu} W	m kg
Iron-cored quasi-Halbach magnetised motor with rectangular magnets	94.23	88.61	2.82	2.60	0.29
Iron-cored quasi-Halbach magnetised motor with trapezoidal magnets	94.24	88.60	2.79	2.63	0.28
Air-cored quasi-Halbach magnetised motor with rectangular magnets	93.50	88.67	2.38	3.78	0.22
Moving-iron permanent magnet motor	92.10	88.79	5.01	2.60	0.33

Based on the data tabulated in Table 4.5, the iron-cored quasi-Halbach magnetised motor with trapezoidal magnets has slightly higher efficiency than iron-cored quasi-Halbach magnetised motor with rectangular magnets. Its armature mass is also slightly lower than that of the iron-cored motor with rectangular magnets. However, its manufacturing cost may be higher due to the process of cutting trapezoidally shaped magnets [13].

Air-cored quasi-Halbach magnetised motor with rectangular magnets has the advantage of low moving mass which can improve the dynamic capability of the compressor. The moving-iron linear motor is ~ 2 % lower in efficiency than the moving-magnet candidates. This together with a large size and weight makes it less attractive for the linear compressor application.

Based on the data in Table 4.5, it is difficult to select the best candidate since their cost and efficiency are quite close to each other. However, for the light weight of

armature and ease of manufacturing, the air-cored quasi-Halbach magnetised magnet with rectangular magnets has been selected for prototyping.

4.6 Conclusions

Finite element technique has been used to optimise the design of the moving-iron linear motor. It has been shown that in order to achieve satisfactory efficiency, the volume of the motor has to be increased significantly. However with the available space on a typical household refrigerator compressor, the efficiency of the moving-iron motor is still much lower than the moving-magnet designs. It has also been shown that the material cost of the moving-iron motor is very close to those of the moving-magnet motors. However, its manufacturing cost is likely to be lower, since the permanent magnets have a simple shape, and will be easier for assembly.

An extensive comparison of performance and material costs for four design variants have been carried out and based on the light weight of armature which is conducive to improve dynamic capability of the compressor system and ease of manufacturing, the air-cored quasi-Halbach magnetised magnet with rectangular magnets has been selected for prototyping.

References

- [1] J. Chai, J. Wang, and D. Howe, "Evaluation of eddy current loss in tubular permanent magnet motors by three-dimensional finite element analysis," *Proceedings of XVII International Conference on Electrical Machines (ICEM2006)*, Paper ID: PSA1-12, Chania, Greece, September 2006.
- [2] S. A. Evans, I. R. Smith, and J. G. Kettleborough, "Permanent magnet linear actuator for static and reciprocating short stroke electromechanical systems," *IEEE/ASME Transactions on Mechatronics*, vol. 6 , no. 1, pp. 36-42, March 2001.
- [3] Z. S. Al-Otaibi and A. G. Jack, "Utilising SMC in single-phase permanent magnet linear motors for compressor applications," *14th IET International*

Conference on Power Electronics, Machines and Drives, PEMD, York, UK, vol. 1, pp. 752-753, 2-4 April 2008.

- [4] T. Ibrahim, J. Wang, and D. Howe, "Analysis of a single-phase, quasi-Halbach magnetised tubular permanent magnet motor with non-ferromagnetic support tube," *14th IET International Conference on Power Electronics, Machines and Drives, PEMD, York, United Kingdom, vol. 1, pp. 762-766, April 2008.*

- [5] A. D. P. Juliani, D. P. Gonzaga, J. R. B. A. Monteiro, M. L. Aguiar, and A. A. Oliveira, "Magnetic field analysis of a brushless DC motor comparing ferrite and NdFeB magnets on rotor," *Proceedings of IEEE Conference on Industrial Electronics and Applications ICIEA 2007, Harbin, China, pp. 260 - 264, May 2007.*

- [6] N. Bianchi, S. Bolognani, F. Tonel, and Page(s):, "Design criteria of a tubular linear IPM motor," *Proceedings of IEEE International Electric Machines and Drives Conference IEMDC 2001, Massachusetts, USA, pp. 1 - 7, June 2001.*

- [7] T. Ibrahim, J. Wang, and D. Howe, "Iron loss calculation in a reciprocating tubular permanent magnet motor with soft magnetic composite," *Proceeding of XVII International Conference on Electrical Machines, ICEM2006, Chania, Greece, September, 2006.*

- [8] A. G. Jack, Z. S. Al-Otaibi, and M. Persson, "Alternative designs for oscillating linear single-phase permanent magnet motors using soft magnetic composites," *International Conference on Electrical Machines and Drives, ICEMS 2006, Nagasaki, Japan, November 2006.*

- [9] J. Wang, D. Howe, and G. W. Jewell, "Analysis and design optimisation of an improved axially magnetised tubular permanent magnet machine," *IEEE Transactions on Energy Conversions, vol. 19, no. 2, pp. 289-295, June 2004.*

- [10] J. Wang, G. W. Jewell, and D. Howe, "A general framework for the analysis and design of tubular linear permanent magnet machines," *IEEE Transactions on Magnetics, vol. 35, no. 3, pp. 1986-2000, May 1999.*

- [11] J. Wang, D. Howe, and M. Inoue, "Magnetic field distribution of quasi-Halbach magnetised cylinder for tubular permanent magnet machines," *Proceedings of 4th International Symposium on Linear Drives and Industry Applications, LDIA 2003, Birmingham, United Kingdom*, pp. 481-484, September 2003.
- [12] Cedrat, "FLUX 2D and 3D User Application Manual," 2005.
- [13] T. Ibrahim, J. Wang, and D. Howe, "Analysis of a short-stroke, single-phase tubular permanent magnet actuator for reciprocating compressors," *6th International Symposium on Linear Drives for Industrial Applications, LDIA2007, Lillie, France*, September 2007.

CHAPTER 5

ANALYSIS OF EDDY CURRENT LOSS AND IRON LOSS IN TUBULAR PERMANENT MAGNET LINEAR MOTORS USING FINITE ELEMENT METHOD

5.1 Introduction

Usually, the eddy current effect in permanent magnets is neglected and the assumption is acceptable for ferrite magnets since their conductivity is a very low, and suitable for a low speed applications [1] [2] [3]. However, in the linear motor design described in Chapter 3, rare-earth permanent magnets such as NdFeB have been used because their high energy product, which is conducive to producing a high trust force density but they have a relatively high electrical conductivity. When the armature reciprocates, the variation of the working points of the permanent magnets and the excitation current will induce eddy currents flow circumferentially in moving permanent magnets and the support tube [4] [5]. The eddy current loss in the permanent magnets will contribute to temperature rise of the linear motor, which may affect the motor performance.

In order to reduce the eddy current loss, circumferential segmentation of the permanent magnets and the supporting tube will be employed, an their effectiveness will be analysed using two- and three-dimensional finite element techniques. The two-dimensional (2-D) finite elements method is employed to quantify the eddy current loss in ring and slit ring permanent magnets as well as the supporting tube as shown in Figs. 5.1 (a) and (b). The significant advantage of the two-dimensional analysis is less time consuming compared to the three-dimensional analysis. However, the two-dimensional analysis leads to overestimation of the eddy current losses [5]. Thus, the three-dimensional finite element analysis is necessary to quantify the eddy current loss more accurately and also to illustrate the influence of circumferentially segmenting the magnets and supporting tube, as shown in Figs. 5.1 (c) and (d) [4], on the loss.

This chapter also describes the calculation of the iron loss in the SMC stator core of the iron-cored quasi-Halbach magnetised motor with rectangular magnets using two-dimensional time-stepped axi-symmetric finite element analysis. The iron loss is evaluated under various armature velocity profiles, on both no-load and on-load. The

influence of the electrical conductivity of the SMC material on the iron loss of the tubular motor has also been investigated.

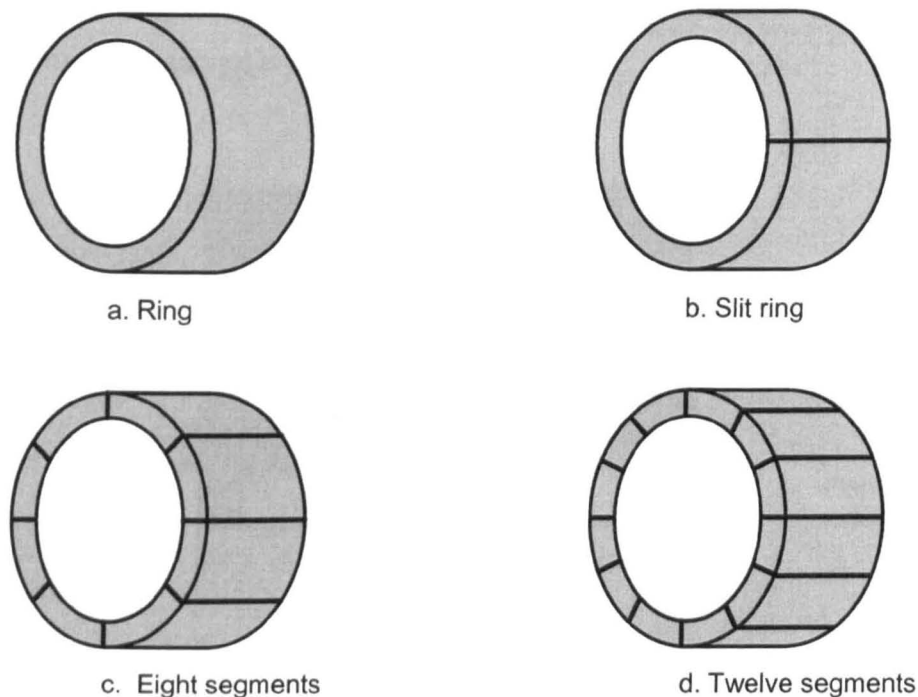


Fig. 5.1 Magnet and supporting tube configurations

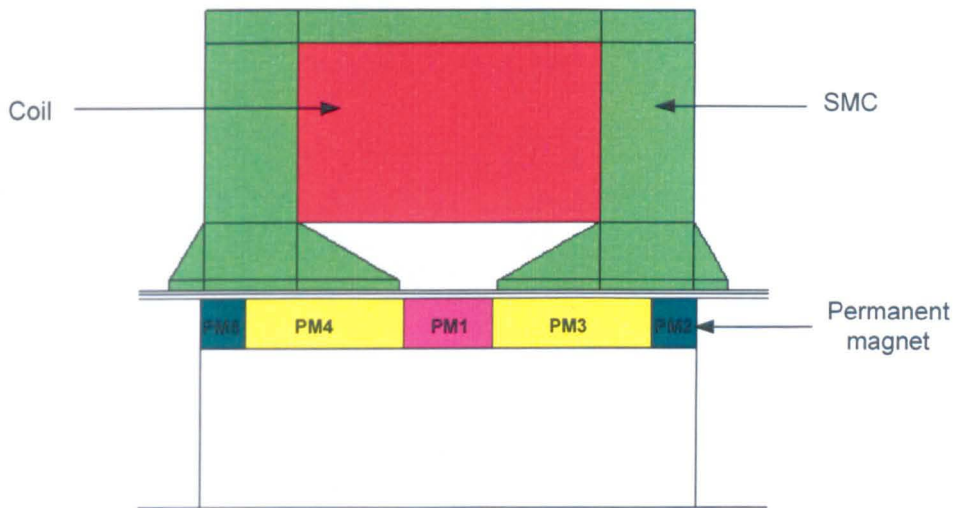
5.2 Eddy current loss

5.2.1 Two- and three dimensional finite element models

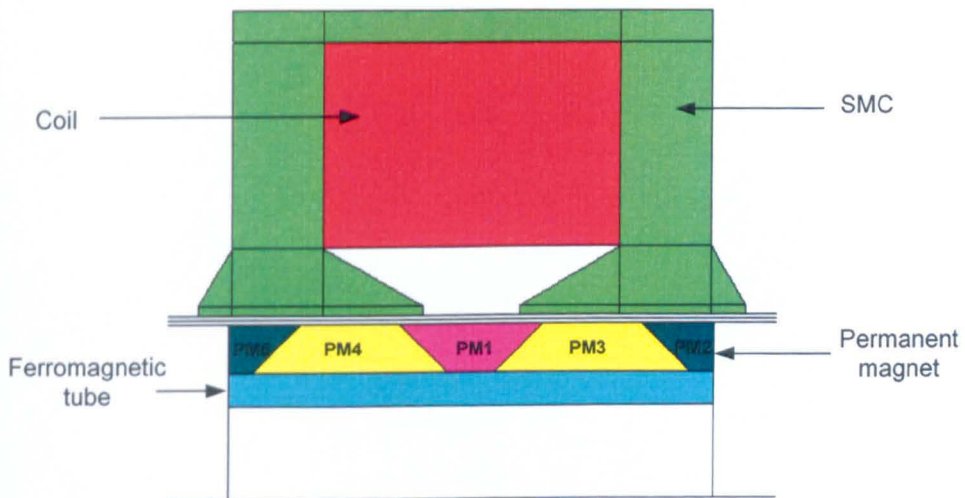
Fig. 5.2 shows the 2-D axis-symmetrical cylindrical model of the tubular permanent magnet linear motors which are used to quantify the eddy current loss in ring and slit permanent magnet configurations. As will be seen the supporting tube in Fig. 5.2 (a) is non-ferromagnetic and non-conducting material, and can be represented as air. However, for the iron-cored quasi-Halbach magnetised motor with trapezoidal magnets as shown Fig. 5.2 (b), the analysis of eddy current loss in the supporting tube needs to be considered, since the mild-steel supporting tube can induce eddy current.

Each radially or axially magnetised ring magnet and the ferromagnetic supporting tube is modelled as a conducting region in the 2-D axi-symmetrical finite element model. The terminal effect of the conducting region is represented by a resistance connected in parallel with the conductor M, as shown in Fig. 5.3. For a complete ring magnet or supporting tube, the induced eddy current will flow in circumferential

direction. The resistance is zero. Meanwhile, for a ring magnet or support tube with a slit, the induced current cannot flow in a complete circle, and this effect is represented by an infinite resistance. In the actual finite element model, the value of the resistor for ring and slit are $1e-10 \Omega$ and $1e10 \Omega$ respectively, and the resistivity of the permanent magnet is set to $0.16e-5 \Omega/m$.



a. Air-cored quasi-Halbach magnetised motor with rectangular magnets



b. Iron-cored quasi-Halbach magnetised motor with trapezoidal

Fig. 5.2 2-D axis-symmetrical cylindrical model linear motors

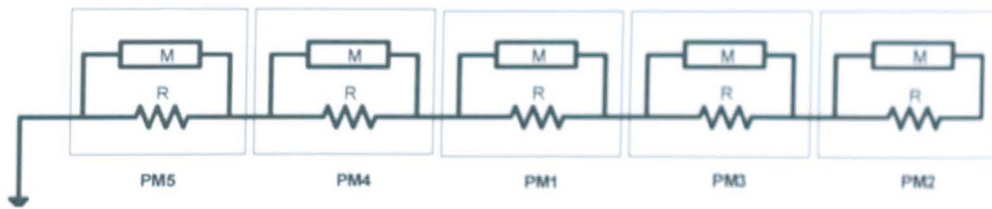
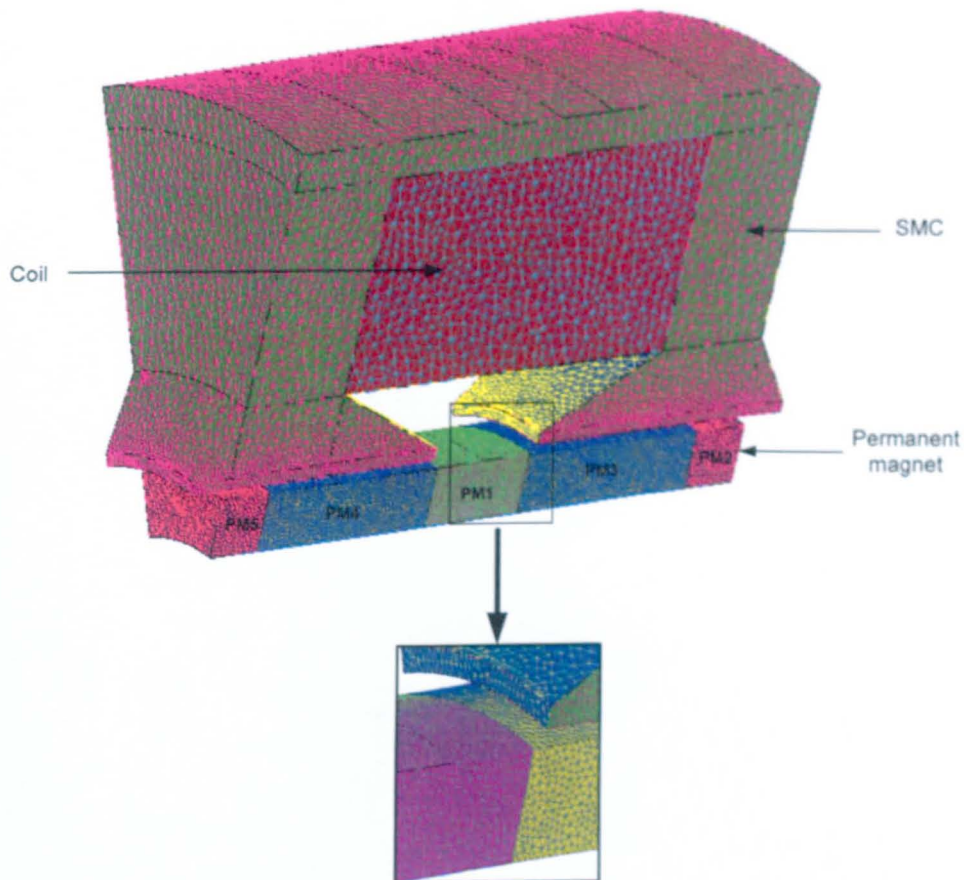
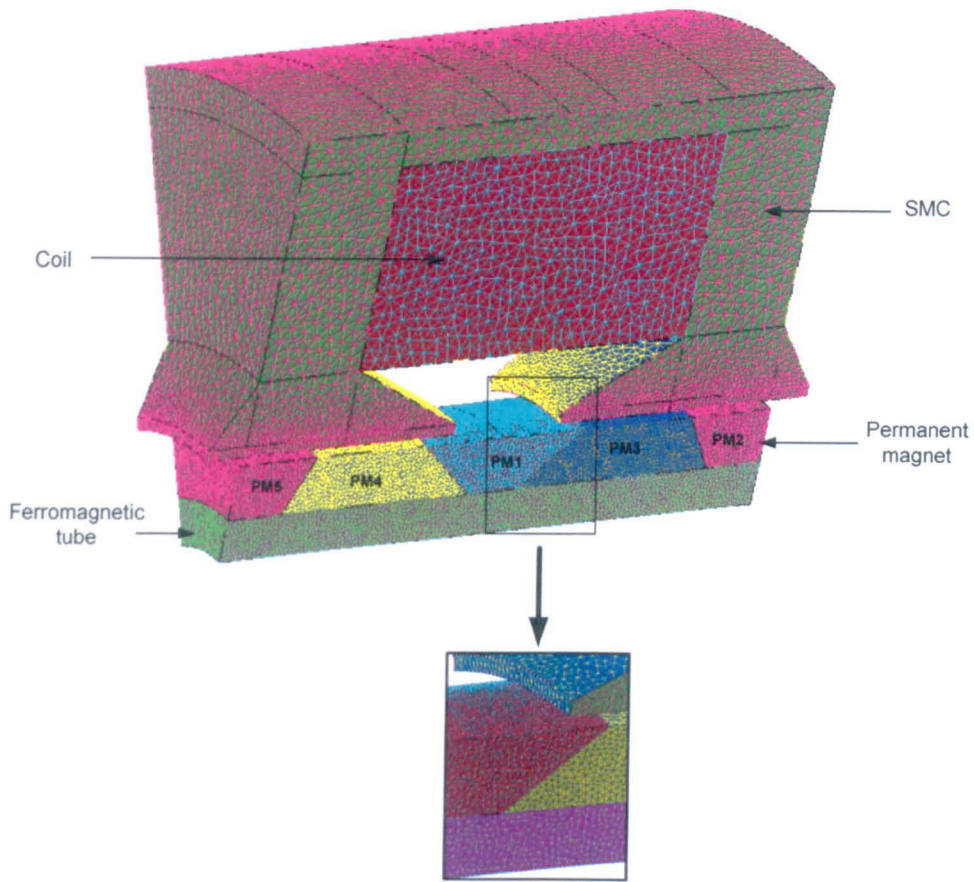


Fig. 5.3 Circuit of 2-D model

Fig. 5.4 shows the three-dimensional (3-D) meshed models of the linear motors, which are used to quantify eddy current loss in circumferentially segmented permanent magnets and the supporting tube. The magnet and the tube are segmented circumferentially into 8 and 12 pieces as shown in Figs. 5.1 (c) and (d). Only one eighth and one twelfth of the motors have to be analysed due to symmetry.



a. Air-cored quasi-Halbach magnetised motor with rectangular magnets



b. Iron-cored quasi-Halbach magnetised motor with trapezoidal magnets

Fig. 5.4 3-D meshed model linear motors

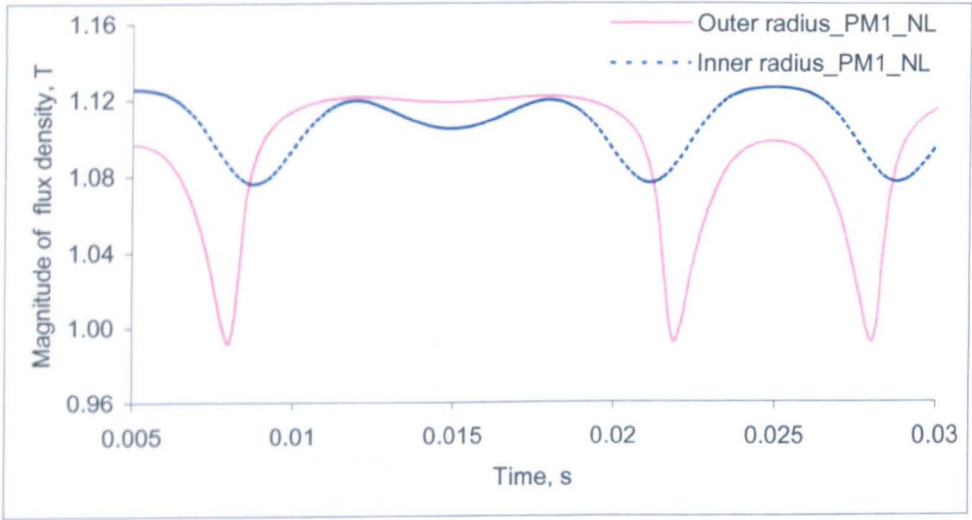
Non linear B-H characteristics of the soft magnetic composite stator core, Somaloy 700, and the mild steel, as well as physical properties of the materials are identical in the 2-D and 3-D models. Since the motor operates close to resonance and exhibits sinusoidal position and velocity profiles, two dimensional and three-dimensional finite element analyses were performed by assuming that the reciprocating motion of the armature follows a sinusoidal velocity profile and that the coil is excited with sinusoidal current waveform which is in phase with the velocity when the motor is operating on-load.

5.2.2 Eddy current loss at no-load condition

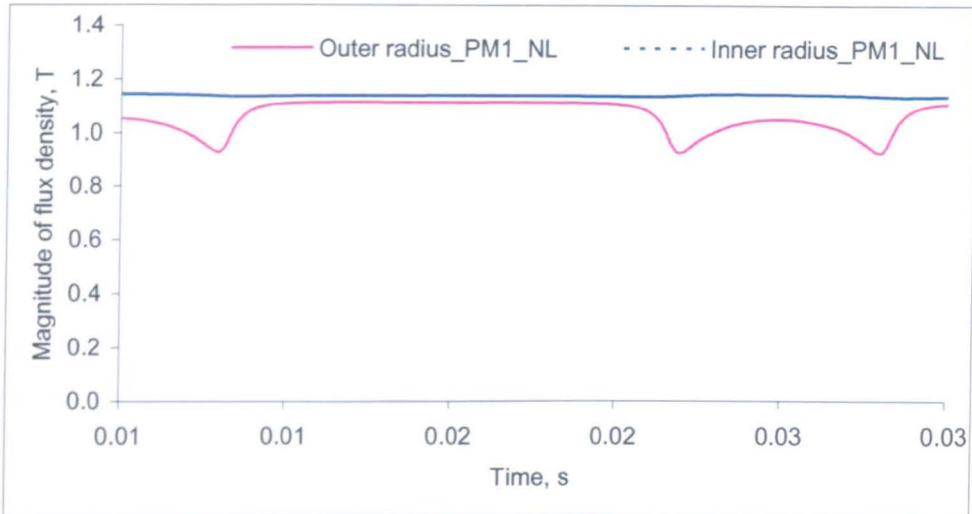
For no-load operation the motor current is zero. The variation of magnet working points take place due to presence of the teeth and the slot, as the armature reciprocates. Consequently, eddy current will be induced in the armature. Figs. 5.5 (a) and (b) show the time variation of flux density of the air-cored and iron-cored

quasi-Halbach magnetised motors, respectively under no-load condition at the axial centre of inner and the outer radius of PM1. It is evident that the magnitude of flux density varies with time and leads to inducing eddy current in the magnet. It is also evident that, the influence of the finite stator core length and the slot on the variation of flux density at a particular points is dependent on its radial distance from the inner bore of the stator core [4].

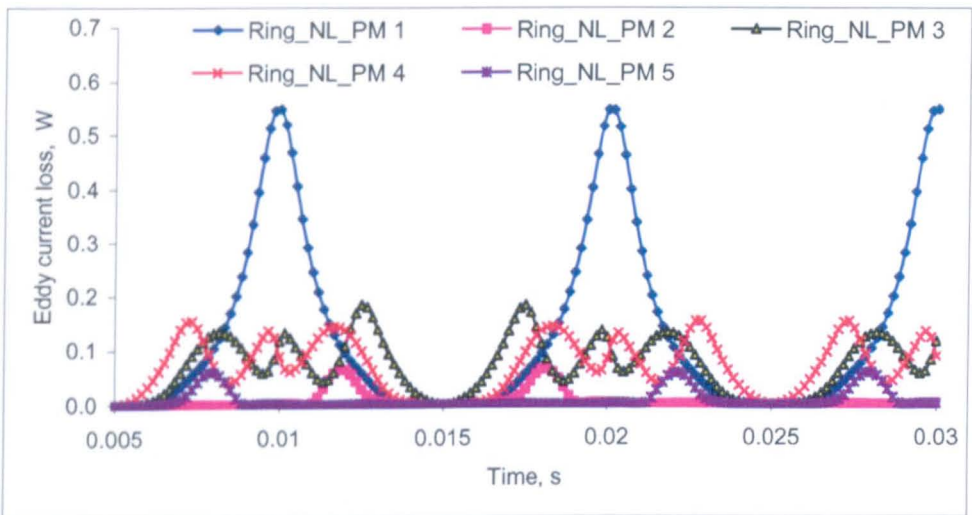
Figs. 5.6 (a) and (b) show the variations of eddy current loss at no-load in ring magnets for the air-cored quasi-Halbach magnetised motor with rectangular magnets and the iron-cored quasi-Halbach magnetised motor with trapezoidal magnets, respectively. The position of PM1, PM2, PM3, PM4 and PM5 are illustrated in Figs. 5.2 and 5.4. As will be seen, the eddy current losses for both motors are dominated by that incurred in PM1 because it is located at the armature centre, and experiences large changes of magnet working points when the armature reciprocates. Therefore, the discussion on eddy current loss will mainly be focussed on the PM1. However, the distribution of eddy current loss in PM2, PM3, PM4 and PM5 are illustrated in Appendix D. For the iron-cored quasi-Halbach magnetised motor with trapezoidal magnets, the eddy current loss in the mild steel supporting tube will also be discussed in detail.



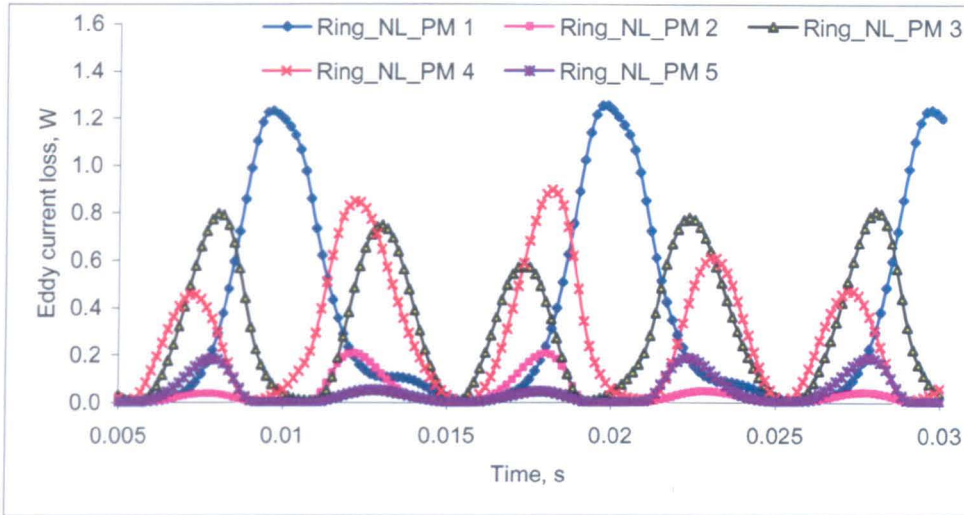
a. Air-cored quasi-Halbach magnetised motor with rectangular magnets



b. Iron-cored quasi-Halbach magnetised motor with trapezoidal magnets
 Fig. 5.5 Variation of flux density in PM1



a. Air-cored quasi-Halbach magnetised motor with rectangular magnets



b. Iron-cored quasi-Halbach magnetised motor with trapezoidal magnets
 Fig. 5.6 Eddy current loss distribution in ring magnets at no-load

5.2.2.1 Air-cored quasi-Halbach magnetised motor with rectangular magnets

Fig. 5.7 shows the variation of eddy current loss in PM1 with time for the air-cored motor when the magnet is segmented into different number of pieces. As will be observed, the eddy current loss reaches maximum at $t = 0.01$ s, 0.02 s and 0.03 s. These time instants correspond to the maximum armature velocity, and the armature position being aligned with the axial centre of the stator. Thus, PM1 experiences the largest change of magnet working points. This trend is true for the magnet with different number of segmentation except for the ring magnet with a slit. Fig. 5.8 shows the 3-D eddy current distribution in the magnets which are circumferentially segmented into 12 pieces at the centre of armature position. As can be seen, the eddy current loss density in PM1 is much greater than that in the other magnets, a similar trend which is observed in Fig. 5.6 (a). It is also evident that the eddy current loss can be significantly reduced by segmenting the magnet. However, the segmentation of permanent magnet into several numbers may increase the manufacturing cost and compromise the mechanical performance [4].

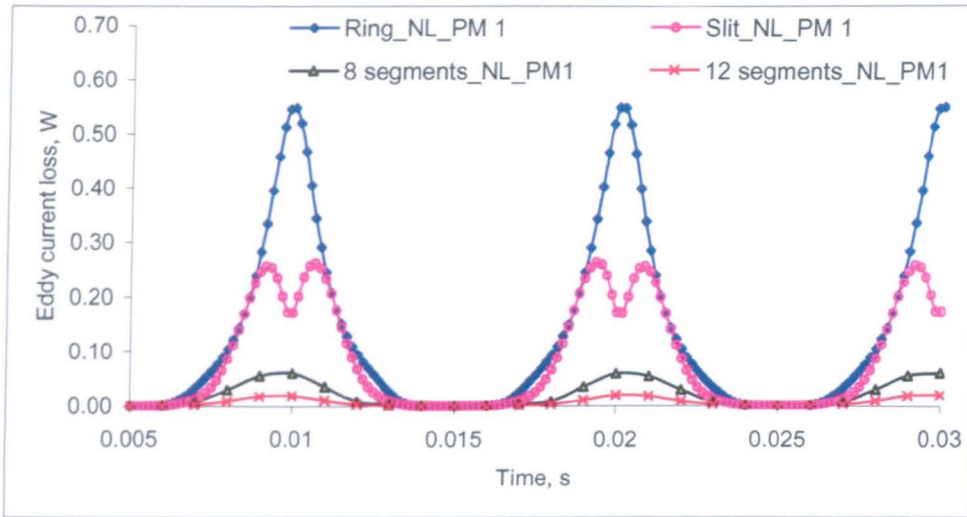


Fig. 5.7 Eddy current loss in PM1 for the air-cored quasi-Halbach magnetised motor with rectangular magnets at no-load condition

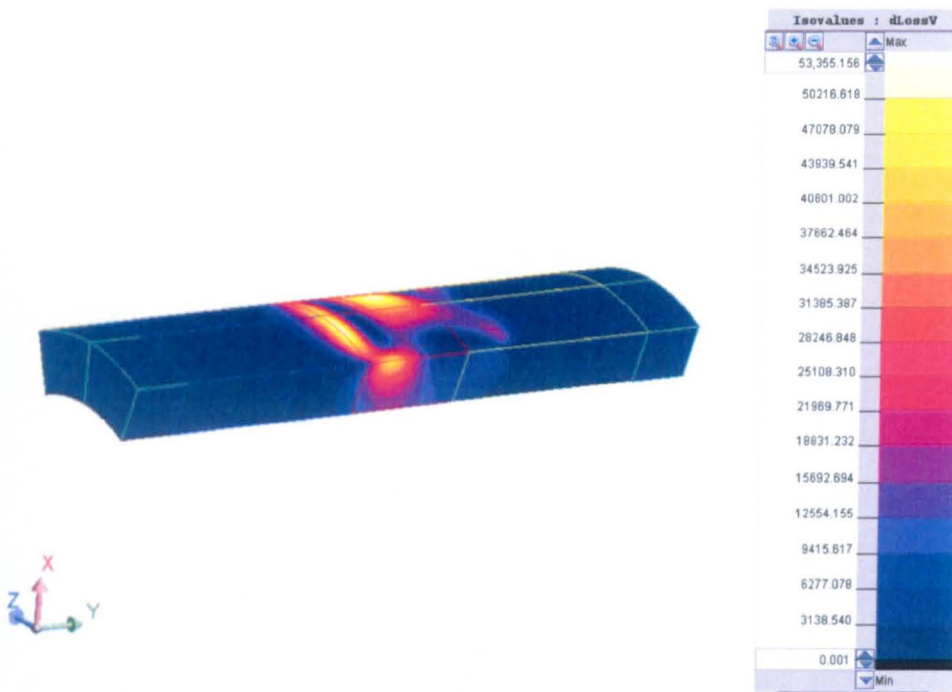


Fig. 5.8 3-D eddy current distribution in air-cored motor with rectangular magnets

Fig. 5.9 shows that the variation of average eddy current loss for the air-cored motor with number of segments. It is evident that, the eddy current loss in the two axially magnetised magnets, PM3 and PM4, and in the two radially magnetised magnets at both ends of the armature, PM2 and PM5, are relatively small compared to the loss in the middle radially magnetised magnet, PM1. The total of eddy current losses in

ring, slit, 8-segment and 12-segment configurations were 0.29 W, 0.17 W, 0.06 W and 0.02 W respectively. Thus, if all the magnets of the air-cored quasi-Halbach linear motor are circumferentially segmented into 12 pieces, the eddy current loss is essentially negligible.

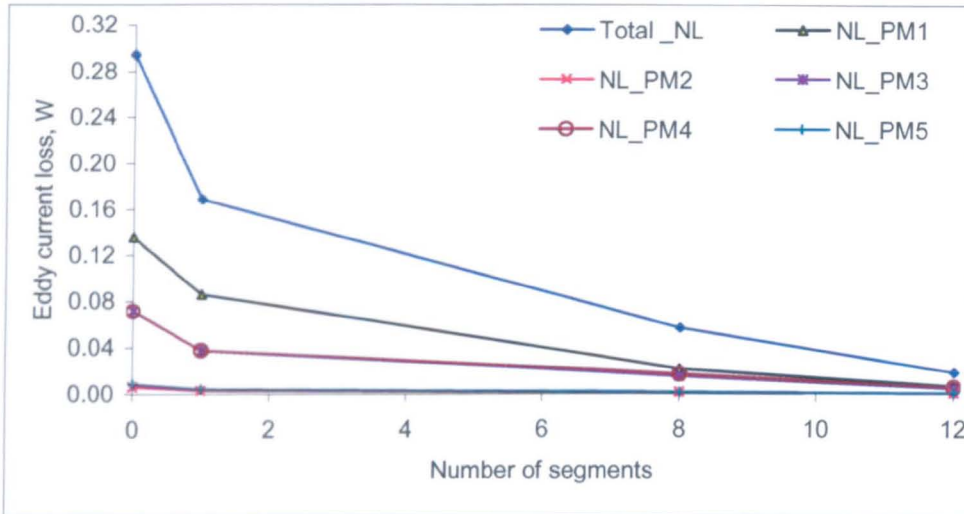


Fig. 5.9 Influence of number of segments on average eddy current loss at no-load condition

5.2.2.2 Iron-cored quasi-Halbach magnetised motor with trapezoidal magnets

Fig. 5.10 shows the time-variations of eddy current loss in PM1, when it is segmented into different number of pieces for the iron-cored motor at no-load condition. A similar trend to those in Fig. 5.7 is observed albeit the magnitude of the eddy current loss is higher due to the use of the mild steel supporting tube.

Fig. 5.11 shows the variations eddy current loss in the mild steel supporting tube with time and number of segments for the iron-cored motor. Figs. 5.12 (a) and (b) show, respectively the 3-D eddy current distribution in the magnets, and the support tube at the centre of axial position when both are segmented into 12 pieces. As will be observed, the eddy current loss in the supporting tube is a much higher than in the magnets, as is evident by comparing Figs. 5.10 and 5.11. This is due to the combined effect of the higher permeability, the higher electrical conductivity and the longer axial length of the supporting tube.

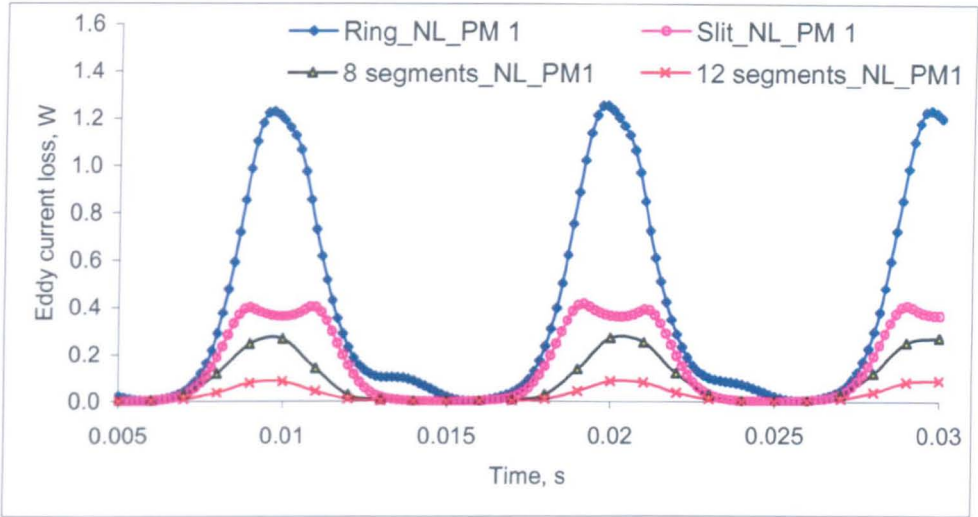


Fig. 5.10 Eddy current loss in PM1 at no-load condition

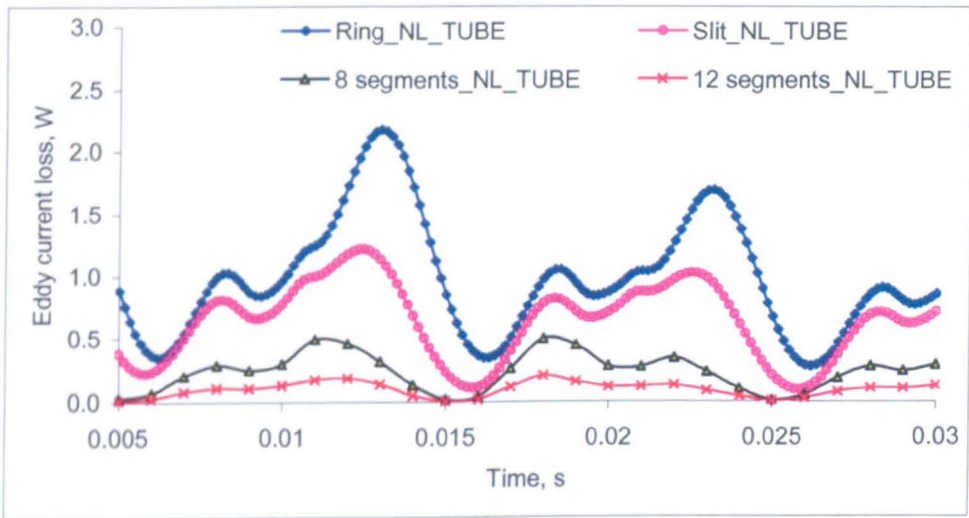
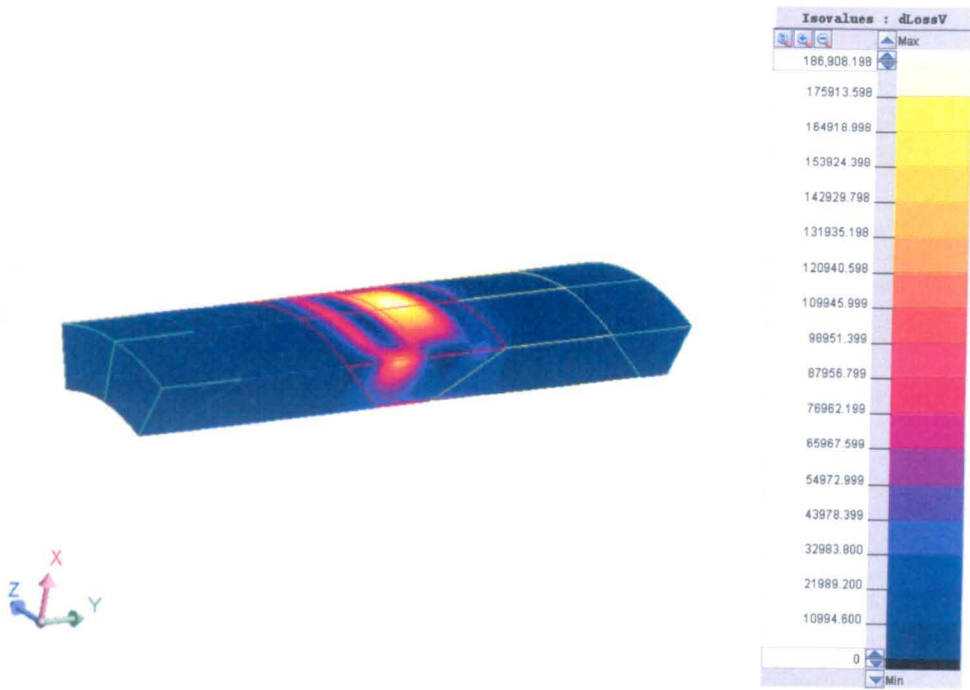
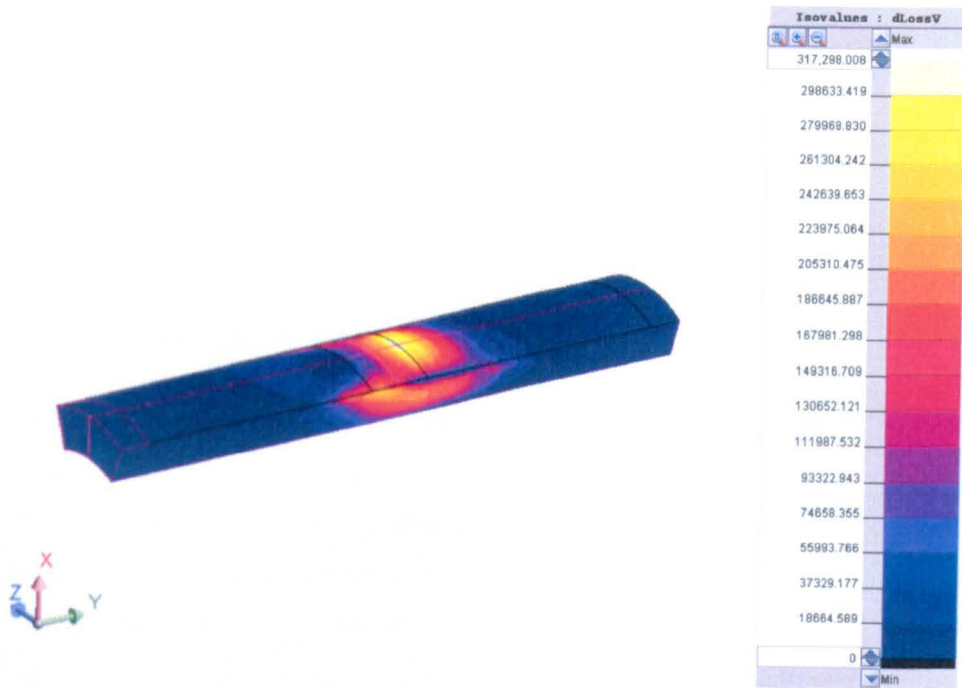


Fig. 5.11 Eddy current loss in the supporting tube at no-load condition



a. Permanent magnets



b. Supporting tube

Fig. 5.12 3-D eddy current distribution in iron-cored motor with trapezoidal magnets

Fig. 5.13 shows the influence of number segments an average eddy current loss in the iron-cored quasi-Halbach magnetised motor with trapezoidal magnet. As can be

seen, the no-load eddy current loss is dominated by the loss in the mild-steel supporting tube, and is significantly higher than that in the air-cored motor. Nevertheless, the results again confirm the effectiveness of segmenting of the permanent magnets and the support tube on the reduction of the eddy current loss. The total eddy current loss at no-load when both the permanent magnets and the mild steel tube are circumferentially segmented into 12 pieces is only 0.17 % of the rated motor output power.

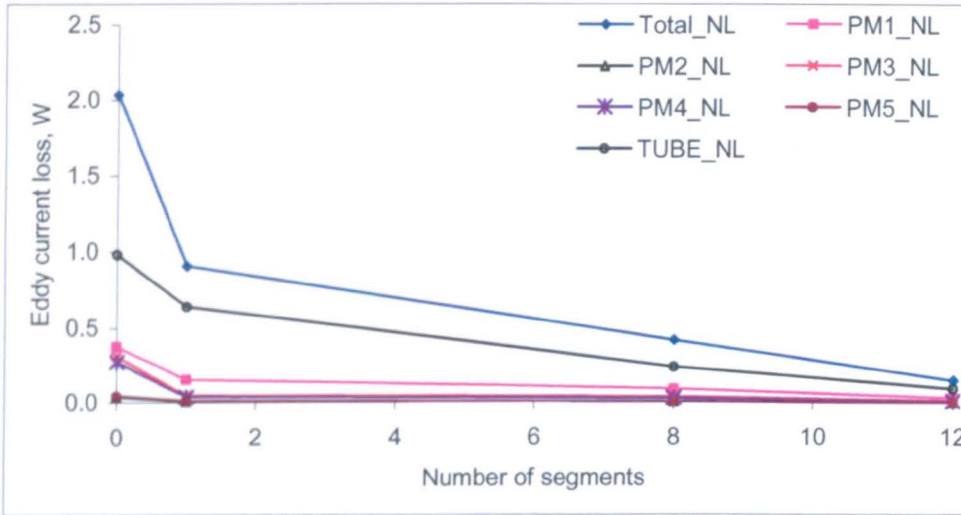


Fig. 5.13 Influence of number of segments on average of eddy current loss at no-load condition

5.2.3 Eddy current loss at on-load condition

In order to calculate the on-load eddy current loss, it is essential to specify the correct phase relationship between the armature position and the coil current [4]. This can be obtained by considering the phasor diagram of the motor shown in Fig. 5.14. As can be seen, if the armature position phasor, X , is used as the reference phasor, the armature velocity phasor, V , and, hence, the emf phasor, E , will lead the position phasor by 90° . To achieve the most efficient motor operation, the motor current phasor, I , should be in phase with the emf phasor, i.e. lead the position phasor by 90° .

Fig. 5.15 shows the relationship of the motor current with the armature velocity where the rms sinusoidal current for the air-cored and the iron-cored motors are 0.52 A and 0.43 A, respectively.

When the coil is excited with a sinusoidal time-varying current, the stator magnetomotive force distribution produces both forward and backward travelling harmonics in the linear motor. These harmonics travel at different speeds to the armature and will induce eddy current losses in both magnets and mild steel support tube. Significant eddy current loss in the armature will not only compromise the motor efficiency, but may also result in excessive heating, which could lead to irreversible deterioration in the motor performance.

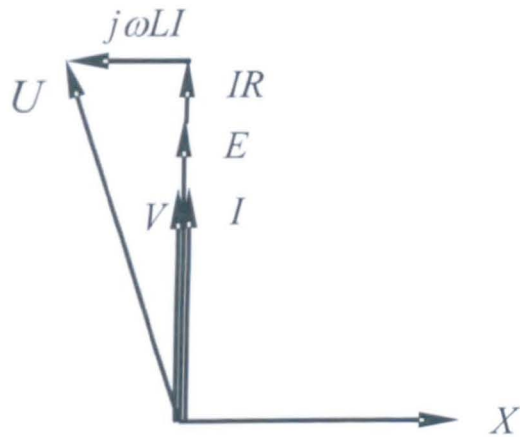


Fig. 5.14 Phasor diagram of motor

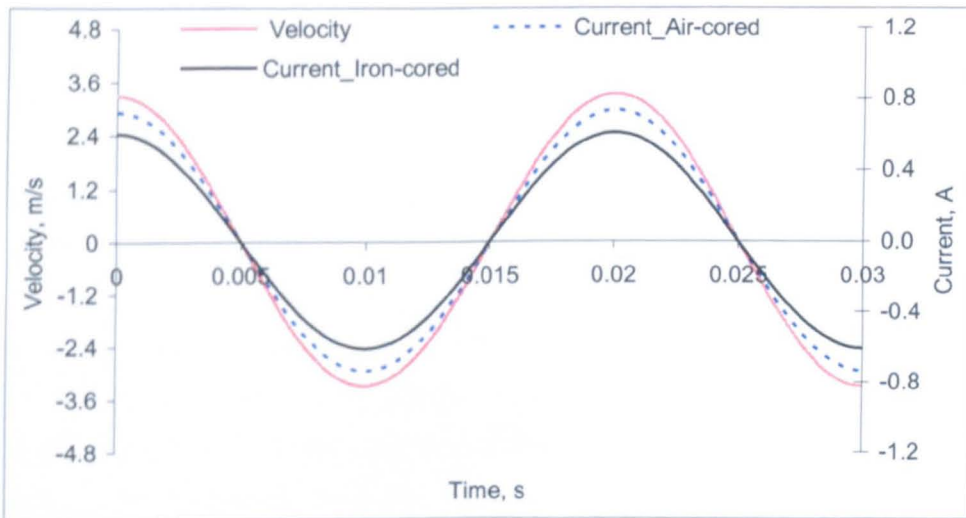


Fig. 5.15 Current supply and velocity waveforms

5.2.3.1 Air-cored quasi-Halbach magnetised motor with rectangular magnets

Fig. 5.16 compares the variations of flux density at the axial centre and outer radius of PM1 with time for the air-cored motor at no-load and on-load conditions. As will be observed, the influence of the armature reaction field on the flux density waveforms in the magnet is not very significant due to its low recoil permeability and, hence, large effective air-gap to the stator mmf [4].

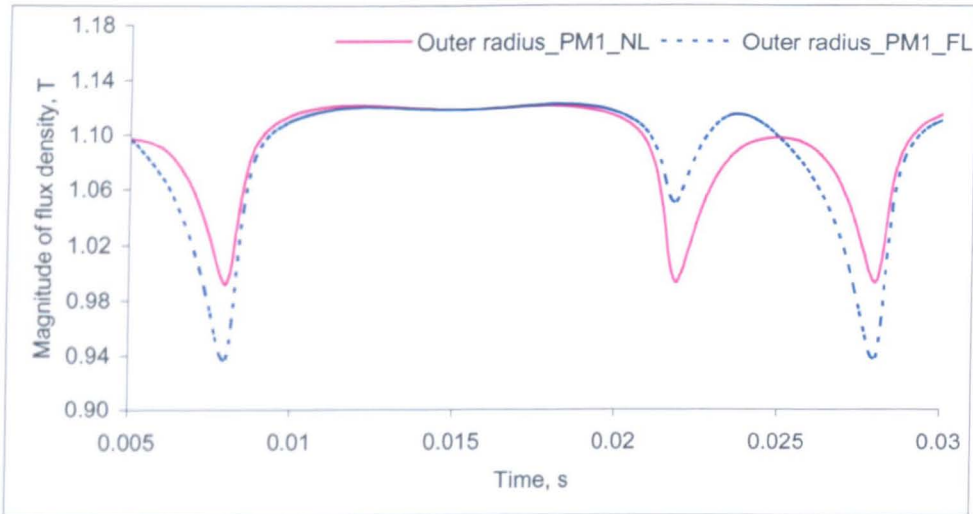


Fig. 5.16 Magnitude of flux density in PM1 at no-load and on-load condition

Fig. 5.17 compares the time variation of no-load and on-load eddy current losses in PM1 when it is a complete ring magnet and when it has a single slit. A similar comparison is given in Fig. 5.18 when PM1 is circumferentially segmented into 8 and 12 segments. As will be observed, the increase of eddy current loss is relatively small with any form of segmentation when load is applied.

Fig. 5.19 shows the variation the total eddy current loss with number of segments at no-load and on-load conditions. Again, it is evident that the eddy current loss is essentially negligible if all the magnets of the air-cored motor are circumferentially segmented into 12 pieces. However, the ring magnets may be used in order to reduce manufacturing cost. The total eddy current loss is still relatively small, i.e. 0.4 % of the rated motor output power [6].

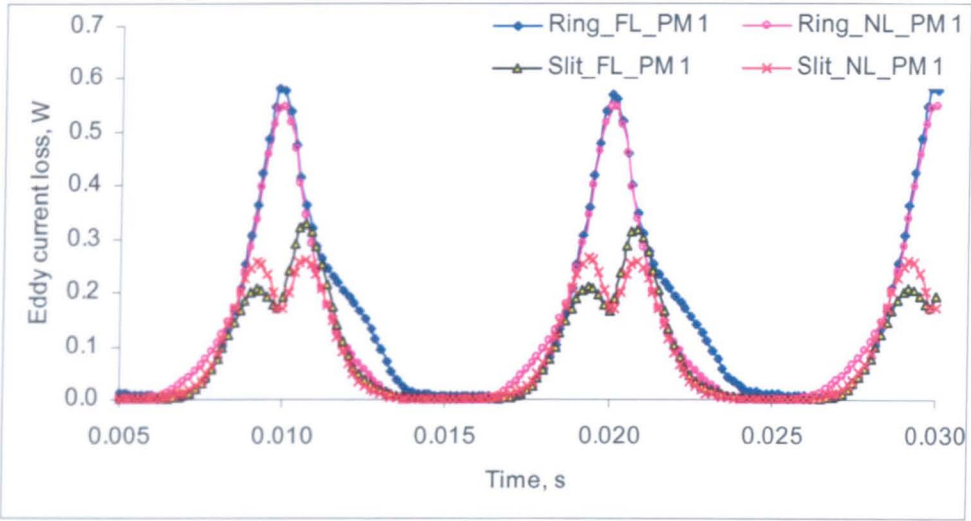


Fig. 5.17 Comparison of eddy current loss between no-load and on-load conditions

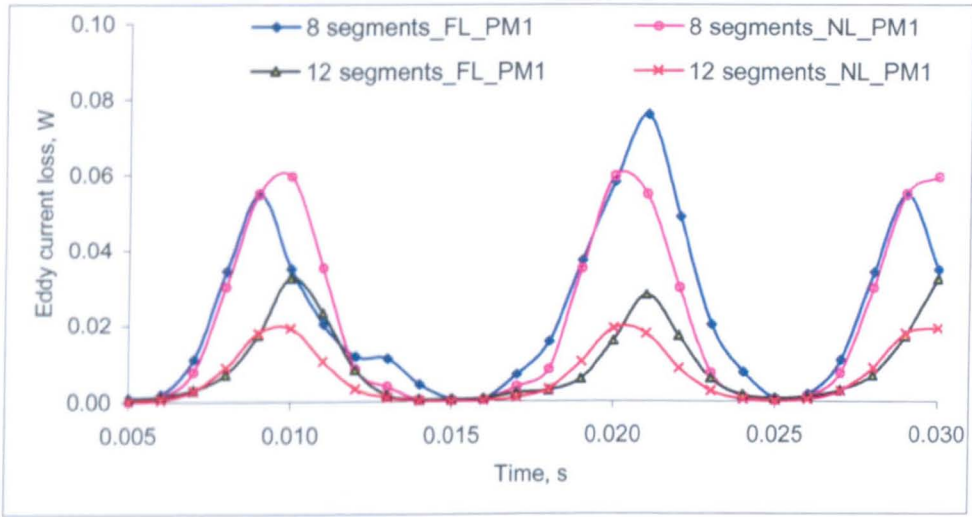


Fig. 5.18 Comparison of eddy current loss between no-load and on-load conditions

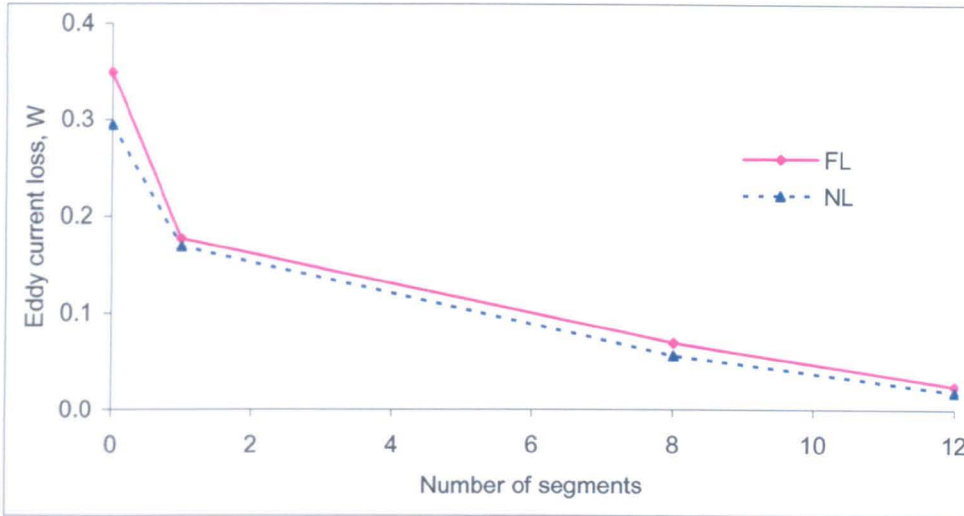
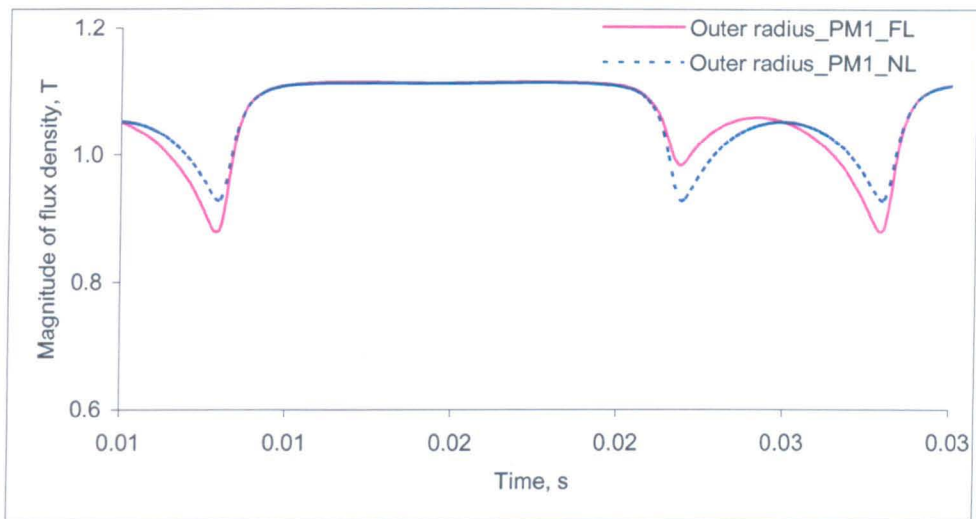


Fig. 5.19 Comparison of average of eddy current loss between no-load and on-load conditions

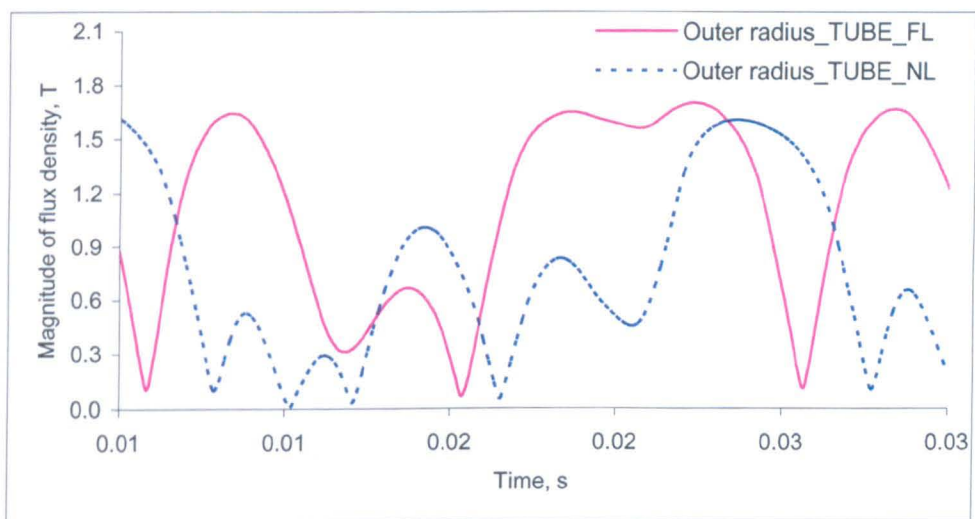
5.2.3.2 Iron-cored quasi-Halbach magnetised motor with trapezoidal magnets

Figs. 5.20 (a) and (b) compare no-load and on-load flux density waveforms at the axial centre and radii of PM1 and supporting tube, respectively, when armature reciprocates sinusoidally at the frequency of 50 Hz and the same stroke length, when the coil is excited with the motor current supply. Similar to the air-cored motor, the influence of the armature reaction on the flux density waveforms in the magnet is not very significant due to a large effective air-gap to the stator mmf. Thus, with any form of segmentation, the increase in eddy current loss in the permanent magnet is relatively small as shown in Fig. 5.21.

However, the flux density variation in the supporting tube due to the armature reaction is much more significant in that both the harmonics content and the magnitude of the flux density variation are increased as shown in Fig. 5.20 (b). This is a consequence of the high permeability of the tube, which effectively provides a flux return path for the armature reaction field.

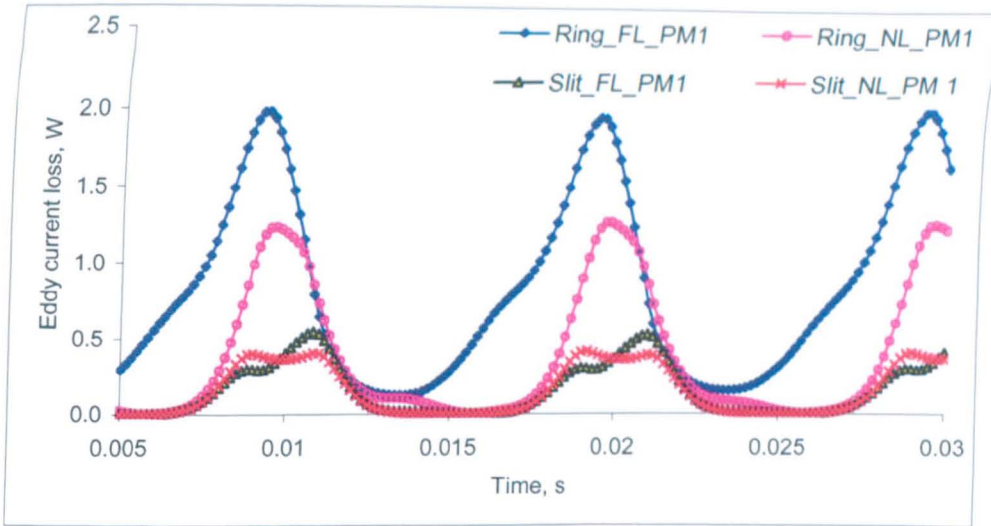


a. Magnitude of flux density in PM1

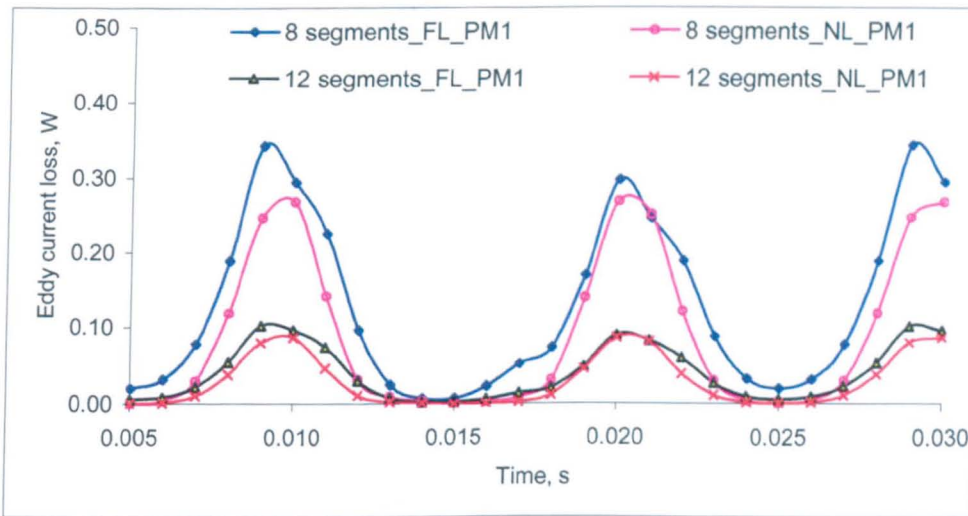


b. Supporting tube

Fig. 5.20 Magnitude of flux density at on-load and no-load conditions



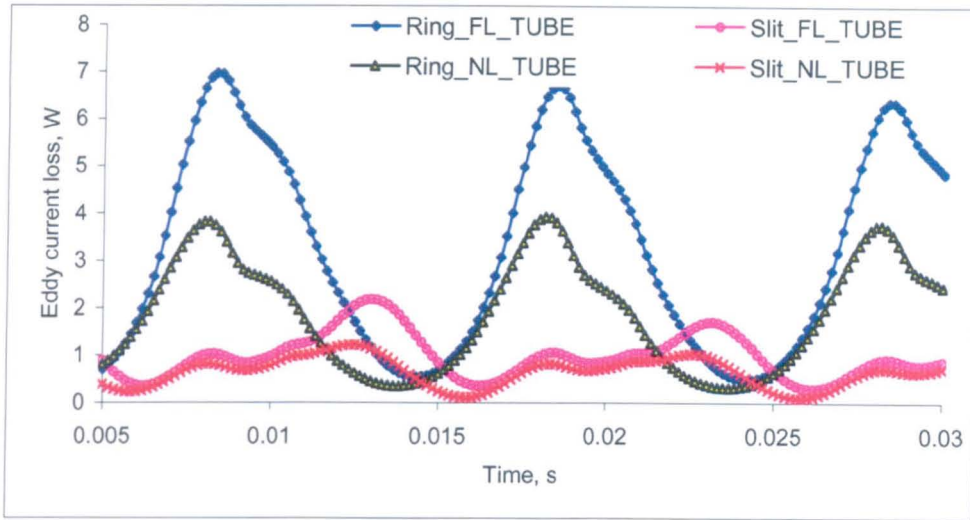
a. Ring and slit magnets



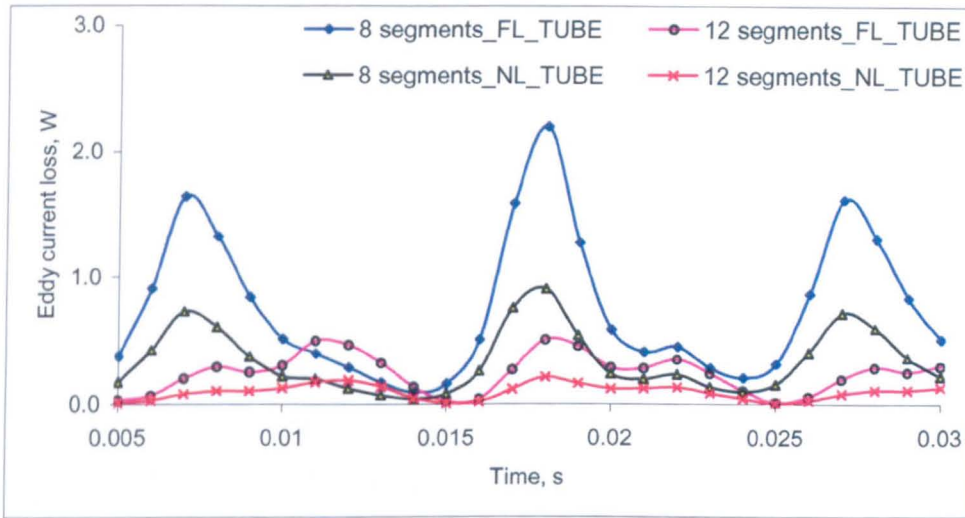
b. 8- and 12-segment magnets

Fig. 5.21 Eddy current loss in PM1 at no-load and on-load conditions

Fig. 5.22 compares the variations of no-load and on-load eddy current losses with time in the ferromagnetic support tube, whilst the average eddy current loss is given in Table 5.1. As will be seen, the on-load eddy current losses is significantly increased compared to the no-load values irrespective of whether the support tube is segmented or not [4].



a. Ring and slit magnets



b. 8- and 12 segment magnets

Fig. 5.22 Eddy current loss in supporting tube at no-load and on-load conditions

Table 5.1 Average of eddy current loss in the supporting tube

Magnet configuration	No-load W	On-load W
Ring	1.80	3.30
Slit	0.64	0.98
8 segments	0.34	0.76
12 segments	0.08	0.24

Fig. 5.23 shows how the total of eddy current loss at no-load and on-load conditions vary with the number of segmentation. The ring configuration will result in the larger eddy current loss, and seriously compromise the motor efficiency. However, if both the magnets and support tube are segmented into 12 pieces, the total on-load eddy current can be reduced to below ~ 0.5 W.

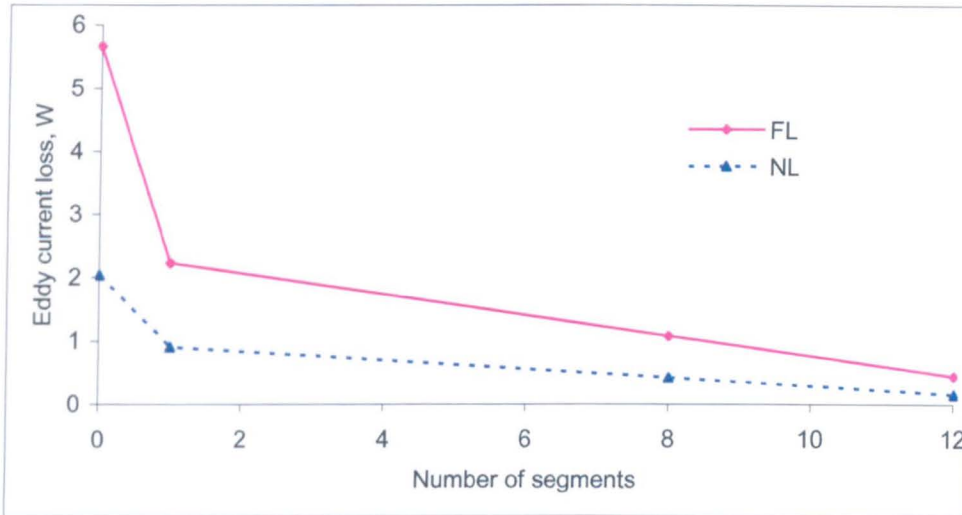


Fig. 5.23 Comparison of eddy current loss between no-load and on-load conditions

5.3 Iron loss calculation

Whilst methods of determining the iron loss in rotating permanent magnet machines have been investigated extensively [7], the calculation of iron loss in linear machines is relatively poorly documented. However, the iron loss in both long stroke, three-phase tubular and short-stroke, single-phase planar permanent magnet machines has been evaluated both analytically and by 2-D finite element analysis based on models formulated in the axi-symmetric cylindrical coordinate system [8] and in the Cartesian coordinate system [9]. In both cases, however, it was assumed that the permanent magnet armature moves at a constant velocity, the iron loss being calculated from magnetic field solutions at a number of equally spaced armature positions spanning a pole-pitch. For a short-stroke reciprocating permanent magnet motor, however, the armature velocity essentially varies sinusoidally with time. Thus, it is not appropriate to assume a constant velocity for the iron loss calculation. In order to maximize the machine efficiency, it is essential to accurately quantify the iron loss which results due to the oscillatory motion of the permanent magnet armature and the sinusoidal time-varying current in the stator coil.

Without loss of generality, the prediction of iron loss for the iron-cored quasi-Halbach magnetised motor with rectangular magnet as shown in Fig. 5.24 will be described in great detail. The relevant design parameters are given in Table 5.2.

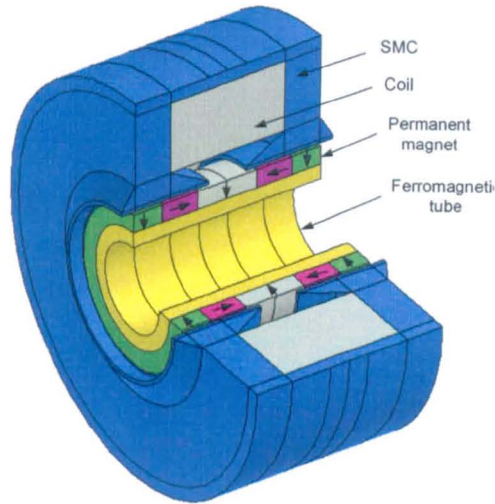


Fig. 5.24 Iron-cored quasi-Halbach magnetised motor with rectangular magnets

Table 5.2 Design parameters of the iron-cored quasi-Halbach magnetised motor with rectangular magnets

Description	Dimension	Units
Outer radius of stator core, R_e	50.0	mm
Yoke thickness, h_{ys}	3.3	mm
Airgap length, G	0.8	mm
Outer radius of magnet, R_m	20.0	mm
Magnet height, h_m	5.0	mm
Supporting tube height, h_{ym}	3.9	mm
Pole pitch, T_p	25.0	mm
Tooth width, T_w	9.4	mm
Tooth pitch width, T_{pw}	40.0	mm
Axial length of radially magnetised magnet, T_{mr}	15.5	mm
Axial length of radially magnetised at ends, T_{mr2}	7.75	mm

Axial length of axially magnetised magnets, T_{mz}	9.5	mm
Slot opening width, b_o	10.0	mm
Tooth tip height, h_t	1.0	
Stator under cut angle, θ	30.0	°
Magnet material	NdFeB	-
Magnet remanence, B_{rem}	1.14	T

To quantify the iron loss of the tubular motor when its armature position and velocity vary sinusoidally with time over a reciprocating cycle, the time period T is divided into N equal time intervals, $\Delta t = T/N$, as illustrated in Fig. 5.25.

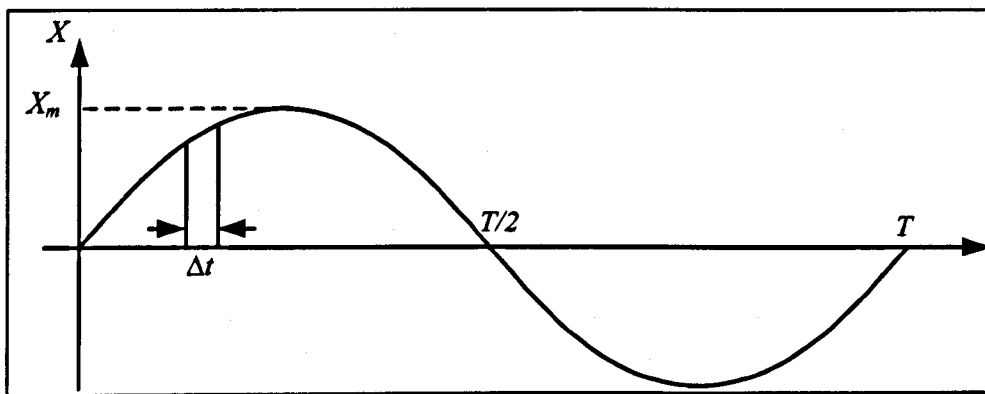


Fig. 5.25 Armature position versus time

At a given time instant $t_i = (i-1)\Delta t$, $i = 1, 2, \dots, (N+1)$, the magnetic field distribution is calculated at the i^{th} armature position x_i with the coil excitation current I_i . Using the Bertotti model [10] [11], the iron loss density, P_{fe} over the cycle can be evaluated from:

$$P_{fe} = P_h + P_c + P_e \quad 5.1$$

where P_h , P_c and P_e are the hysteresis loss density, the classical eddy current loss density and excess eddy current loss density, respectively. These are given by:

$$P_h = k_h f B_m^\alpha K(B_m) \quad 5.2$$

$$P_e = \frac{\alpha d^2}{12\delta} f^2 N \sum_{i=1}^N (B_{i+1} - B_i)^2 \quad 5.3$$

$$P_e = k_e f^{1.5} \sqrt{N} \sum_{i=1}^N |B_{i+1} - B_i|^{1.5} \quad 5.4$$

where B_i is the flux density at x_i and B_m is the peak flux density over the cycle, and f , σ , δ , and d are the frequency, electrical conductivity, mass density and lamination thickness, respectively. For SMC materials, the classical eddy current loss component is zero. However, the excess eddy current loss component which is associated with domain wall effects may still exist. Thus, the coefficients α , k_h and k_e , associated with the hysteresis and excess eddy current loss components, are determined from measurements on SMC samples. For Somaloy 700, $\alpha = 1.75$, $k_h = 0.08$ and $k_e = 1.60 \times 10^{-4}$. $K(B_m)$ is a correction factor which is introduced to account for the additional iron loss which results due to excursions around minor hysteresis loops [12], and is given by:

$$K(B_m) = 1 + (0.65 / B_m) \sum \Delta B_j \quad 5.5$$

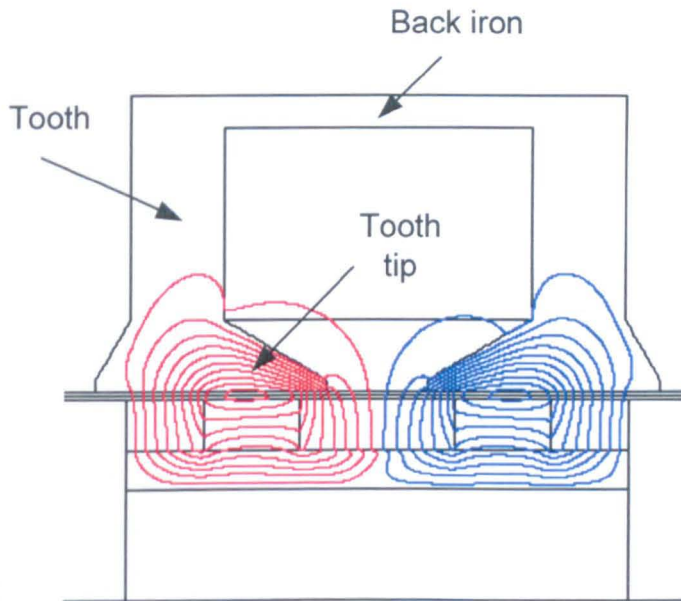
where ΔB_j is the change in flux density during the j^{th} excursion around a minor loop. It should be noted that the foregoing method makes it possible to account for any time-varying armature velocity if the time interval Δt is sufficiently small. The total iron loss can be obtained by volume integration of the iron loss density over the stator core, with due account of the tubular geometry [8].

5.3.1 No-load condition

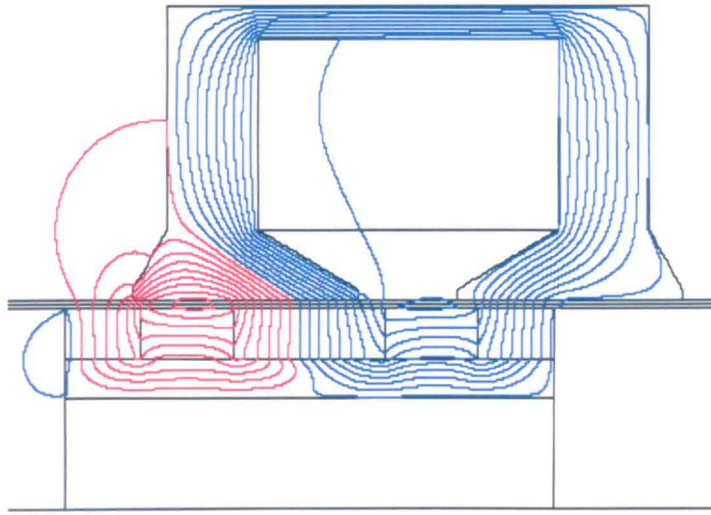
Figs. 5.26 (a) and (b) show no-load flux distributions at the initial armature position $X = 0$ and at the maximum stroke position $X = 10.5$ mm, respectively. As will be seen, at the initial position, the magnetic field distribution is symmetric and the flux produced by the permanent magnets is virtually "short-circuited" by the tooth tips. Consequently, the net flux-linkage with the coil is zero, and the flux density in the tooth body and back-iron (yoke) is also zero. At the rated stroke position, on the other hand, most of the flux from the permanent magnets flows through the teeth and back-

iron, and the flux-linkage with the coil is a maximum. Fig. 5.27 shows the flux density waveforms, which result in no-load, in tooth body, back-iron and tooth tip, as indicated in Fig. 5.26 (a) when the armature position varies sinusoidally with time. As can be seen, the flux density waveforms in the tooth body and back-iron are almost sinusoidal, while in the tooth tip the flux-density waveform is almost trapezoidal but exhibits the presence of minor loops.

Fig. 5.28 shows the variation of the no-load iron loss with frequency and the magnitude of the stroke, X_m , assuming that the motion of the armature follows a sinusoidal waveform. As will be seen, the iron loss increases almost linearly with an increase in frequency. This is a consequence of the hysteresis loss being dominant in the SMC material at low frequencies. For a given frequency, the iron loss increases with an increase in stroke. This is due to the fact that the peak armature velocity, given by $2\pi f X_m$, is proportional to X_m . A higher peak velocity gives rise to faster variation of the magnetic field, and, hence, increased iron loss.



a. Initial armature position



b. Maximum stroke position

Fig. 5.26 No-load flux distributions at two armature positions

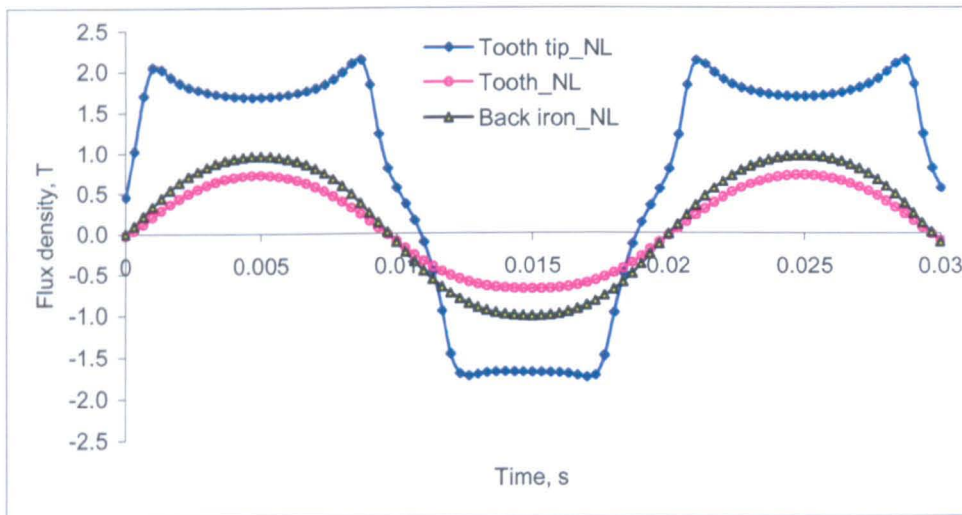


Fig. 5.27 Flux density waveforms over a reciprocating cycle

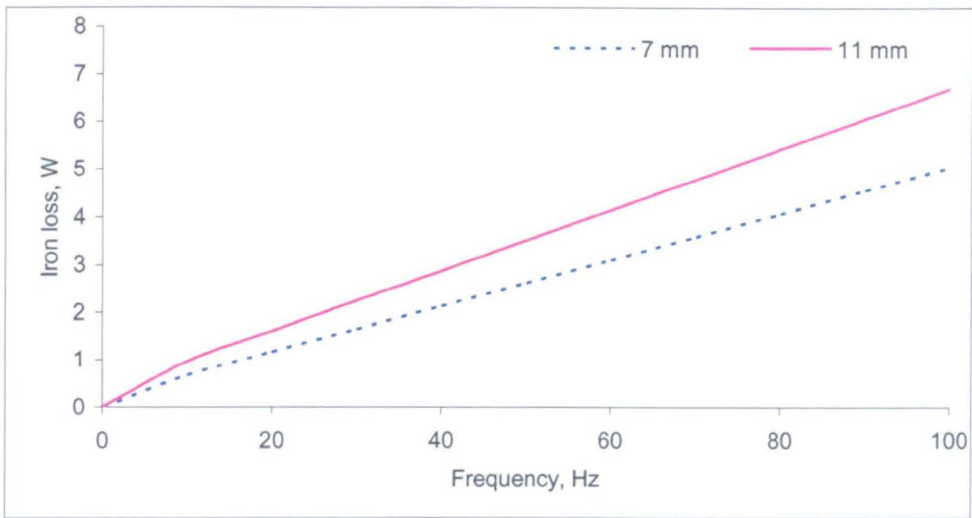


Fig. 5.28 Variation of no-load iron loss with frequency and stroke

For the purpose of comparison, the iron loss of the machine is also evaluated assuming that the armature moves at both a constant rms velocity ($\sqrt{2}\pi f X_m$) and a constant average velocity ($4fX_m$) as shown in Fig. 5.29.

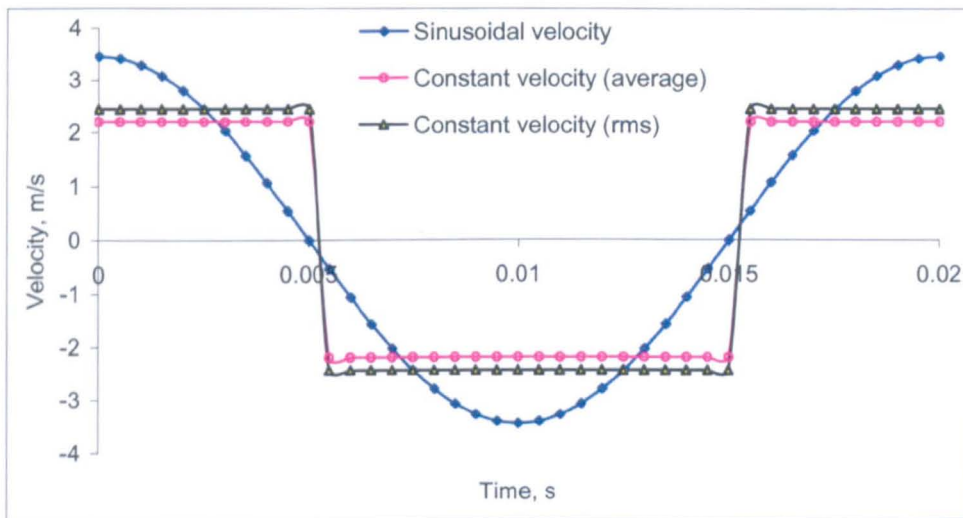


Fig. 5.29 Variation of velocity for 11.0 mm stroke

Fig. 5.30 compares the variation of the no-load iron loss with frequency for an armature stroke of 11.0 mm for the three different velocity waveforms. It can be seen that the iron loss which results with the sinusoidal velocity waveform is $\sim 0.92\%$ less than that which results with the constant rms velocity and 3.68% higher than that

with the average velocity. Thus, evaluation of the iron loss in a short-stroke, reciprocating permanent magnet motor assuming constant velocity will lead to either a slight overestimate if the rms velocity is used or a slight underestimate if the average velocity is used, although the percentage difference is relatively small.

Although the electrical conductivity of SMC materials is 3 orders of magnitude lower than that of solid mild steel, the tubular motor topology provides a good path for induced eddy currents to flow in the circumferential direction. Thus, a significant additional eddy current loss may result. The influence of the electrical conductivity of the SMC on the iron loss has been investigated. Fig. 5.31 shows the no-load eddy current density distribution which results in the SMC stator core at 50 Hz with the armature displaced of 5.0 mm from the central position. The conductivity of Somaloy 700 is assumed to be 2.22×10^3 S/m. As can be seen, in most of the stator core the induced eddy current density is very small. However, in the tooth tip regions the eddy current density is $\sim 10^4$ A/m². Fig. 5.32 shows the variation of the total eddy current loss in the SMC stator with frequency. It is evident that if the motor operates at 50Hz frequency, as is the case for this particular application, the additional eddy current loss due to the non-zero conductivity of the SMC is ~ 0.1 W, and can be practically neglected. However, at a frequency of 100 Hz, the eddy current loss increases by a factor of ~ 4 to 0.42 W, which may not be negligible in many applications.

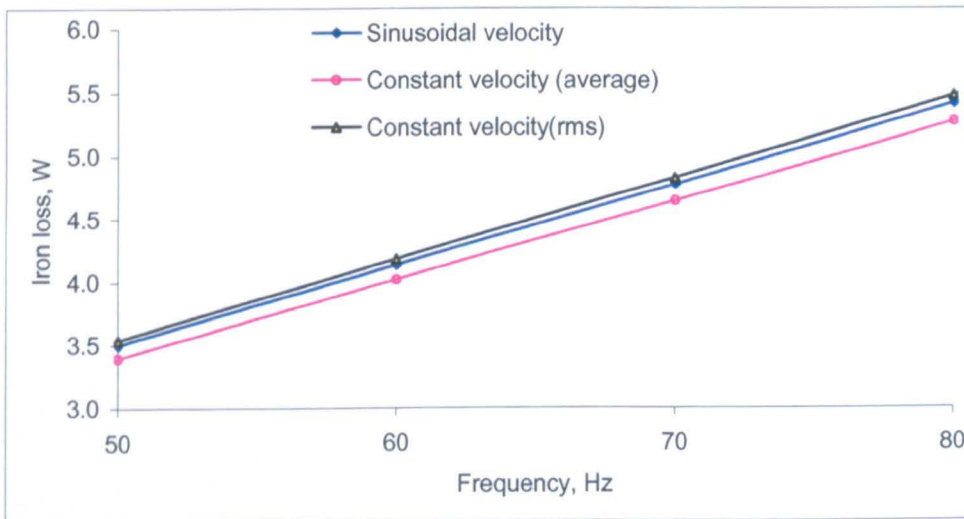


Fig. 5.30 Variation of no-load iron loss with frequency, assuming three armature velocity profiles and $X_m = 11.0$ mm



Fig. 5.31 Eddy current density distribution in SMC stator at 50 Hz with armature position at 5.0 mm

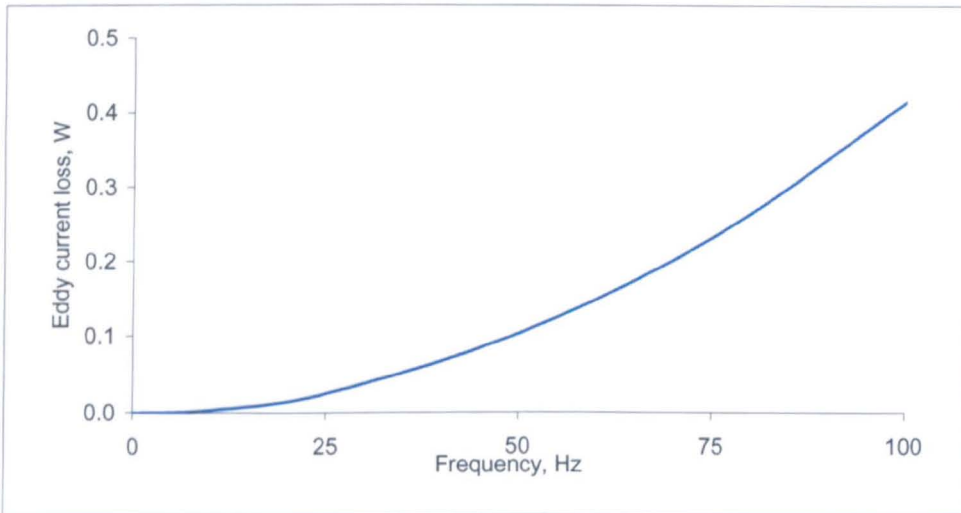


Fig. 5.32 Variation of total no-load eddy current loss in SMC stator with frequency

5.3. On-load condition

To determine the on-load iron loss the sinusoidal armature position and current waveforms are considered at N equal time steps, as shown in Fig. 5.33, and at each time step the magnetic field distribution is calculated. The iron loss is then determined as before.

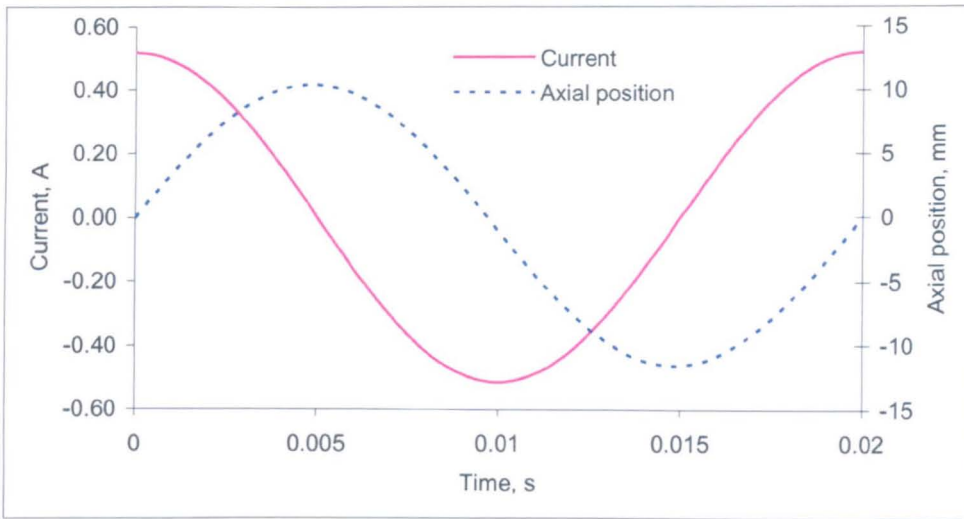


Fig. 5.33 Current and armature position waveforms for on-load iron loss calculation

The iron loss was determined for a stroke of 11.0 mm and an rms current of 0.37 A which are enough to produce the rated output power, 88.5 W. Fig. 5.34 shows the armature velocity and resultant thrust force waveforms over full cycle. As will be seen, the force and velocity waveforms are almost in phase with each other, i.e. the machine is operating in motoring mode.

Fig. 5.35 shows on-load flux distributions at two armature positions, viz. $X = 0.0$ mm and $X = 11.0$ mm, whilst Fig. 5.36 compares the no-load and on-load flux density waveforms in the tooth tip, tooth body and back-iron. At $X = 0.0$ mm the coil current is at its peak value, and results in a strong armature reaction field and, therefore, a significant tangential component of flux density in the air-gap. This tangential flux density component is responsible for the thrust force production, since, from Maxwell's stress tensor method, $F_z = \frac{1}{2\mu_0} B_r B_z$, where B_r is the radial flux density component.

In contrast at $X = 11.0$ mm, the coil current is close to zero, and the flux density distribution in Fig. 5.35 (b) is virtually the same as that on no-load, Fig. 5.26 (b). The peak on-load flux density in the tooth body and back-iron is increased significantly due to the armature reaction. In the tooth tip region, however, the on-load flux density waveform is closer to a sine-wave and the increase in peak flux density is less pronounced, although the existence of small minor loops is clearly evident. It should also be noted that the armature reaction field produces a phase shift in the flux

density waveforms.

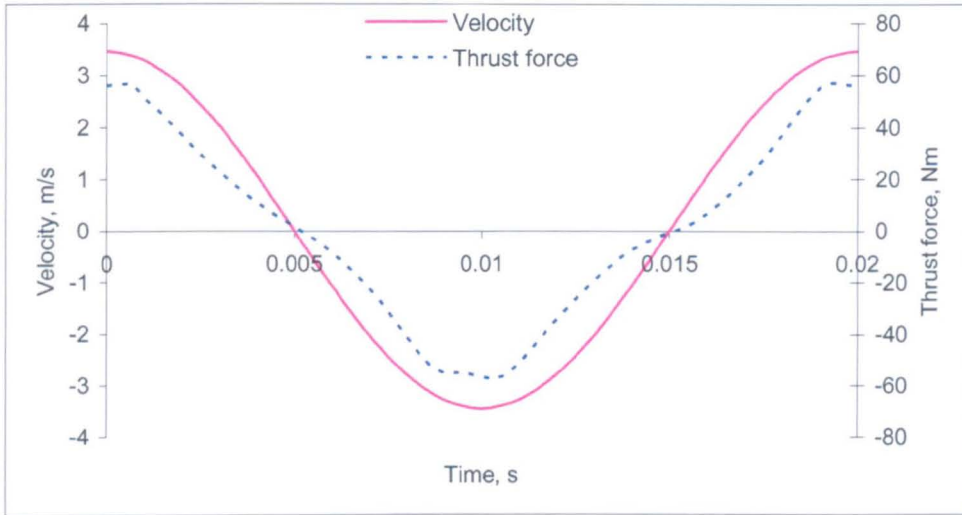
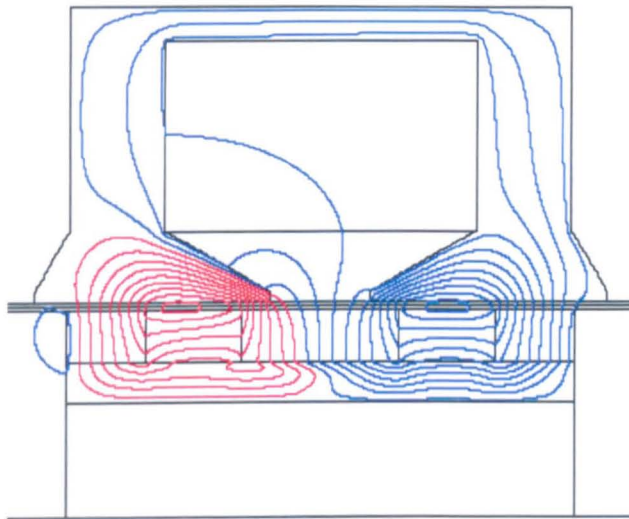
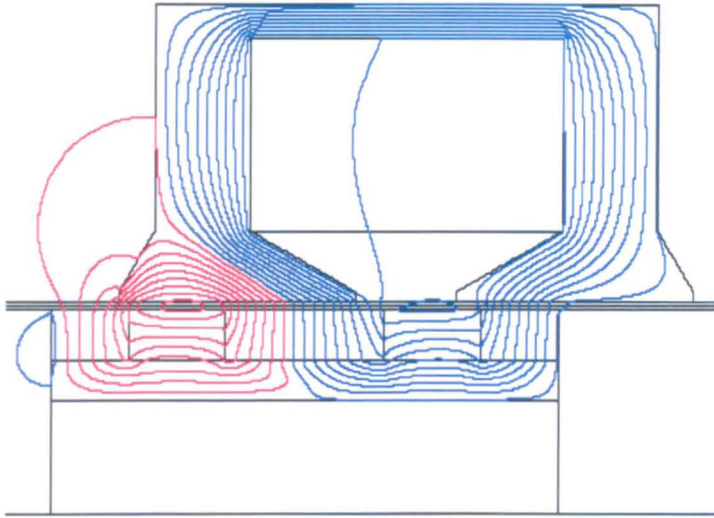


Fig. 5.34 Thrust force and armature velocity waveforms

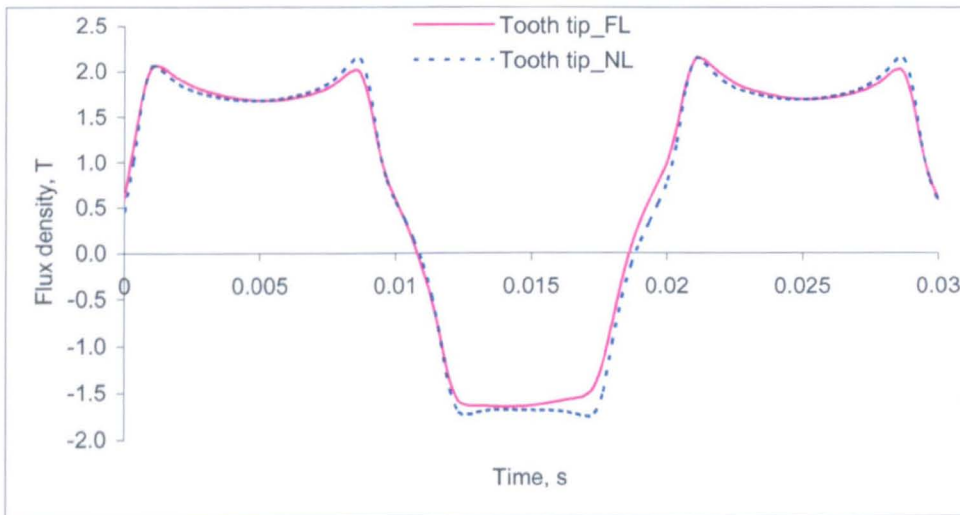


a. Initial armature position

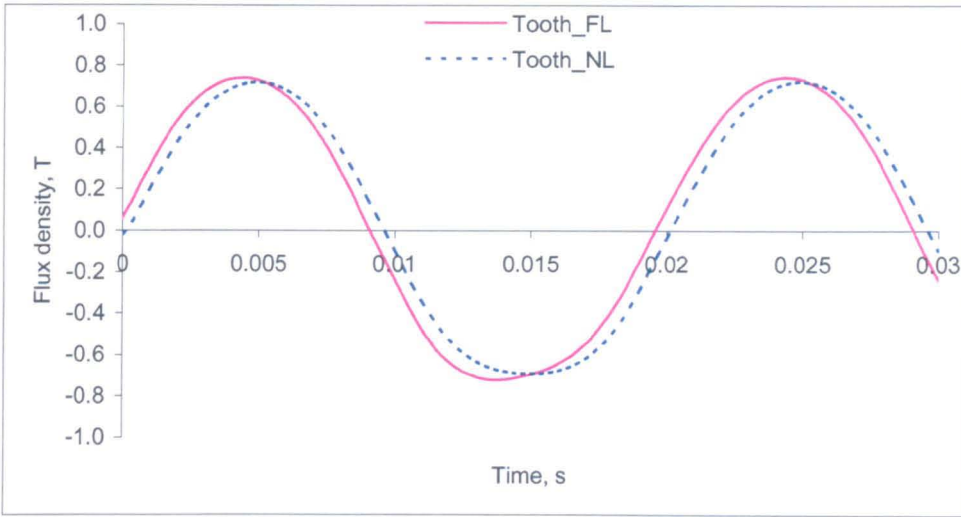


b. Maximum armature position

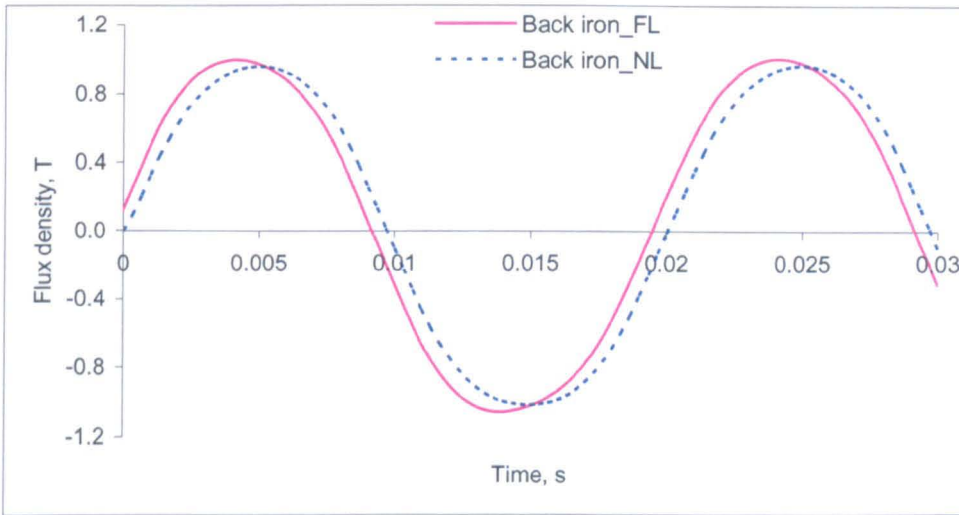
Fig. 5.35 On-load flux density distributions at two armature positions



a. Tooth tip



b. Tooth body



c. Back-iron

Fig. 5.36 Comparison of no-load and on-load flux density waveforms

Fig. 5.37 compares the variation of the no-load and on-load iron losses as a function of frequency for an armature stroke of 11.0 mm. As will be seen, the on-load loss is increased by approximately 7.5 % as a consequence of the higher peak flux density in the tooth body and back-iron. In both cases, the eddy current loss in the stator core is not taken into account.

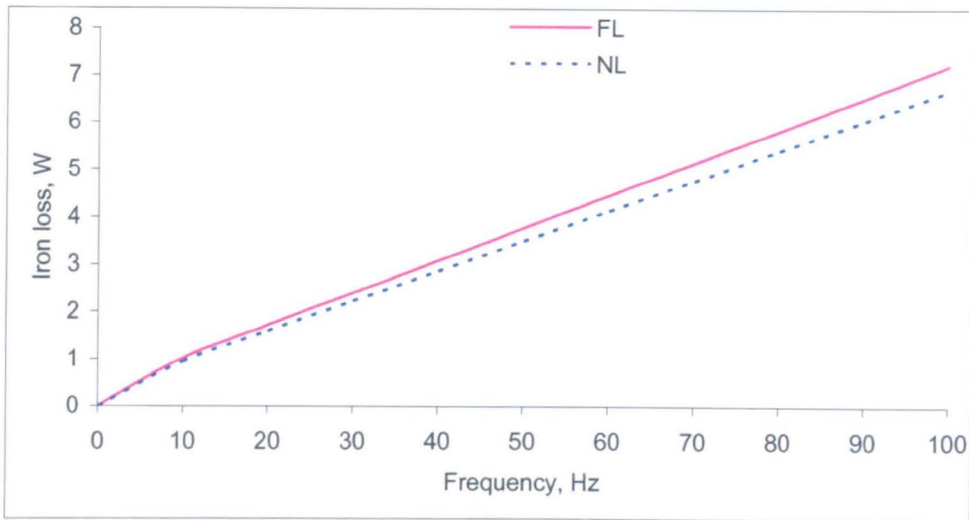


Fig. 5.37 Variation of no-load and on-load iron losses with frequency at fixed armature amplitude of 11.0 mm

The iron loss of two other design variants i.e the air-cored quasi-Halbach magnetised motor with rectangular magnet and the iron-cored quasi-Halbach magnetised magnet with trapezoidal magnets has been predicted in the similar way, but the results are not presented.

5.4 Conclusions

The eddy current losses in the permanent magnets and the supporting tube of the air-cored quasi-Halbach magnetised motor with rectangular magnets and the iron-cored quasi-Halbach magnetised motor with trapezoidal magnets have been analysed using time step two- and three-dimensional finite element analysis. The use of segmentations offers the significant advantage in reducing eddy current loss in the permanent magnets and supporting tube. The eddy current loss with ring magnets and support tube represents 0.4 % and 6.4 % of the rated output power for the air-cored and the iron cored motors, respectively. By circumferentially segmenting the armature, the eddy current loss of the air-cored and iron-cored motors can be reduced to 0.03 % and 0.45 % of the rated output power respectively. The eddy current loss of the air-cored motor is much lower due to the absence of a ferromagnetic tube. The ferromagnetic tube in the iron-cored motor incurs 85.0 % of the total eddy current loss. The circumferential segmentation of the tube is less effective due to its longer axial length, and its higher permeability and electrical conductivity.

The iron loss of the iron-cored quasi-Halbach magnetised motor with rectangular magnets has been evaluated under both no-load and on-load conditions using 2-D time-stepped finite element analysis. This allows the iron loss to be calculated with arbitrary armature velocity and stator current waveforms, with due account of minor hysteresis loops. It has been shown that the no-load iron loss which results with a sinusoidal armature velocity is very close to that which would result if the armature moves at a constant velocity equal to the average value of the sinusoidal velocity profile. The eddy current loss in the solid tubular SMC stator core has also been quantified, and shown to be very small at the 50 Hz operating frequency of the application under consideration.

References

- [1] P. J. Hor, Z. Q. Zhu, and D. Howe, "Eddy current loss in a moving-coil tubular permanent magnet motor," *IEEE Transactions on Magnetics*, vol. 35, no. 5, pp. 3601-3603, September 1999.
- [2] Y. Kawase, T. Ota, and H. Fukunaga, "3-D eddy current analysis in permanent magnet of interior permanent magnet motors," *IEEE Transactions on Magnetics*, vol. 36, no. 4, pp. 1863-1866, July 2000.
- [3] D. Ishak, Z. Q. Zhu, and D. Howe, "Eddy current loss in the rotor magnets of permanent-magnet brushless machines having fractional number of slots per pole," *IEEE Transactions on Magnetics*, vol. 41, no. 9, pp. 2462-2469, September 2005.
- [4] J. Chai, J. Wang, and D. Howe, "Evaluation of eddy current loss in tubular permanent magnet motors by three-dimensional finite element analysis," *Proceedings of XVII International Conference on Electrical Machines (ICEM2006)*, Paper ID: PSA1-12, Chania, Greece, September 2006.
- [5] Y. Amara, J. Wang, and D. Howe, "Analytical prediction of eddy current loss in modular tubular permanent magnet machines," *IEEE Transactions on Energy Conversion*, vol. 20, no. 4, pp. 761-760, December 2004.

- [6] Z. S. Al-Otaibi and A. G. Jack, "Utilising SMC in single-phase permanent magnet linear motors for compressor applications," *14th IET International Conference on Power Electronics, Machines and Drives, PEMD, York, UK*, vol. 1, pp. 752-753, 2-4 April 2008.
- [7] K. Atallah and D. Howe, "The calculation of iron losses in brushless permanent magnet dc motors," *Journal of Magnetism and Magnetic Materials*, vol. 133, no. 1-3, pp. 578-582, 1998.
- [8] Y. Amara, J. Wang, and D. Howe, "Stator iron loss of tubular permanent magnet machines," *IEEE Transactions on Industry Applications*, vol. 41, no. 4, pp. 989-995, July/August 2005.
- [9] K. B. Jang, T. H. Kim, Y. D. Chun, and J. Lee, "Iron loss calculation in a flux-concentration - type LOA," *IEEE Transactions on Magnetics*, vol. 41, no. 10, pp. 4024-4026, October 2005.
- [10] G. Bertotti, "Generalised properties of power losses in soft ferromagnetic materials," *IEEE Transactions on Magnetics*, vol. 24, no. 1, pp. 621-630, January 1988.
- [11] G. Bertotti, A. Boglietti, M. Chiampi, D. Chiarabaglio, F. Fiorillo, and M. Lazzari, "An improved estimation of iron losses in electrical machines," *IEEE Transactions on Magnetics*, vol. 27, no. 6, pp. 5007-5009, January 1991.
- [12] F. Fiorillo and A. Novikov, "An improved approach to power losses in magnetic laminations under non-sinusoidal induction waveform," *IEEE Transactions on Magnetics*, vol. 26, no. 5, pp. 2904-2910, September 1990.

CHAPTER 6

EXPERIMENTAL VALIDATION OF SHORT-STROKE, SINGLE-PHASE TUBULAR PERMANENT MAGNET MOTORS

6.1 Introduction

An extensive comparison of material cost and efficiency of four design variants has been carried in Chapter 5 in order to obtain the most suitable linear motor for household refrigerator compressor system. Based on light weight of armature and ease of manufacturing, the air-cored quasi-Halbach magnetised motor with rectangular magnets has been selected for prototyping. This chapter describes briefly the prototyping process of the motor based on the design dimension given in Table 3.2. A static test rig will also be constructed in order to measure flux-linkage, cogging force and static thrust force of the air-cored quasi-Halbach motor and the results compared with those obtained from finite element analysis.

This chapter also describes the iron loss measurement of the iron-cored quasi-Halbach magnetised motor with rectangular magnets. Iron loss measurement in rotary and linear permanent magnet machines have been discussed in [1] [2] [3] [4] [5] [6]. The iron loss is normally obtained by subtracting the copper loss from the measured input power [3] and the rotor eddy current loss is neglected. In this study, the eddy current loss in the moving-magnet armature will be taken into account in order to obtain better results [7] [8] [9]. To quantify no-load iron loss, the input power of the iron-cored quasi-Halbach magnetised motor with rectangular magnets is measured at the resonant frequency. At this condition, the motor current is minimum [10] and the armature reaction field is negligible. The copper loss resulting the eddy current loss are also small. The measured iron losses are compared with the results obtained from finite element predictions.

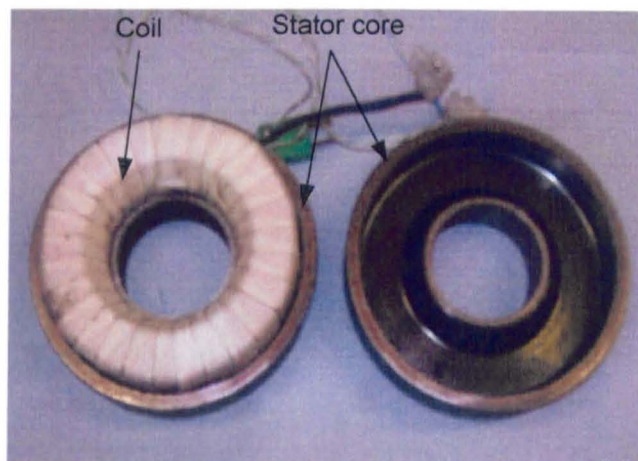
6.2 Prototyping of air-cored quasi-Halbach magnetised motor with rectangular magnet

Figs. 6.1 (a) and (b) show the armature and stator core components of the air-cored quasi-Halbach magnetised motor with rectangular magnets, respectively. In order to reduce eddy current loss, the radially and axially magnetised magnets have been circumferentially segmented into 8 pieces and 12 pieces, respectively, and mounted to a lightweight fibre reinforce polymer tube, Tufset. The carbon fibre was used to

strengthen the magnetic armature and to protect the magnets, as shown in Fig. 6.1 (a).



a. Armature



b. Stator and coil

Fig. 6.1 Prototype of air-cored quasi-Halbach magnetised motor with rectangular magnets

The stator core has been manufactured from Somaloy 700 +0.4 % Kenolube and compacted at 800 MPa by Hoganäs [11] [12]. As will be seen, two-halves of the stator core are used for ease of assembly. The stator is housed in a non-magnetic casing together with spring to facilitate resonant operation as shown in Fig. 6.2. Linear bearings which support the moving armature are mounted at both ends of the casing. The complete assembly of the air-cored motor is shown in Fig. 6.3. For the static measurements, however, the springs were not assembled.



Fig. 6.2 Motor casing

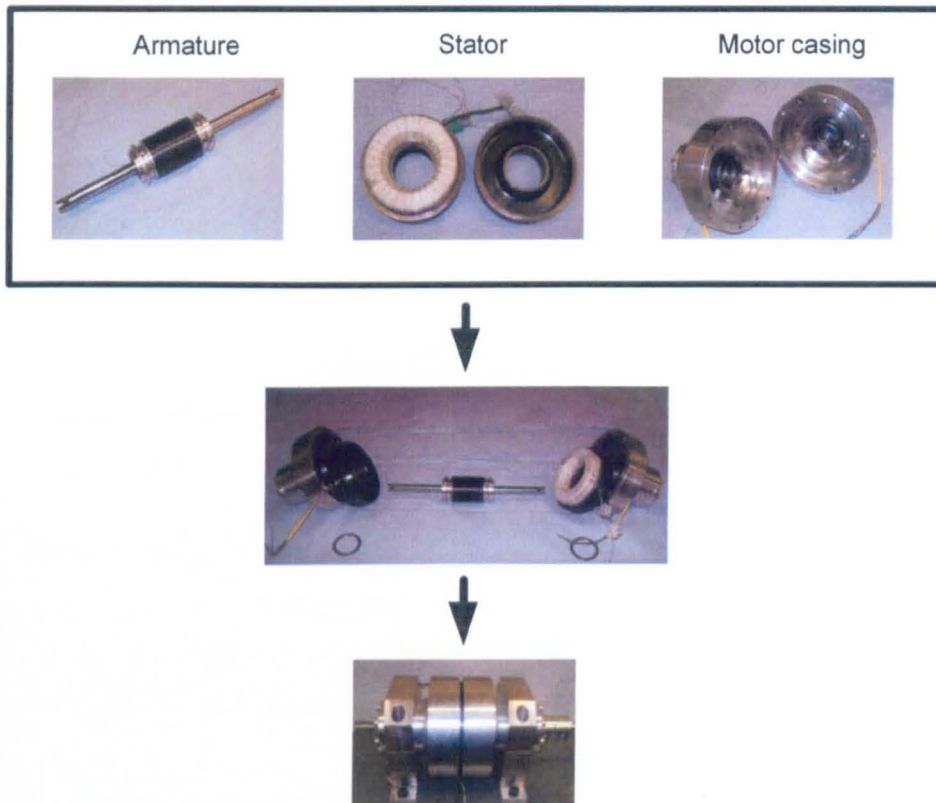


Fig. 6.3 Exploded and assembled view of the air-cored motor

6.3 Static test rig

Fig. 6.4 shows the static test-rig which was used to measure the variation of flux-linkage, cogging force and thrust force with armature position. The test rig comprises

the air-cored motor, micrometer barrel, load cell, linear variable differential transformer (LVDT) displacement transducer and flux meter (not shown). Generally, the micrometer barrel is used to adjust the armature displacement, and the load cell, the LVDT and the flux-meter are employed to measure the thrust force, axial position and flux-linkage of the coil, respectively.

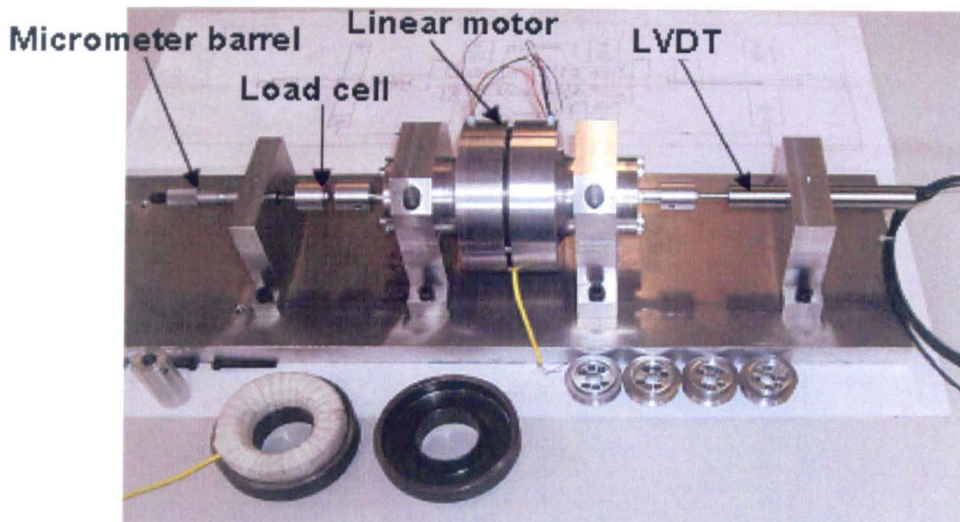


Fig. 6.4 Static test-rig for single-phase air-cored quasi-Halbach magnetised motor with rectangular magnets [13]

6.4 Static test results

6.4.1 Flux linkage

In this design study, the flux linkage is measured in weber (Wb) using flux meter. Initially, the motor coil is connected to the flux meter terminal and the armature position is at zero displacement, i.e $z = 0.0$ mm. Again, micrometer barrel is used to adjust the armature displacement.

Fig. 6.5 compares the measured and finite element predicted of coil flux-linkage. As will be seen, the measured flux-linkage is slightly greater than that of finite element prediction. This may be due to that fact that the remanence of the magnets in the prototype motor is greater than the data sheet value used in the finite element predictions. However, a higher flux-linkage will provide a better thrust force.

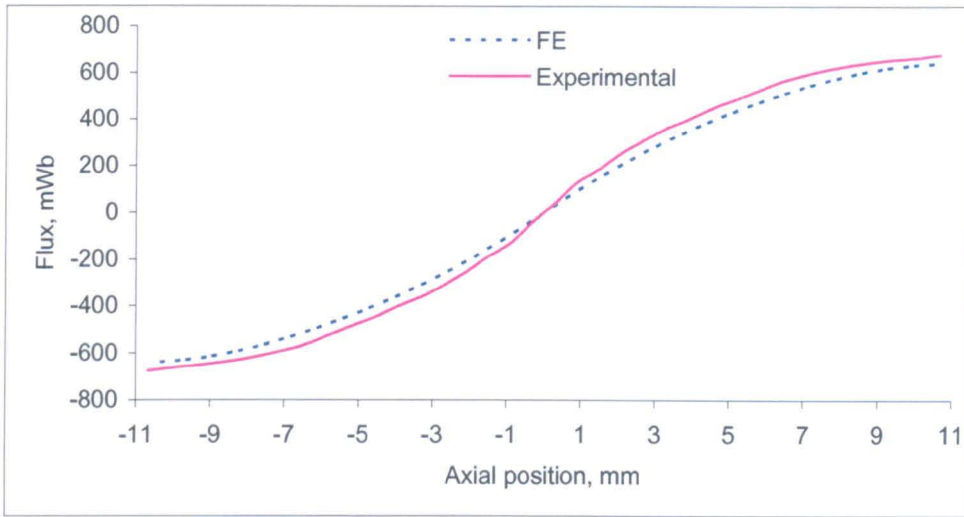


Fig. 6.5 Comparison of measured and predicted coil flux-linkage

6.4.2 Cogging force

Cogging force was measured when the motor was not excited. Fig. 6.6 compares the measured and FE predicted cogging force waveforms. There is a reasonably correlation between the measurement and predictions, bearing in mind that cogging is very sensitive to tolerances in the magnetic material properties and mechanical assembly [13].

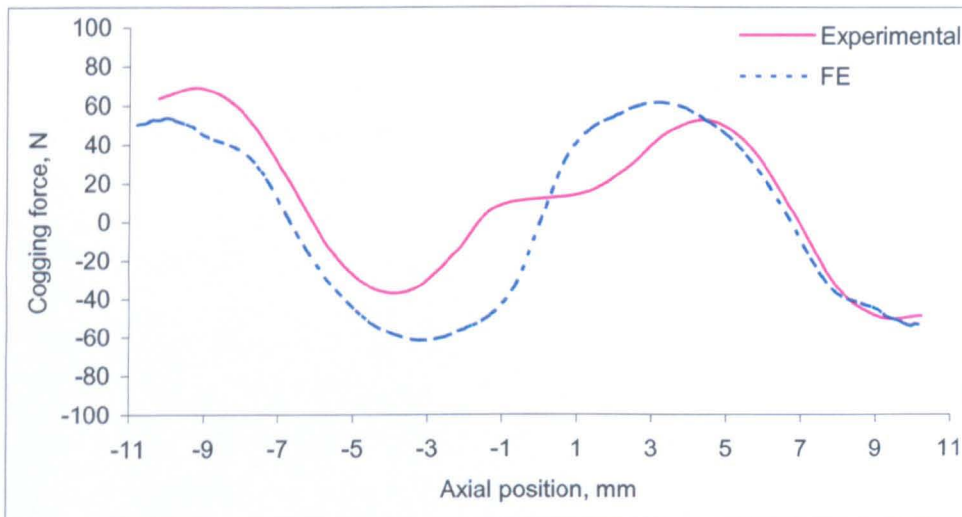


Fig. 6.6 Comparison of measured and predicted cogging force

6.4.3 Static thrust force

When the motor was excited with constant currents of 0.5 A and 0.75 A, the resultant force variations with armature displacement were measured by the force transducer. The net thrust force at a given armature position was obtained by subtracting the cogging force component from the measured value. Fig. 6.7 compares the variation of the measured and finite element predicted thrust force with respect to axial displacement of the armature. As will be seen, the measured thrust force is slightly greater than that of finite element prediction. This result is consistent with those observed in Fig. 6.5, and may be due to that fact that the remanence of the magnets in the prototype motor is greater than the data sheet value used in the finite element predictions.

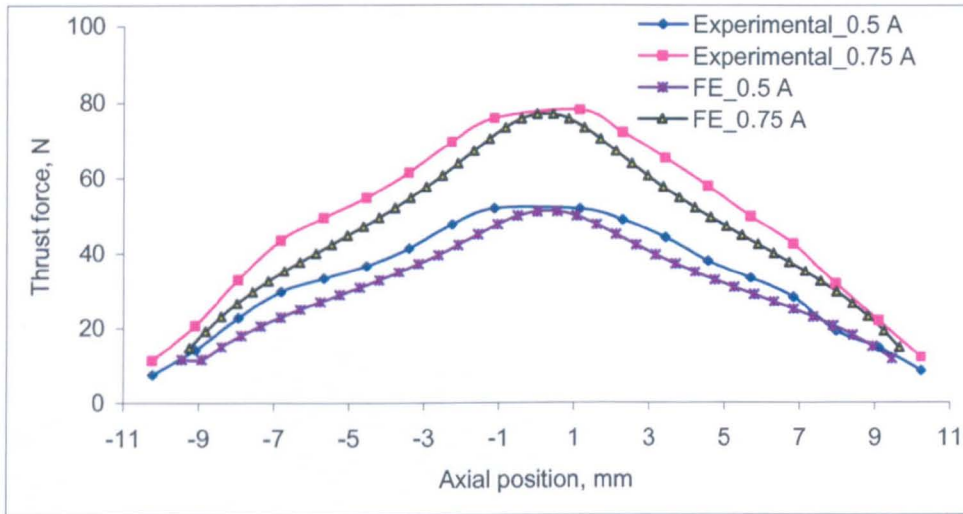


Fig. 6.7 Variation of measured and predicted thrust force with axial position

6.5 Iron loss test rig

The iron-cored quasi-Halbach magnetised motor with rectangular magnets has been constructed and based on design dimension given in Table 5.2. In this case, the armature has been constructed using two axially magnetised ring magnets and 12 segments for each radially magnetised magnet, mounted on a ferromagnetic tube.

For the iron loss test rig, the linear bearings which may cause the friction loss are not employed instead the flexure springs as shown in Fig. 6.8 are employed and act as springs and bearings [14] [15]. In this case, the friction loss is assumed negligible.

A different non-magnetic motor casing has also been designed to accommodate the springs and other motor components, such as the armature, the stator core and the coil, as shown in Fig. 6.8.

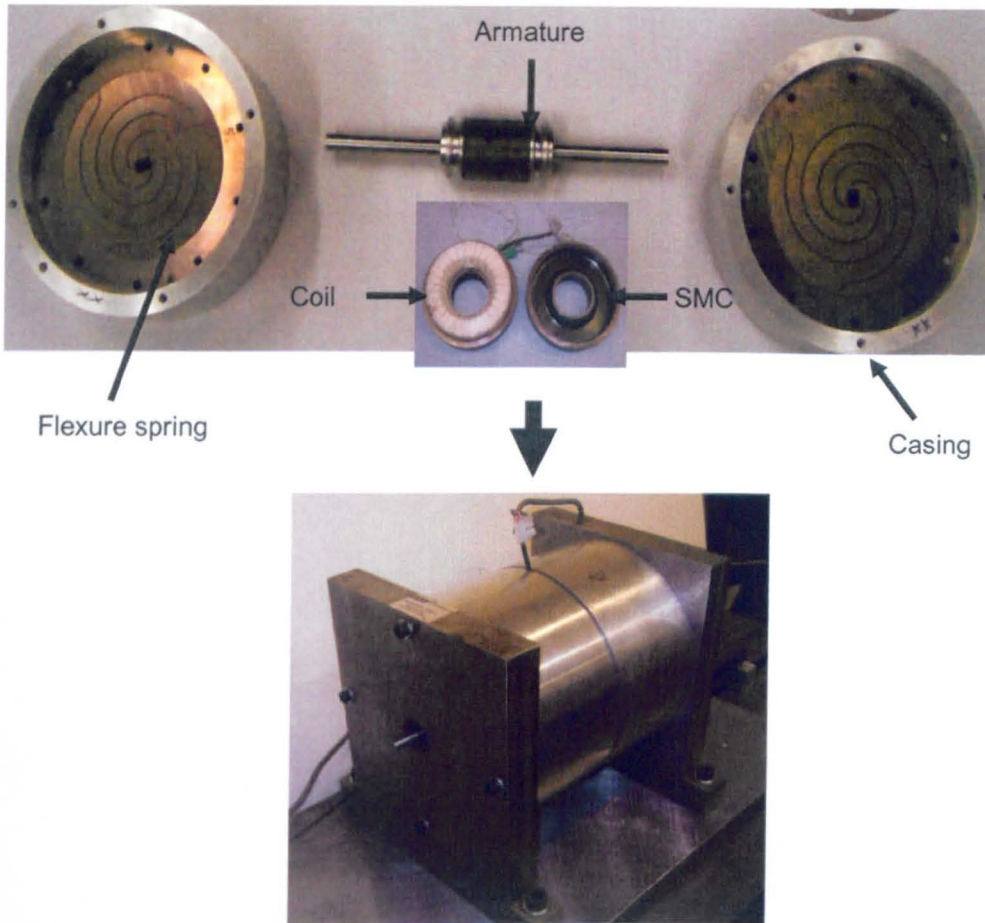


Fig. 6.8 Linear motor components

Fig. 6.9 shows the test-rig configuration which was used to measure the iron loss of the iron-cored quasi-Halbach linear motor. The function generator is used generate variable frequency and amplitude signals which are amplified by a linear power amplifier. A step-up transformer is used to increase the voltage applied to the motor. A power analyser was employed to measure the motor input power, input current, voltage and the power factor. All results are displayed in the digital monitor of the power analyser. A digital oscilloscope was used to measure and record the instantaneous data such as motor current, voltage and the displacement of the armature.

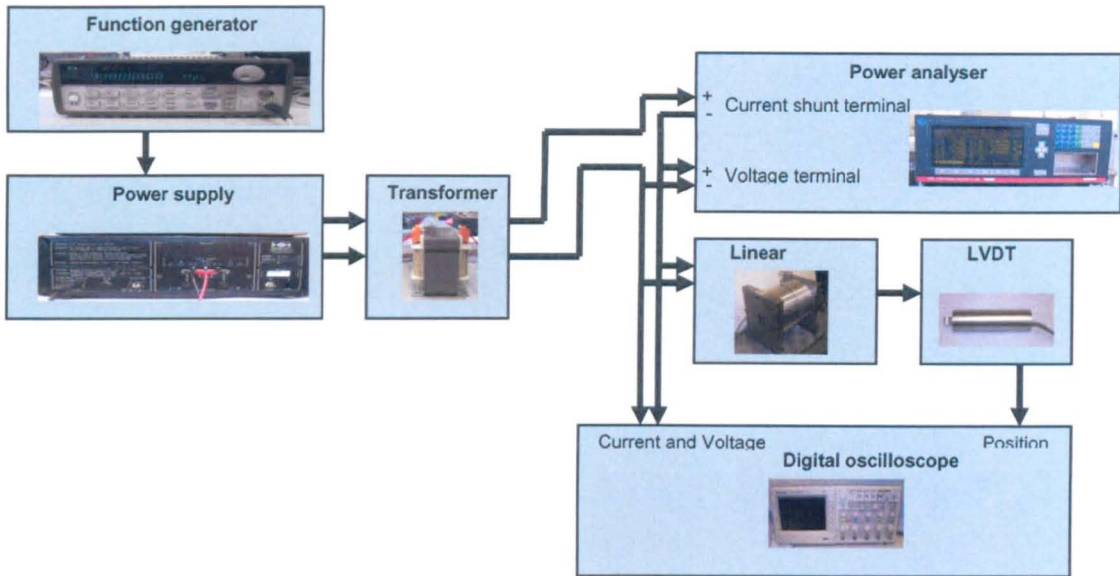
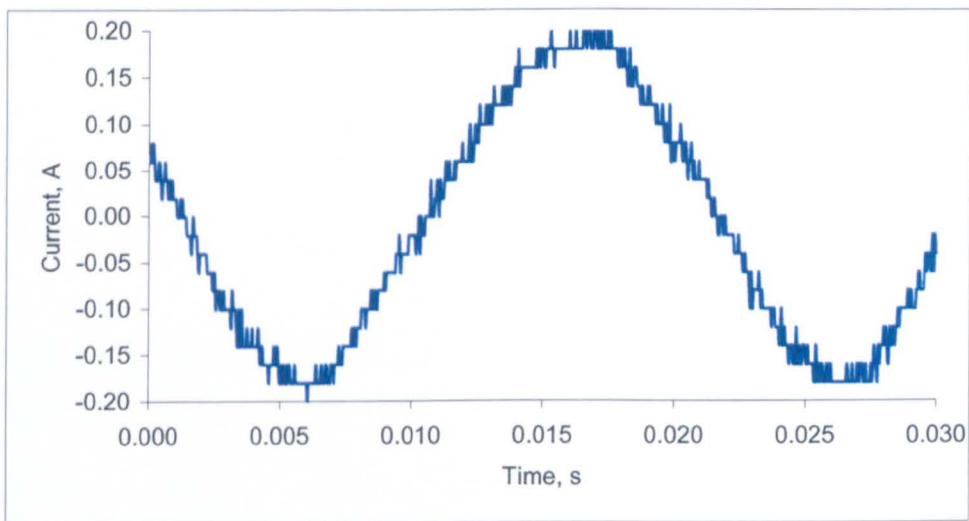
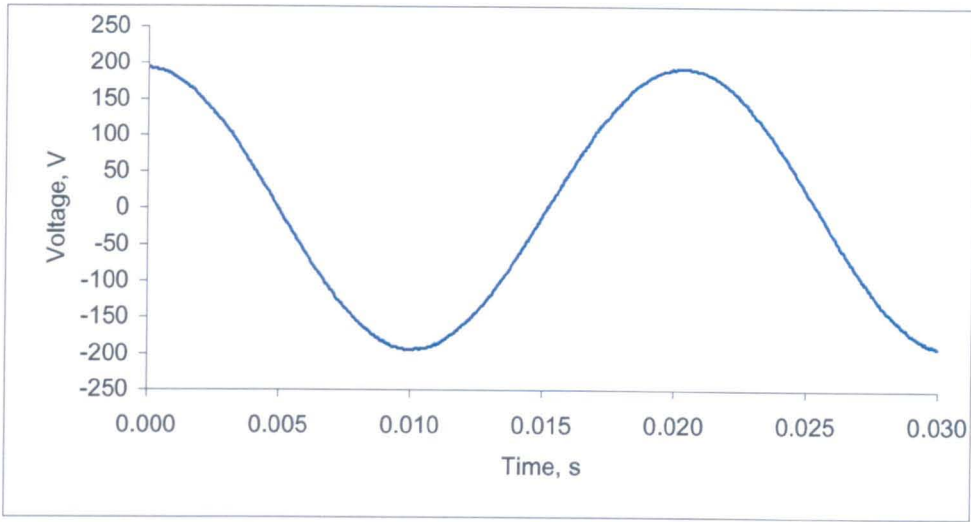


Fig. 6.9 Schematic diagram of the iron loss test rig

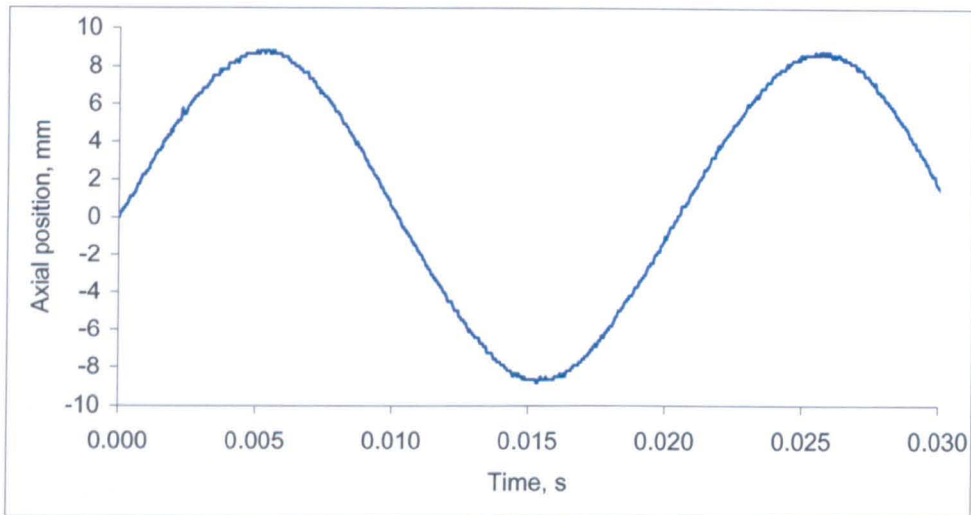
Fig. 6.10 shows the measured waveforms of the current, voltage, and armature displacement at no-load with a stroke of 9.0 mm and a resonant frequency of 49 Hz. As can be seen, the waveforms are essentially sinusoidal. The quantisation effect in the current waveform is due to discretisation by the digital scope when the data was saved.



a. Motor current



b. Voltage



c. Axial position

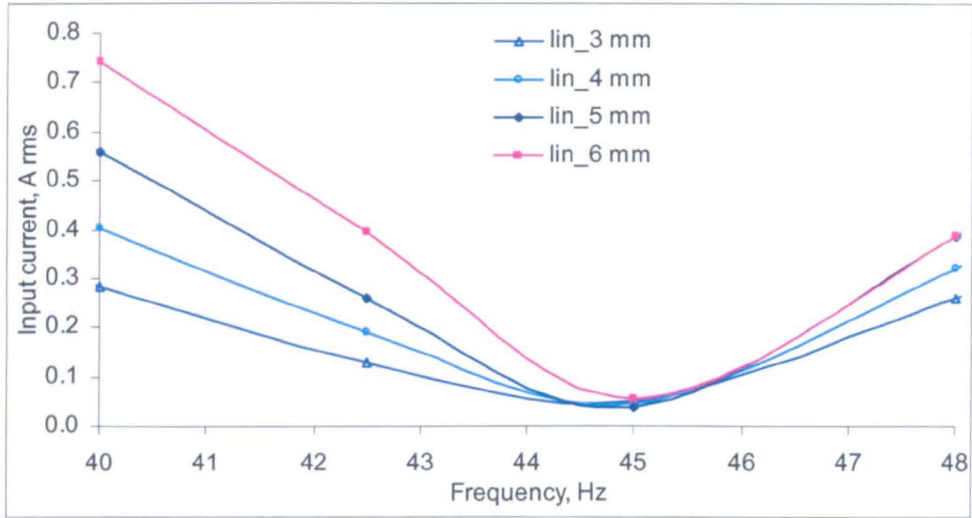
Fig. 6.10 Measured results as functions of time at 9.0 mm stroke

6.6 Iron loss results

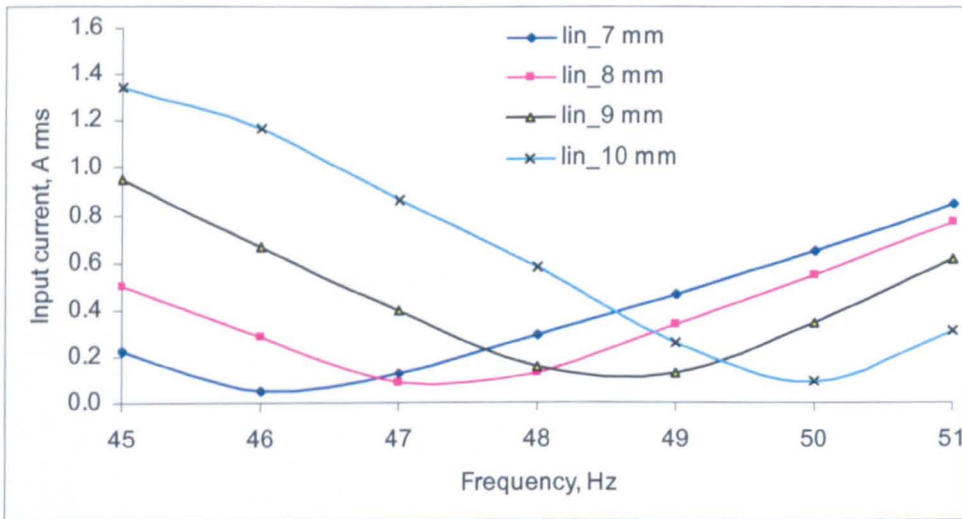
6.6.1 Measured data

Figs. 6.11 (a) and (b) show the variations of measured input current at different stroke with frequency. As will be seen, for a given stroke, the motor current is minimum at the resonant frequency. The resonant frequency, f_r , for stroke equal to 3.0 mm to 6.0 mm is the same, i.e. 45 Hz. However, the resonant frequency varies when the stroke is greater than 6.0 mm as shown Fig. 6.11 (b). This is due to the

non-linear force-displacement characteristic of the disc spring. The stiffness increases as the displacement being greater than 6.0 mm. The resonant frequencies for 7.0 mm, 8.0 mm, 9.0 mm and 10.0 mm strokes are 46 Hz, 47 Hz, 48 Hz and 50 Hz respectively.



a. 3.0 mm to 6.0 mm stroke

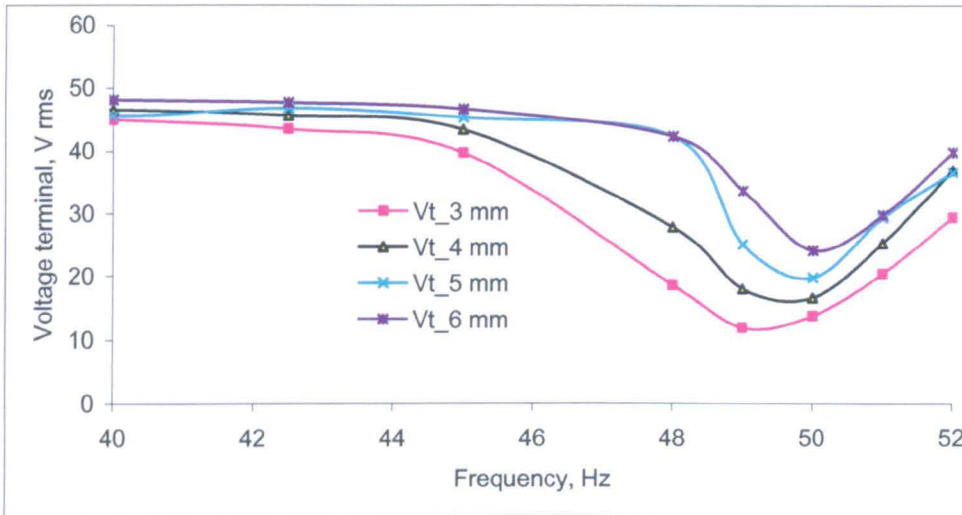


b. 7.0 mm to 10.0 mm stroke

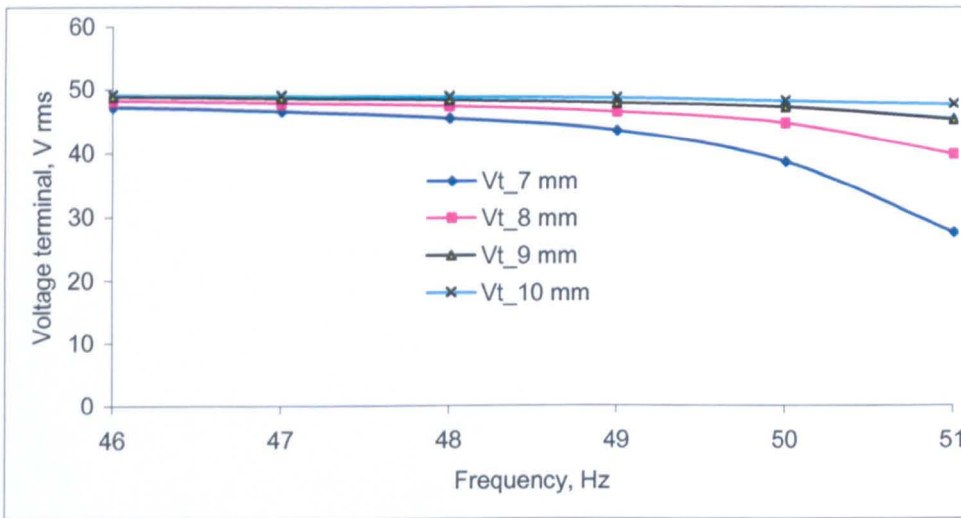
Fig. 6.11 Variations of input current at different stroke with frequency

Fig. 6.12 shows variations of motor input voltage with frequency for different values of stroke. As will be seen, the minimum voltage occurs at a frequency slightly higher than the resonant frequency. This is due to the fact that although at the resonant

frequency, the current is minimum, the system impedance is high since the total system resistance is at its maximum [10]. As the frequency increases beyond the resonant frequency, the decrease in the total system impedance due to both decreases in resistance and inductance, is faster than the increase in current. Consequently, the voltage continues to decrease until such a trend is reversed.



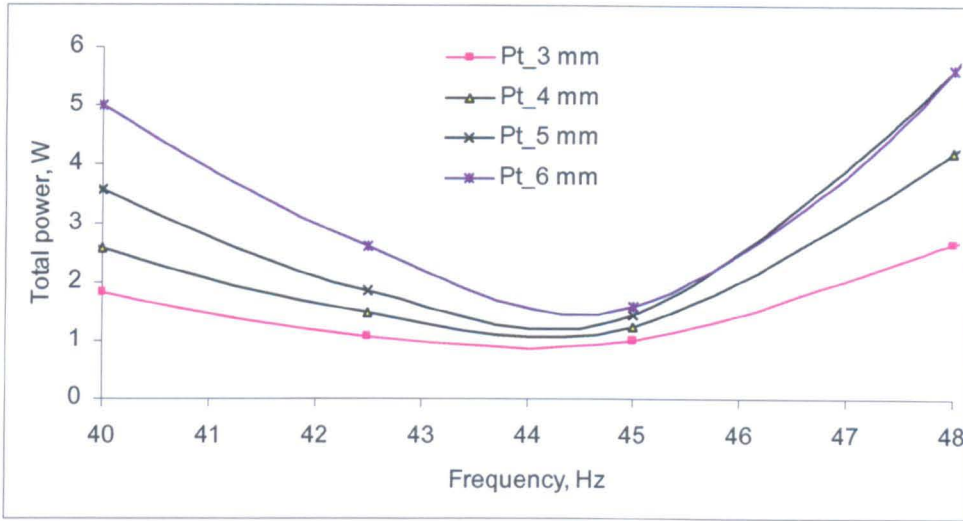
a. 3.0 mm to 6.0 mm stroke



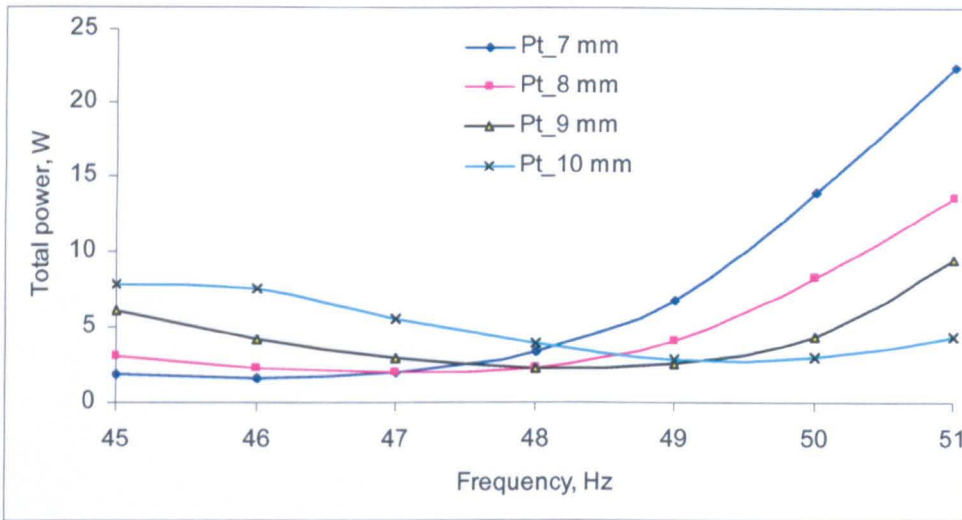
b. 7.0 mm to 10.0 mm stroke

Fig. 6.12 Variations of voltage terminal at different stroke with frequency

Fig. 6.13 shows the variations of the total power at different strokes with frequency. As will be observed, the output power at the resonant frequency is minimum due to the minimum motor current.



a. 3.0 mm to 6.0 mm stroke



b. 7.0 mm to 10.0 mm stroke

Fig. 6.13 Variations of total power at different stroke with frequency

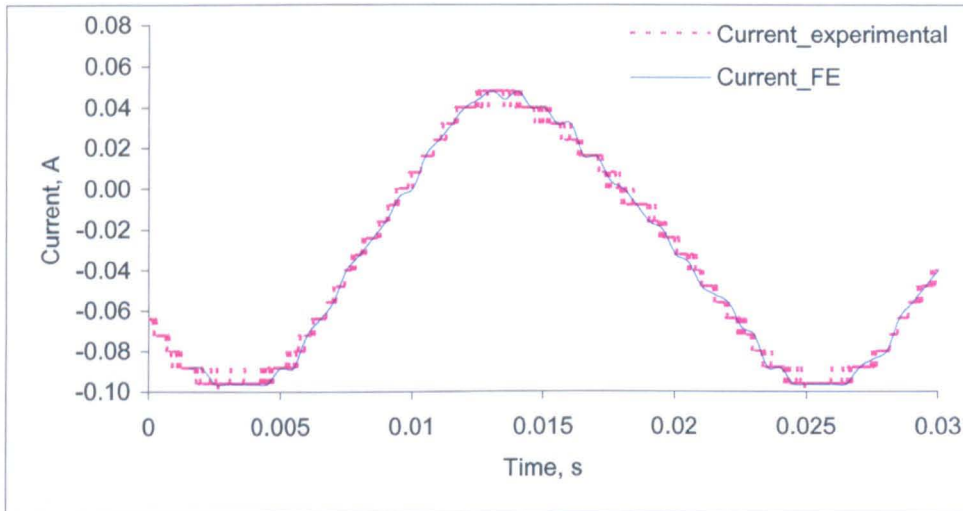
6.6.2 Comparison with finite element analysis

The measured current and armature displacement waveforms at a given stroke and frequency were fed into the finite element model. By way of example, Figs. 6.14 (a), (b) compare the measured current and displacement waveforms, respectively, with

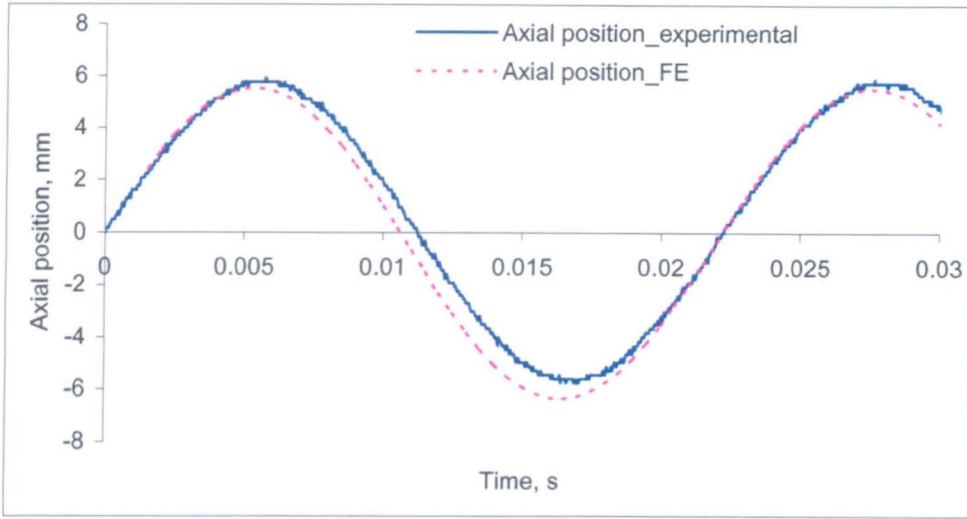
that used in the finite element prediction at 6.0 mm stroke and 45 Hz frequency. As will be seen, at resonance, the current is very small, and the quantisation effect of the measurement is neglected in the prediction.

Fig. 6.14 (b), it can be observed that, the axial displacement is not entirely symmetrical with respect to the centre. This may be due to the fact that the stiffness of the springs located at two sides is not identical. However, this asymmetry is not represented in the finite element model.

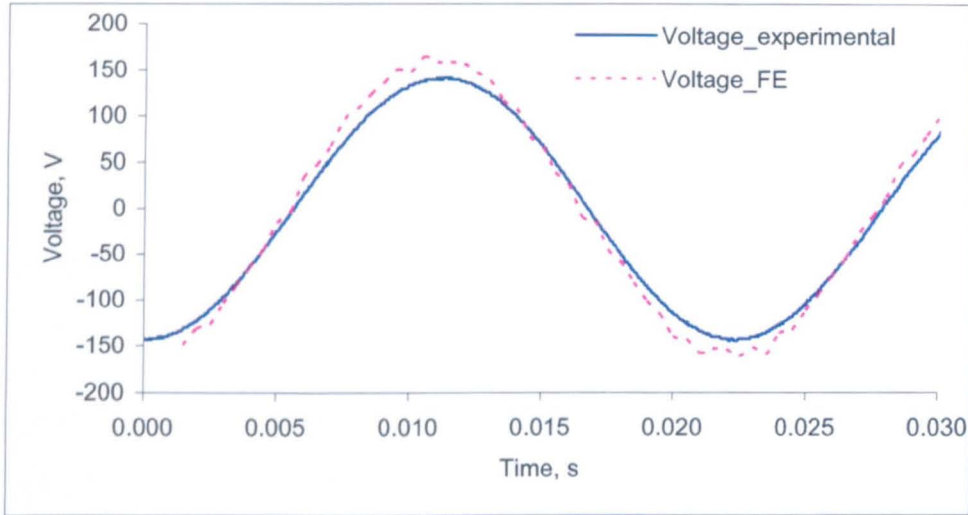
Fig. 6.14 (c) compares the measured and finite element predicted motor voltage waveforms. As will be seen, the experimental result agrees reasonably well with finite element prediction.



a. Motor current



b. Axial position



c. Voltage terminal

Fig. 6.14 Comparison of measured and predicted results at 6 mm stroke

Since at resonance conditions, the no-load current is very small and the resulting armature reaction field is negligible. The no-load iron loss, P_{fe} , can be determined by subtracting the copper loss, P_{cu} , and the eddy current loss, P_{eddy} , from the measuring total input power, P_t , as given by

$$P_{fe} = P_t - P_{cu} - P_{eddy} \quad 6.1$$

The P_{cu} and the P_{eddy} are obtained by $i_{rms}^2 R$ and finite element prediction as described in Chapter 5, respectively, and the data of P_t , P_{cu} , P_{eddy} and f_r are tabulated in Table 6.1.

Table 6.1 Total power, copper loss and eddy current loss at different stroke

Stroke length (mm)	P_t (W)	P_{cu} (W)	P_{eddy} (W)	f_r (Hz)
3.0	1.000	0.026	0.007	45
4.0	1.248	0.023	0.008	45
5.0	1.435	0.015	0.006	45
6.0	1.589	0.029	0.006	45
7.0	1.687	0.030	0.012	46
8.0	1.999	0.080	0.027	47
9.0	2.612	0.197	0.061	48
10.0	2.915	0.096	0.072	50

Fig. 6.7 compares the variation of the measured and finite element predicted iron loss with armature stroke at the corresponding resonant frequency, f_r . As will be seen, the finite element calculations agree reasonably well with the experimental results and the average percentage error is relatively small, i.e. 4.79 %. Theoretically, the same method may be used to obtain measured iron loss at on-load conditions. However, since the copper loss and eddy current loss are larger or comparable to the iron loss, the subtraction using equation 6.1 will result in a large error. The measurement accuracy will be further compounded by the fact that the vibration of the test rig increases under on-load conditions, and the power/energy dissipated through the vibration, which is a part of motor input power, cannot be quantified.

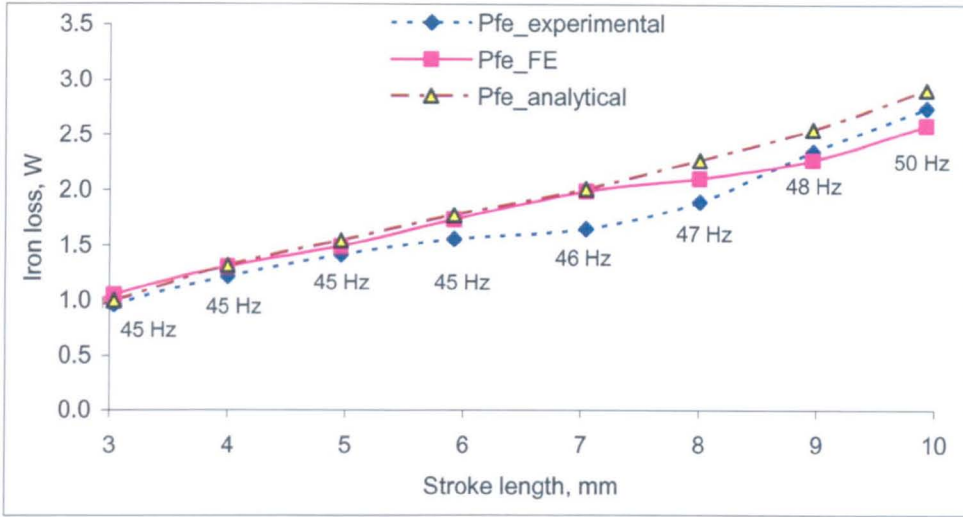


Fig. 6.15 Comparison of measured and predicted iron loss

6.7 Performance test

The efficiency of the iron-cored quasi-Halbach magnetised motor with rectangular magnets is evaluated by the experimental setup shown in Fig. 6.16, where the two identical motors are connected back-to-back, one operating as motor and the other as generator whose output is connected to a variable resistor. Mechanical springs to facilitate resonant operation are incorporated in both the machines.

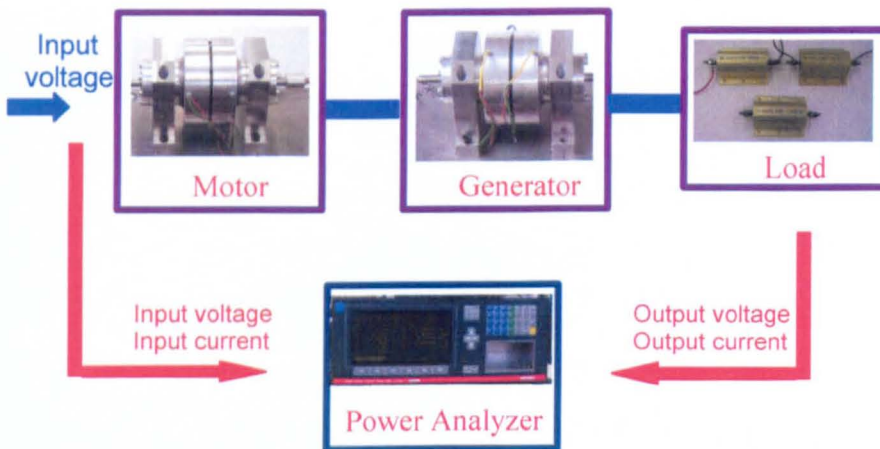


Fig. 6.16 Schematic of load test set-up for prototype motor

The motor is supplied by a variable frequency/amplitude sinusoidal power source, and the input and output powers of the motor and generator are measured by the

power analyzer. The losses of the machine under testing include the mechanical loss P_{mi} and the electromagnetic loss P_{ei} . The mechanical loss is due to the bearing friction and vibration of the test rig, and the electromagnetic loss consists of the copper loss, P_{cu} , the iron loss, P_{iron} and the eddy current loss, P_{eddy} , of the moving-magnet armature. The sum of P_{iron} and P_{eddy} is denoted by P_{ie} . To separate these loss components, three no-load tests were performed at a given supply frequency and armature stroke. The first no-load test was carried out with one motor only, and the total loss measured as the input power P_{L1} is given by:

$$P_{L1} = P_{mi} + P_{ie} + P_{cu1} \quad 6.2$$

The second no-load test was performed with two machines back-to-back connected but the magnetic armature of the second machine was replaced by a dummy one with the same weight. Thus, the loss in the second machine is purely mechanical. Assume that the mechanical loss of the two machines are identical, the total no-load loss is given by:

$$P_{L2} = 2P_{mi} + P_{ie} + P_{cu2} \quad 6.3$$

In the third no-load test, the second machine is equipped with the magnetic armature which results in iron loss and eddy current loss. Again assume that these two loss components are identical in the two machines, the total no-load loss is given by:

$$P_{L3} = 2P_{mi} + 2P_{ie} + P_{cu3} \quad 6.4$$

The copper loss in each test can be quantified by measuring the input current and the coil resistance. Hence, the mechanical loss and the sum of the iron and eddy current loss can be evaluated by:

$$\begin{aligned} P_{mi} &= (P_{L2} - P_{cu2}) - (P_{L1} - P_{cu1}) \\ P_{ie} &= (P_{L3} - P_{cu3}) - (P_{L2} - P_{cu2}) \end{aligned} \quad 6.5$$

The variations of these two loss components as functions of supply frequency and armature stroke can be obtained by performing tests at different frequencies and strokes.

Load tests were performed on the back-to-back connected motor-generator system. The mechanical loss of the system can be separated from the measured input and output powers using the data obtained in the no-load tests. The copper loss of each machine is calculated from measured current and coil resistance and the efficiencies of the motor and generator are evaluated by measured input and output powers and the iron loss components obtained in the no load tests. Fig. 6.17 shows the variation of the machine efficiencies with supply frequency for a fixed stroke of 10.0 mm when the generator was connected to a 440 Ω resistive load and its output power varies from 72 W to 80 W.

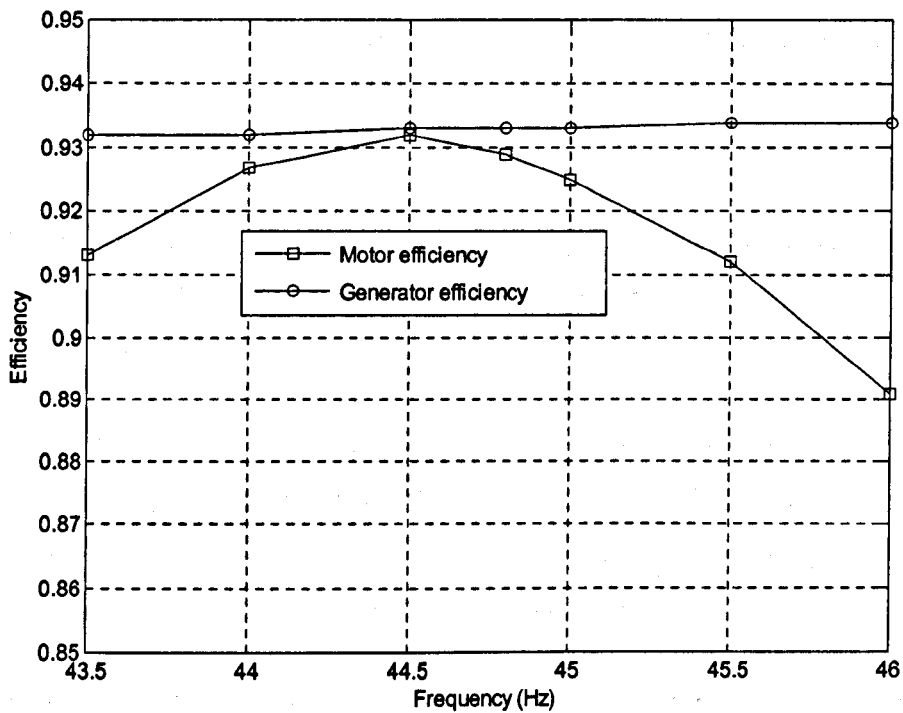


Fig. 6.17 Measured motor and generator efficiencies as functions of frequency at 10.0mm stroke

The resonant frequency of the system is 44.5 Hz when the equivalent stiffness of compressed gas is not present. As will be seen, the efficiency of the generator is fairly constant with frequencies and above 93 %, which is close to the predicted value of 94 %. However, the efficiency of the motor deteriorates when the operational frequency is higher or lower than the resonant frequency of 44.5 Hz. Nevertheless, the efficiency at resonant frequency is around 93 %, which is also close to the predicted value of 94 %.

6.8 Conclusions

A test rig has been constructed in order to measure the static performances of the air-cored quasi-Halbach magnetised motor with rectangular magnets. The measured flux linkage, cogging force and static thrust force of the motor agree reasonably well with the finite element predictions.

An iron loss test rig has also been constructed in order to measure the iron loss of the iron-cored quasi-Halbach magnetised motor with rectangular magnets. The iron loss has been predicted at resonant frequencies at various strokes and the measured results were also agreed reasonably well with the finite element predictions. The performance of the iron-cored quasi-Halbach magnetised motor with rectangular magnets has also been measured and the maximum motor efficiency is 93 %.

References

- [1] G. Bertotti, "General properties of power losses in soft ferromagnetic materials," *IEEE Transactions on Magnetics*, vol. 24, no. 1, pp. 621-630, January 1988.
- [2] B. Stumberger, V. Gorican, G. Stumberge, A. Hamler, M. Trlep, and M. Jesenik, "Accuracy of iron loss calculation in electrical machines by using different iron loss models," *Journal of Magnetism and Magnetic Material*, vol. 272-276, no. 1, pp. E1723-E1725, May 2004.
- [3] H. Lee, H. Moon, S. Wang, and K. Park, "Iron loss analysis of linear oscillating actuator for linear compressor," *The International Journal for Computation and Mathematics in Electrical and Electronic Engineering*, vol. 25, no. 2, pp. 487-495, 2006.
- [4] C. Mi, G. R. Salmon, and R. Bonert, "Modelling of iron losses of permanent magnet synchronous motors," *IEEE Transactions on Industry Applications*, vol. 39, no. 3, pp. 734-742, June 2003.
- [5] M. Utsuno, M. Takai, T. Mizuno, and H. Yamada, "Comparison of the losses of a moving-magnet type linear oscillatory actuator under two driving

methods," *IEEE Transactions on Magnetics*, vol. 38, no. 5, pp. 3300-3302, September 2002.

- [6] T. Ibrahim, J. Wang, and D. Howe, "Iron loss calculation in a reciprocating tubular permanent magnet motor with soft magnetic composite," *Proceeding of XVII International Conference on Electrical Machines, ICEM2006, Chania, Greece*, September, 2006.
- [7] Y. Amara, J. Wang, and D. Howe, "Stator iron loss of tubular permanent magnet machines," *IEEE Transactions on Industry Applications*, vol. 41, no. 4, pp. 989-995, July/August 2005.
- [8] J. Chai, J. Wang, and D. Howe, "Evaluation of eddy current loss in tubular permanent magnet motors by three-dimensional finite element analysis," *Proceedings of XVII International Conference on Electrical Machines (ICEM2006), Paper ID: PSA1-12, Chania, Greece*, September 2006.
- [9] Cedrat, "FLUX 2D and 3D User Application Manual," 2005.
- [10] J. Wang and D. Howe, "Modelling of linear reciprocating compressor system," *Carbon Thrust Project Number 2003-3-51-1-1, University of Sheffield*, June 2004.
- [11] J. Wang, Z. Lin, and D. Howe, "Analysis of a short stroke, single phase quasi-Halbach magnetised tubular permanent magnet motor for linear compressor applications," *IET Electric Power Application*, vol. 2, no. 3, pp. 193-200, January 2008.
- [12] Hogan, "Somaloy brochure available at: www.hoganas.com."
- [13] T. Ibrahim, J. Wang, and D. Howe, "Analysis of a single-phase, quasi-Halbach magnetised tubular permanent magnet motor with non-ferromagnetic support tube," *14th IET International Conference on Power Electronics, Machines and Drives, PEMD, York, United Kingdom*, vol. 1, pp. 762-766, April 2008.

- [14] Z. S. Al-Otaibi and A. G. Jack, "Utilising SMC in single-phase permanent magnet linear motors for compressor applications," *14th IET International Conference on Power Electronics, Machines and Drives, PEMD, York, UK*, vol. 1, pp. 752-753, April 2008.
- [15] Z. S. Al-Otaibi and A. G. Jack, "Spiral flexure springs in single phase linear-resonant motors," *Proceeding of Universities Power Engineering Conference, UPEC2007, Brighton, United Kingdom*, pp. 184-187, September 2007.

CHAPTER 7

CONCLUSIONS AND FUTURE WORKS

7.1 Conclusions

An extensive literature review has been conducted encompassing various topologies and technologies of linear motor in order to identify the most promising candidates for refrigerator compressors. Tubular moving-magnet linear motors offer significant advantages in terms of the achievable force density, efficiency, reliability and simplicity of construction. Three design variants were selected viz. a single-slot tubular moving-magnet linear motor, with different magnet configurations including iron-cored and air-cored quasi-Halbach magnetised armatures having a rectangular or trapezoidal cross-section.

Analytical models are useful tool to aid the design of permanent magnet linear motors especially in order to obtain initial dimensioning of motor and also the technique is less time consuming compared to finite element method. In this design study, analytical formulae for predicting the open-circuit magnetic field distribution, the flux linkage, and the back-emf and thrust force of the selected motors have been established. The accuracy of the analytically derived formulae has been validated by comparing results with those deduced from finite element analyses. It has been shown that the analytically finite element predicted open-circuit magnetic field distribution and back-emf agree reasonably well for all these motors under consideration.

A design methodology to achieve optimal performance of the direct-drive linear compressor system employing the iron-cored quasi-Halbach magnetized motor with trapezoidal magnets and the air-cored quasi-Halbach magnetized motor with rectangular magnets have been described, and the influence of the leading design parameters on the system efficiency have been studied analytically. It has been shown that in such a direct-drive system, the compressed gas has a significant effect on the input impedance of the electrical system, and it is essential that the gas load effect is taken into account in the design optimization. Due to the limitation of analytical solution which cannot accommodate complex geometries and material non-linearities, the leading design parameters have been refined with finite element analysis, which results in slightly different design values and improved efficiency. The

efficiency of the iron-cored quasi-Halbach magnetized motor with trapezoidal magnets is higher than that of the air-cored quasi-Halbach magnetized motor with rectangular magnets. However, its manufacturing cost may be higher due to the process of cutting trapezoidally shaped magnets.

An alternative design, a moving-iron tubular permanent magnet motor for refrigerator compressor systems has been proposed and optimised using finite element method. Initially, the leading design parameters are optimised individually, however, one parameter may influence other parameters in term of optimal performance of the motor. Therefore, two leading parameters are required to optimise simultaneously. Both procedures shown the same results of leading dimension parameters were obtained. It has also been shown that in order to achieve satisfactory efficiency, the volume of the motor has to be increased significantly. However with the available space on a typical household refrigerator compressor, the efficiency of the moving-iron motor is ~ 2 % lower than the moving-magnet designs. In addition, the material cost of the moving-iron motor is very close to those of the moving-magnet motors due to employ a cheap magnet material. However, its manufacturing cost is likely to be lower, since the permanent magnets have a simple shape, and will be easier for assembly.

An extensive analysis of eddy current loss in the moving-magnet armatures has been undertaken. The eddy current losses in the permanent magnets and the supporting tube of the iron-cored quasi-Halbach magnetised motor with trapezoidal magnets and the air-cored quasi-Halbach magnetised motor with rectangular magnets have been analysed using time-stepped two- and three-dimensional finite element analysis. The use of segmentations offers the significant advantage in reducing eddy current loss in the permanent magnets and supporting tube. By circumferentially segmenting the magnets, the eddy current loss of the air-cored motor is relatively small and can be negligible due to the absence of a ferromagnetic tube. However, the eddy current loss in the iron-cored motor needs to be considered due to the loss in the supporting tube was contributed significantly to the total eddy current loss. This is due to the circumferential segmentation of the tube is less effective due to its longer axial length, and its higher permeability and electrical conductivity.

The iron loss of the iron-cored quasi-Halbach magnetised motor with rectangular magnets has been evaluated under both no-load and on-load conditions using two-dimensional time-stepped finite element analysis. This allows the iron loss to be

calculated with arbitrary armature velocity and stator current waveforms, with due account of minor hysteresis loops. It has been shown that the no-load iron loss which results with a sinusoidal armature velocity is very close to that which would result if the armature moves at a constant velocity equal to the average value of the sinusoidal velocity profile.

Comparisons of material costs and performance for four design variants have been carried out and based on the light weight of armature which is conducive to improve dynamic capability of the compressor system and ease of manufacturing, the air-cored quasi-Halbach magnetised magnet with rectangular magnets has been selected for prototyping. A test rig has been constructed in order to measure the static performances of the motor. The measured flux linkage, cogging force and static thrust force of the motor agree reasonably well with the finite element predictions.

An iron loss test rig has also been constructed in order to measure the no-load iron loss of the iron-cored quasi-Halbach magnetised motor with rectangular magnets. The no-load iron loss has been predicted at resonant frequencies where at this condition, the motor current is minimum and the armature reaction field is negligible, thus allows the flux density in the stator core purely dominated from permanent magnets. The influence of the copper loss resulting in the eddy current loss is also small. The measured current and armature displacement waveforms from the test rig at a given stroke and frequency were fed into the finite element model. The measured iron losses were compared and agreed reasonably well with the finite element predictions. Theoretically, iron loss at on-load conditions can be measured by supplying current to the motor. However, since the copper loss and eddy current loss are larger or comparable to the iron loss, the subtraction from the input power will result in a large error. The measurement accuracy will also be further compounded by the fact that the vibration of the test rig increases under on-load conditions, and the power/energy dissipated through the vibration, which is a part of motor input power, cannot be quantified.

The techniques to separate electromagnetic and mechanical loss by three different measurements were introduced in order to measure the performance of the iron-cored quasi-Halbach magnetised motor with rectangular magnets. It has been shown that the measured motor efficiency is much higher than conventional induction motor and may possibly reduce the CO₂ emission from refrigerator compressor system.

7.2 Future works

Some issues which are worthy of further investigations are:

- Rotational loss calculation

In this design study, the iron loss calculation is purely based on alternating flux density either in axial or radial direction using Bertotti equation. However, rotational loss which is a part of iron loss has been discussed broadly in electrical machines. The loss is significant especially in designing high efficiency motor in order to obtain more accurate results. Theoretically, the rotational loss occurs when the flux density vector rotates, and its locus moves along an ellipse instead of a straight line. This condition normally occurs at the tooth tip and the corner joints of the stator core as shown in Fig. 5.26 (b). Based on the result shown in Fig. 3.6, both radial and axial flux density components in the tooth tip region are significant and the associated rotational loss should be analysed and quantified.

- Implement to air-conditioning compressor system

The design methodology for linear permanent magnet motors described in this thesis may be applicable to direct-drive air-conditioning systems which have a similar compressor system to domestic refrigerators. The air-conditioning appliances are widely used especially in tropical regions such as in Middle East, Asia and Africa and their power consumption is massive. It is therefore worthy of investigating the potential energy saving of employing drive-drive linear compressors for air-conditioning systems.

APPENDICES
Appendix A
List of publications

Journal

1. **T. Ibrahim, J. Wang, and D. Howe,** "Analysis and experimental verification of a single-phase, quasi-Halbach magnetised tubular permanent magnet motor with non-ferromagnetic tube, *IEEE Transactions on Magnetics*, vol. 44, no. 11, pp. 4361-4364, November 2008.

Conference paper

2. **T. Ibrahim, J. Wang, and D. Howe,** "Iron loss calculation in a reciprocating tubular permanent magnet motor with soft magnetic composite," *Proceeding of XVII International Conference on Electrical Machines, ICEM2006, Chania, Greece, September, 2006.*
3. **T. Ibrahim, J. Wang, and D. Howe,** "Analysis of a short-stroke, single-phase tubular permanent magnet actuator for reciprocating compressors," *6th International Symposium on Linear Drives for Industrial Applications, LDIA2007, Lillie, France, September 2007.*
4. **T. Ibrahim, J. Wang, and D. Howe,** "Analysis of a single-phase, quasi-Halbach magnetised tubular permanent magnet motor with non-ferromagnetic support tube," *14th IET International Conference on Power Electronics, Machines and Drives, PEMD, York, United Kingdom, vol. 1, pp. 762-766, April 2008.*
5. **T. Ibrahim, J. Wang, and D. Howe,** "Analysis and experimental verification of a single-phase, quasi-Halbach magnetised tubular permanent magnet motor " *IEEE International Magnetic Conference, INTERMAG2008, Madrid, Spain, 4-8 May 2008.*
6. **J. Wang, T. Ibrahim, and D. Howe,** "Design optimisation of short-stroke, single phase tubular permanent magnet motor for refrigeration applications," *Proceedings of the 2008 International Conference on Electrical Machines, ICEM2008, Portugal, Paper ID 1402, September 2008.*

Appendix B

Magnetisation formulae of trapezoidal magnets

The coefficients in equation 2.6 are defined below:

$$M_{mT1} = \frac{-4B_{rem}}{T_{lp}\mu_r m_n} \left(\cos m_n \left(\frac{T_p + \frac{T_{mr}}{2} + T_{mz} - \frac{h_m}{2}}{2} \right) \sin m_n \left(\frac{T_p - \frac{T_{mr}}{2} - T_{mz} + \frac{h_m}{2}}{2} \right) \right)$$

$$M_{mT2} = \frac{4B_{rem} \left(\frac{T_{mr}}{2} + T_{mz} + \frac{h_m}{2} \right)}{T_{lp}\mu_r m_n h_m} \left(\cos m_n \left(\frac{T_{mr} + 2T_{mz}}{2} \right) \sin m_n \left(\frac{h_m}{2} \right) \right) +$$

$$\frac{2B_{rem}}{T_{lp}\mu_r m_n h_m} \left[\left(\frac{-2 \sin m_n \left(\frac{T_{mr} + 2T_{mz}}{2} \right) \sin m_n \left(\frac{h_m}{2} \right)}{m_n^2} \right) + \left(\frac{\frac{T_{mr}}{2} + T_{mz} - \frac{h_m}{2}}{m_n} \right) \left(\sin m_n \left(\frac{T_{mr}}{2} + T_{mz} - \frac{h_m}{2} \right) \right) \right] -$$

$$\frac{2B_{rem}}{T_{lp}\mu_r m_n h_m} \left(\frac{\frac{T_{mr}}{2} + T_{mz} + \frac{h_m}{2}}{m_n} \right) \left(\sin m_n \left(\frac{T_{mr}}{2} + T_{mz} + \frac{h_m}{2} \right) \right).$$

$$M_{mT4} = \frac{4B_{rem}}{T_{lp}\mu_r m_n} \left(\sin m_n \left(\frac{T_{mr}}{2} + \frac{h_m}{2} \right) \right)$$

$$M_{mT3} = \frac{4B_{rem} \left(\frac{T_{mr}}{2} - \frac{h_m}{2} \right)}{T_{lp}\mu_r m_n h_m} \left(\cos m_n \left(\frac{T_{mr}}{2} \right) \sin m_n \left(\frac{h_m}{2} \right) \right) +$$

$$\frac{2B_{rem}}{T_{lp}\mu_r m_n h_m} \left[\left(\frac{-2 \sin m_n \left(\frac{T_{mr}}{2} \right) \sin m_n \left(\frac{h_m}{2} \right)}{m_n^2} \right) + \left(\frac{\frac{T_{mr}}{2} - \frac{h_m}{2}}{m_n} \right) \left(\sin m_n \left(\frac{T_{mr}}{2} - \frac{h_m}{2} \right) \right) \right] -$$

$$\frac{2B_{rem}}{T_{lp}\mu_r m_n h_m} \left(\frac{\frac{T_{mr}}{2} + \frac{h_m}{2}}{m_n} \right) \left(\sin m_n \left(\frac{T_{mr}}{2} + \frac{h_m}{2} \right) \right)$$

$$M_{znT1} = \frac{-4B_{rem} \left(\frac{T_{mr}}{2} + T_{mz} + \frac{h_m}{2} \right)}{T_{ip} \mu_r h_m m_n} \left(\sin m_n \left(\frac{T_{mr} + 2T_{mz}}{2} \right) \sin m_n \frac{h_m}{2} \right) +$$

$$\frac{2B_{rem}}{T_{ip} \mu_r m_n h_m} \left[\left(\frac{2 \cos m_n \left(\frac{T_{mr} + 2T_{mz}}{2} \right) \sin m_n \frac{h_m}{2}}{m_n^2} \right) + \left(\frac{\frac{T_{mr}}{2} + T_{mz} - \frac{h_m}{2}}{m_n} \right) \left(\cos m_n \left(\frac{T_{mr}}{2} + T_{mz} - \frac{h_m}{2} \right) \right) \right] -$$

$$\frac{2B_{rem}}{T_{ip} \mu_r m_n h_m} \left(\frac{\frac{T_{mr}}{2} + T_{mz} + \frac{h_m}{2}}{m_n} \right) \left(\cos m_n \left(\frac{T_{mr}}{2} + T_{mz} + \frac{h_m}{2} \right) \right).$$

$$M_{znT2} = -\frac{4B_{rem}}{T_{ip} \mu_r m_n} \left(\sin m_n \left(\frac{T_{mr} + 2T_{mz}}{2} \right) \sin m_n \frac{h_m}{2} \right)$$

$$M_{znT3} = \frac{4B_{rem} \left(\frac{T_{mr}}{2} - \frac{h_m}{2} \right)}{T_{ip} \mu_r h_m m_n} \left(\sin m_n \left(\frac{T_{mr}}{2} \right) \sin m_n \frac{h_m}{2} \right) -$$

$$\frac{2B_{rem}}{T_{ip} \mu_r m_n h_m} \left[\left(\frac{2 \cos m_n \left(\frac{T_{mr}}{2} \right) \sin m_n \left(\frac{h_m}{2} \right)}{m_n^2} \right) + \left(\frac{\frac{T_{mr}}{2} - \frac{h_m}{2}}{m_n} \right) \left(\cos m_n \left(\frac{T_{mr}}{2} - \frac{h_m}{2} \right) \right) \right] +$$

$$\frac{2B_{rem}}{T_{ip} \mu_r m_n h_m} \left(\frac{\frac{T_{mr}}{2} + \frac{h_m}{2}}{m_n} \right) \left(\cos m_n \left(\frac{T_{mr}}{2} + \frac{h_m}{2} \right) \right).$$

Appendix C
Coefficient of the iron-cored linear motors

Let

$$\begin{aligned} C_{1n} &= BI_0(m_n R_s); C_{2n} = BK_0(m_n R_s); \\ C_{3n} &= BI_1(m_n R_m); C_{4n} = BK_1(m_n R_m); \\ C_{5n} &= BI_0(m_n R_m); C_{6n} = BK_0(m_n R_m); \\ C_{7n} &= BI_1(m_n R_0); C_{8n} = BK_1(m_n R_0); \\ C_{9n} &= BI_0(m_n R_0); C_{10n} = BK_0(m_n R_0) \end{aligned}$$

$$\begin{aligned} F_{AN}(m_n r) &= \frac{P_n}{m_n} \int_{m_n R_0}^{m_n r} \frac{BK_1(x) dx}{BI_1(x)BK_0(x) + BK_1(x)BI_0(x)} \\ F_{BN}(m_n r) &= \frac{P_n}{m_n} \int_{m_n R_0}^{m_n r} \frac{BI_1(x) dx}{BI_1(x)BK_0(x) + BK_1(x)BI_0(x)} \end{aligned}$$

Let A_{In} , B_{In} , and $A_{II n}$ and $B_{II n}$ are solution of the following linear equations:

$$\begin{bmatrix} 1 & -\frac{C_{2n}}{C_{4n}} & 0 & 0 \\ \frac{C_{3n}}{C_{1n}} & 1 & \frac{C_{3n}}{C_{5n}} & \frac{C_{4n}}{C_{10n}} \\ \frac{C_{5n}}{C_{1n}} & -\frac{C_{6n}}{C_{4n}} & 1 & -\frac{C_{6n}}{\mu_r C_{10n}} \\ 0 & 0 & -\frac{\mu_r C_{9n}}{C_{5n}} & 1 \end{bmatrix} \begin{bmatrix} A_{In} \\ B_{In} \\ A_{II n} \\ B_{II n} \end{bmatrix} = \begin{bmatrix} 0 \\ C_{3n}F_{AN}(m_n R_m) - C_{4n}F_{BN}(m_n R_m) \\ \frac{1}{\mu_r} [C_{5n}F_{AN}(m_n R_m) + C_{6n}F_{BN}(m_n R_m)] - B_n \\ \mu_r B_n \end{bmatrix}$$

a_{In} , b_{In} , $a_{II n}$ and $b_{II n}$ are given by:

$$\begin{aligned} a_{In} &= \frac{A_{In}}{C_{1n}}; -b_{In} = \frac{B_{In}}{C_{4n}}; \\ a_{II n} &= -\frac{\mu_r A_{II n}}{C_{5n}}; -b_{II n} = -\frac{B_{II n}}{C_{10n}}; \end{aligned}$$

Appendix D
Coefficient of the air-cored linear motor

Let $A'_{In}, B'_{In}, A'_{IIIn}, B'_{IIIn}$ and A'_{IIIIn} are solution of the following linear equations:

$$\begin{bmatrix} 1 & -\frac{C_{2n}}{C_{4n}} & 0 & 0 & 0 \\ \frac{C_{3n}}{C_{1n}} & 1 & \frac{\mu_r C_{3n}}{C_{5n}} & -\frac{C_{4n}}{C_{8n}} & 0 \\ \frac{C_{5n}}{C_{1n}} & -\frac{C_{6n}}{C_{4n}} & 1 & -\frac{C_{6n}}{\mu_r C_{10n}} & 0 \\ 0 & 0 & -\frac{\mu_r C_{7n}}{C_{5n}} & 1 & \frac{C_{7n}}{C_{9n}} \\ 0 & 0 & -\frac{C_{9n}}{C_{5n}} & -\frac{C_{10n}}{\mu_r C_{8n}} & 1 \end{bmatrix} \begin{bmatrix} A'_{In} \\ B'_{In} \\ A'_{IIIn} \\ B'_{IIIn} \\ A'_{IIIIn} \end{bmatrix} = \begin{bmatrix} 0 \\ C_{3n}F_{AN}(m_n R_m) - C_{4n}F_{BN}(m_n R_m) \\ \frac{1}{\mu_r} [C_{5n}F_{AN}(m_n R_m) + C_{6n}F_{BN}(m_n R_m)] - B_n \\ 0 \\ B_n \end{bmatrix}$$

$a'_{In}, b'_{In}, a'_{IIIn}, b'_{IIIn}$ and a'_{IIIIn} are given by:

$$\begin{aligned} a'_{In} &= \frac{A'_{In}}{C_{1n}}; b'_{In}; \\ a'_{IIIn} &= -\frac{\mu_r A'_{IIIn}}{C_{5n}}; b'_{In} = \frac{B'_{In}}{C_{4n}}; \\ a'_{IIIIn} &= -\frac{\mu_r A'_{IIIIn}}{C_{9n}}; b'_{IIIn} = -\frac{B'_{IIIn}}{C_{8n}}; \end{aligned}$$

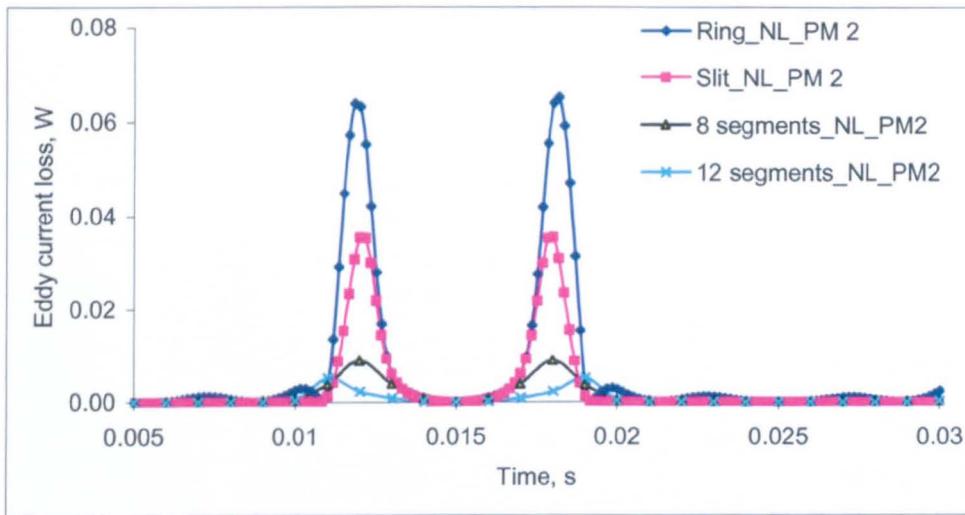
Appendix E

Analysis of eddy current loss in tubular permanent magnet linear motors using finite element method

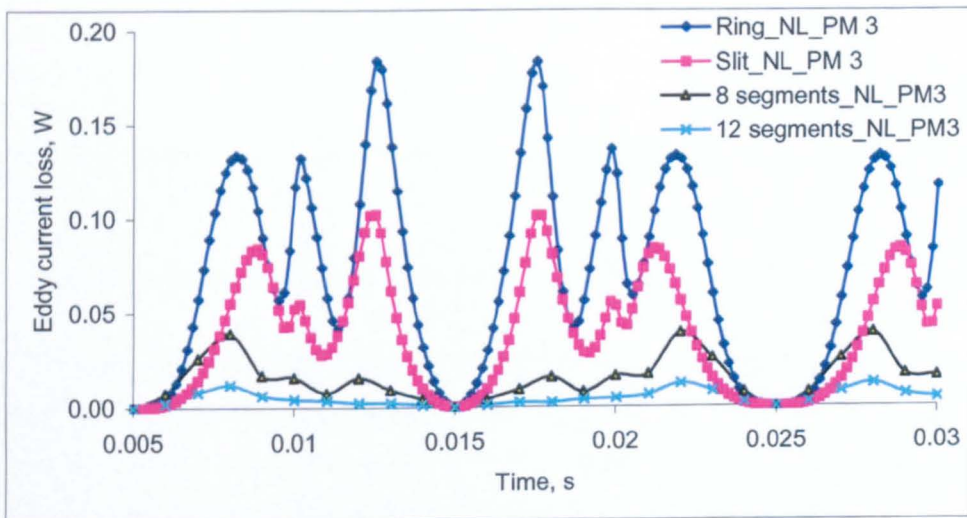
E.1 Eddy current at no-load condition

E.1.1 Air-cored quasi-Halbach magnetised motor with rectangular magnets

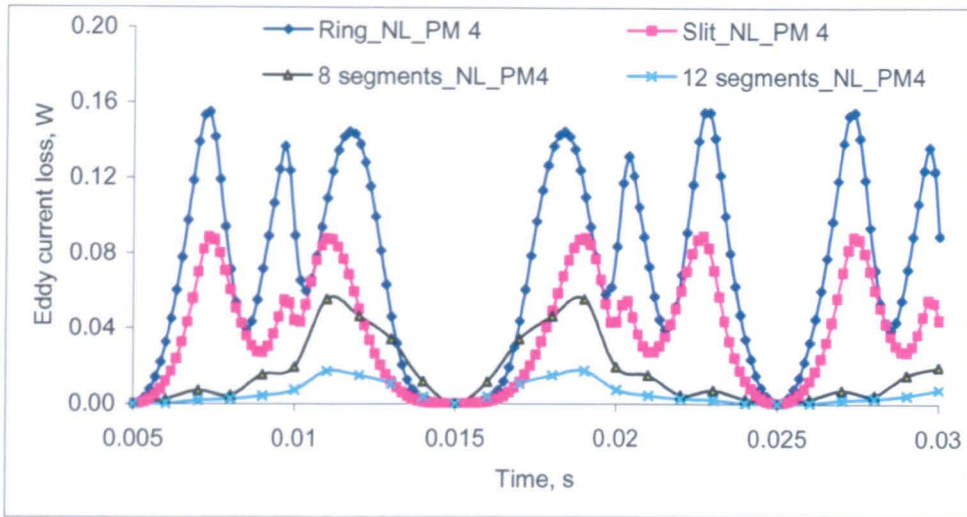
Fig. E.1 shows the variation of eddy current loss at no-load condition in permanent magnets with time for the air-cored motor when the magnet is segmented into different number of pieces. As will be observed, it is evident that the eddy current loss can be significantly reduced by segmenting the magnet.



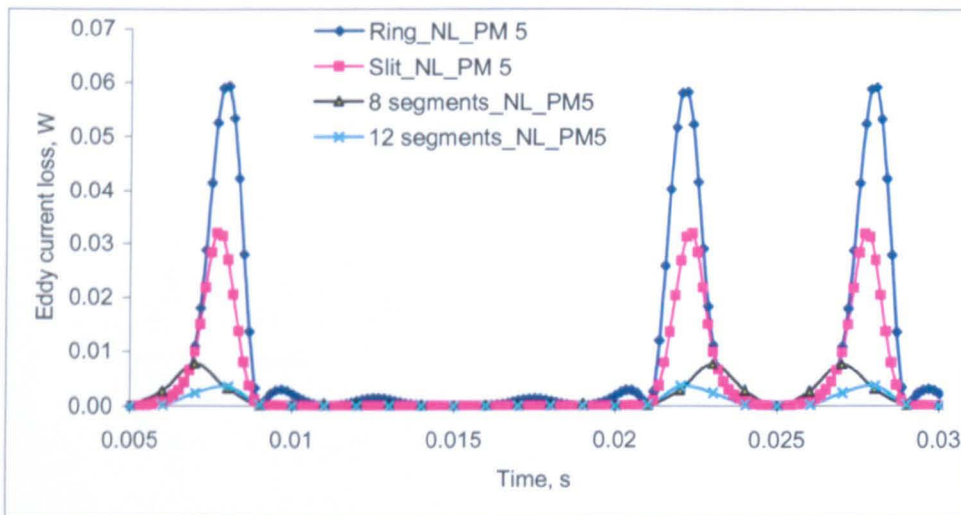
a. PM2



b. PM3



c. PM4

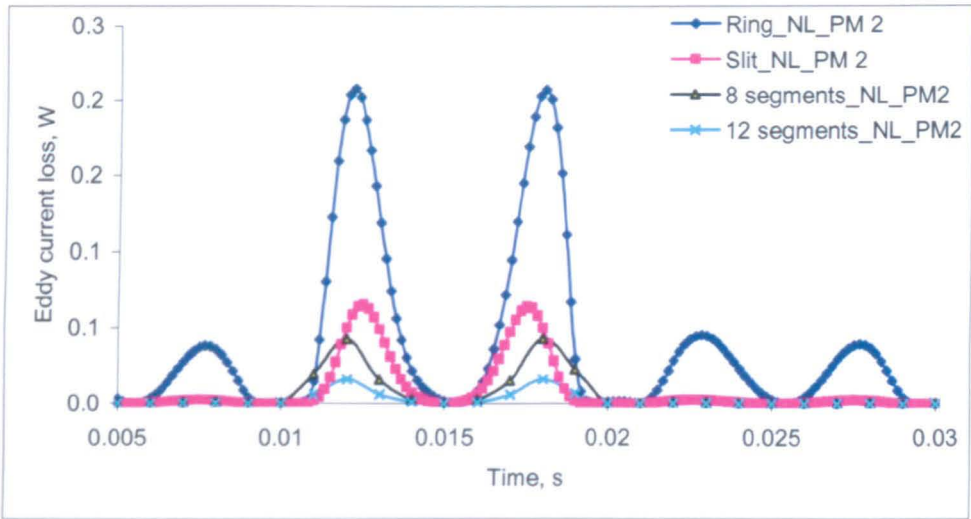


d. PM5

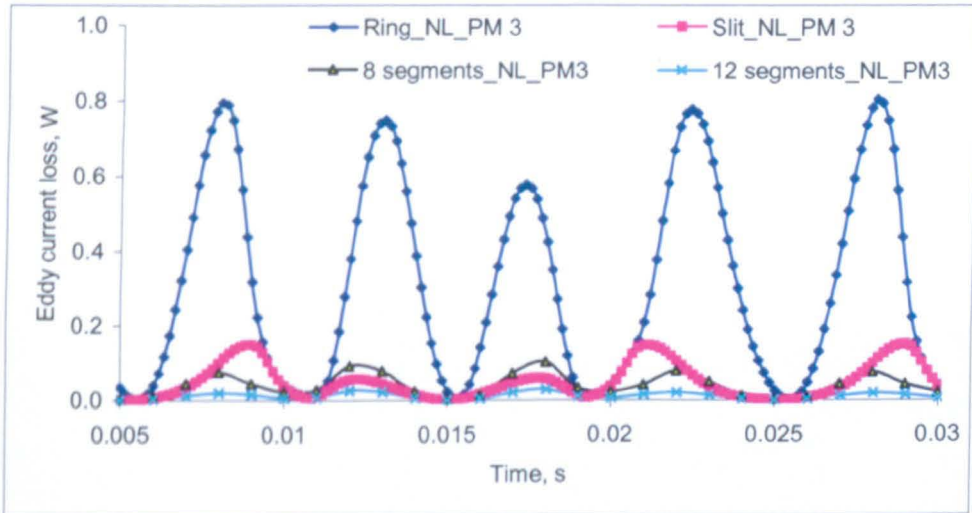
Fig. E.1 Eddy current loss in permanent magnets for air-cored motor at no-load condition

E.1.2 Iron-cored quasi-Halbach magnetised motor with trapezoidal magnets

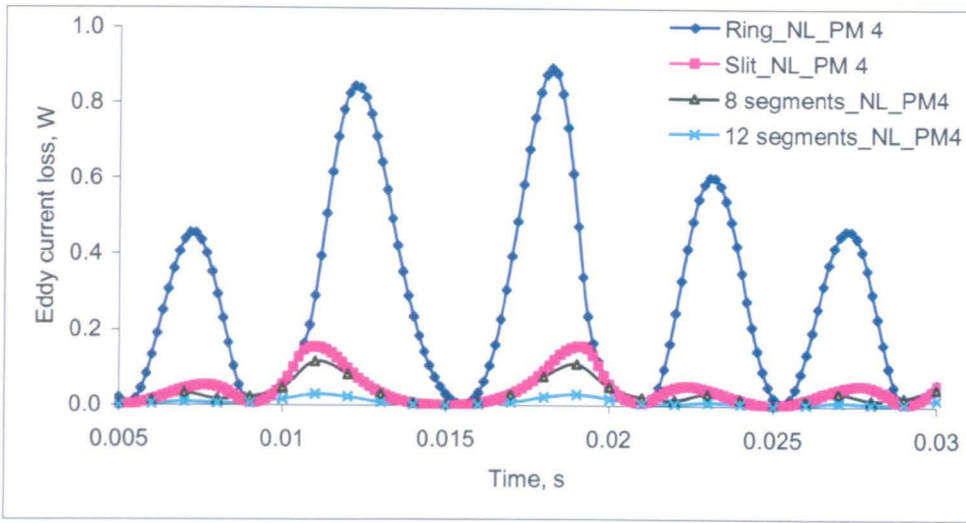
Fig. E.2 shows the time-variations of eddy current loss in permanent magnets for the iron-cored quasi-Halbach magnetised motor with trapezoidal magnets at no-load condition. A similar trend to those in Fig. E.1 is observed albeit the magnitude of the eddy current loss is higher due to the use of the mild steel supporting tube.



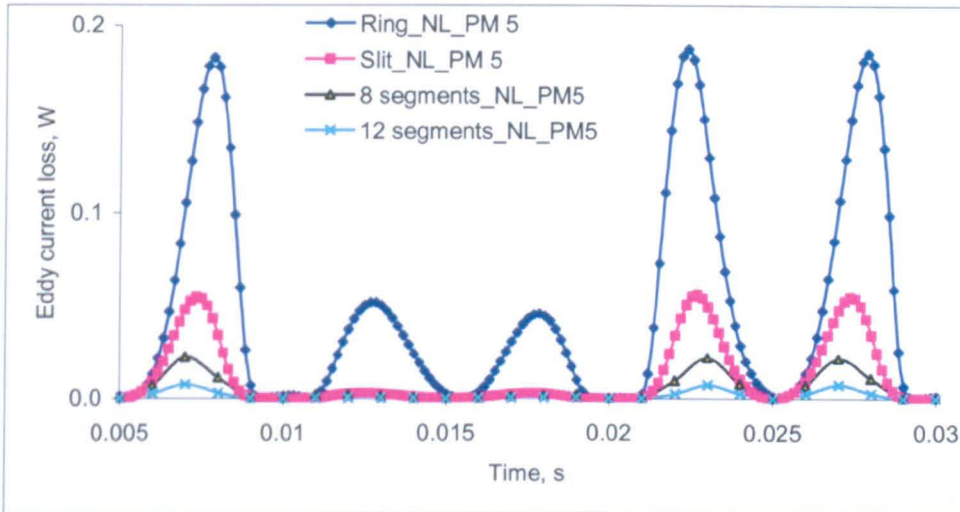
a. PM2



b. PM3



c. PM4



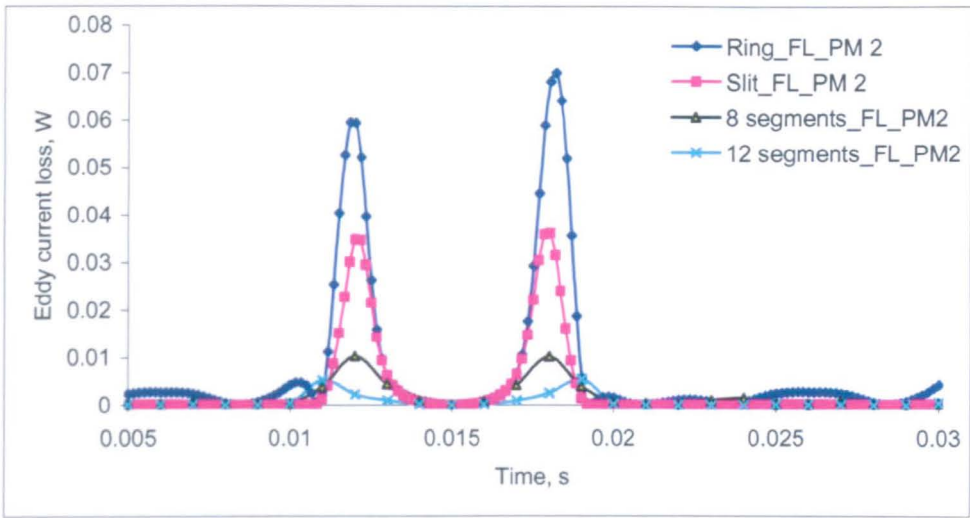
d. PM5

Fig. E.2 Eddy current loss in permanent magnets for iron-cored motor at no-load condition

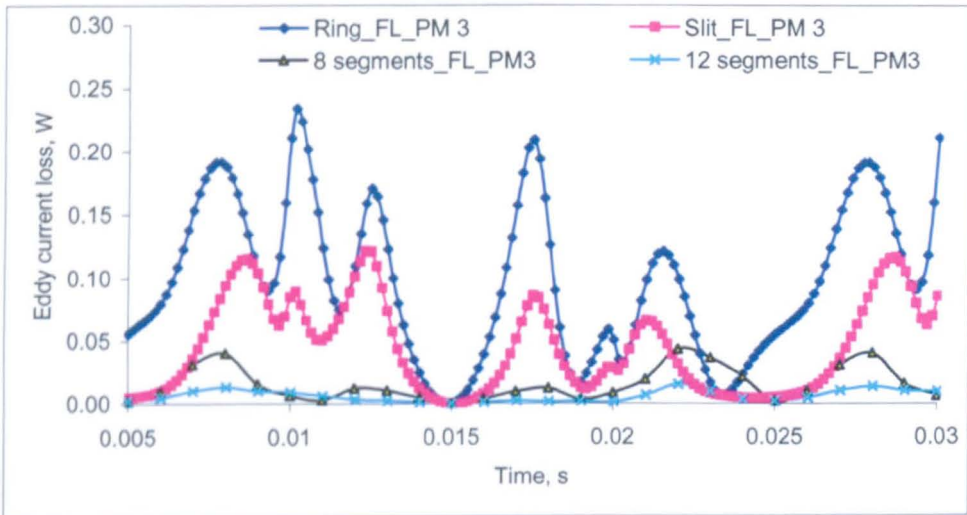
E.2 Eddy current at on-load condition

E.2.1 Air-cored quasi-Halbach magnetised motor with rectangular magnets

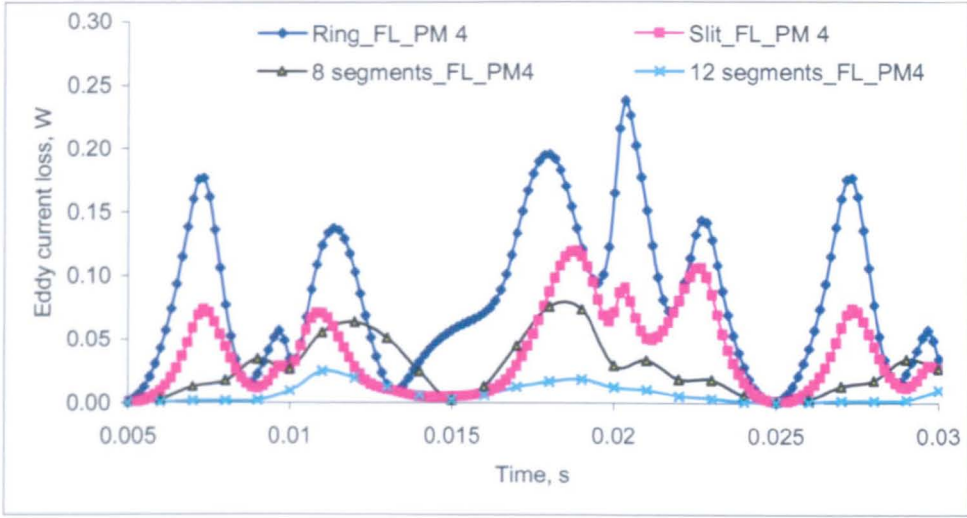
Fig. E.3 shows the time-variations of eddy current loss in permanent magnets, when it are segmented into different number of pieces for the air-cored motor at the same on-load condition as that specified in section 5.2.3. A similar trend to those in Fig. E.1 is observed albeit the magnitude of the eddy current loss is slightly higher due minimum influence of the armature reaction field.



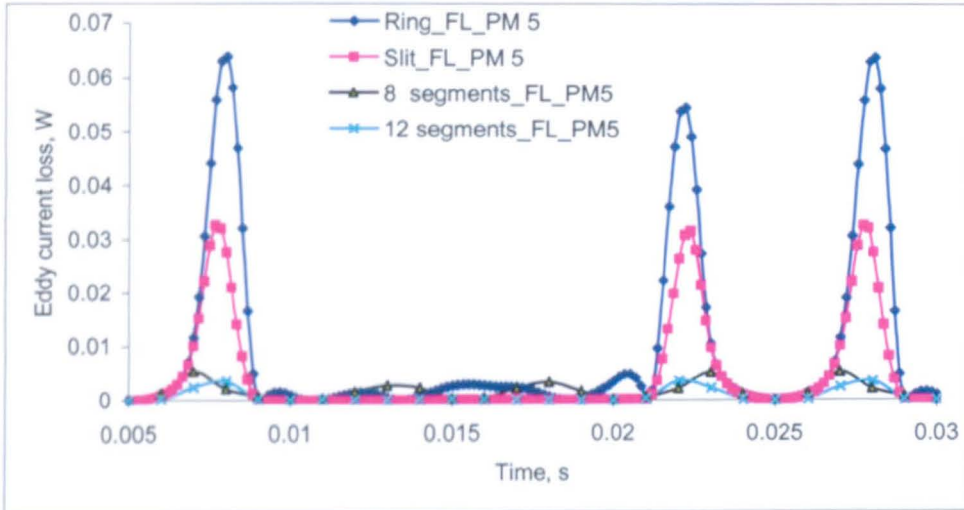
a. PM2



b. PM3



c. PM4

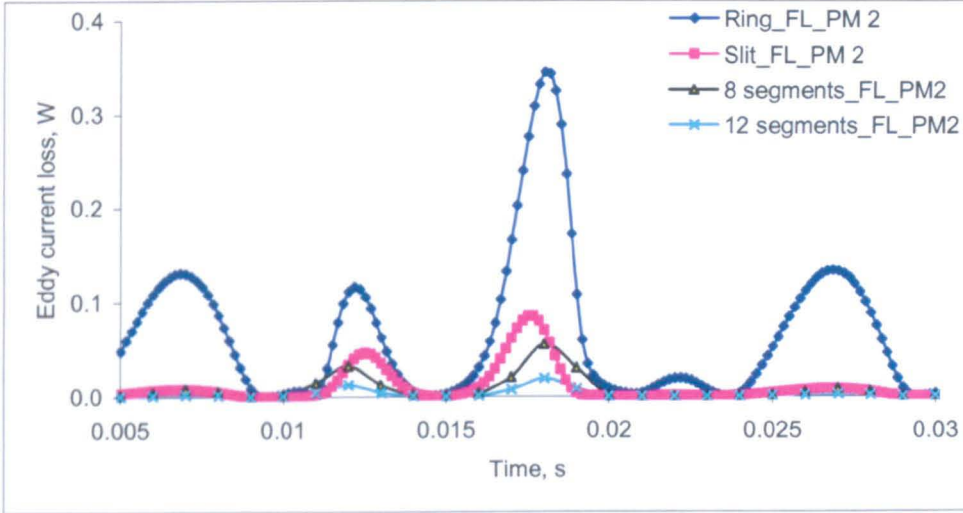


d. PM5

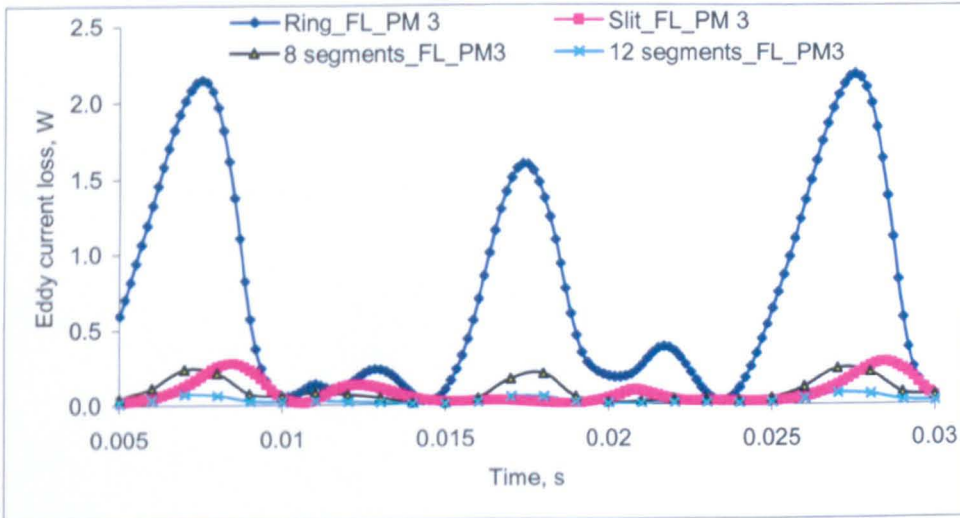
Fig. E.3 Eddy current loss in permanent magnets for air-cored motor at on-load condition

E.2.2 Iron-cored quasi-Halbach magnetised motor with trapezoidal magnets

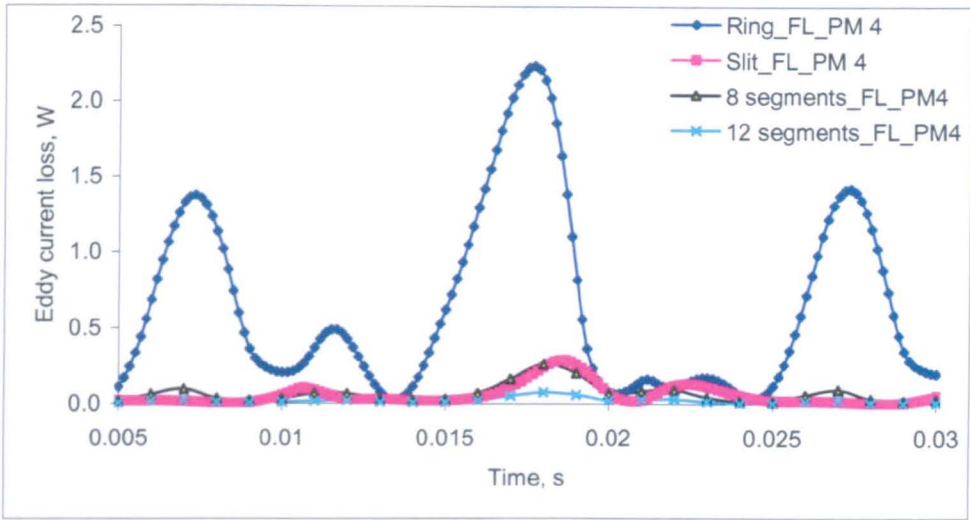
Fig. E.4 shows the time-variations of eddy current loss in permanent magnets for the iron-cored motor at the same on-load condition as that specified in section 5.2.3. Similar to the air-cored motor, the influence of the armature reaction on the flux density waveforms in the magnet is not very significant due to a large effective air-gap to the stator mmf. Thus, with any form of segmentation, the increase in eddy current loss in the permanent magnet is relatively small.



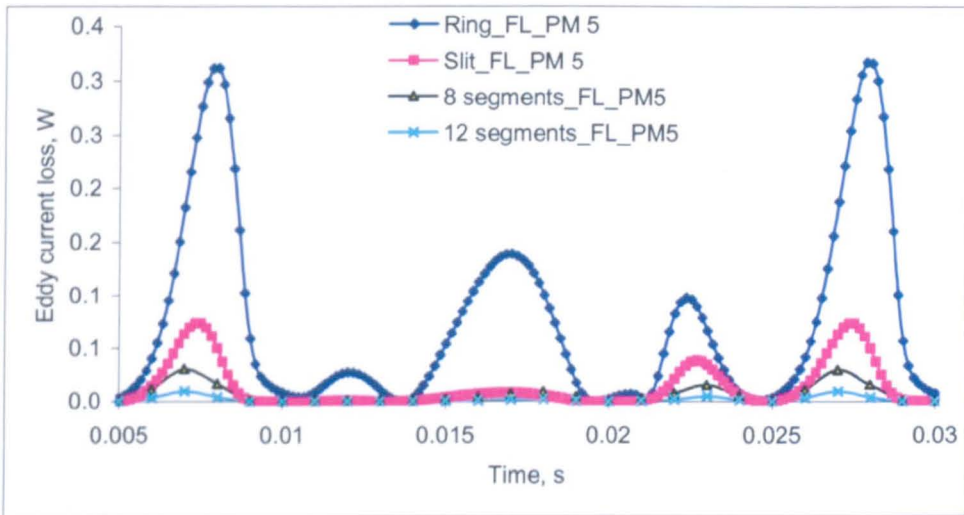
a. PM2



b. PM3



c. PM4



d. PM5

Fig. E.4 Eddy current loss in permanent magnets for iron-cored motor at on-load condition

Appendix F

Analytical solutions of iron-cored quasi-Halbach magnetised motor with Trapezoidal magnets

```
%-----  
% This Matlab function performs design analysis of a single phase, short -stroke,  
% quasi-Halbach magnetised motor with trapezoidal magnets.  
%-----
```

```
%-----  
% B-H curve of mild steel  
%-----
```

```
%      H      B  
BHm=[ 0.0000000E+00 0.0000000E+00  
      0.4010000E+03 0.5338420E+00  
      0.1101000E+04 0.1122760E+01  
      0.3001000E+04 0.1620190E+01  
      0.5201000E+04 0.1779050E+01  
      0.1030100E+05 0.1908120E+01  
      0.1400100E+05 0.1954620E+01  
      0.2000100E+05 0.2007300E+01  
      0.2990100E+05 0.2071410E+01  
      0.1002010E+06 0.2335230E+01];
```

```
%-----  
% B-H curve of Somaloy700 +0.5%Kenolube, cured at 500 C Density 7.32  
%-----
```

```
%      H      B  
BHstl=[0.00      0.00  
      97.56      0.05  
      184.01      0.10  
      244.07      0.15  
      304.13      0.20  
      360.09      0.25  
      413.60      0.30  
      467.11      0.35  
      522.40      0.40  
      578.85      0.45  
      635.30      0.50  
      696.62      0.55  
      759.67      0.60  
      824.00      0.65  
      897.37      0.70  
      970.75      0.75  
     1054.54      0.80  
     1139.52      0.85  
     1240.39      0.90  
     1348.17      0.95  
     1467.65      1.00  
     1611.74      1.05  
     1777.34      1.10  
     1970.42      1.15  
     2209.75      1.20
```

2504.06	1.25
2874.68	1.30
3343.02	1.35
3947.70	1.40
4719.33	1.45
5698.88	1.50
6923.93	1.55
8417.63	1.60];

%-----
 % Iron loss constants (Somaloy 700)
 %-----

kh = 0.08;
 alf = 1.75;
 ke = 1.60e-04;
 sgm = 0.0;
 dst = 7.32e03;
 sth = 0.0;

%-----
 % Design parameters of linear motor
 %-----

Re = 0.05	% Outer radius of stator core(m)
Rm = 0.02	% Outer radius of magnets(m)
hm = 0.005	% Radial thickness of magnets(m)
Tp = 0.025	% Pole Pitch
Tl = 0.2	% Separation distance (8xTp)
msr = 0.42	% Ratio of Tmr to Tp
b0 = 0.01	% Slot opening width (m)
Tpw = 0.04	% Tooth pitch width (m)
Xrs = 0.0105	% Rated stroke (m)(0.0105)

%-----
 % Constants and fixed design parameters of linear motor
 %-----

Brem = 1.14;	% Remanence of magnet
u0 = pi*4e-7;	% Permeability in free space
ur = 1.05;	% Relative recoil permeability of magnet
Pf = 0.65;	% Packing factor
ht = 0.001;	% Height of tooth tip
alp = 30;	% Tooth tip angle (deg)
g = 0.0008;	% Airgap length
Btm = 1.0;	% 1.3 Maximum no load flux density in tooth
Bym = 1.0;	% 1.1 Maximum no load flux density in stator yoke
Bymm = 1.6;	% Maximum no load flux density in translator yoke
Nc = 1;	% Number of turns per pole per phase
rho0 = 1.68e-8;	% Resistivity of copper at 20 degree
rtc = 0.0068e-8;	% Temperature coefficient of copper
aT = 43;	% Ambient temperature
DT = 37;	% Maximum temperature rise of winding temperature
Af = 1.15;	% armature reaction factor (approximately inverse of power factor)
current = 0.5	% Current supply
Vac = 240;	% AC supply voltage (V)
Vm = sqrt(2)*Vac;	% Peak voltage
f = 50.0;	% Supply frequency

```

pi2 = 2*pi;

%-----
% Thermodynamic constants and fixed design parameters of compressor
%-----
global ru q4 np

Xs = 8.25e-3;      % Preset piston position (m)
Xm0 = 11.05e-3;   % Maximum piston amplitude
Ap = 5.31e-4;     % Piston area (m^2),NLX11KK compressor data
Bv = 1.10;        % Viscous damping (N/m/s), estimated from NLX11KK
                    % compressor data
mp = 0.1;         % Piston moving mass (kg)

Td = -40:5:80;

%-----
% Pressure of saturated liquid and vapor (R600a)
%-----
Pslv = [0.028493 0.036560 0.046360 0.058143 0.072175 0.088737 0.10813 0.13065...
        0.15664 0.18642 0.22033 0.25873 0.30198 0.35045 0.40451 0.46456...
        0.53099 0.60419 0.68459 0.77260 0.86866 0.97322 1.0867 1.2097
        1.3427]*1.0e6;
np = 1.1073;      % polytropic gas constant of R600a
tc = 55           %input(' Condensor temperature (C) = ');
te = -25         %input(' Evaporator temperature (C) = ');
Ps = interp1(Td,Pslv,te); % Suction pressure
Pd = interp1(Td,Pslv,tc); % Condenser pressure
AP = Ap*Ps/pi;
rp = Pd/Ps;
cn = 1/np;
ruc = (Pd^cn-Ps^cn)/(Pd^cn+Ps^cn);

%-----
% Input parameters
%-----

disp(' The unit of all dimensional parameters is in meter');
Nsp = 1          %input(' Number of slots = ');
if (Nsp == 1)
    Twp = 0.0;   % only one concentric coil used
else
    Twp = input(' Coil pitch (Tp,m) = ');
end
v = pi*f*Xrs;   % maximum linear velocity (m/s)
Gr = Xm0-Xrs;   % Top clearance at rated operation
Rs = Rm+g;      % Rs value
Tlp = Tl+2*Tp;  % Separation distance + 2*pole pitch
Tlpi = pi2/Tlp;

%-----
% Performance prediction
%-----
vcs= 1/1.3507;  % specific volume at the suction temp.(32C) and pressure
h1 = 612.39;    % enthalpy at the suction temp.(32C) and pressure (Ps)
h2 = 732.79;    % enthalpy at the condensor pressure(Pd) and entropy
h3 = 336.23;    % enthalpy at the condensor temperature(55C) and pressure (Pd)
h14= h1-h3;

```

```

Tmr = Tp*msr;      % Tmr value = Tp*ratio
Tmz = Tp-Tmr;     %Tmz value
Ro = Rm-hm;       % Outer diameter of ferromagnetic tube
Tpf = Tp/2;
Tpt = Tp-b0;

```

```

%-----
% Carter's coefficient
%-----

```

```

gp = g + hm/ur;
bgp= b0/2/gp;
Gam= 4/pi*(bgp*atan(bgp)-0.5*log(1+bgp*bgp));
Kc = Tp/(Tp-Gam*gp);
ge = g+(Kc-1)*gp;
Rse= Rm+ge;

```

```

%-----
% Calculation of Field Coefficients
%-----

```

```

Mra = zeros(200);
Mrb = zeros(200);
Ham = zeros(200);
Hbm = zeros(200);
if Tl==0
    Np = 20;
else
    Np = 100;
end
ic = input(' Calculate coefficients ? (Y or N)', 's');
if (strcmp(ic,'Y'))
    for n = 1:Np
        mn = n*Tlpi;
        mrs = mn*Rse;
        mrm = mn*Rm;
        mro = mn*Ro;
        C1(n) = besseli(0,mrs);
        C2(n) =esselk(0,mrs);
        C3(n) = besseli(1,mrm);
        C4(n) =esselk(1,mrm);
        C5(n) = besseli(0,mrm);
        C6(n) =esselk(0,mrm);
        C9(n) = besseli(0,mro);
        C10(n) =esselk(0,mro);
        Rspan = [mro mrm];
        options = odeset('RelTol',1e-4);
        [Ma,habm] = ode23('Fam',Rspan,[0;0],options);
        ham = habm(:,1);
        hbm = habm(:,2);
        Mb = Ma;
        P1(n) = (-2*Brem/(Tlp*ur*mn))*(sin(mn*Tp)-sin(mn*(Tmr/2+Tmz-hm/2)));
        %
        P2(n)= (2*Brem/(Tlp*ur*hm*mn))*(Tmr/2-hm/2+Tmz)*(sin(mn*(Tmr/2+Tmz+hm/2))-
            sin(mn*(Tmr/2+Tmz-hm/2)))+...

```

```

(2*Brem/(Tlp*ur*hm*mn))*((Tmr/2+Tmz-hm/2)*sin(mn*(Tmr/2+Tmz-hm/2)) -
(Tmr/2+Tmz+hm/2)*sin(mn*(Tmr/2+Tmz+hm/2)))+...
(2*Brem/(Tlp*ur*hm*mn*mn))*(cos(mn*(Tmz+Tmr/2-hm/2))-
cos(mn*(Tmr/2+Tmz+hm/2)));
%
P3(n) = (2*Brem/(Tlp*ur*hm*mn))*(Tmr/2+hm/2)*(sin(mn*(Tmr/2+hm/2))-
sin(mn*(Tmr/2-hm/2)))+...
(2*Brem/(Tlp*ur*hm*mn))*((Tmr/2-hm/2)*sin(mn*(Tmr/2-hm/2))-
(Tmr/2+hm/2)*sin(mn*(Tmr/2+hm/2)))+...
(2*Brem/(Tlp*ur*hm*mn*mn))*(cos(mn*(Tmr/2-hm/2))-
cos(mn*(Tmr/2+hm/2)));
P4(n) = (2*Brem/(Tlp*ur*mn))*(sin(mn*(Tmr/2+hm/2)));
P(n) = (2*P1(n)-P2(n)-P3(n)+2*P4(n))*ur*mn;
ham = ham*P(n)/mn;
hbm = hbm*P(n)/mn;
B1(n) = 4*Brem*(Tmr/2+Tmz+hm/2)*(cos(mn*(Tmr/2+Tmz+hm/2))-
cos(mn*(Tmr/2+Tmz-hm/2)))/(Tlp*ur*hm*mn)+...
4*Brem*(sin(mn*(Tmr/2+Tmz+hm/2))-sin(mn*(Tmr/2+Tmz-
hm/2)))/(Tlp*ur*hm*mn^2)+...
4*Brem*((Tmr/2+Tmz-hm/2)*cos(mn*(Tmr/2+Tmz-hm/2))-
(Tmr/2+Tmz+hm/2)*cos(mn*(Tmr/2+Tmz+hm/2)))/(Tlp*ur*hm*mn);
%
B2(n) = (4*Brem/(Tlp*ur*mn))*(cos(mn*(Tmr/2+Tmz-hm/2))-cos(mn*(Tmr/2+hm/2)));
%
B3(n) = -4*Brem*(Tmr/2-hm/2)*(cos(mn*(Tmr/2+hm/2))-cos(mn*(Tmr/2-
hm/2)))/(Tlp*ur*hm*mn)+...
-4*Brem*(sin(mn*(Tmr/2+hm/2))-sin(mn*(Tmr/2-
hm/2)))/(Tlp*ur*hm*mn^2)+...
-4*Brem*((Tmr/2-hm/2)*cos(mn*(Tmr/2-hm/2))-
(Tmr/2+hm/2)*cos(mn*(Tmr/2+hm/2)))/(Tlp*ur*hm*mn);
B(n) = (B1(n)+B2(n)+B3(n));
c2c4 = C2(n)/C4(n);
c3c1 = C3(n)/C1(n);
c3c5 = ur*C3(n)/C5(n);
c4c10 = C4(n)/C10(n);
c5c1 = C5(n)/C1(n);
c6c4 = C6(n)/C4(n);
c6c10 = C6(n)/C10(n)/ur;
c9c5 = ur*C9(n)/C5(n);
Am = eye(4,4);
Am(1,2) = -c2c4;
Am(2,1) = c3c1;
Am(2,3) = c3c5;
Am(2,4) = c4c10;
Am(3,1) = c5c1;
Am(3,2) = -c6c4;
Am(3,4) = -c6c10;
Am(4,3) = -c9c5;
jam = length(ham);
jbm = length(hbm);
ja(n) = jam;
jb(n) = jbm;
Mra(1:jam,n) = Ma;
Mrb(1:jbm,n) = Mb;
Ham(1:jam,n) = ham;

```

```

Hbm(1:jbm,n) = hbm;
Rhm = [0;ham(jam)*C3(n)-hbm(jbm)*C4(n);(ham(jam)*C5(n)+hbm(jbm)*C6(n))/ur-
B(n);ur*B(n)];
An = inv(Am)*Rhm;
aI(n) = An(1)/C1(n);
bI(n) = An(2)/C4(n);
aII(n) = -ur*An(3)/C5(n);
bII(n) = -An(4)/C10(n);
end;
save coefhic aI bI aII bII Mra Mrb Ham Hbm ja jb;
else
load coefhic;
end;

```

```

%-----
% Calculate flux coefficients of nth harmonic in tooth and yoke regions
%-----

```

```

Btpm = 0.0;
for n = 1:Np
mn = n*Tlpi;
mrs = Rse*mn;
mro = Ro*mn;
Ktpn = sin(mn*Tpt/2);
Brn(n) = (aI(n)*besseli(1,mrs)+bI(n)*besselk(1,mrs));
Krn = Rse*Brn(n);
Krn0 = Ro*(aII(n)*besseli(1,mro)+bII(n)*besselk(1,mro))/mn;
phit(n) = 2*pi2*Ktpn*Krn/mn;
phym(n) = pi2*Krn0;
Btpm = Btpm-Krn*Ktpn/mn;
end;

```

```

%-----
% Calculation of total flux in tooth and yokes
%-----

```

```

for i = 1:361
z(i) = Tp/180*(i-181);
Brs(i) = 0.0;
Mr(i) = 0.0;
Mr1(i) = 0.0;
Mr2(i) = 0.0;
Mr3(i) = 0.0;
Mr4(i) = 0.0;
Mz(i) = 0.0;
Mz1(i) = 0.0;
Mz2(i) = 0.0;
Mz3(i) = 0.0;
psit(i) = 0.0;
psym(i) = 0.0;
for n = 1:Np;
mn = n*Tlpi;
Brs(i) = Brs(i)-Brn(n)*cos(mn*z(i));
Mr(i) = Mr(i)+((2*P1(n)-2*P2(n))+2*P4(n)-2*P3(n))*cos(mn*z(i));
Mr1(i) = Mr1(i)+2*P1(n)*cos(mn*z(i));
Mr2(i) = Mr2(i)+2*P2(n)*cos(mn*z(i));

```

```

Mr3(i) = Mr3(i)+2*P3(n)*cos(mn*z(i));
Mr4(i) = Mr4(i)+2*P4(n)*cos(mn*z(i));
Mz(i) = Mz(i)+ B(n)*sin(mn*z(i));
Mz1(i) = Mz1(i)+ B1(n)*sin(mn*z(i));
Mz2(i) = Mz2(i)+ B2(n)*sin(mn*z(i));
Mz3(i) = Mz3(i)+ B3(n)*sin(mn*z(i));
psit(i) = psit(i)-phit(n)*cos(mn*(Tpf-z(i)));
psym(i) = psym(i)+phym(n)*sin(mn*z(i));
end;
psiy(i) = psit(i)/2;
end;

%-----
% Calculation of the thickness of back iron (yoke)
%-----
phimax = max(abs(psym*0.8)); % Smooth out the peak
Rb = sqrt(Ro^2-phimax/pi/Bymm); % Thickness of the back-iron
hym = Ro-Rb;

%-----
% Calculate stator yoke thickness, tooth and slot width
%-----
c = max(psiy)/Bym/pi;
Re-sqrt(Re*Re-c); % Radial thickness of stator yoke
hys = input(' Input the thickness of stator yoke = ');
Rh = Re-hys;
wb = 2*pi*7800*Tp*(Ro^2-Rb^2); % weight of back-iron
wm = 2*pi*7500*(Tmr+Tmz)*(Rm^2-Ro^2); % weight of magnets
twm = wm+wb;

Tw2 = max(psit)/Btm/(pi*(Rh+Rs+ht));
Sw2 = Tpw-Tw2;
Tw1= Tw2;
Sw1= Sw2;
a = tan(alp*pi/180);
thh = (Sw1-b0)/2*a;
hs = Rh-Rs; % tooth height
Sa = (hs-ht-thh)*(Tpw-Tw1);%(Sw1+Sw2)/2; % Slot area

%-----
% Calculate the slot volume per pole pair and permissible rms current density
%-----

a = Sw1;
b = Sw2;
R1= Rs+ht+thh;
R2= Rh;
c = (b-a)/(R2-R1);
Vs = 2*pi*(0.5*(a-c*R1)*(R2^2-R1^2)+1/3*c*(R2^3-R1^3));
Vs = Vs*Nsp; % Total slot volume
As = pi2*(Re^2*(Tp+Xrs)+(Re^2-Rs^2)); % Total surface dissipation area
rho = rho0+rtc*(DT+aT-20); % Resistivity of copper at operating temperature

```

```

%-----
% Calculate mmf drops in stator and mover cores
%-----
Brsm = abs(max(Brs)); % maximum flux density at the stator bore
Hym = interp1(BHm(:,2),BHm(:,1),Bymm); % Hm in mover yoke
Hys = interp1(BHstl(:,2),BHstl(:,1),Bym*Af); % Hm in stator yoke
Hyt = interp1(BHstl(:,2),BHstl(:,1),Btm*Af); % Hm in stator teeth
DG = u0*(2*(hs-ht-thh)*Hyt+Tp*(Hys+Hym))/Brsm; % Fictitious air gap due to mmf
drops
Rsea = Rse + DG;

%-----
% Re-calculate field solution
%-----
Rse = Rsea;
for n = 1:Np
    mn = n*Tlpi;
    mrs = mn*Rse;
    mrm = mn*Rm;
    mro = mn*Ro;
    C1(n) = besseli(0,mrs);
    C2(n) = besserk(0,mrs);
    C3(n) = besseli(1,mrm);
    C4(n) = besserk(1,mrm);
    C5(n) = besseli(0,mrm);
    C6(n) = besserk(0,mrm);
    C9(n) = besseli(0,mro);
    C10(n) = besserk(0,mro);
    Rspan = [mro mrm];
    options = odeset('RelTol',1e-4);
    [Ma,habm] = ode23('Fam',Rspan,[0;0],options);
    ham = habm(:,1);
    hbm = habm(:,2);
    Mb = Ma;
    P1(n) = (-2*Brem/(Tlp*ur*mn))*(sin(mn*Tp)-sin(mn*(Tmr/2+Tmz-hm/2)));
    %
    P2(n) = (2*Brem/(Tlp*ur*hm*mn))*(Tmr/2-hm/2+Tmz)*(sin(mn*(Tmr/2+Tmz+hm/2))-
        sin(mn*(Tmr/2+Tmz-hm/2)))+...
        (2*Brem/(Tlp*ur*hm*mn))*((Tmr/2+Tmz-hm/2)*sin(mn*(Tmr/2+Tmz-hm/2))-
        (Tmr/2+Tmz+hm/2)*sin(mn*(Tmr/2+Tmz+hm/2)))+...
        (2*Brem/(Tlp*ur*hm*mn*mn))*(cos(mn*(Tmz+Tmr/2-hm/2))-
        cos(mn*(Tmr/2+Tmz+hm/2)));
    %
    P3(n) = (2*Brem/(Tlp*ur*hm*mn))*(Tmr/2+hm/2)*(sin(mn*(Tmr/2+hm/2))-
        sin(mn*(Tmr/2-hm/2)))+...
        (2*Brem/(Tlp*ur*hm*mn))*((Tmr/2-hm/2)*sin(mn*(Tmr/2-hm/2))-
        (Tmr/2+hm/2)*sin(mn*(Tmr/2+hm/2)))+...
        (2*Brem/(Tlp*ur*hm*mn*mn))*(cos(mn*(Tmr/2-hm/2))-
        cos(mn*(Tmr/2+hm/2)));
    P4(n) = (2*Brem/(Tlp*ur*mn))*(sin(mn*(Tmr/2+hm/2)));
    P(n) = (2*P1(n)-P2(n)-P3(n)+2*P4(n))*ur*mn;
    ham = ham*P(n)/mn;
    hbm = hbm*P(n)/mn;
    B1(n) = 4*Brem*(Tmr/2+Tmz+hm/2)*(cos(mn*(Tmr/2+Tmz+hm/2))-
        cos(mn*(Tmr/2+Tmz-hm/2)))/(Tlp*ur*hm*mn)+...

```

```

4*Brem*(sin(mn*(Tmr/2+Tmz+hm/2))-sin(mn*(Tmr/2+Tmz-
hm/2)))/(Tlp*ur*hm*mn^2)+...
4*Brem*((Tmr/2+Tmz-hm/2)*cos(mn*(Tmr/2+Tmz-hm/2))-
(Tmr/2+Tmz+hm/2)*cos(mn*(Tmr/2+Tmz+hm/2)))/(Tlp*ur*hm*mn);
%
B2(n) = (4*Brem/(Tlp*ur*mn))*(cos(mn*(Tmr/2+Tmz-hm/2))-cos(mn*(Tmr/2+hm/2)));
%
B3(n) = -4*Brem*(Tmr/2-hm/2)*(cos(mn*(Tmr/2+hm/2))-cos(mn*(Tmr/2-
hm/2)))/(Tlp*ur*hm*mn)+...
-4*Brem*(sin(mn*(Tmr/2+hm/2))-sin(mn*(Tmr/2-
hm/2)))/(Tlp*ur*hm*mn^2)+...
-4*Brem*((Tmr/2-hm/2)*cos(mn*(Tmr/2-hm/2))-
(Tmr/2+hm/2)*cos(mn*(Tmr/2+hm/2)))/(Tlp*ur*hm*mn);
B(n) = (B1(n)+B2(n)+B3(n));
c2c4 = C2(n)/C4(n);
c3c1 = C3(n)/C1(n);
c3c5 = ur*C3(n)/C5(n);
c4c10 = C4(n)/C10(n);
c5c1 = C5(n)/C1(n);
c6c4 = C6(n)/C4(n);
c6c10 = C6(n)/C10(n)/ur;
c9c5 = ur*C9(n)/C5(n);
Am = eye(4,4);
Am(1,2) = -c2c4;
Am(2,1) = c3c1;
Am(2,3) = c3c5;
Am(2,4) = c4c10;
Am(3,1) = c5c1;
Am(3,2) = -c6c4;
Am(3,4) = -c6c10;
Am(4,3) = -c9c5;
jam = length(ham);
jbm = length(hbm);
ja(n) = jam;
jb(n) = jbm;
Mra(1:jam,n) = Ma;
Mrb(1:jbm,n) = Mb;
Ham(1:jam,n) = ham;
Hbm(1:jbm,n) = hbm;
Rhm = [0;ham(jam)*C3(n)-hbm(jbm)*C4(n);(ham(jam)*C5(n)+hbm(jbm)*C6(n))/ur-
B(n);ur*B(n)];
An = inv(Am)*Rhm;
aI(n) = An(1)/C1(n);
bI(n) = An(2)/C4(n);
aII(n) = -ur*An(3)/C5(n);
bII(n) = -An(4)/C10(n);
end;
%-----
% Calculate flux linkage, force and emf coefficients of nth harmonic
%-----
for n = 1:Np
mn = n*Tlpi;
mrs = Rse*mn;
mnb = mn*b0/2;
kdn = sin(mnb)/mnb;

```

```

if (Twp <= 0)
    kpn = 1.0;
else
    kpn = 1-cos(mn*Twp);
end
Krn = Rse*(aI(n)*besseli(1,mrs)+bI(n)*besselk(1,mrs));
kn = Krn*kdn*kpn;
KT(n) = pi2*kn;
phi(n) = KT(n)/mn;
end;

%-----
% Calculation of the flux linkage of stator winding
%-----
for i = 1:101
    zd(i) = Xrs/50*(i-51);
    psi(i) = 0.0;
    emf(i) = 0.0;
    for n = 1:Np
        mn = n*Tlpi;
        mrs = mn*Rse;
        psi(i) = psi(i)- phi(n)*sin(mn*zd(i));
        emf(i) = emf(i)- KT(n)*cos(mn*zd(i));
    end
end
psi = psi*Nc;
KEPT = mean(emf); % Average emf constant per turn
KFPT = KEPT; % Average force constant per turn

%-----
% Calculation of iron loss
%-----
Ay = pi*(Re^2-(Re-hys)^2); % Yoke area
At = Tw2*(pi*(Rh+Rs+ht)); % Tooth area
av = 2*v/pi; % Average velocity
Atp = pi*((Rs+ht+thh)^2-Rs^2); % Tooth tip area
Btn = phit/At; % Flux coefficient at tooth per area
Byn = phit/2/Ay; % Flux coefficient at yoke per area
Btpx = phit/Atp; % Flux coefficient at tooth tip per area
Bt = psit/At; % Total flux at tooth per area(flux density)
By = psiy/Ay; % Total flux at yoke per area (flux density)
Btp = psit/Atp; % Total flux at tooth tip per area (flux
density)

for i = 1:361
    dBt(i) = 0.0;
    dBy(i) = 0.0;
    dBtp(i) = 0.0;
    for n = 1:Np;
        mn = n*Tlpi;
        dBt(i) = dBt(i)+mn*av*Btn(n)*sin(mn*(Tpf-z(i)));
        dBy(i) = dBy(i)+mn*av*Byn(n)*sin(mn*(Tpf-z(i)));
        dBtp(i) = dBtp(i)+mn*av*Btpx(n)*sin(mn*(Tpf-z(i)));
    end;
end;
end;

```

```

T = 2*Tp/av; % Electrical period
fl = 1/T; % Electrical frequency at v
dt = Tp/180/av; % Time step
Bthm = (max(Bt)-min(Bt))/2; % Peak value of flux density in teeth
Byhm = (max(By)-min(By))/2; % Peak value of flux density in yoke
Btpm = (max(Btp)-min(Btp))/2;
th_w = 2*pi*((Re-hys)^2-(Rs+ht+thh)^2)*Tw2*dst; % Tooth weight
yk_w = 2*Ay*Tp*dst; % Yoke weight
%tp_w = 4*pi*Rs*(Tpt*ht+thh*(Tpt+Tw2)/2)*dst; % Tooth tip weight
tp_w = 2*(((Rs+ht+thh)^2-Rs^2)*Tw2*pi+((Rs+ht)^2-Rs^2)*(Sw1-
b0)/2*pi+(((Rs+ht+thh)^2-(Rs+ht)^2)*(Sw1-b0)/2)/2*pi)*dst;
c1 = 0.0;
c2 = 0.0;
c3 = 0.0;
c4 = 0.0;
c5 = 0.0;
c6 = 0.0;
for j=1:361
    c1 = c1 + (dBt(j)^2)*dt;
    c2 = c2 + ((abs(dBt(j)))^1.5)*dt;
    c3 = c3 + (dBy(j)^2)*dt;
    c4 = c4 + ((abs(dBy(j)))^1.5)*dt;
    c5 = c5 + (dBtp(j)^2)*dt;
    c6 = c6 + ((abs(dBtp(j)))^1.5)*dt;
end

%Iron loss in tooth
Phit = kh*fl*(Bthm^alf)*th_w;
Pcit = sgm*sth*sth/12/dst*f*c1*th_w;
Peit = ke*fl*c2*th_w;

%Iron loss in yoke
Phiy = kh*fl*(Byhm^alf)*yk_w;
Pciy = sgm*sth*sth/12/dst*f*c3*yk_w;
Peiy = ke*fl*c4*yk_w;

%Iron loss in tooth tip
Phitp = kh*fl*(Btpm^alf)*tp_w;
Pcftp = sgm*sth*sth/12/dst*f*c5*tp_w;
Peitp = ke*fl*c6*tp_w;

%
Pirnt = Phit+Pcit+Peit;
Pirny = Phiy+Pciy+Peiy;
Pirntp = Phitp+Pcftp+Peitp;

% Total iron loss
Pirm = Pirnt+Pirny+Pirntp;

%-----
% Calculate self inductances per turn (bipolar winding)
%-----
Ls = 0.0;
for n=1:Np

```

```

mn = n*Tlpi;
mrs = mn*Rse;
mro = mn*Ro;
mnb = mn*b0/2;
kdn = sin(mnb)/mnb;
if (Twp <= 0)
    kpn = sin(mn*Tlp/4);
else
    kpn = 1-cos(Nsp*Twp*mn/2);
end
Jm(n) = 2*kpn*kdn/Tlp;
c1n = besseli(0,mro);
c2n =esselk(0,mro);
c3n = besseli(0,mrs);
c4n =esselk(0,mrs);
c5n = besseli(1,mrs);
c6n =esselk(1,mrs);
Detn = c2n*c3n-c1n*c4n;
Ln = Jm(n)*(c2n*c5n+c1n*c6n)*kpn*kdn/mn/Detn;
Ls = Ls + Ln;
end
Ls = u0*2*pi*Rse*Ls;

%-----
%Calculate slot leakage inductance
%-----
le= Rh-(Rh-thh-ht-Rs)/2;
%le = (Rh+Rs+ht+thh)/2; % Average radius of coil
Lsk0 = u0*2*pi*((Rs+ht)*(ht/b0+2*thh/(Sw1+b0))
+le*(hs-ht-thh)/3/Sw1);
Ls0 = Ls + Nsp*Lsk0; % Total self-inductance per turn

%-----
% Calculate resistance and inductance constants
%-----
omega = pi2*f;
m = twm + mp; % Total moving mass

%-----
% Calculate steady state compressor characteristic
%-----

ic = input(' Calculate characteristic data ? (Y or N)', 's');
if (strcmp(ic, 'Y'))
for i = 1:100
ru = 0.01*i;
Ru(i) = ru;
if (ru <= ruc)
q2 = pi;
q4 = 2*pi;
fhr(i) = 0.0;
else
a1 = ((Ps/Pd)^cn*(1+ru)-1)/ru;
q2 = acos(a1);
a1 = ((Pd/Ps)^cn*(1-ru)-1)/ru;

```

```

    q4 = 2*pi-acos(a1);
    fhr(i) = (np/(np-1))*(rp*(cos(q2)+1)+cos(q4)-1)/ru;
end
Qspan = [0 q2];
clear FFs1 FFs2 FFk1 FFk2
options = odeset('RelTol',1e-4);
[qt FFs1] = ode23('Fs1',Qspan,[0;0],options);
is1 = length(FFs1(:,1));
ik1 = length(FFs1(:,1));
if (q4<= pi)
    fsr(i) = FFs1(is1,1)+rp*(pi-q2)-q4;
    fkr(i) = FFs1(ik1,2);
else
    Qspan = [pi q4];
    [qt FFs2] = ode23('Fs2',Qspan,[0;0],options);
    is2 = length(FFs2(:,1));
    ik2 = length(FFs2(:,2));
    fsr(i) = FFs1(is1,1)+FFs2(is2,1)+rp*(pi-q2)-q4;
    fkr(i) = FFs1(ik1,2)+FFs2(ik2,2);
end
end
Fs = fsr*(AP/2);
fkr = fkr*AP;
fhr = fhr*AP;
save charadata Ru Fs fsr fkr fhr
else
    load charadata
end
keq0 = fkr/Xm0;
heq0 = fhr/Xm0;
[keqm,im] = max(keq0);
keqa = mean(keq0(im:100)); % Average stiffness of gas
rue = Xrs/Xm0;
heqa = interp1(Ru,heq0,rue); % Equivalent gas damping at rated operation
K = m*(omega)^2 - keqa; % Spring constant
Fsa = mean(Fs(im:100)); % Average static force of gas
Xs = Xm0 - Fsa/K; % Piston preset position
X0E = Xs+Fsa/K;
for i=1:100
    U(i) = X0E(i)*Ru(i);
    keq(i) = fkr(i)/X0E(i);
    heq(i) = fhr(i)/X0E(i);
    if (i<im)
        etv(i)=0;
    else
        etv(i)=1.0-(X0E(i)-U(i))/2/U(i)*((Pd/Ps)^cn-1); % Clearance volumetric efficiency
    end
end
end
%-----
%Determine the number of turns per pole per phase
%-----
we = pi2*f;
Jrms = (we*Bv+heqa)*Xrs/(KEPT*Sa*Pf)/sqrt(2); % Jrms is determined by
Deta = (K+keqa-we^2*m)^2+(we*Bv+heqa)^2; % required compressing force
JSP = Jrms*Sa*Pf;

```

```

ic = input(' input Ls0 ? (Y or N)', 's');
if (strcmp(ic, 'Y'))
    Ls0 = input(' Permeance of stator coil = ');
end
KLO = omega*Ls0*JSP; % Bipolar winding
KR0 = 2*pi*Nsp*le*rho*Jrms;
KREC = we*JSP*(KEPT^2)*(we*Bv+heqa)/Deta;
KLEC = we*JSP*(KEPT^2)*(K+keqa-we^2*m)/Deta;
Nc = round(Vac/sqrt((KREC+KR0)^2+(KLO+KLEC)^2));
ic = input(' input Nc ? (Y or N)', 's');
if (strcmp(ic, 'Y'))
    Nc = input(' Number of turns = ');
end
%-----
% motor parameters
%-----
emf = Nc*emf; % emf constant
F = emf*Jrms*Pf*Sa;
R = Nsp^2*pi*le*rho/Pf/Sa*Nc*Nc; % phase resistance
Le = Ls0*Nc^2; % phase inductance
Ke = KEPT*Nc; % Average emf constant
Kt = KFPT*Nc; % Average force constant
for i = 361
    z(i) = Tp/180*(i-181);
    Force(i) = 0.0;
    Force(i) = Force(i)+Kt*z(i)*0.5;
end;
%-----
% Performance prediction
%-----
vcs = 1/1.3507; % specific volume at the suction temp.(32C) and pressure
h1 = 612.39; % enthalpy at the suction temp.(32C) and pressure (Ps)
h2 = 732.79; % enthalpy at the condensor pressure(Pd) and entropy
h3 = 336.23; % enthalpy at the condensor temperature(55C) and pressure(Pd)
h14 = h1-h3;
%-----
% Calculate performance at a given frequency
%-----
we = 2*pi*f;
Xe = we*Le;
Ze2 = R^2+Xe^2;
a1 = sqrt(Ze2)/Kt;
c1 = K-we^2*m+(we*Kt)^2*Le/Ze2;
c2 = we*Bv+we*Kt^2*R/Ze2;
fAv = f*Ap/vcs;
[Um, ium] = max(U);
for i = 1:iium
    V(i) = a1*sqrt((c1+keq(i))^2+(c2+heq(i))^2)*U(i)/sqrt(2);
    Det = (K+keq(i)-we^2*m)^2+(we*Bv+heq(i))^2;
    Rec = Kt*Kt*we*(we*Bv+heq(i))/Det;
    Lec = Kt*Kt*(K+keq(i)-we^2*m)/Det;
    Res(i) = R+Rec;
    Les(i) = Le+Lec;
end

```

```

Rep(i) = Kt*Kt*we*heq(i)/Det;
Rev(i) = (Kt*we)^2*Bv/Det;
Zes(i) = sqrt(Res(i)^2+(we*Les(i))^2);
I(i) = V(i)/Zes(i);
cosf(i) = Res(i)/Zes(i);
Po(i) = Rep(i)*I(i)^2;
Pcu(i) = R*I(i)^2;
Pi(i) = V(i)*I(i)*cosf(i)+Pirn;
Pom(i) = Pi(i)-Pcu(i)-Pirn;
etam(i) = Pom(i)/Pi(i);
Pv(i) = Rev(i)*I(i)^2;
eta(i)= Po(i)/Pi(i);
    md(i) = 2*U(i)*fAv*etv(i);           % mass flow rate
    Pc(i) = h14*md(i)*1000;             % Cooling capacity in W
    Cop(i)= Pc(i)/Pi(i);                % Coefficient of performance
end
disp(' Performance at 0.85 volumetric efficiency')
Motoreff = interp1(etv(im:iium),etam(im:iium),0.865)
Systemeff = interp1(etv(im:iium),eta(im:iium),0.865)
Outpower = interp1(etv(im:iium),Pom(im:iium),0.865)
Copperloss = interp1(etv(im:iium),Pcu(im:iium),0.865)
COP = interp1(etv(im:iium),Cop(im:iium),0.865)
PC = interp1(etv(im:iium),Pc(im:iium),0.865)
POM = interp1(etv(im:iium),Pom(im:iium),0.865)
XRS = interp1(etv(im:iium),U(im:iium),0.865)

disp(' 1D arrays: i -- index for piston amplitude U')
disp(' V(i)    --- Supply rms voltage (V)')
disp(' I(i)    --- Supply rms current (A)')
disp(' Res(i)  --- Equivalent system resistance (ohm)')
disp(' Les(i)  --- Equivalent system inductance (H)')
disp(' Zes(i)  --- Equivalent system impedance (ohm)')
disp(' Rep(i)  --- Equivalent resistance for useful work (ohm)')
disp(' Rev(i)  --- Equivalent resistance due to viscous damping (ohm)')
disp(' Po(i)   --- Output power (W)')
disp(' Pi(i)   --- Input power (W)')
disp(' Pv(i)   --- Power consumption on the viscous damping (W)')
disp(' cosf(i) --- Power factor)')
disp(' eta(i)  --- Efficiency of linear compressor system')
disp(' etam(i) --- Efficiency of linear motor)')
disp(' etv(i)  --- Efficiency of Clearance volumetric efficiency')
disp(' md(i)   --- Mass flow rate)')
disp(' Pc(i)   --- Cooling capacity in Watt)')
disp(' Cop(i)  --- Coefficient of performance)')

```